Integrated ultra-high-Q nonlinear photonic platform for on-chip optoelectronic systems

Thesis by
Kiyoul Yang

In Partial Fulfillment of the Requirements for the
degree of
Doctor of Philosophy

CALIFORNIA INSTITUTE OF TECHNOLOGY
Pasadena, California

2018
Defended June 14, 2017

Kiyoul Yang
ORCID: 0000-0002-0587-3201

To my parents,
늘 제 곁에 있어주셔서 감사합니다.
존경하는 아버지, 어머니께 헌정합니다.

ACKNOWLEDGEMENTS

First and foremost, I would like to express my gratitude to advisor, Prof. Kerry Vahala, for his support and guidance. Prof. Vahala has always devoted to serve his role as an academic mentor and research advisor. Also, his thoughtful evaluation provided a lot of guidance, and I have learned invaluable lessons in planning and managing research projects. It has been a privilege to be his student.

I would also like to thank Dr. Scott Diddams for his support and encouragement during my graduate studies. I was fortunate to have him as my another mentor and to have a chance to work with his group since 2012. It was also an invaluable experience to work at his group in NIST, and I truly enjoyed discussions and the collaboration – many thanks to Dr. Scott Papp as well for his support.

My appreciation also goes to my colleagues. I enjoyed productive collaboration with Xu Yi and Qi-Fan Yang in Caltech and also created an exciting collaboration with Katja Beha, Dan Cole, and Pascal Del'Haye in NIST. I gratefully acknowledge Dongyoon Oh, Hansuek Lee, Myoung-Gyun Suh, Seung Hoon Lee, Boqiang Shen, Heming Wang, Xinbai Li, Yu-Hung Lai, Barry Baker, Lin Chang, Yonghwi Kim, Sophia Cheng, Guy Derose, Melissa Melendes, and Matthew Sullivan for their support. I also want to thank William Loh, Kukjoo Kim, Tackhoon Kim, Hyunsoo Cho, Sum Kim, Han Chao, Sungwook Chang, and Minseok Jang for their friendship.

I want to thank Prof. Changhuei Yang who helped me settle in and was devoted to our discussion. In particular, I enjoyed the moment when we solved optics and math problems on the board together over a long discussion. I want to thank Prof. Stefan Maier and Prof. Vincenzo Giannini for their support from England. I want to thank Prof. Atwater, Prof. Emami, Prof. Hajimiri, and Prof. Scherer for their service as my graduation committee and insightful inputs to this thesis. I likewise thank my former advisor, Prof. Kyung Cheol Choi. I was fortunate to start research with him, and he has served as my mentor for my academic career.

Finally, my deepest gratitude goes to Wonji Choi and my family. Wonji Choi has really changed my life here, and made it meaningful and enjoyable. My family is endless source of encouragement, enthusiasm, endeavor, and patience in my daily life. I am happy and thankful to be part of this family. Wish I could reach my dad in heaven and tell him that I finished my study.

ABSTRACT

Silicon technology provided a concrete basis of the integrated microelectronics revolution, and it might usher disruptive advances in photonics again. An integrated photonic system can potentially revolutionize instrumentation, time standards, spectroscopy, and navigation. Driven by these applications, various high-Q platforms have emerged over the last decade. However, applications require to satisfy challenging combinations of ultra-high-Q (UHQ) cavity performance, monolithic integration, and nonlinear cavity designs: the monolithic integration of UHQ devices still remains elusive. In this thesis, an integrated UHQ microcavity is demonstrated for the first time. A silicon nitride waveguide is monolithically integrated with a silicon oxide cavity, and the integrated waveguide can provide nearly universal interface to other photonic devices. Significantly, this thesis discusses far beyond setting a new record for integrated Q factor: the integrated UHQ cavity provides functionality as soliton source with electronic-repetition-rates. Demonstration of low-pump-power soliton generation at 15 GHz was previously possible in only discrete devices but essentially required for integrated self-referenced comb, which can unlock new level of performance and scale in an optoelectronic system. In addition, nonlinear cavity design is another outstanding challenge towards a further development on the optoelectronic system, and will be discussed in this thesis. The dispersion-engineered platform can potentially tailor the spectral bandwidth of frequency comb, and extend the frequency comb to visible and ultraviolet band. Importantly, the design methods are directly transferable to the integrated platform.

PUBLISHED CONTENT AND CONTRIBUTIONS

† equal contribution

[1] **K.Y. Yang**†, D. Y. Oh†, S. H. Lee†, Q.-F. Yang, X. Yi, B. Shen, H. Wang, and K. Vahala, "Bridging ultrahigh-Q devices and photonic circuits", **Nature Photonics** (2018) 10.1038/s41566-018-0132-5,

K.Y.Y. participated in the conception of the project, co-developed the device structure, co-demonstrated the numerical design, developed microfabrication process, prepared the devices, co-demonstrated the soliton generation and the Brillouin lasing, prepared the data and participated in the writing of the manuscript.

[2]D. T. Spencer, et al., "An optical-frequency synthesizer using integrated photonics", **Nature** (2018) 10.1038/s41586-018-0065-7,

K.Y.Y. co-developed the silica soliton source, co-fabricated the devices, and led Caltech's contributions for the scientific collaboration (DARPA DODOS program) under Prof. Vahala's supervision.

[3]D. Y. Oh†, **K.Y. Yang**†, C. Fredrick†, G. Ycas, S. A. Diddams, and K. J. Vahala, "Coherent ultra-violet to near-infrared generation in silica ridge waveguides", **Nature Communications 8**, 13922 (2017) 10.1038/ncomms13922,

K.Y.Y. participated in the conception of the project, developed the dispersion engineering method, co-demonstrated the numerical design, developed microfabrication process, prepared the devices, prepared the data and participated in the writing of the manuscript.

[4] **K.Y. Yang**, et al., "Broadband dispersion-engineered microresonator on a chip", **Nature Photonics 10**, 316–320 (2016) 10.1038/nphoton.2016.36,

K.Y.Y. proposed the conception of the project, demonstrated the numerical design, developed microfabrication process, prepared the devices, co-developed the dispersion measurement setup, prepared the data and participated in the writing of the manuscript.

[5]X. Yi†, Q.-F. Yang†, **K.Y. Yang**†, M.-G. Suh, and K. Vahala, "Soliton frequency comb at microwave rates in a high-Q silica microresonator", **Optica 2**, 1078–1085 (2015) 10.1364/OPTICA.2.001078,

K.Y.Y. participated in the conception of the project, demonstrated the mode spectrum engineering, fabricated the devices, demonstrated the numerical calculation, and participated in the writing of the manuscript.

[6]H. Lee†, T. Chen†, J. Li†, **K.Y. Yang**, S. Jeon, O. Painter, and K. J. Vahala, "Chemically etched ultrahigh-Q wedge-resonator on a silicon chip", **Nature Photonics 6**, 369–373 (2012) 10.1038/nphoton.2012.109,

K.Y.Y. co-demonstrated the numerical calculation and the microfabrication, and prepared the data (Fig.1c and Fig.5).

[7]J. Li, H. Lee, **K.Y. Yang**, and K. J. Vahala, "Sideband spectroscopy and dispersion measurement in microcavities", **Optics Express 20**, 26337–26344 (2012) 10.1364/OE.20.026337,

K.Y.Y. co-demonstrated the dispersion measurement and the numerical calculation, prepared the data (Fig.4), and participated in the writing of the manuscript.

LIST OF RELATED PUBLICATIONS

[1]Y.-H. Lai, **K.Y. Yang**, M.-G. Suh, and K. J. Vahala, "Fiber taper characterization by optical backscattering reflectometry", **Optics Express 25**, 22312 (2017) 10.1364/OE.25.022312.

[2]S. H. Lee†, D. Y. Oh†, Q.-F. Yang†, B. Shen†, H. Wang†, **K.Y. Yang**, Y.-H. Lai, X. Yi, and K. Vahala, "Towards visible soliton microcomb generation", **Nature Communications 8**, 1295 (2017) 10.1038/s41467-017-01473-9.

[3]Q.-F. Yang†, X. Yi†, **K.Y. Yang**, and K. Vahala, "Counter-propagating solitons in microresonators", **Nature Photonics 11**, 560–564 (2017) 10.1038/nphoton.2017.117.

[4]Q.-F. Yang†, X. Yi†, **K.Y. Yang**, and K. Vahala, "Stokes solitons in optical microcavities", **Nature Physics 13**, 53–57 (2017) 10.1038/nphys3875.

[5]X. Yi†, Q.-F. Yang†, X. Zhang†, **K.Y. Yang**, X. Li, and K. Vahala, "Single-mode dispersive waves and soliton microcomb dynamics", **Nature Communications 8**, 14869 (2017) 10.1038/ncomms14869.

[6]P. Del'Haye, A. Coillet, T. Fortier, K. Beha, D. C. Cole, **K.Y. Yang**, H. Lee, K. J. Vahala, S. B. Papp, and S. A. Diddams, "Phase-coherent microwave-to-optical link with a self-referenced microcomb", **Nature Photonics 10**, 516–520 (2016) 10.1038/nphoton.2016.105.

[7]M.-G. Suh†, Q.-F. Yang†, **K.Y. Yang**, X. Yi, and K. J. Vahala, "Microresonator soliton dual-comb spectroscopy", **Science 354**, 600–603 (2016) 10.1126/science.aah6516.

[8]Q.-F. Yang†, X. Yi†, **K.Y. Yang**, and K. Vahala, "Spatial-mode-interaction-induced dispersive waves and their active tuning in microresonators", **Optica 3**, 1132–1135 (2016) 10.1364/OPTICA.3.001132.

[9]X. Yi†, Q.-F. Yang†, **K.Y. Yang**, and K. Vahala, "Active capture and stabilization of temporal solitons in microresonators", **Optics Letters 41**, 2037–2040 (2016) 10.1364/OL.41.002037.

[10]X. Yi†, Q.-F. Yang†, **K.Y. Yang**, and K. Vahala, "Theory and measurement of the soliton self-frequency shift and efficiency in optical microcavities", **Optics Letters 41**, 3419–3422 (2016) 10.1364/OL.41.003419.

[11]D. Y. Oh†, D. Sell†, H. Lee, **K.Y. Yang**, S. A. Diddams, and K. J. Vahala, "Supercontinuum generation in an on-chip silica waveguide", **Optics Letters 39**, 1046–1048 (2014) 10.1364/OL.39.001046.

TABLE OF CONTENTS

[1] Section 2.3 has appeared in Nature Photonics 6, 369-373, 2012

[2]Main body of this chapter has appeared in Nature Photonics 10, 316-320, 2016; Subsection 3.3.2, and 3.4.1 have appeared in Optics Express 20, 26337-26344, 2012; Subsection 3.4.3 have appeared in Optica 2, 1078-1085, 2015.

[3] Section 4.3-4.7 have appeared in Nature Communications 8, 13922, 2017

[4]Section 5.2-5.6 have appeared in Arxiv 1702.05076, 2017. Section 5.7 has appeared in Arxiv 1708.05228.
[5]This section added more detail after discussion with Prof. Emami in thesis defense.

LIST OF ILLUSTRATIONS

LIST OF TABLES

NOMENCLATURE

AFM. Atomic force microscope.

EOM. Electro-optic modulators.

FSR. Free-spectral-range.

FWM. Four-wave-mixing.

GVD. Group Velocity Dispersion.

SBS. Stimulated Brillouin scattering.

SEM. Scanning electron microscope.

UHQ. Ultra-high-Q.

WGM. Whispering-gallery mode.

Chapter 1

INTRODUCTION TO INTEGRATED NONLINEAR OPTICS

1.1 Abstract

In the last decades, there has been remarkable progress in boosting optical Q factor in micro- and millimeter-scale optical resonators. Numerous cavity platforms routinely exceed a Q factor of 10^6 [1–4], and enable access to an wide range of nonlinear phenomena [1, 5–12]. The high Q nonlinear cavities have been also demonstrated on integrated silicon platform, and the silicon technology can potentially unlock new level of performance and scale in photonics and optoelectronics. In particular, frequency comb-related technology can revolutionize time standard [13], spectroscopy [14], high speed optical communications [15, 16], and quantum technology [17]. Here, we will review the physical picture to describe the operation of frequency comb in an integrated photonic platforms.

1.2 Fundamental background of optical microcavities

An ideal microcavity stores light indefinitely and would have resonant frequencies at precise value. The discrepancy from the ideal model is described by cavity Q factor, and the Q factor is proportional to the optical field decaying time in a unit of optical period[1]:

$$Q_0 = \omega \frac{E_s}{P_d} = \frac{\omega\tau}{2} \tag{1.1}$$

where ω is resonance frequency, E_s is the energy in the resonator system, P_d is the dissipated power, and τ is amplitude decay time. In addition, resonance decay rate κ is expressed as $2\pi\omega/Q_0$, and attenuation constant α is $n/c\tau$ where n is effective index, and c is the light velocity in vacuum. Here, the finesse and intracavity power are described in eqn.1.2. The quantities can be commonly used at any cavity platforms:

$$\begin{aligned} F &= \frac{FSR}{\kappa} \\ P_{cav} &= P_{in} \cdot \kappa_{ext} \cdot \frac{F}{2\pi} = P_{in} \cdot \kappa_{ext} \cdot \frac{FSR}{\omega} Q_0 \end{aligned} \tag{1.2}$$

where FSR is free spectral range of the microcavities, κ_{ext} is the external coupling rate of cavity, and P_{in} is input power.

There are several types of microcavities – whisphering gallery mode (WGM), Fabry-Perot, and photonic crystal cavities[1]. In general, photonic crystal cavities have extremely small mode volume and allow to drag external emitters inside the cavity[18, 19]. Therefore the cavity can maximize the field intensity at the position of the emitter and increase the emitter-cavity coupling. Fabry-Perot cavities have similar advantage, and cavity QED has been mostly demonstrated using those cavity platforms. On the other hands, the WGM cavities have remarkable progress on Q factor and performs ultra-high-Q on chip-based microresonators. In particular, high Q has great advantage on nonlinear optics as the key performance scales quadratically with Q factor. In this thesis, we will mainly focus on WGM cavity and the applications of nonlinear optics in the WGM cavity platform.

1.2.1 WGM cavities

The circulating waves (time-dependent magnetic wave) in WGM cavities are described by

$$H(r,z) = e^{im\phi} \begin{bmatrix} H^r(r,z) & iH^\phi(r,z) & H^z(r,z) \end{bmatrix} \tag{1.3}$$

where m (= 0, 1, 2,...) is the azimuthal mode number, and the cylindrical coordinates (r, ϕ, z) are aligned with respect to the resonator's axis of rotational symmetry (axisymmetric). The

azimuthal mode number m defines the number of optical periods along the cavity circumference at the resonance frequency, and the momentum (proportional to the azimuthal mode number) is regularly spaced quantity in WGM cavity. For example, the momentum is intrinsically conserved in four-wave-mixing if signal and idler mode numbers are symmetrically located with respect to the pump mode[20].

Let's talk about resonance frequency which is related to energy conservation in nonlinear optics. The cavity resonance frequencies can be expressed using Taylor expansion[21]:

$$\omega_\mu = \omega_0 + D_1 \cdot \mu + \frac{1}{2} D_2 \cdot \mu^2 + \frac{1}{6} D_3 \cdot \mu^3 + \cdots \tag{1.4}$$

where ω_μ is resonance frequency of μ-th mode, $(D_1/2\pi)$ is FSR, $(D_2/2\pi)$ and $(D_3/2\pi)$ correspond to 1st and 2nd order derivative of FSR. Those terms are basically from dispersion parameter ($\beta_1 = \frac{1}{2\pi R D_1}$ and $\beta_2 = -\frac{D_2}{(2\pi)^2 R D_1^3}$), and we will discuss more detail in Chapter 3. It is worth checking how to determine FSR from cavity geometry. The resonance frequencies are determined as:

$$2\pi n_{eff} R = m\lambda_m \tag{1.5}$$

where n_{eff} is the effective index of optical mode, and λ_m is the wavelength of the m-th mode ($\omega_m = mc/n_{eff}R$). Then FSR is expressed as:

$$FSR = \frac{D_1}{2\pi} = \frac{1}{2\pi}\frac{d\omega_m}{dm} = \frac{1}{2\pi}\frac{c}{n_{eff}R} \tag{1.6}$$

We can note that FSR corresponds to cavity round trip time, and the FSR can be determined by WGM cavity radius[22].

In the next section, we will discuss the optical wave propagation in WGM cavities and the WGM properties (i.e. dispersion, mode volume) critically determine the nonlinear optic operations in microcavities. The circulating optical wave is defined by a set of orthonormal eigenmode and its time-varying amplitude (A in section 1.3). The eigenmode equation can be separated with the equation of time-varying amplitude[23, 24]. We will discuss the eigenmode equation in this section (1.2), and the time-varying equation in following section (1.3).

1.2.2 WGM cavity eigenmode analysis– Numerical method

Here is the wave equation in favor of H and we assume $P_{NL} = 0$:

$$\nabla \times ([\epsilon]^{-1} \nabla \times H) = -\frac{1}{c^2}\frac{\partial^2 H}{\partial t^2} \tag{1.7}$$

The analytic solution of WGM was discussed in Ref.[24–26], and we would like to review the numerical method to solve the eigenmode equation of WGM cavity. By using Galerkin's method[27], the conjugation of the differentiable test vector (here, T is the test vector) is multiplied and the order of differentiation is reduced using the method of partial integration. The test vector Consequently, eqn.1.7 can be written as [28, 29]

$$\iint_{\Omega}[(\triangledown\times T^{*})([\epsilon]^{-1}\ \triangledown\times H)+\frac{1}{c^{2}}T^{*}\cdot\frac{\partial^{2}H}{\partial t^{2}}]d\Omega=0 \tag{1.8}$$

Eqn.1.8 can have spurious solutions [29–31] and those solutions[1] do not satisfy the relation $\triangledown\cdot H=0$ [29]. The extra penalty term is applied to suppress the spurious solutions:

$$\iint_{\Omega}[(\triangledown\times T^{*})([\epsilon]^{-1}\ \triangledown\times H)-\alpha(\triangledown\cdot T^{*})(\triangledown\cdot H)+\frac{1}{c^{2}}T^{*}\cdot\frac{\partial^{2}H}{\partial t^{2}}]d\Omega=0 \tag{1.9}$$

where α is the weight of the penalty term and $\alpha=1$ was taken for all simulation in this thesis. The terms in eqn.1.3 are now substituted into eqn.1.9, and the terms of the integrand are given by [28]

$$\begin{aligned}(\triangledown\times T^{*})([\epsilon]^{-1}\ \triangledown\times H)&=(\frac{A}{r^{2}}+\frac{B}{r}+rC)/(\epsilon_{||}\epsilon_{\perp})\\ \alpha(\triangledown\cdot T^{*})(\triangledown\cdot H)&=(\frac{D}{r^{2}}+\frac{E}{r}+F)\\ T^{*}\cdot\frac{\partial^{2}H}{\partial t^{2}}&=G\end{aligned} \tag{1.10}$$

where[2]

$$\begin{aligned}A&=\epsilon_{\perp}[T^{\phi}H^{\phi}-m(T^{\phi}H^{r}+H^{\phi}T^{r})+m^{2}T^{r}H^{r}]+\epsilon_{||}m^{2}T^{z}H^{z}\\ B&=\epsilon_{\perp}[T_{r}^{\phi}(H^{\phi}-mH^{r})+H_{r}^{\phi}(T^{\phi}-mT^{r})]-\epsilon_{||}m(T^{z}H_{z}^{\phi}+H^{z}T_{z}^{\phi})\\ C&=\epsilon_{\perp}T_{r}^{\phi}H_{r}^{\phi}+\epsilon_{||}[(T_{r}^{z}-T_{z}^{r})(H_{r}^{z}-H_{z}^{r})+T_{z}^{\phi}H_{z}^{\phi}]\\ D&=T^{r}H^{r}-m(T^{\phi}H^{r}+H^{\phi}T^{r})+m^{2}T^{\phi}H^{\phi}\\ E&=(T_{r}^{r}+T_{z}^{z})(H^{r}-mH^{\phi})+(H_{r}^{r}+H_{z}^{z})(T^{r}-mT^{\phi})\\ F&=(T_{r}^{r}+T_{z}^{z})(H_{r}^{r}+H_{z}^{z})\\ G&=-4\pi^{2}f^{2}(T^{r}H^{r}+T^{\phi}H^{\phi}+T^{z}H^{z})\end{aligned} \tag{1.11}$$

[1] the spurious solutions fall into either $\triangledown\times H=0,\triangledown\cdot H\neq 0$ for $\omega=0$ or $\triangledown\times H\neq 0,\triangledown\cdot H\neq 0$ for $\omega\neq 0$

[2] H_{j}^{i} denotes the partial derivative of H^{i} with respect to j, and f is the frequency of the mode resonance.

The terms of the integrand doesn't depend on the azimuthal coordinate ϕ, so the partial derivative equation can be two dimensional problem and this approach saves computation time. In addition, this approach needs to fix azimuthal mode number (m) and refractive index (this variable requires to assume the wavelength of optical mode) as an initial condition of the PDE. The inaccuracy in the initial condition can be corrected using the method in the next subsection (1.2.3).

1.2.3 WGM cavity dispersion analysis

Dispersion of microcavity comes from wavelength-dependent refractive index of optical material. The numerical method for eigenmode equation requires the azimuthal mode number as an initial boundary condition, and the refractive index of the optical medium is another variable that needs to be set from the beginning. However, the refractive index depends on the resonance frequencies (dispersion) and interestingly the resonance frequency is the solution of the eigenmode equation – we need to start the calculation with initial guess on the solution. This might make us to think Newton-Raphson method that start with initial guess which is reasonably close to the true root. The calculation of cavity dispersion can be split into these steps below:

1. Initial guess on the resonance frequency:

$$\omega_{m,0} = mc/n_{eff}R \tag{1.12}$$

2. Solve the PDE with refractive index $n(\omega_{m,0})$. Then we will get the eigenmode with the resonance frequency ($\omega_{m,1}$). If $\omega_{m,1} - \omega_{m,0} = 0$, then the solution of the PDE is $\omega_{m,1}$. If not, proceed step (3).

3. Use the new resonance frequency (i.e. $\omega_{m,1}$ in step 2) for the refractive index in PDE, and solve the PDE to get the resonance frequency. Iterate the process until the solution of PDE converges.

This process was introduced in previous literatures[32, 33], and used for all calculations in this thesis. In addition, the geometric dispersion (will be described further in Chapter 3) can be obtained when refractive index is constant.

1.3 Theoretical background of soliton in optical devices

1.3.1 Optical wave propagation in nonlinear media

In order to review the nonlinear propagation of optical wave, let's start from Helmholtz's equation which directly comes from Maxwell's equation. In this thesis, the optical media are nonmagnetic and in the absence of free charges:

$$\nabla \times \nabla \times E = \frac{\omega^2}{c^2} E + \frac{\omega^2}{\epsilon_0 c^2} P \tag{1.13}$$

where $c = 1/\sqrt{\epsilon_0 \mu_0}$ is the light speed in vacuum. Here the induced polarization P consists of two parts ($P = P_L + P_{NL}$) where P_L and P_{NL} represent linear and nonlinear induced polarization, respectively. In the fundamental level, the nonlinear response (P_{NL}) is originated from aharmonic motion of bound electrons and the total polarization satisfies the power series equation[34]

$$\widetilde{P}(t) = \epsilon_0 \sum_i \chi^{(i)} \widetilde{E}^i(t) = \sum_n P(\omega_n) e^{-j\omega_n t} \tag{1.14}$$

where $\chi^{(i)}$ is i-th order susceptibility. Eqn.1.14 also needs an assumption that the polarization depends only on the instantaneous strength of the electric field and this condition requires lossless and dispersionless optical medium. Here it is important to note that the polarization power term (eqn.1.14) doesn't converge in cases of resonant excitation of atomic system or super-intense field induced nonlinear response[34].

1.3.2 Optical soliton generation in waveguide

As discussed in section 1.2, the wave equation is solved by using the method of variable separation, and the propagation equation can be separated with the eigenmode equation[23]. The modal distribution equation obtains the optical properties of the eigen mode (e.g. dispersion and nonlinearity), and the corresponding characteristics are linked to the propagation equation. The propagation term of the pulse can be approximated as $A(z, \omega - \omega_0)e^{jk_0 z}$ where A is slow varying function[3]. The expression for the field is introduced into eqn.1.13 and create the following equation:

$$2j\beta \frac{\partial A}{\partial z} - (\beta^2 - \beta_0^2)A = 0 \tag{1.15}$$

[3] $E(z, \omega) = A(z, \omega - \omega_0)e^{jk_0 z} + A^*(z, \omega + \omega_0)e^{-jk_0 z} \simeq A(z, \omega - \omega_0)e^{j\beta_0 z}$

Here $\partial^2 A/\partial z^2$ can be dropped as A is slowly-varying amplitude, and β can be expressed as the combination of dispersion and Kerr effect induced phase shift:

$$\beta = \beta_0 + \Delta\beta_{NL} + \beta_1(\omega - \omega_0) + \frac{1}{2}\beta_2(\omega - \omega_0)^2 \tag{1.16}$$

where β_1, β_2, and $\Delta\beta_{NL}$ are group velocity, group velocity dispersion, and the nonlinear contribution to the propagation constant, respectively[34]. The nonlinear contribution can be expressed as:

$$\Delta\beta_{NL} = \Delta n_{NL}\omega_0/c = n_2 I\omega_0/c \tag{1.17}$$

Here I is the intensity of optical wave ($2n_{lin}(\omega_0)\epsilon_0 c|\widetilde{A}(z,t)|^2$), and the nonlinear contribution is proportional to the optical wave intensity. Eqn.1.16 is intoduced into eqn.1.15:

$$\frac{\partial A}{\partial z} - j\Delta\beta_{NL}A - j\beta_1(\omega - \omega_0)A - \frac{1}{2}j\beta_2(\omega - \omega_0)^2 A = 0 \tag{1.18}$$

This equation can be transformed to the time domain. The factor $e^{-j(\omega-\omega_0)t}$ is multiplied to eqn.1.18 and each terms are integrated over $(\omega - \omega_0)$ (more detail in ref[34]):

$$\frac{\partial \widetilde{A}}{\partial z} + \beta_1\frac{\partial \widetilde{A}}{\partial t} + \frac{1}{2}j\beta_2\frac{\partial^2 \widetilde{A}}{\partial t^2} - j\Delta\beta_{NL}\widetilde{A} = 0 \tag{1.19}$$

The coordinate transformation can simplify this equation by introducing the retarded time $\tau = t - z/v_g$:

$$\frac{\partial \widetilde{A}_s}{\partial z} + \frac{1}{2}j\beta_2\frac{\partial^2 \widetilde{A}_s}{\partial \tau^2} = j\gamma|\widetilde{A}_s|^2\widetilde{A}_s \tag{1.20}$$

This equation is referred to as the nonlinear Schrodinger's equation[4], and describes the optical pulse propagation through optical media. The second term in left hand side shows the dispersion contribution on the pulse propagation, and the longer wavelength components of the pulse propagates faster than the shorter wavelength components if the group velocity dispersion β_2 is positive (anomalous dispersion). On the other hand, the term on the right hand side shows the contribution of nonlinearity and the nonlinearity induces the longer

[4]Korteweg-de Vries (KdV) equation is another mathematical model to describe wave propagation ($\partial_t \widetilde{A}_s + \partial_z^3 \widetilde{A}_s - 6\phi\partial_z \widetilde{A}_s$=0).

wavelength components to travel slower than the shorter wavelength components (self phase modulation) [23, 34].

The pulse can be propagated through optical media with an invariant shape under the circumstances that the dispersion contribution compensates the effects of nonlinearity. Such pulses are referred as temporal optical soliton, and the ansatz of eqn.1.20 is in the form of $A = Bsech(\tau/\tau_0)$[23, 34]. Here it is worth tracking the process that continuous wave (CW) wave generates soliton pulses in optical waveguide[23], so we can understand how to generate soliton pulse from non-solitary wave. The interplay between the nonlineaer and dispersive effects causes inherent instability (c.f. modulation instability) that leads a breakup of the CW radiation into a train of short pulses[23]. We can apply linear stability analysis in order to understand the modulation instability.

$$A = (\sqrt{P_0} + a)e^{j\gamma P_0 z} = \bar{A} + ae^{j\gamma P_0 z} \tag{1.21}$$

Here we assume that the optical wave is CW and remains time independent during the propagation. Then the steady state solution of eqn.1.20 is given as $\bar{A} = \sqrt{P_0}e^{j\gamma P_0 z}$ where $P_0 = |A_0|^2$, and $a(z,t)$ is perturbation term to examine the stability. By substituting eqn.1.21 in eqn.1.20, we can obtain[5]

$$\frac{\partial a}{\partial z} + \frac{1}{2}j\beta_2\frac{\partial^2 a}{\partial \tau^2} = j\gamma(a + a^*)P_0 \tag{1.22}$$

Here, the frequency components of a and a^* needs to be coupled, so a has solution in the general form:

$$a = a_1 e^{j(kz-\omega\tau)} + a_2 e^{-j(kz-\omega\tau)} \tag{1.23}$$

This equation provides a set of two homogeneous equations:

$$\begin{pmatrix} jk - j\beta_2\omega^2 - j\gamma P_0 & -j\gamma P_0 \\ -j\gamma P_0 & jk - j\beta_2\omega^2 - j\gamma P_0 \end{pmatrix}\begin{pmatrix} a_1 \\ a_2 \end{pmatrix} = 0 \tag{1.24}$$

This set has nontrivial solution if $k^2 = (\beta_2\omega^2)^2 + 2\beta_2\omega^2\gamma P_0$, and the perturbation term will grow exponentially if k is imaginary ($\beta_2^2\omega^2 + 2\beta_2\omega\gamma < 0$). The condition for instability

[5] The right hand side of eqn.1.20 can be approximated as $|A|^2A = [(\sqrt{P_0} + a)(\sqrt{P_0} + a^*)](\sqrt{P_0} + a)e^{j\gamma P_0 z} \approx |\bar{A}|^2\bar{A} + P_0(a + a^*)e^{j\gamma P_0 z}$ as $aa^* \ll 1$.

is then $\beta_2 < -2\frac{\gamma P}{\omega^2}$, so the dispersion needs to be anomalous. Gain spectrum is defined as $G(\omega) = Im[k] = 2\sqrt{-(\beta_2\omega^2)^2 - 2\beta_2\omega^2\gamma P_0}$. The experimental demonstrations are shown in Ref.[35, 36] with more detail, and the theoretical detail are shown in Ref.[23]

The linear stability analysis provides only the understanding of the initial sideband growth but clearly the perturbation becomes large enough that the linear analysis breaks down. Then the progression of the modulated state is governed by the nonlinear regime (eqn.1.20), and the the generated pulse trains can be evolved to the form of soliton solution of the nonlinear wave propagation equation. Experimental demonstrations are shown in Ref.[37] with more detail.

1.3.3 Optical soliton propagation in waveguide – supercontinuum generation

The optical soliton (pulse) can extend spectral bandwidth by propagating through a strongly nonlinear device[38–40]. The optical devices allow efficient nonlinear interaction with relatively lower pulse energy and shorter propagation length. The equation of pulse propagation through nonlinear devices is expressed as:

$$\frac{\partial\widetilde{A}}{\partial z} + \frac{\alpha}{2} + \frac{1}{2}j\beta_2\frac{\partial^2\widetilde{A}}{\partial t^2} = j\gamma(1 + j\tau_{shock}\frac{\partial}{\partial t})(\widetilde{A}\int_{-\infty}^{+\infty} R(T') \times |\widetilde{A}(z, T - T')|^2 dT' + j\Gamma_R(z, T)) \tag{1.25}$$

This equation is exactly same with eqn.1.20 but additionally has the second term in the left hand side (attenuation α) and the terms in the right hand side (nonlinear source). Here τ_{schock} is the shock time scale, the response function $R(t) = (1 - f_R)\delta(t) + f_R h_R(t)$ includes instantaneous electronic and delayed Raman contribution (f_R determines the portion of Raman contribution, and h_R is experimentally determined by Raman cross section), and Γ_R is Raman noise. If we ignore the contribution from Raman (e.g. pulses of width > 5 ps), then the right hand side becomes $j\gamma\widetilde{A}|\widetilde{A}|^2$. The numerical simulation of supercontinuum generation is solved by split-step Fourier method, and further details are shown in Ref.[23, 40, 41].

It is also worth checking dispersive wave generation occurred during soliton propagation. The dispersive waves, which can also be understood in terms of an analogy to Cherenkov radiation[42], are generally formed when a soliton radiates into spectral region of normal dispersion and it is one of powerful methods to expand the spectral width of the soliton[43]. Soliton pulse is launched at the optical waveguide with anomalous dispersion, and there can be a certain condition that the phase of soliton pulse ($\phi(\omega_s, z) = \omega_s t - \beta_s z + \gamma P z/2$) is matched with the phase of the pulse at different wavelength ($\phi(\omega_{DW}, z) = \omega_{DW} t - \beta_s z$) that generally has normal dispersion[44]. Here, ω_s and β_s are the frequency and the propagation

constant of soliton pump; ω_{DW} and β_{DW} are the frequency and the propagation constant of dispersive wave.

$$\begin{aligned} \phi(\omega_s, z) &= \phi(\omega_{DW}, z) \\ \omega_s t - \beta_s z + \gamma P z/2 &= \omega_{DW} t - \beta_s z \\ \beta(\omega_{DW}) - \beta(\omega_s) + (\omega_{DW} - \omega_s)/v_g &= \gamma P/2 \end{aligned} \tag{1.26}$$

Once the phase-matching condition is fulfilled, the soliton starts to radiate its power to the other spectral region. The dispersive wave appeared when the optical attenuation at ω_{DW} is compensated by the transferred energy and soliton signal (usually weak).

1.3.4 Temporal optical solitons in microcavities

Optical cavities is resonant at its eigenmodes, and the instantaneous field is the summation of the resonance modes[45, 46]. We can obtain the coupled rate equation for the modal field dynamics[6]:

$$\frac{\partial \widetilde{A}_\mu}{\partial t} = -\frac{\kappa}{2}\widetilde{A}_\mu + \delta_{\mu 0}\, f e^{-j(\omega_p - \omega_0)t} + jg \sum_{\mu 1, \mu 2, \mu 3} \widetilde{A}_{\mu 1}\widetilde{A}_{\mu 2}\widetilde{A}^*_{\mu 3} e^{-j(\omega_{\mu 1} + \omega_{\mu 2} - \omega_{\mu 3} - \omega_\mu)t} \tag{1.27}$$

where g is Kerr nonlinear coefficient in microcavity ($= \hbar\omega_0^2 c n_2 / n_0^2 V_{eff}$), and $f = \sqrt{\frac{\kappa_{ext} P_{in}}{\hbar\omega_0}}$. Using phase transformation $a_\mu = \widetilde{A}_\mu e^{-j(\omega_\mu - \omega_p - \mu D_1)t}$, we obtain:

$$\frac{\partial a_\mu}{\partial t} = -(j(\omega_\mu - \omega_p - \mu D_1) + \frac{\kappa}{2})a_\mu + \delta_{\mu 0} f + jg \sum_{\mu 1, \mu 2} a_{\mu 1} a_{\mu 2} a^*_{\mu 1 + \mu 2 - \mu} e^{-jD_1(\mu 1 + \mu 2 - \mu 3 - \mu)t} \tag{1.28}$$

As the four-wave mixing occurs only when $\mu 1 + \mu 2 - \mu 3 - \mu = 0$, eqn.1.28 is simplified:

$$\frac{\partial a_\mu}{\partial t} = -(j(\omega_\mu - \omega_p - \mu D_1) + \frac{\kappa}{2})a_\mu + \delta_{\mu 0} f + jg \sum_{\mu 1, \mu 2} a_{\mu 1} a_{\mu 2} a^*_{\mu 1 + \mu 2 - \mu} \tag{1.29}$$

In optical cavities, temporal soliton is initiated from parametric oscillation[46, 47] and the four wave mixing process can be also described by the coupled mode equation of $\mu = 0, \pm m$ (m is mode number of first oscillating modes) [45, 48].

[6] This coupled mode equation is also originated from Helmholtz equation

$$\frac{\partial}{\partial t}\begin{pmatrix} a_m \\ a^*_{-m} \end{pmatrix} = \begin{pmatrix} -\frac{\kappa}{2} - j(\omega_m - \omega_p - mD_1) + 2jga_0^2 & jga_0^2 \\ -jga_0^2 & -\frac{\kappa}{2} + j(\omega_{-m} - \omega_p + mD_1) - 2jga_0^2 \end{pmatrix}\begin{pmatrix} a_m \\ a^*_{-m} \end{pmatrix} \tag{1.30}$$

The parametric oscillation gain can be obtained from the coupled mode equation in the same manner with modulation instability gain in fiber, and the threshold of the parametric oscillation can be accordingly obtained as[20, 45, 46, 48–50]:

$$P_{th} = \frac{\kappa^3 n_0^2 V_{eff}}{8\kappa_{ext}\omega_0 c n_2} \tag{1.31}$$

It is worth to note that the parametric oscillation is determined by κ (cavity Q factor), V_{eff} (cavity mode volume), and n_2 (nonlinearity). Also, κ_{ext} is another important variable that determines the threshold power and it can be further discussed in Chapter 5.

The initial parametric oscillation can be described with relatively simpler coupled mode equation, but the complexity of the computation increases as nonlinear process evolves further[45, 51]. The coupled mode equation can be simplified to Lugiato-Lefever equation (LLE) [52] and the LLE significantly reduces the computation of cavity temporal soliton generation (and provides intuitive understanding). Here, the optical field $a_\mu(t)$ is transformed from the coordinate μ (corresponds to ω) to the coordinate ϕ (azimuthal angle which corresponds to the location in optical cavity), and the cavity field is expressed as the summation of a_μ for all μ.

$$A(\phi, t) = \sum a_\mu(t) e^{j\mu\phi} \tag{1.32}$$

The following equation can be obtained by multiplying $e^{j\mu\phi}$ onto eqn.1.29 for every μ and computing the summation.

$$\begin{aligned} \sum_\mu \frac{\partial a_\mu e^{j\mu\phi}}{\partial t} = &-\sum_\mu (j(\omega_\mu - \omega_p - \mu D_1) + \frac{\kappa}{2}) a_\mu e^{j\mu\phi} + f \\ &+ jg \sum_\mu \sum_{\mu 1, \mu 2} a_{\mu 1} a_{\mu 2} a^*_{\mu 1+\mu 2-\mu} e^{j\mu\phi} \end{aligned} \tag{1.33}$$

The first term in the right hand side can be approximated as $\omega_\mu - \omega_p - \mu D_1 \approx \delta\omega - D_2\mu^2/2$. The third term is $\sum_\mu \sum_{\mu 1,\mu 2} a_{\mu 1} a_{\mu 2} a^*_{\mu 1+\mu 2-\mu} e^{j\mu\phi} = \sum_{\mu 1,\mu 2,\mu 3} a_{\mu 1} a_{\mu 2} a^*_{\mu 3} e^{j(\mu 1+\mu 2-\mu 3)\phi} =$

$\sum_{\mu 1} a_{\mu 1} e^{j\mu 1\phi} \sum_{\mu 2} a_{\mu 1} e^{j\mu 2\phi} \sum_{\mu 1} a_{\mu 3} e^{-j\mu 3\phi}$. Each term in right hand side is equivalent to eqn.1.32, so finally the term can be simplified as $|A|^2 A$.

$$\frac{\partial A}{\partial t} = -j\delta\omega A + j\frac{D_2}{2}\frac{\partial^2 A}{\partial \phi^2} - \frac{\kappa}{2}A + f + jg|A|^2 A \tag{1.34}$$

This is generalized LLE, and the analytic solution of this equation can be obtained by treating loss (κ) and pump (f) as perturbation[53, 54]. The unperturbed equation (κ=0, f=0) has a solution in the form of $A = Bsech(\phi/\phi_\tau)$ and the ansatz of the eqn.1.34 is the form of $A = Bsech(\phi/\phi_\tau)e^{j\varphi}$ – an additional phase term was added to the solution form of unperturbed nonlinear Schrodinger equation (or KdV equation)[7]:

$$\begin{aligned} B &= \sqrt{\frac{2\delta\omega}{g}} \\ \phi_\tau &= \sqrt{\frac{D_2}{\delta\omega}} \\ cos\varphi &= \sqrt{\frac{2\delta\omega}{g}}\frac{\kappa}{\pi f} \end{aligned} \tag{1.35}$$

As $|cos\varphi| = \sqrt{\frac{2\delta\omega}{g}}\frac{\kappa}{\pi f} \leq 1$, the maximum detuning ($\delta\omega_{max}$) is restricted to $\frac{g}{2}(\frac{\pi f}{\kappa})^2$. Here the soliton amplitude B is a function of detuning and Kerr nonlinear coefficient; the pulse width ϕ_τ is a function of detuning and dispersion. The nonlinear coefficient and dispersion are determined from cavity design, and the detuning is only variable that we can control in the lab. The maximum detuning ($\delta\omega_{max}$) can be converted to $\kappa\pi^2 P_{in}/16P_{th}$ and determines the minimum operating power of soliton (P_{min}) accordingly [55]:

$$P_{min} = \frac{16P_{th}}{\pi^2\kappa}\delta\omega = \frac{16P_{th}}{\pi^2\kappa}\frac{D_2}{\phi_\tau^2} \tag{1.36}$$

The optical spectrum in frequency domain has same hyperbolic secant form as the time domain[47] as below:

$$\begin{aligned} a_\mu &= \frac{1}{2\pi}\int_{-\pi}^{\pi} A(\phi)e^{-j\mu\phi}d\phi = \frac{B\phi_\tau}{2}e^{j\varphi}sech(\frac{\pi\phi_\tau\mu}{2}) \\ P_\mu &= \kappa_{ext}|a_\mu|^2\hbar\omega_0^2 \end{aligned} \tag{1.37}$$

[7] This paragraph was added after discussing with Prof. Ali Hajimiri in thesis defense.

Here a_μ is the result of Fourier transform of the soliton solution in time domain, and the coupled output power P_μ can be obtained in the form of square hyperbolic secant[8]. The experimental results demonstrated excellent agreement with the theory, and the results will be introduced in this thesis[9].

1.4 Frequency comb – system application of soliton physics

The soliton physics in previous section is basic ingredient that composes the system level operation of frequency comb. The frequency comb is the series of precisely spaced, narrow spectral lines, and all the spectral lines are mode-locked[39, 56]. This development enables precise counting of optical cycles on femtosecond level, and can provide a gear to connect THz-level optical waves with electronics-compatible microwaves. The comb technology have found widespread use in optical clocks[57, 58], spectroscopy[59–61], distance measurement[62], astronomic spectroscopy[63, 64], and frequency synthesis[65, 66]. In this section, we will review the operating principle, the frequency comb structure, and the stabilization technique of the comb. Further detail can be found in Ref.[39, 56], and this thesis breifly introduces the frequency comb technology to digest the related research, which will be discussed in Chapt.3 - 5.

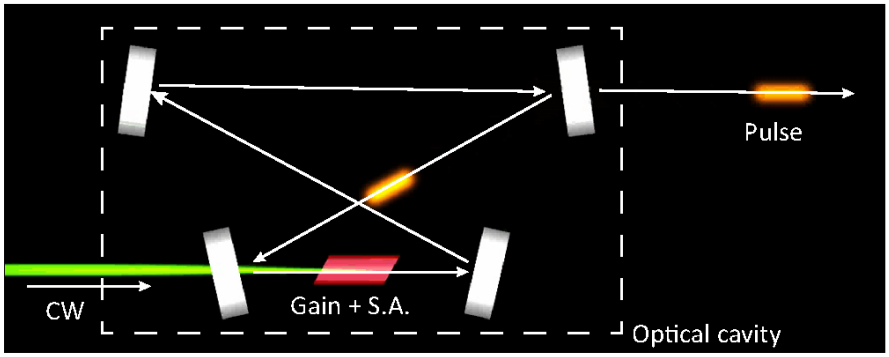

Figure 1.1: **Principle of mode locked laser** Schematic illustration of mode locked laser operation. CW laser (e.g. frequency-doubled 532 nm Nd:YVO_4 laser in Ref[39]) is coupled to optical cavity, and short pulse is generated if relative phases of all longitudinal modes are locked. Gain medium (e.g. Ti:S crystal) compensates the circulating loss in the cavity, and saturable absorber (S.A.; e.g. Kerr lens mode locking in Ref[39]) might sharpen the pulse in time domain by suppressing side components of the pulse. This figure is adopted from the presentation materials given by S. Diddams and K. Vahala.

[8] This paragraph was added after discussing with Prof. Azita Emami and Prof. Ali Hajimiri in candidacy exam.

[9] Experimental results are shown in section 3.4 (Fig. 3.17b shows the optical spectrum with $sech^2$ envelope), and section 5.6.

1.4.1 Principle of frequency comb operation

A frequency comb had been demonstrated using a mode locked laser which produces ultrashort optical pulses with a constant repetition rate[39], and the mode locking was achieved by fixing relative phases of all longitudinal modes[39, 67]. As an example, let's consider a passively mode-locked laser which is composed of a saturable absorber, gain medium, and partially reflecting mirror (cf. Fig.1.1). The steady state assumes one single short pulse in the optical cavity, and the single pulse experiences saturable absorber and gain medium in every single round trip. The saturable absorber suppresses the weak light around the pulse center, and gain medium compensates for the loss of a circulating pulse. As a result, the absorption and gain can be balanced and the ultra short pulse can be generated inside the mode locked laser – short pulse, which is the result of all longitudinal mode locking in the time domain corresponds to the wide frequency comb in the spectral domain. The mode-locked pulse expands its spectral span using pulse broadening[39, 56], and the broadened pulse provide mode-locked frequency comb lines in the spectral domain.

1.4.2 Frequency comb in time- and frequency-domain

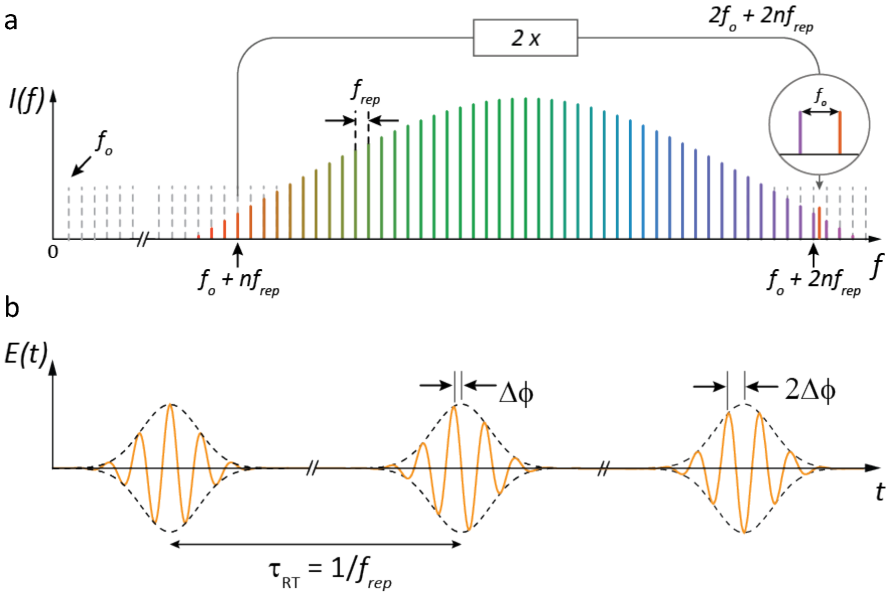

Figure 1.2: **Principle of frequency comb** (**a**) Frequency domain representation of an optical frequency comb. The frequencies of n-th comb lines is $f_n = f_o + n \cdot f_{rep}$ where f_o, and f_{rep} are the offset frequency and the mode spacing. The frequency f_n is doubled using nonlinear crystal, and generates beatnotes with the frequency f_{2n} in order to directly detect f_o. (**b**) Time domain representation of an optical frequency comb. The pulse repetition rate corresponds to frequency comb mode spacing (f_{rep}), and the phase shift $\Delta\phi$ is given as $2\pi f_o / f_{rep}$. (**a-b**) are adopted from Jones, et al.[39], Kippenberg, et al.[5].

Frequency of nth comb line (n is integer) is (see Fig.1.2a):

$$f_n = f_o + n \cdot f_{rep} \tag{1.38}$$

where f_o is carrier offset frequency which is the frequency of the comb closest to DC, and f_{rep} is the comb spacing in the spectral domain. f_{rep} can be simply measured from the microwave beatnote in the photodiode. f_o needs $f-2f$ technique that generate the beatnote between f_{2n} and $2 \cdot f_n$ as shown below[39, 56]:

$$2f_n - f_{2n} = 2(f_o + n \cdot f_{rep}) - (f_o + 2n \cdot f_{rep}) = f_o \tag{1.39}$$

f_o is determined between DC and f_{rep}, and it is originated from the mismatch between phase velocity and group velocity of the frequency comb system[39, 56]. As long as f_{rep} is in detectable- and electronics-compatible rate, the offset frequency can be detected and stabilized using electronics as well. It is also important to note that highly nonlinear fiber[68] was used to broaden the spectral span of the mode locked laser from 30 THz to 350 THz while maintaining the coherence of the pulse[39, 56]. The principle of supercontinuum generation and more details will be discussed in the following sections.

Fig.1.2b shows the time domain representation of an optical frequency comb, and it can be simply considered as a Fourier transformed frequency comb in the time domain. The pulse repetition rate is given as $1/f_{rep}$, and the phase shift $\Delta\phi$ between neighboring pulses is given as $2\pi f_o/f_{rep}$. It is important to note that the relative carrier-envelope phase $\Delta\phi$ is another presentation of the mismatch between phase velocity and group velocity, and the relation it haas with the carrier offset frequency is:

$$2\pi f_o = \Delta\phi f_{rep} \tag{1.40}$$

The mismatch can be controlled using the high-reflector mirror with adjustable tilt. The tilting of the mirror changes a linear phase shift with frequency and thereby modifies the offset frequency. Also, the mirror can be translated in the optical system as well, so as to adjust the repetition rate of the comb[39].

1.4.3 Stabilization of frequency comb

The repetition rate is directly measured using the photo-diode, and the received electric signal goes to a feedback loop which controls the mirror translation (cavity repetition rate control) and lock f_{rep} with the output of a highly stable RF oscillator. The $f-2f$ technique allows one to measure the carrier offset frequency using the photo-diode, and the control signal is fed into the tilt angle control of the reflective mirror (optical dispersion control) and locks the group delay of the pulse, which basically adjusts the carrier offset frequency[69].

1.5 Discussions – Towards integrated frequency comb system

We reviewed the fundamental backgrounds of microcavities, soliton physics, and frequency comb. Those fundamental components essentially need to collaborate on the realization of an integrated photonic system, and the new miniature realization can potentially revolutionize instrumentation, time standard, and navigation.

Microcavities can build up an intracavity power, and confine the optical power within the cavity micro-structure. As discussed in this chapter, the high-Q (low loss) factor increases the circulating power linearly and the power consumption of nonlinear process scales inverse quadratical with the Q factor. It is essential for the new miniature realization to drop the operating power consumption down to the power level that on-chip light sources can provide, so UHQ performance has to be satisfied in this aspect. This thesis will introduce cavity Q studies that enable to transfer UHQ functions from crystalline or microtoroid cavities to fully integration form[10].

Dispersion engineering is another key component to connect the microcavities with soliton physics. Considering the propagation of ultrashort pulses through optical media, dispersion compensates the nonlinearity-induced phase shift, and the interplay between the dispersion and the nonlinearity determines the functionalities of nonlinear optical devices. The microcavity nonlinear optics has created lots of new, interesting problems on dispersion engineering[21] that haven't considered in other field, and this thesis will introduce the cavity dispersion studies that realize soliton frequency comb generation and broadband dispersion engineering over an octave span[11].

Photonic system design provides the pathway to realize frequency comb using soliton physics and microcavities. This thesis will shortly introduce the system design and experiments that demonstrated a self-referenced comb operation and an optical frequency synthesizer as results of collaborations with multi-institutions and industry[12].

[10] Chapter 2 will introduce chip-based microcavity based on standard MEMS process[22], and chapter 5 will show fully integrated silica resonator with silicon nitride planar waveguide[70].

[11] Chapter 3 will introduce dispersion/ mode spectrum engineering in UHQ silica microcavities[55, 71], and chapter 4 will continue the discussion on nanophotonic waveguide[72].

[12] Chapter 5 will introduce the demonstration of self-referenced frequency comb and optical frequency synthesizer[73].

Chapter 2

INTRODUCTION TO ON-CHIP ULTRA-HIGH-Q MICRORESOANTORS

2.1 Abstract[1]

An ultra-high-Q resonator stores the light at resonance frequencies for extremely long decay time, and can build high power inside the small mode volume[1]. Nevertheless, the extremely high Q factors have only been realized in Fluoride based crystalline materials and the silicon chip-based high Q resonator had been elusive in the beginning of the ultra-high-Q resonator field. In the early 2000s, a clever method was demonstrated using a silica fiber tip that created a micro-sphere and achieved the extremely high Q[8, 74]. This idea brought silicon oxide into the ultra-high-Q field, and it was finally continued to ultra-high-Q operation on the silicon chip. In this chapter, we will discuss the chip-based ultra-high-Q development which starts from the microtoroid[2] to monolithic disk resonator[22].

[1] Section 2.3 has appeared in Nature Photonics 6, 369-373, 2012

2.2 Micro-toroid resonator

2.2.1 Fabrication process

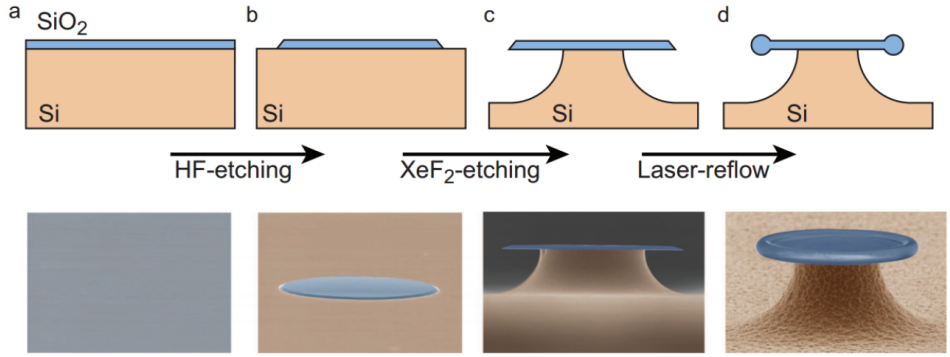

Figure 2.1: **Micro-toroid microfabrication process** Upper panels depict the schematic illustration of the process steps, and lower panels show false colored SEM images. **(a)** Silicon oxide is grown on a silicon wafer using thermal oxidation. **(b)** The silica layer is patterned using photolithography, buffered hydrofluoric acid etch, and residue cleaning. **(c)** XeF_2 etch is applied to create silica undercut and generate air cladding around silica layer. **(d)** CO_2 laser reflow is applied to silica structure, so a toroidal structure is formed on the outer rim of the disk. Figure is kindly provided by P.Del'Haye[33].

In this section, toroid fabrication steps will be discussed with more details on each step – specifically oxidation, wet etch, and dry etch. Those basic processes became essential steps for silica-based optical device fabrication[22, 55, 70, 71, 75].

Devices were fabricated on silicon wafers which have thermally grown oxide layer (thickness: $\approx$ 1-2 μm) on top of them (Fig.2.1a). The thickness of the silica layer can determine the final structure of the micro-toroid (e.g. minor radii)[33]. Here, thermal oxidation has two different types of growth methods – (i) dry oxidation, and (ii) wet oxidation. The chemical reactions are

$$Si(s) + O_2(g) \rightleftharpoons SiO_2(s) \tag{2.1}$$

for dry oxidation, and

$$Si(s) + 2H_2O(g) \rightleftharpoons SiO_2(s) + 2H_2(g) \tag{2.2}$$

for wet oxidation. The hydrogen in wet oxidation may generates OH^- bonds in silica layer, and the chemical bond generates strong material loss in infrared wavelengths. On the other hand, dry oxidation has a much slower growth rate than wet oxidation[33, 76, 77].

Photoresist was patterned on the silica surface, and acted as etch mask during buffered hydrofluoric acid etching (Fig.2.1b). Buffered HF contains ammonium fluoride (NH_4F) in order to maintain the concentration of HF during the etch process ($NH_4F \rightleftharpoons NH_3 + HF$), but the etch solution needs to be changed when a long etch duration is required.

XeF_2 is applied to create a silicon undercut after wet etching and residue cleaning (Fig.2.1c). Here, XeF_2 has high etch selectivity (1000:1 for silicon compared to silica) and the chemical reaction is

$$2XeF_2(g) + Si(s) \rightleftharpoons 2Xe(g) + SiF_4(g) \tag{2.3}$$

in a water-free environment, while the chemical reaction with water vapor damages the silica structure as below:

$$2XeF_2(g) + 2H_2O(g) \rightleftharpoons 2Xe(g) + O_2(g) + 4HF(g) \tag{2.4}$$

Then a CO_2 laser is used to heat and melt the outer rim of silica disk ("reflow" process; Fig.2.1d). Because of the poor thermal conductivity of silica, the outer rim of the disk can be efficiently melt and form the new structure. The silica on the silicon pillar usually doesn't change the structure during the "reflow" step because of the high thermal conductivity of silicon. Further details are explained in Ref.[2, 78].

2.2.2 Micro-toroid resonator structure

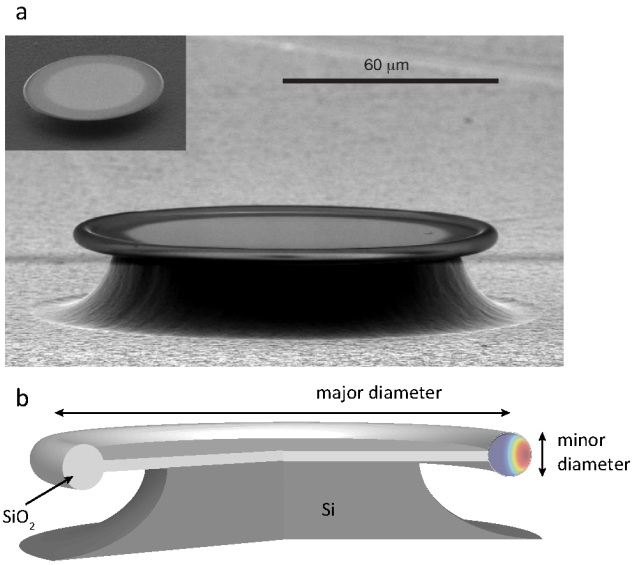

Figure 2.2: **Illustration on structural features of micro-toroid resonator** (**a**) Measured SEM image of micro-toroid resonator after CO_2 laser reflow. Inset depicts the SEM image of microdisk prior to laser reflow step. Major diameter is 120 μm, and minor diameter is 7 μm. The toroidal microresonator had an intrinsic Q factor of 100 million. (**b**) Schematic illustration of toroidal microresonator structure. The major diameter and minor diameter are defined on the figure, and the calculated mode profile is superimposed on the schematic illustration. **a** is from Armani, et al.[2], the mode profile in **b** was taken from P. Del'Haye[33].

Fig.2.2 illustrates the structural features of toroidal microresonator, and the contents mainly refer the results in Ref.[2, 78]. As described in previous section, the toroidal rim structure

is formed at the periphery of circular micro-disk (see the inset in **a**) as a result of CO_2 laser reflow. The surface roughness of the toroidal structure was defined at the laser annealing process, and the thickness of the toroidal rim (minor diameter) is defined by microdisk thickness and silicon undercut depth. The perspective SEM view in **a** shows the toroidal microresonator after CO_2 laser reflow, and the intrinsic Q factor of the resonator was measured to be 100 million[2]. Here, Q factor of the microresonator was measured using tapered fiber. The waveguide coupler and Q measurement method will be further discussed in following section. The diameter of toroidal rim (major diameter) was 120 μm and the thickness of the rim (minor diameter) was 7 μm. Fig 2.2b shows the schematic illustration of toroidal microresonator structure. The calculated mode profile is superimposed on the toroidal resonator schematic.

2.2.3 Modal coupling of ultra-high-Q resonator

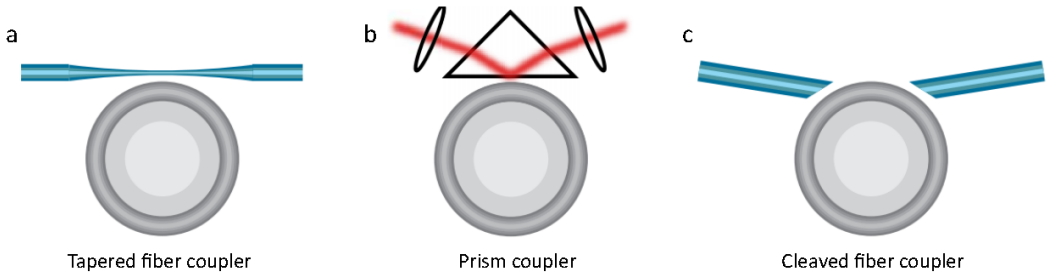

Figure 2.3: **Resonator coupling methods** (**a**) Tapered fiber coupler[79]. Single mode fiber is thermally heated while pulling the fiber slowly. Then adiabatic tapered profile is fabricated for single mode operation, and the taper thickness can adjust the effective index of waveguide mode for efficient coupling with resonator. (**b**) Prism coupler[80]. The resonance mode is excited by the inclined focusing of the probe beam on the inner surface of the glass prism. The incident angle is determined by the refractive indices of resonator and prism. (**c**) Cleaved fiber coupler[81]. Similar approach with prism, but prism is altered by cleaved fiber. Figure is kindly provided by P.Del'Haye[33].

The evanescent mode coupling provide much efficient excitation using phase-matched field tunneling, while free-space excitation of WGM resonator is extremely inefficient due to phase velocity mismatch between air and silica. In order to achieve the evanescent mode coupling, (i) the coupler power needs to be transferred into the evanescent field and then (ii) the near field should be in close proximity to the resonator for energy transfer.

Fig.2.3 shows ultra-high-Q resonator coupling methods (a: tapered fiber coupler; b: prism coupler, c: cleaved fiber coupler). The tapered fiber transfers the transmitting power into the evanescent wave by reducing the taper width; prism coupler and cleaved fiber use the total internal reflection at the prism surface and fiber cleaved surface. Then the evanescent field is in close proximity to the resonator surface by adjusting the gap between fiber (or prism)

and resonator mechanically. The effective index of the coupler mode is close to the index of silica (fiber and prism are made by glass), so the phase mismatch became lower than the free spacing coupling.

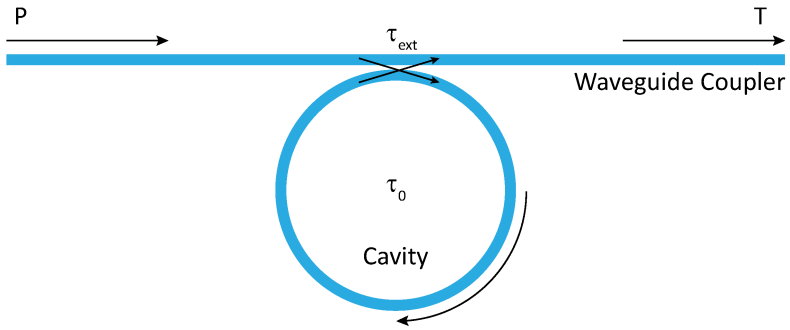

Figure 2.4: **Schematic of resonator-waveguide coupled system** Illustration of waveguide and resonator coupling at resonance frequency ω_0. τ_0^{-1} and τ_{ext}^{-1} indicate an internal cavity loss rate, and an external coupling rate. P and T indicate a power input and output of the waveguide coupler. Arrows indicate the direction of power transfer, and we neglected counter propagating wave in resonator as well as parasitic loss of the system (τ_{ext}^{-1}). The schematic and illustrations are inspired and adopted from H. Haus[82] and Kippenberg[49].

Let's consider the circumstances after the evanescent field of waveguide is in the proximity of a microresonator. If the cavity satisfies $U(t+T) - U(t) \approx TdU/dt$ (U is normalized amplitude of the mode, and T is cavity round trip), the waveguide-resonator coupling can be described as below:

$$\frac{d}{dt}U = -(\frac{1}{2\tau_0} + \frac{1}{2\tau_{ext}})U + \frac{1}{\sqrt{\tau_{ext}}}s_{in} \tag{2.5}$$

where ω_0 is resonance frequency, τ_0^{-1} is internal cavity loss rate, τ_{ext}^{-1} is external coupling rate, $|U(t)|^2$ correspond to the stored energy in the resonator, and $|s_{in}|^2$ is the launched power in the waveguide as indicated as P in the Fig.2.4. Here we assumed zero detuning[2] ($\omega_0 = \omega_P$; ω_P is input laser frequency), single mode operation in both the waveguide and resonator, and neglected parasitic losses.

In the steady state ($\frac{d}{dt}U = 0$), the stored energy within the resonator ($|U(t)|^2$) is

$$\begin{aligned} 0 &= -(\frac{1}{2\tau_0} + \frac{1}{2\tau_{ext}})U + \frac{1}{\sqrt{\tau_{ext}}}s_{in} \\ |U(t)|^2 &= \frac{1}{(1/2\tau_0 + 1/2\tau_{ext})^2}\frac{|s_{in}|^2}{\tau_{ext}} \end{aligned} \tag{2.6}$$

The circulating power P_{cav} is (τ_{rt} is cavity round trip time)

$$P_{cav} = \cdot|U(t)|^2/\tau_{rt} \tag{2.7}$$

[2]Please read Ref [49] and Ref [33] if you want to see more detail in case of the non-zero detuning.

and the transmission T is (t is transmission field and T is transmission through the waveguide):

$$\begin{aligned} t &= -s_{in} + \sqrt{\frac{1}{\tau_{ext}}} U \\ T &= |t/s_{in}|^2 = (\frac{\tau_{ext} - \tau_0}{\tau_{ext} + \tau_0})^2 \end{aligned} \tag{2.8}$$

In the under-coupling ($\tau_{ext}^{-1} < \tau_0^{-1}$), the field transmitted through waveguide is stronger than the field coupled from the resonator field $|U(t)|$.

$$\begin{aligned} |U(t)|^2 &< |s_{in}|^2 \\ P_{cav} &< \tau_{rt} \cdot |s_{in}|^2 \\ T &> 0 \end{aligned} \tag{2.9}$$

In the critical-coupling ($\tau_{ext}^{-1} = \tau_0^{-1}$), the external coupling rate corresponds to the internal cavity loss rate. The stored energy, circulating power, and transmission follow the relationship as shown below:

$$\begin{aligned} |U(t)|^2 &= |s_{in}|^2 \\ P_{cav} &= \tau_{rt} \cdot |s_{in}|^2 \\ T &= 0 \end{aligned} \tag{2.10}$$

In the over-coupling ($\tau_{ext}^{-1} > \tau_0^{-1}$), the field through waveguide is weaker than the field coupled from the resonator field. So the result of the destructive interference again becomes non-zero in transmission.

$$\begin{aligned} |U(t)|^2 &< |s_{in}|^2 \\ P_{cav} &< \tau_{rt} \cdot |s_{in}|^2 \\ T &> 0 \end{aligned} \tag{2.11}$$

Fig.2.5 shows plot of transmission and circulating power as a function of τ_{ext} (here we assumed $\tau_0 = 1$) and here the circulating power is normalized to $P_{cav,max} = \tau_{rt} \cdot |s_{in}|^2$. It is important to note that the circulating power is maximized at the critical coupling condition ($\tau_{ext} = \tau_0$), and the relations between external coupling rate and coupled power will be discussed frequently in Chapter 5. In this thesis, tapered fiber is the cavity coupling method used in Chapter 2 and 3. Ref.[79, 83] introduced more details on the tapered fiber coupler.

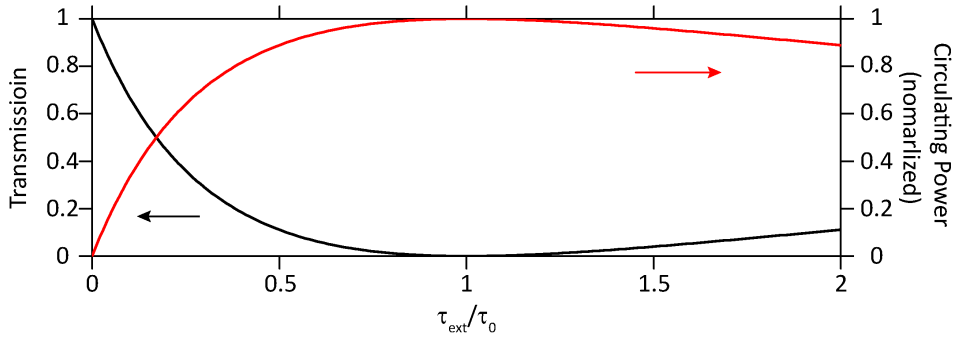

Figure 2.5: **Plot of transmission and circulating power as a function of external coupling rate** Transmission (T) and circulating power (P_{cav}) in eqn.2.8 & 2.7 are plotted as a function of τ_{ext} and τ_0.

2.2.4 Micro-toroid Q factor characteristics

2.2.4.1 Q factor measurement

The quality factor of the resonator is defined by the ratio between the stored energy ($|U|^2$) and the dissipated energy (P_d) in one oscillation cycle, and represents how well the resonator can store the energy.

$$Q = 2\pi \cdot \omega_0 \cdot \frac{P_d}{|U|^2} = 2\pi \cdot \omega_0 \cdot \tau \tag{2.12}$$

where ω_0 is the resonance frequency, and τ is cavity life time[3]. In the weakly damped cavity, the quality factor can be approximated as $Q = \omega_0/\Delta\omega$, where $\Delta\omega$ is the cavity linewidth.

It is also interpreted using resonance mode in time and frequency domain[49]:

$$U(t) = U(0)e^{(i\omega_0 - 1/2\tau)t} \rightleftharpoons U(\omega) = \frac{U(0)}{i(\omega_0 - \omega) - 1/2\tau} \tag{2.13}$$

The measurement of cavity linewidth ($\Delta\omega$) is one of direct methods to estimate the Q factor of the oscillator, and the transmission ($T(\Delta\omega)$) reproduces the transfer function of $|U(\omega)|^2$ in steady state. Therefore, the frequency scan to measure the cavity linewidth needs to be much slower than the cavity storage time. For example, the 200 M cavity lifetime (τ) is approximately 0.3 μs at 1550 nm wavelength, and the spectral scan for 1 MHz linewidth needs to be much slower than the lifetime. The coherence time of the scanning laser set the lower boundary of the scanning speed (New Focus laser: short term linewidth< 200 kHz). Also, the cavity temperature is increased as scan rate is lower. The linewidth becomes broadened in the scan from the blue to the red side of resonance.

[3]the cavity life time in waveguide-coupled resonator can be defined as $\tau^{-1} = \tau_0^{-1} + \tau_{ext}^{-1}$

Ring down measurement can avoid the systematic error in the measurement of the resonator Q factor. The measurement method directly records the photon lifetime in time domain, so the scan speed needs to be much faster than cavity lifetime. Then consequently it doesn't need to consider the laser coherence time or thermal broadening. However, in case that the cavity lifetime is short (low Q resonator), the ring down period becomes too short and the oscilloscope doesn't have enough resolution to record the short period ring down trace.

2.2.4.2 Q factor of micro-toroid resonators

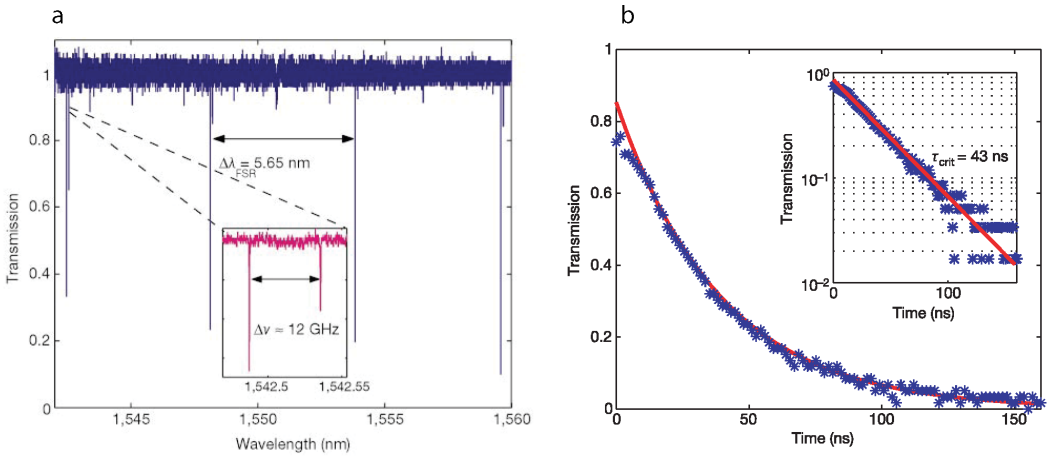

Figure 2.6: **Q factor characteristics of toroidal microresonator** (**a**) Transmission spectrum of a toroidal resonator. Tapered fiber was used to measure the coupled transmission of the resonator, and FSR is 5.65 nm. The inset shows the lowest order mode. Q factor of the resonance mode can be measured by fitting the linewidth of dip in the transmission spectrum. (**b**) Ring down measurement at critical coupling. The measured lifetime (43 ns) corresponds to an intrinsic Q factor of 125 million. **a-b** are from Armani, et al.[2].

Fig.2.6 depicts the transmission spectrum of toroidal micro-resonator, and the ring down trace of the optical mode at critical coupling point. Both transmission scan and ring down trace were measured through a tapered fiber in close proximity. The taper width and cavity-fiber gap were carefully controlled[2, 49] to achieve the proper phase-matching condition. Non-resonant loss[4] was observed less than 5 % according to Ref.[2]. It was the record value for chip-based devices, and achieved nearly four orders of magnitude improvement compared to the other reports from wafer-scale processed devices[84, 85] at this time. Further improvement of Q factor had been reported in Ref.[49], and the maximum Q factor record from the toroidal microresonator is nearly 500 million (diameter $15\mu m$) so far[5].

[4] see page 39 of Ref.[49] for further explanation.
[5] see page 119 of Ref.[49] for further information.

2.3 Chemically etched UHQ resonator on a chip

2.3.1 Wedge resonator fabrication process

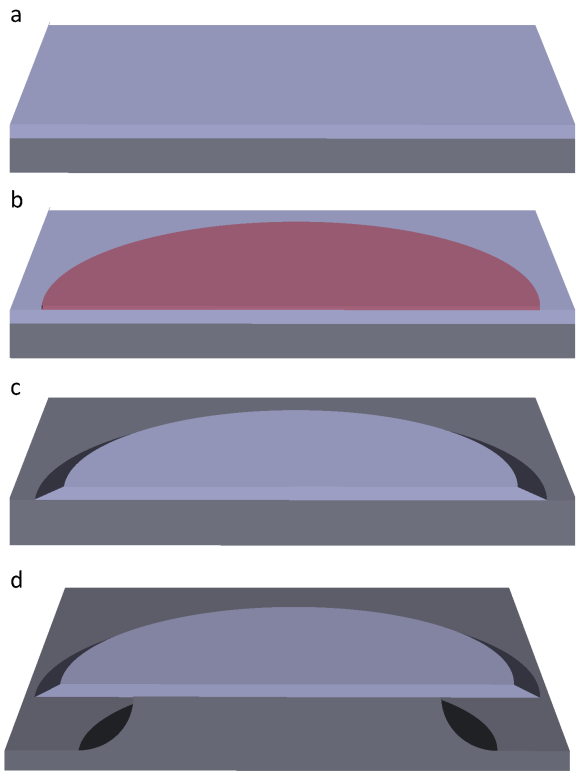

Figure 2.7: **Wedge disk microfabrication process (a)** Silicon oxide is grown on silicon wafer using thermal oxidation. **(b)** Photoresist is patterned using a GCA 6300 stepper on thermally grown oxide. **(c)** Buffered hydrofluoric acid etch is processed. Photoresist acts as an etch mask, and then is removed after the etch process. **(d)** Silicon is isotropically etched by xenon difluoride to creat air-cladding around the wedge resonator.

As noted earlier, the fabrication of wedge disk avoids the specialized fabrication step such as laser reflow. Consequently the wedge disk structure can be lithographically defined, so that we can control its size and achieve millimeter- and centimeter-scale diameter.

Fig.2.7 shows the microfabrication process. Devices were fabricated on float zone silicon wafers, and here wafer doping concentration can determine silicon oxide index as well as optical Q factor (see table 1 in Ref[86]). An 8-μm-thick Oxide layer is grown on the silicon surface, and specifically initial and final growth steps are dry oxidation – it determines surface roughness as well as mechanical properties. Photoresist was coated on silicon oxide layer, and the resist was patterned using GCA 6300 stepper. Here, hexamethyldisilazane (HMDS) can be used to improve the adhesion between silica film and photoresist. Besides, the thickness of photoresist can also efficiently control the adhesion at the interface and this adhesion strength determines the angle of wedge surface after buffered hydrofluoric acid

etch. Fig.2.8 shows the cross-section SEM images of etched silica wedges with different wedge angles, and these are the results of adhesion control using both resist thickness control and HMDS[6]. In addition, the exposure time can also change the wedge angle; however, it usually changes the roughness of the wedge surface (related to Q factor) and the control range is narrow.

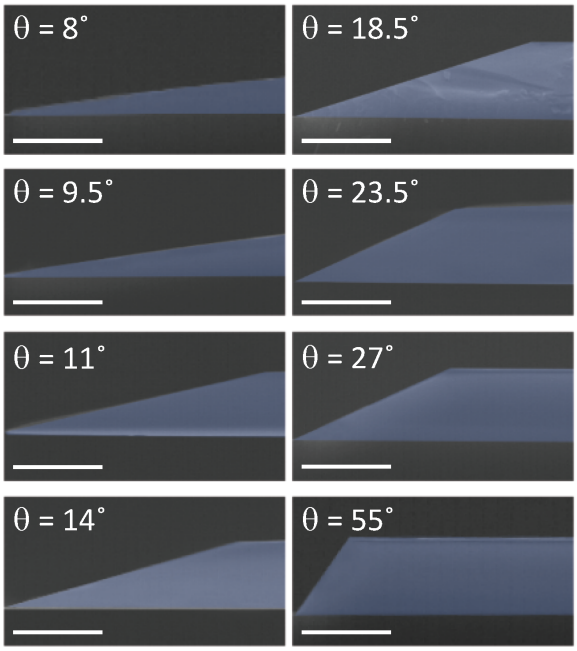

Figure 2.8: **Wedge disk angle control** The adhesion between photoresist and silica surface controls the angle of silica wedge structure after buffered hydrofluoric acid etch. The angle varies from 8° to 55° (photoresist thickness≈ 1500 nm.) – recently 70° wedge angle was achieved using thinner photoresist (photoresist thickness≈ 500 nm.).

Fig.2.9 shows the buffered hydrofluoric acid etch process as a function of etch time. The etch speed (Transene, buffer-HF improved) is approximately 100 nm/ min, and it depends on temperature. If etch speed is faster than optimal, then the surface roughness is increased and consequently Q drops. Otherwise, if etch speed is slow due to low temperature, then crystallization of hydrofluoric acid begins and the etch quality is degraded as well. At the beginning of hydrofluoric acid etch, the etch process starts at the silica surface that photoresist doesn't cover. This etch process is almost isotropic and has higher surface roughness (this is the foot region). As the etched surface penetrates deeper under the photoresist, the etch process is no longer isotropic and the roughness becomes very smooth. The foot region, which is created at the beginning, start to disappear once silicon surface appears, and then gradually disappears (see Fig.2.10) as the etched surface moves far from photoresist edge (etchant flow might be slower and stable).

[6]The angle control was discussed with Prof. Axel Scherer in candidacy exam, so more discussion was added in this thesis.

Photoresist layer is removed after hydrofluoric acid etch, and the xenon difluoride etch is applied to isotropically undercut silicon. Then the undercut creates air-cladding around wedge resonator, and the undercut depth is determined from both mechanical stability[87] and mode coupling between the optical mode and silicon structure. As a result, silica surface has 0.15, 0.46, 0.70 nm surface roughness on the top, side, and bottom of the silica wedge structure (see table2.1 for more detail).

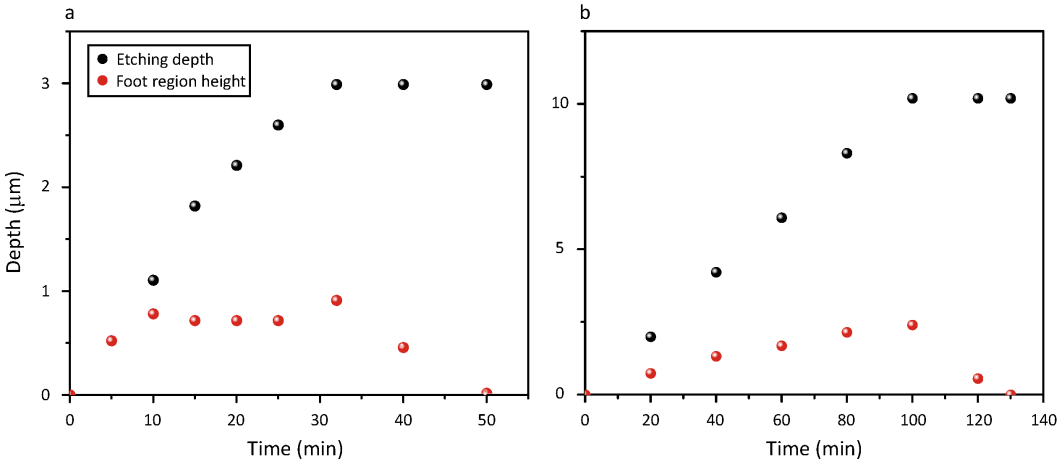

Figure 2.9: **Buffered hydrofluoric acid etch process** Etching depth and foot region height as a function of etching time. Initially photoresist was patterned on oxide, and the foot region thickness starts to drop once the etched depth reaches the original oxide thickness (**a**: 3 μm, **b**: 10 μm). Additional etch was applied to remove the remaining foot region. The data in **a** was used in Lee, et al.[22].

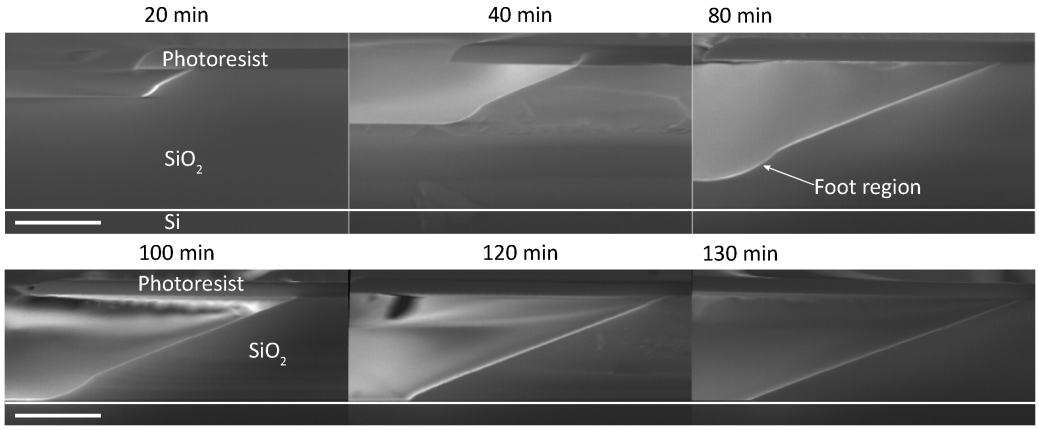

Figure 2.10: **Cross-sectional SEM image of wedge surface during buffered hydrofluoric acid etch process** SEM images of wedge structure. As a function of time, etch depth increases and foot region height is saturated and drops. The scale bar indicates 6 μm on the top three panels, and 8.5 μm on the bottom three panels. Because of electron beam charging effect, the images were blurred and not clear. The parts of figures were used in Lee, et al.[22].

Wedge angle	Top	Bottom	Side
10°	0.15 nm	0.70 nm	0.46 nm
30°	0.15 nm	0.70 nm	0.75 nm

Table 2.1: **Surface roughness of silica wedge disk** r.m.s surface roughnesses were measured on silica wedge disk using AFM. Here, the correlation length is on the order of a few hundred nanometers. It is interesting to note that the surface roughnesses obtained from different wedge angle are different. The data are from the method of Lee, et al.[22].

2.3.2 Q-factors

Fig.2.11 presents measurements showing the effects of wedge angle, diameter, and oxide thickness on Q-factor. On this figure, four oxide thicknesses are shown with two wedge angles and diameters over 0.2 mm to 7.5 mm. The inset is provided to show a spectral scan for the case of a record Q-factor of 875 million. The resonance mode is under-coupled with tapered fiber, and the sinusoidal curve is a calibration scan performed using a fiber interferometer. From this figure, Q clearly depends on resonator diameter, oxide thickness, and wedge angle – mainly because of mode location and surface roughnesses. Here, we would like to explain that dependence and connect the properties with optical mode location and surface roughness, which was measured using AFM.

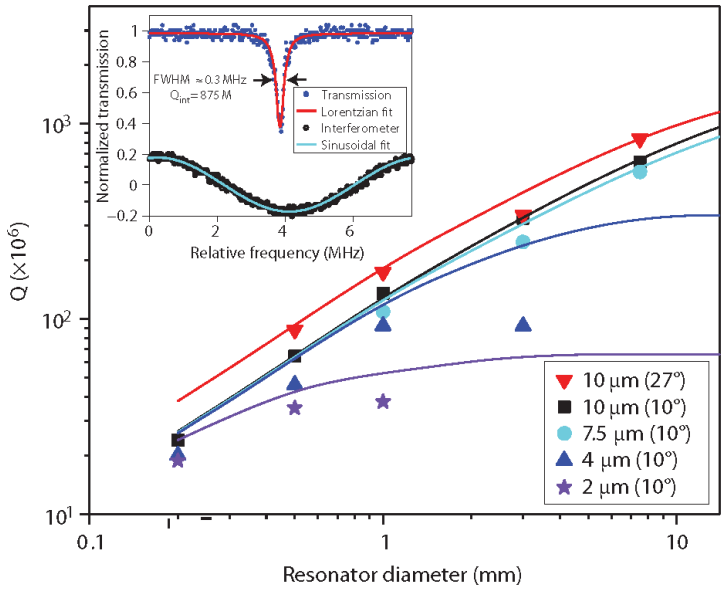

Figure 2.11: **Wedge disk Q-factor versus resonator diameter with oxide thickness** Q data are taken from the following set (M, million): D≈ 7.5 mm, Q≈ 799 M, 875 M; D≈ 3 mm, Q≈ 326 M, 331 M; D≈ 1 mm, Q≈ 169 M, 174 M; D≈ 0.5 mm, Q≈ 88 M, 91 M. Solid lines show the Q-factor prediction. Inset shows the spectral scan of 875 M mode. This figure is from Lee, et al.[22]

Radius As shown in Fig.2.11, Q-factors of wedge disks are higher as resonator diameter

increases. Diameter of disk resonator corresponds to waveguide bending, and the optical mode distribution can be modified depending on the diameter. In larger diameter disk (smaller bending effect), the optical mode shifts inwards further than the optical mode in smaller diameter disk (larger bending effect). In addition, longer wavelength optical mode, which experiences less bending effect than shorter wavelength mode, shifts inwards further than the optical mode in shorter wavelength. As noted in Table.2.1, the surface roughness is not uniform over every surface of wedge structure. For example, side surface has approximately 5 times higher roughness than top surface. Therefore, the Q-factor of the optical mode depends on resonator diameter which determine the mode location and the mode field distribution over the structure. A larger diameter optical mode is defined inwards further than the smaller diameter optical mode, and thus the optical mode experiences the roughnesses of top and bottom surfaces instead of the roughnesses of side and bottom. In silica wedge disk with thickness over 7.5 μm, Q-factor increases as resonator diameter increases. It is also interesting to note that the Q factor is saturated at a certain diameter in 2-μm-thick and 4-μm-thick oxide resonator, because the optical mode already shifts inward enough not to experience the side wall roughness.

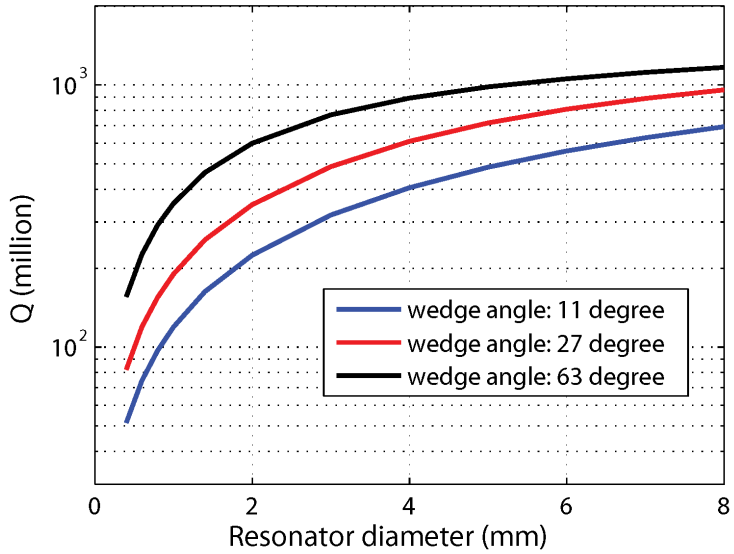

Figure 2.12: **Wedge disk Q factor prediction** Optical Q factor versus resonator diameter with three distinct wedge angles (θ=11, 27, 63°). This figure is from the supplementary information of Lee, et al.[22]

Wedge angle Wedge angle is also another strong variable that changes Q-factor by changing the optical mode location and distribution. In Fig.2.11, we can compare Q factors of 10-μm-thick oxide resonators with different wedge angles (10° and 27°). As wedge angle is higher, then the silica cross-sectional area associated with wedge interface decreases and consequently top and bottom surface have stronger contribution on total scattering roughness

that the optical mode experiences. As discussed in the previous part, the combination of top and bottom surface roughnesses creates less total scattering roughness than the one from the combination of side and bottom surface roughnesses. Therefore, the Q-factors from the wedge angle of 27° tends to be higher than those from the other angle, even though the side wall roughness of 27° is worse than the one of 10°. Fig.2.12 shows Q factor prediction as function of resonator diameter and wedge angle. Here, Q factor is calculated with oxide thickness of 10 μm and the surface roughness of 63° is assumed to be at a similar level with those in other wedge angles.

2.3.3 Resonator size control

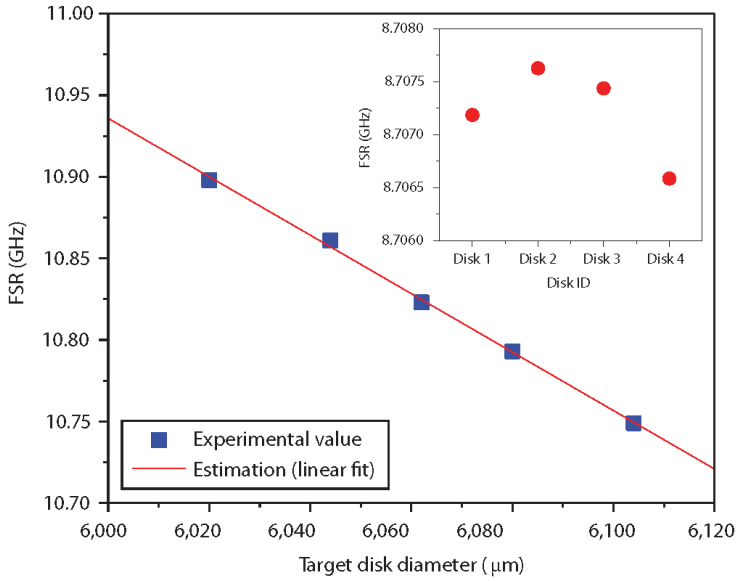

Figure 2.13: **Wedge disk FSR control** FSR of wedge disk at five distinct sizes are measured with 2.4 MHz r.m.s variance. Inset shows FSR measured on disks with the same target FSR (variance of 0.45 MHz). This figure is from Lee, et al.[22]

Fig.2.13 shows the measured FSR of wedge disks with five different target disk diameters. Here, the disk diameter was adjusted using the diameter of photo-mask pattern under identical fabrication conditions (i.e. exposure time, photoresist coating conditions, wet etch time). The measured FSR shows 2.4 MHz r.m.s. variance with respect to the target design, and it is relative variance of less than 1:4500. The inset shows results from wedge disks fabricated with the same target disk diameter. The measured FSR shows precision with variance of 0.45 MHz and it corresponds to relative variance of 1:20000. As discussed in section 2.2, the previous UHQ resonator needs specialized fabrication step in order to smooth the resonator surface and increase Q factor. However, the specialized step deformed and melted the structure of device as well as surface. Therefore, it was challenging to precisely define the structure size and geometry. Wedge resonator can achieve UHQ without

the specialized fabrication steps so that it enables one to precisely define the resonator structure as well[7].

2.4 Discussion – nonlinear optics applications

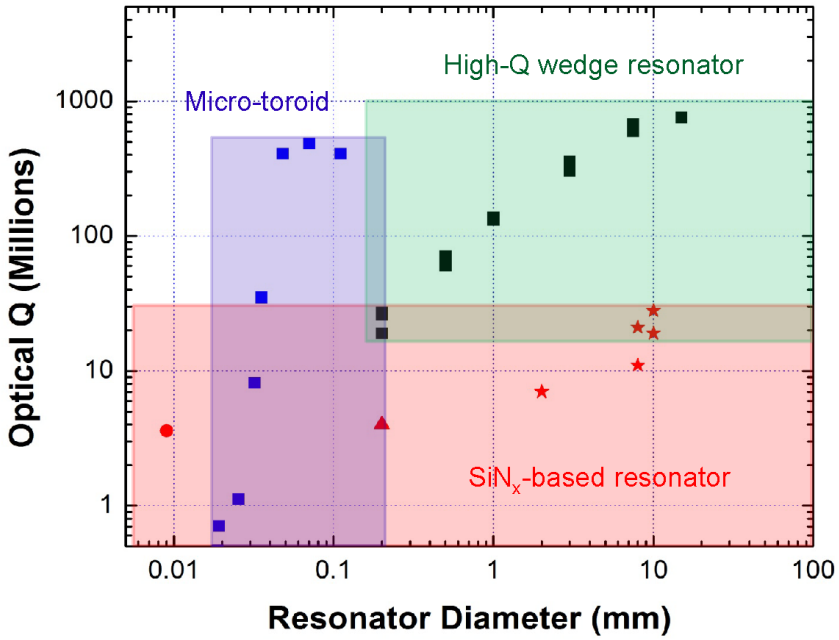

Figure 2.14: **Chip-based resonator Q factor versus diameter** Q factors of toroidal microresonators[2, 49, 78], wedge disk resonators[22], and Si_3N_4 based resonators[88, 89]. This figure is kindly provided by H. Lee.

Fig.2.14 shows Q factor records of toroidal microresonators[2, 49, 78], wedge disk resonators[22], and nitride[8] based resonators[88, 89]. The chip-based silica resonators recorded Q factors exceeding 100 million from hundreds micron to millimeters diameter, and the high Q enables to store extremely high circulating power inside small mode volume. The chip-based UHQ platforms successfully demonstrated a wide range of applications in nonlinear optics including parametric oscillation[20], Raman lasing[92, 93], Brillouin scattering[9, 22], and harmonic generation[7] since it was demonstrated[2].

It is also important to note that UHQ wedge disk enables one to engineer the device structure using standard MEMS process. The precise fabrication method allows to tailor the nonlinear properties of the UHQ microresonators (Chapter 3), and enable to extend the process steps towards fully integrated UHQ silica cavity with planar waveguide structure (Chapter 5).

[7] Chapter 3 will introduce more detail on UHQ resonator geometry control.

[8] Further development in nitride platform has been demonstrated in Ref.[4, 90, 91] after this figure was presented.

Chapter 3

NONLINEAR OPTICAL CAVITIES: LITHOGRAPHIC DISPERSION DESIGN FOR NONLINEAR OPTICS

3.1 Abstract[1]

The long photon storage time (high Q) and small mode area of optical microcavity induce strong nonlinear interaction with resonator medium[1]. This enables access to the wide range of applications in chip-based nonlinear optics[5, 7, 8, 20, 22]. As has been discussed in the last chapter, the UHQ performance had been realized with CMOS-compatible process so it allows the precise control of cavity geometry[22]. Interestingly the precise control of cavity geometry can tailor the chromatic dispersion of the optical mode, and the dispersion strongly manipulates the nonlinear optical phenomena in the cavity[23]. In this chapter, we will discuss the cavity design method for nonlinear optics, and the method allows higher-order, wide bandwidth dispersion control[71] as well as mode spectrum engineering[55]. Simultaneously, the micro-fabrication method for the cavity design maintains the UHQ performance as well[55, 71]. As a demonstration, soliton frequency comb had been generated in mode-spectrum-engineered UHQ cavity and wideband frequency comb was shown in the dispersion-engineered resonator.

[1]Main body of this chapter has appeared in Nature Photonics 10, 316-320, 2016; Subsection 3.3.2, and 3.4.1 have appeared in Optics Express 20, 26337-26344, 2012; Subsection 3.4.3 have appeared in Optica 2, 1078-1085, 2015.

3.2 Dispersion in WGM resonators

3.2.1 Material dispersion

The bound electrons of a dielectric medium interact with electromagnetic waves, and the dielectric medium absorbs the electromagnetic radiation through the bound electron oscillation at the characteristic resonance frequencies. Different types of resonances create the frequency dependent medium response, and the frequency dependences lead to different speed of light that the electromagnetic waves experience in the medium as a function of wavelength. Specifically, the dispersion of the material index plays an important role in multi-spectral wave propagation such as short optical pulses and optical frequency combs because the dispersion induces different travel speed at different spectral components [23]. Material dispersion is one of the strongest contributions to the total dispersion of the optical element (e.g. waveguide and resonator), and specifically there are several materials used for the optical nonlinear resonator platform[1, 3, 10–12, 94].

Materials	**Refractive index**	n_2 $(10^{-20}m^2W^{-1})$	β_2 (ps^2/km)	λ_0 (nm)
SiO_2	1.44	2.2	-28	1280
Si_3N_4	1.98	25	100	> 2500
MgF_2	1.37	0.9	-10	1350
CaF_2	1.43	3.2	-0.1	1550

Table 3.1: **Comparison of different WGM resonator materials**

Dispersion relation has been differently presented within the fields of photonics, condensed matter physics, and fiber optics. Here, we would like to connect the different ways to present the dispersion relation all together and particularly define dispersion terms that are frequently used in WGM resonator.

$$\begin{aligned}\beta = \frac{\omega}{c}n(\omega) &= \sum_{i=1}^{n}\left(\frac{1}{m!}\frac{d^m\beta}{d\omega^m}\Big|_{\omega=\omega_0}(\omega-\omega_0)^m\right) \\ &\approx \beta_0 + \beta_1(\omega-\omega_0) + \beta_2(\omega-\omega_0)^2\end{aligned} \tag{3.1}$$

Using a Taylor expansion with respect to the angular optical frequency ω, the propagation constant β can be expressed as eqn.3.1 (n is the refractive index of the medium as a function of ω) and dispersion is most commonly defined using β of light in a dielectric medium[23]. The first order dispersion, β_1 ($= \frac{d\beta}{d\omega} = \frac{1}{v_g}$), is inversely proportional to group velocity ($v_g = \frac{d\beta}{d\omega}$). The envelope of the optical pulse (at center frequency ω_0) propagates in dielectric medium with the group velocity, and the shape of the pulse doesn't change without nonlinearity. In addition, the group velocity depends on the center frequency (ω_0) so that pulses with different center frequency propagate at different velocities in a material with the

first order dispersion. The second order dispersion, β_2 ($= \frac{d^2\beta}{d\omega^2}$) corresponds to group velocity dispersion (GVD) which is the change of inverse group velocity with the angular optical frequencies. In the fiber optics and ultrafast optics communities, the wavelength dependent second order dispersion is most common to specify the dispersion of group velocity[23]. The GVD dispersion parameter D and the group delay dispersion (GDD) have been commonly used in WGM resonator dispersion[11, 95–98], and those terms can be written as (ϕ is phase shift, and L is the travel length in dielectric material) [23, 33]:

$$D = \frac{d\beta_1}{d\lambda} = \frac{d^2\beta}{d\lambda d\omega} = \frac{d\omega}{d\lambda} \cdot GVD = -\frac{2\pi c}{\lambda^2} \cdot GVD \tag{3.2}$$

$$GDD = \frac{d^2\phi}{d\omega^2} = L\frac{d^2\beta}{d\omega^2} = L \cdot \beta_2 \tag{3.3}$$

Fig.3.1 shows dispersion parameter of several materials that are used for WGM resonator platforms. Table3.1 shows more detail dispersion parameter values as well as other nonlinear parameters. λ_0 is the wavelength where dispersion parameter D becomes zero. Here we define "normal" dispersion when D<0, GVD>0, GDD>0, and "anomalous" dispersion when D>0, GVD<0, GDD<0.

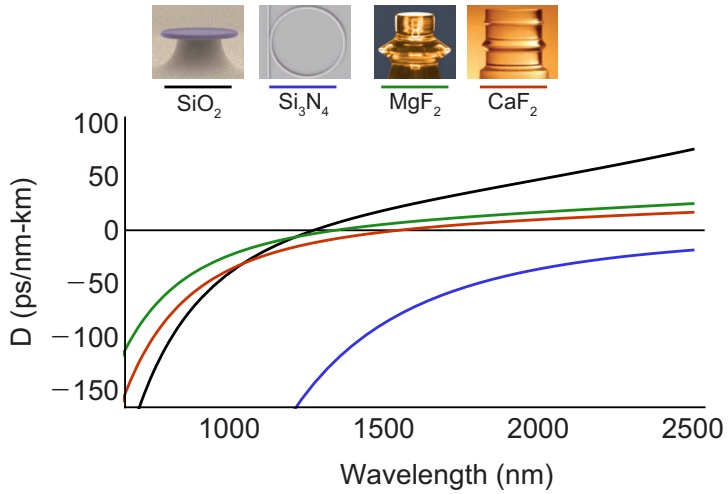

Figure 3.1: **Material dispersion of various WGM resonator platform** GVD dispersion parameters of WGM resonator materials as a function of wavelength

3.2.2 Dispersion in optical microresonators

As explained in previous subsection, the dispersion is dominantly determined by material dispersion which originates from a wavelength dependent material index. However, when the light travels through optical waveguide, the additional effects contribute to the total dispersion and those effects basically come from the structure of the waveguide – geometric dispersion, modal dispersion, and polarization mode dispersion[6, 32]:

Geometric dispersion In specific spatial mode with polarization, the spatial index distribution ($n(x, y, z)$) also contributes on total dispersion of the optical mode and the amount of geometric dispersion is a function of wavelength as well. This chapter mainly shows geometric dispersion engineering.

Modal dispersion In specific polarization, different spatial modes experience a different amount of geometric dispersion. Sections 3.4.2, 3.4.3, and 3.5.3.3 discuss modal dispersion and its engineering.

Polarization mode dispersion In the specific spatial mode, different polarization induces different amounts of geometric dispersion because of (mostly) antisymmetric wavegude structure. Subsection 3.5.3.3 discusses polarization mode dispersion.

The mode spectrum of optical resonator is the only accessible parameter for dispersion measurement, while optical fibers and other components have several exiting method using the group delay of optical pulses[99, 100], interferences to determine the phase shifts, and so on. The resonance frequencies of WGM resonator are defined by

$$f_\mu = \frac{\mu \cdot c}{2\pi \cdot R \cdot n_{eff}} \tag{3.4}$$

Here, f_μ is the resonance frequency at azimuthal mode number μ, n_{eff} is the effective index, and R is the radius of WGM resonator. Combining eqn.3.1 with eqn.3.4 yields

$$\beta = \frac{\mu}{R} \tag{3.5}$$

$$\beta_1 = \frac{d\beta}{d\omega} = \frac{d(\mu/R)}{d(2\pi f_\mu)} = \frac{1}{2\pi R} \cdot \frac{d\mu}{df_\mu} = \frac{1}{2\pi R \cdot FSR} \tag{3.6}$$

$$\beta_2 = \frac{d^2\beta}{d\omega^2} = \frac{1}{(2\pi)^2 R} \cdot \frac{d}{df_\mu}\left(\frac{1}{FSR}\right) = -\frac{1}{(2\pi)^2 R \cdot FSR^3} \cdot \frac{dFSR}{d\mu} \tag{3.7}$$

Furthermore, the mode frequencies of microresonator are often expressed using Taylor expansion[21]. Here $\omega_\mu = 2\pi f_\mu$, $D_1/2\pi = FSR$, and D_2 is deviation of FSR ($\frac{dFSR}{d\mu}$):

$$\omega_\mu = \omega_0 + \mu D_1 + \frac{1}{2}\mu^2 D_2 \tag{3.8}$$

3.3 Resonator dispersion measurement

As discussed in the previous section, resonator dispersion can be directly measured by mode spectrum, and the resonance frequencies can be measured with precise references such

as mode-locked comb[32, 101, 102], calibrated fiber interferometer[55, 70, 103–105], and external RF source[71, 98, 106]. One requirement is that measurement bandwidth needs to be wide enough to observe deviation of mode spacing larger than experimental noise. For instance, resonance linewidth, laser scan resolution, and reference precision can be the major sources of experimental noise. In this section, we will review the several methods for the dispersion measurement. In particular another wideband dispersion method, which covers from 1400 nm to 2100 nm, will be introduced using EOM (Electro-optic modulator)-assisted dispersion measurement, difference frequency generation, and external comb broadening.

Frequency comb-assisted diode laser spectroscopy[32, 102] In this method, the scanning laser is swept over the measurement bandwidth within few seconds and the transmission spectrum over the bandwidth is recorded on a high resolution oscilloscope. The wideband transmission spectrum records the resonance dips of the microresonator, and the scanning laser is partially split into a self-referenced comb in order to generate beat signal of the laser with the frequency reference. The signal of beat note is filtered in the RF domain with a narrow bandpass filter, so the filter-transmitted signal can be detected only when the scanning laser passes the comb line with frequency offset which corresponds to the filter passband frequency. The filter-passed signal can give the frequency value of the scanning laser, and the frequency information can precisely calibrate the transmission spectrum with resonance mode dips. This measurement scheme is a rapid method that can provide high precision simultaneously. The experimental error would only be limited by resonance linewidth, and there is no limitation on the range of mode spacing measurement (e.g. from few GHz to several THz). However it requires mode-hopping-free laser over entire measurement range and the measurement bandwidth is limited by both frequency comb and scanning laser. This method will be further reviewed and discussed in section 3.3.1.

Diode laser spectroscopy using calibrated fiber loop[55, 70, 103–105] This method is almost similar to the frequency comb-assisted diode laser spectroscopy except for the frequency reference. This method uses fiber interferometer or fiber-loop cavity with a FSR of tens of MHz, so that the frequency reference has fiber dispersion and imprecision from the linewidth of fiber cavity or an interferometer signal which needs to be calibrated.

EOM-assisted dispersion measurement[71, 98, 106] The scanning diode laser is sent through an EOM, and the modulator generates sidebands at a spacing equivalent to the RF source frequency. The RF frequency becomes same with resonance mode FSR when the dip is spectrally overlapping with two sidebands. This method doesn't require self-referenced comb (but provide exact and direct referencing using RF tone) as well as wide mode-hoping free laser. However, this method can only measure lower FSR ($< 2 \times f_{RF}$; f_{RF} is EOM modulation frequency) and can scan only few FSR at one transmission trace. This method will be further discussed in section 3.3.2

3.3.1 Review: Frequency comb assisted diode laser spectroscopy

3.3.1.1 Measurement principle

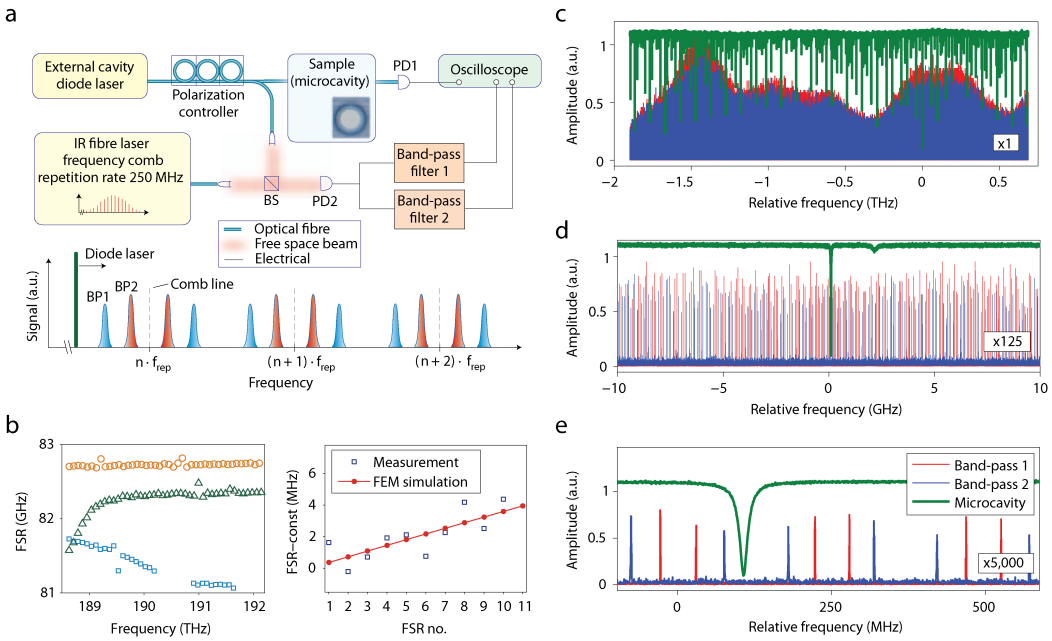

Figure 3.2: **Frequency comb assisted diode laser spectroscopy** (**a**) A diode laser is swept to generate beat note with referenced comb. The beat note is detected by a photodiode (PD2) and split into two band-pass filters (BP 1&2) generating calibration markers of diode laser. (**b**) Measured FSR from different mode families (left), and the deviation of the FSR as a function of mode number (right). (**c-e**) Transmission spectra of microresonator with calibration markers. (**a-e**) were kindly provided by P. Del'Haye[32].

Fig.3.2a shows the set-up of the frequency comb assisted diode laser spectroscopy method[32]. Here, an external cavity diode laser (ECDL) around 1550 nm was used (New Focus Velocity, short term linewidth < 300 kHz) to generate a RF beat note with self-referenced frequency comb (Menlo Systems GmbH, f_{rep} = 250 MHz). The beat notes were detected by a fast photodiode (200 MHz bandwidth), and the signal is sent to a narrowband band-pass filter (full width half maximum ≈ 1 MHz). The frequency marker is detected when the diode laser frequency (f_D) is

$$f_D = f_c \pm f_{BP} = f_{CEO} + n \cdot f_{rep} \pm f_{BP} \tag{3.9}$$

where f_c is comb frequency, f_{BP} is bandpass filter center frequency, f_{CEO} is carrier envelope offset frequency of Menlo comb, and f_{rep} is repetition rate of the comb. Increasing number of bandpass filters can generate more frequency calibration peaks within each interval of one repetition rate (f_{rep}).

In this work, one laser scan gives more than 64000 calibration peaks with sufficient signal-to-noise ratio. The instantaneous frequency is interpolated using those calibration markers, and

it leads to a resolution of ≈ 1 MHz. This resolution is mainly determined by the diode laser scanning behavior (not perfectly linear scanning) and the frequency stability of frequency comb. The resolution can be further improved if the number of bandpass filters increases with oscilloscope channels. In addition, the bandwidth of the bandpass filter determines the maximum scanning speed (= $\frac{1}{\Gamma^2}$). As a proof-of-concept, Fig.3.2b-e shows measured mode spectra of ultra-high-Q optical microcavities and further detail can be found in either the caption of Fig.3.2 or Ref[32, 33].

This method is also adopted for diode laser spectroscopy using calibrated fiber loop as explained earlier, and it is widely used for rapid dispersion measurement method[55, 70, 103–105]. This method was also used for the results in Chapter 5.

3.3.1.2 Wideband dispersion measurement

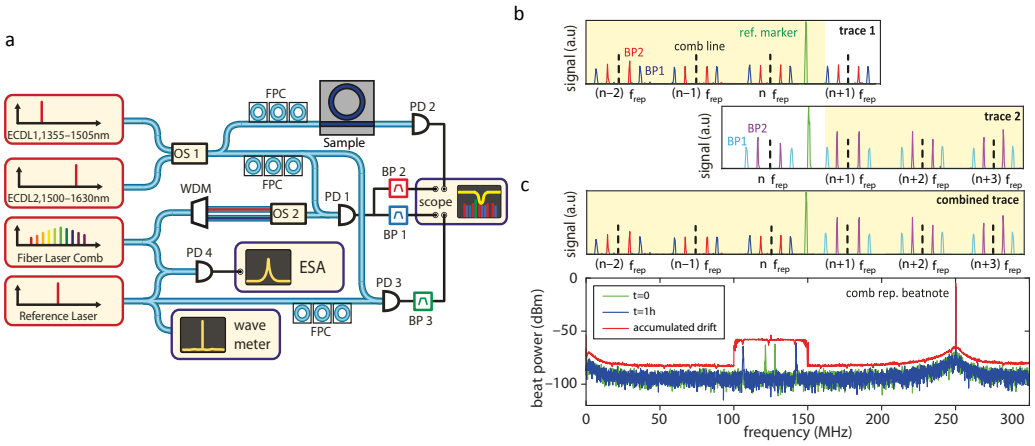

Figure 3.3: **Frequency-comb-assisted broadband spectroscopy with cascaded diode lasers** (**a**) Two diode lasers are used for wideband frequency scan. Fully stabilized frequency comb generates beat notes with scanning laser, and synchronized optical switches (OS) are used for improved signal-to-noise ratio with wavelength-division multiplexer (WDM). Reference laser is used for combining the two individual traces into a single continuous trace. (**b**) Procedure to combine two diode laser scan traces using the reference laser. (**c**) Measurement of reference laser drift within an hour. (**a-c**) are edited from Liu, et. al. [102]

Frequency comb assisted diode laser spectroscopy is precise and rapid method to measure mode spectra of microresonator, but it has bandwidth limitation which comes from either frequency comb or scanning diode laser (also needs to be mode hoping free). In order to achieve wider bandwidth dispersion measurement based on the method, two widely tunable mode-hop-free diode lasers (laser1 = 1355 - 1505 nm; laser2 = 1500 - 1630 nm) were used as shown in Fig.3.3. The principle of dispersion measurement is exactly same with Ref[32], so BP1 and BP2 generates the frequency markers when diode laser frequency is $f_{CEO} + n \cdot f_{rep} \pm f_{BP}$. In order to combine two individual transmission traces into a single continuous trace, an auxiliary reference laser (wavelength overlap between laser 1 and 2)

and additional bandpass filter are used to record reference frequency marker. Wavelength-division multiplexer (WDM) and optical switches (OS) filtered out the comb lines, which don't contribute to the beat signals, so as to increase signal-to-noise ratio of the frequency markers. Further detail can be found in Ref.[102].

3.3.2 Review: EOM comb assisted dispersion measurement

3.3.2.1 Measurement principle

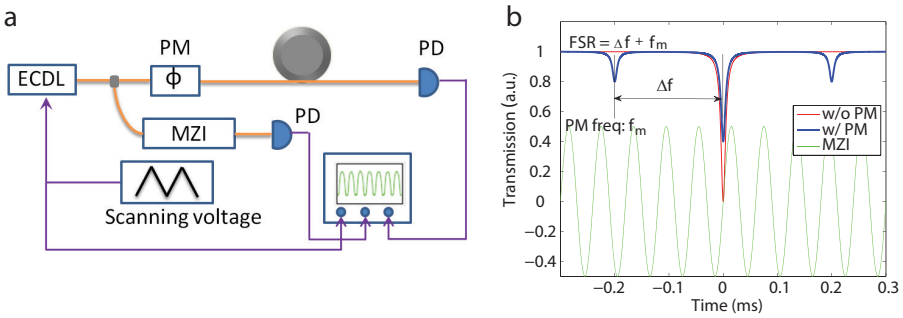

Figure 3.4: **EOM comb assisted dispersion measurement** (**a**) The ECDL is sent through an EOM, and the phase modulator (PM) creates sidebands at a spacing equivalent to the RF source frequency. Mach-Zehnder interferometer (MZI) generates frequency reference to measure the offset frequency Δf (panel b). (**b**) Schematic transmission traces of the sideband spectroscopy. The red trace shows the transmission trace when PM is off, while the blue trace shows the transmission trace when PM is on. Two phase modulation sideband appear, and the green MZI trace (usually MZI FSR is from few MHz to several tens MHz) can be used to measure Δf. (**a-b**) are edited from Li, et. al.[98]

Fig.3.4 shows the experimental set-up for sideband spectroscopy using EOM comb[98]. Here, the scanning diode laser split into phase modulator (PM) and Mach-Zehnder interferometer (MZI) for creating sidebands and frequency calibration signal, respectively. First, PM generates two sidebands apart from scanning laser frequency by modulation frequency ($\pm f_m$) and two side spectral dips appear once the probe laser frequency is $f_{res} \pm f_m$ (f_{res} is the resonance frequency of the microcavity). Then, spectral dips from resonances with mode number m and $m+1$ can be overlapped once $f_m = FSR/2$ and also spectral dip from resonance with mode number $m+1$ is spectrally overlapped once $f_m = FSR$. MZI generates sinusoidal signal with a period of several MHz, and the periodic signal additionally calibrates scanning laser frequency.

The cavity FSR is determined by

$$FSR = f_m + \frac{T_o}{T_{MZI}} FSR_{MZI} \tag{3.10}$$

where T_o and T_{MZI} correspond to oscilloscope time intervals for the offset frequency and MZI period, and FSR_{MZI} is the FSR of MZI. Then consequently the uncertainty of cavity

FSR is,

$$\delta FSR = \delta f_m + \frac{\delta T_o}{T_{MZI}} FSR_{MZI} + \frac{T_o \delta T_{MZI}}{T_{MZI}^2} FSR_{MZI} + \frac{T_o}{T_{MZI}} \delta FSR_{MZI} \tag{3.11}$$

δf_m is determined by uncertainty of the modulation frequency, which is usually less than 1 Hz. The uncertainty of resonance peak determination (linewidth of dip $\approx$ 2 MHz at 100 million Q) and MZI fitting can contribute on δT_o and δT_{MZI} respectively, and in practice the second term and the third term of eqn.3.11 are on the order of 100 kHz in the measurement. FSR_{MZI} is measured via the power spectral density (PSD) from a balanced photodetector and the uncertainty of MZI FSR is measured to ±2.7 kHz over 6.723 MHz FSR (see more detail from Ref.[98]). Therefore, the uncertainty of cavity FSR measurement is mainly determined by the second and third term of the eqn.3.11 and this is at the level of hundreds kHz (might be depending on cavity linewidth). This method was used for the measurement results in subsection 3.4.1.4.

3.3.2.2 Wideband measurement

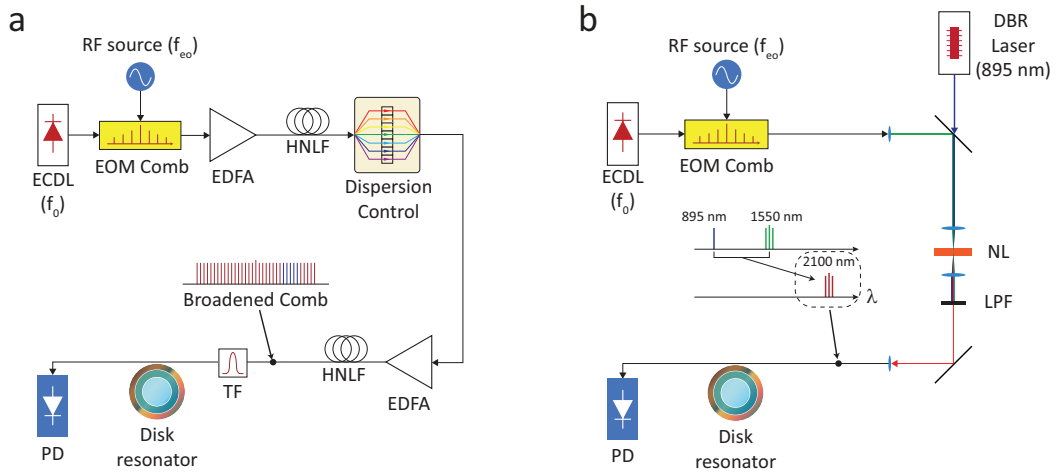

Figure 3.5: **Wideband dispersion measurement using EOM comb** (**a**) Broadband (1400−1700 nm) FSR measurement setup using externally broadened EOM comb. ECDL: External cavity diode laser, EDFA: Erbium doped fibre amplifier, HNLF: Highly nonlinear fibre, TF: Tunable bandpass filter, PD: Photodetector. (**b**) FSR measurement setup at 2100 nm using difference frequency generation between a 895 nm distributed Bragg reflector (DBR) laser and 1550 nm EOM comb. NL: Nonlinear crystal, LPF: Lowpass optical filter. (**a-b**) are edited from Yang, et al.[71].

As discussed earlier, the sideband spectroscopy has a relatively simple requirement so that the method can be easily applied to any different wavelengths as long as there is a scanning laser and modulators. To measure the FSR quickly and over a broad range of wavelengths, we have modified a method reported in Ref.[98]. Here we will discuss the method to measure wideband (1400 - 1700 nm) cavity dispersion as well as dispersion at 2 microns using

nonlinear optical techniques. These methods directly applied for the measurement results in section 3.5.3.3.

External broadened EOM comb Fig.3.5a shows the experimental setup that measures FSR using broadended EOM comb in 1400 - 1700 nm wavelength. ECDL is sent through EOMs with the modulatioin frequency (f_{eo}), and multiple modulators generate EOM comb with the f_{eo}-spacing near the pump. Further details on this EOM comb are provided in Ref.[107]. EDFA amplifies EOM comb, and HNLF spectrally broadens EOM comb over 100-nm-span centered around 1550 nm. Amplitudes and phases of the EOM comb is adjusted, amplified, and broadened again through wave-shaper, EDFA, and HNLF. Then it becomes spectrally broadened the EOM comb over 700-nm-span and the line spacing was tunable and set to coincide approximately with the resonator FSR. Tunable bandpass filter selectively transmits comb lines such as multiple sidebands (3-dB-bandwidth = 3 nm so approximately 15 comb teeth with 22 GHz line spacing), and sidebands are coupled into a cavity for FSR measurement. The filter bandwidth results in an FSR value that is spectrally averaged over the 3 nm spectral span, and it tends to smooth the data with respect to avoided mode crossings. The signal from photodiode was recorded on an oscilloscope, and a single transmission dip would appear when the microwave frequency in EOM coincides with the FSR of the resonator at the selected wavelength. The resolution in determination of the FSR by both methods was estimated to be about 100 kHz (consistent with Ref.[98] as expected).

Difference frequency generation Fig.3.5b illustrates the difference frequency generation setup to generate an EOM comb at 2100 nm. EOM comb is generated by ECDL and modulators, is sent through NL crystal with 895-nm-DBR laser. As a result of difference frequency generation via NL crystal, f_{eo}-spaced comb lines are generated at 2100 nm wavelength regime, and pass through lowpass filter which transmits only 2100-nm comb lines. Transmitted comb lines are coupled into the disk resonator and used exactly the same as the sidebands in Ref.[98] to measure cavity FSR.

3.4 Dispersion control, mode spectrum engineering, and soliton generation in UHQ resonator

Dispersion of the microresonator is determined by material dispersion and geometric dispersion[32]. Material selection strongly determines the optical resonator dispersion (c.f. Fig.3.1), and geometric dispersion can adjust the material dispersion properties by changing structural parameter of the resonator. Single-wedge disk resonator has great controllability on resonator diameter (subsection 2.3.3) and oxide thickness (via adjusting thermal oxidation time[2]) as well as wedge angle (subsection 2.3.1) using microfabrication, and we will introduce dispersion control method in single-wedge disk by adjusting wedge angle which can modify the contribution of geometric dispersion over wide spectral span.

3.4.1 Single-wedge dispersion control

As introduced in the last chapter, single wedge disk has three different structural parameters that decide resonator geometry accordingly: wedge angle, oxide thickness, and resonator diameter. Each parameter can control the strength of geometric dispersion contribution as discussed below:

Wedge angle The magnitude of wedge angle can decide the strength of mode confinement (related to effective index and its wavelength dependency) as well as the optical mode location (related to travel length). The stronger modal confinement (anomalous; see more detail in section3.4.1.2) compensates for the dispersion from the optical mode location shift (normal[3]) when wedge angle is reduced. The compensation makes balanced geometric dispersion in spectral domain, and the magnitude of the contribution is a function of wedge angle. This method has limitations on compensation of extremely high material dispersion.

Oxide thickness When oxide is much thicker than the wavelength of optical mode (> 3-4λ), then the total dispersion almost follow the material dispersion and the oxide thickness doesn't contribute on geometric dispersion[38]. However, when the oxide thickness approaches to the wavelength of the optical mode, then the oxide thickness starts to mediate the geometric dispersion efficiently and it can be even stronger than the contribution from wedge angle control (because mode location doesn't change at this case and only modal confinement becomes stronger as thickness decreases). This method often needs to sacrifice Q factor of the optical mode because of stronger scattering loss[22].

Resonator diameter As discussed earlier, resonator diameter can change the location of the optical mode and consequently the contribution of geometric dispersion can be controlled.

[2]For example, 1 μm: ~ 5 hrs; 2 μm: ~ 15.5 hrs; 3 μm: ~ 33 hrs. Here growth temperature is $1000^{\circ}C$ and the growth method is wet oxidation[108].

[3]In lower wedge angle disk, the optical mode shifts inwards further as wavelength increases than the mode in higher wedge angle resonator. It corresponds to effective radius reduction, and consequently FSR increases as the wavelength becomes longer. Therefore it is geometric dispersion contribution towards normal dispersion.

When the diameter is changed, FSR of microresonator is proportionally changed[22, 33] thus here dispersion and FSR are not separately controllable.

In this section and chapter, we will mainly focus on geometric dispersion control using wedge angle. Chapter 4 will discuss the geometric dispersion control using strong modal confinement related to oxide thickness, and Appendix.**??** will discuss dispersion engineering using oxide thickness control.

3.4.1.1 Single-wedge dispersion control – Principle

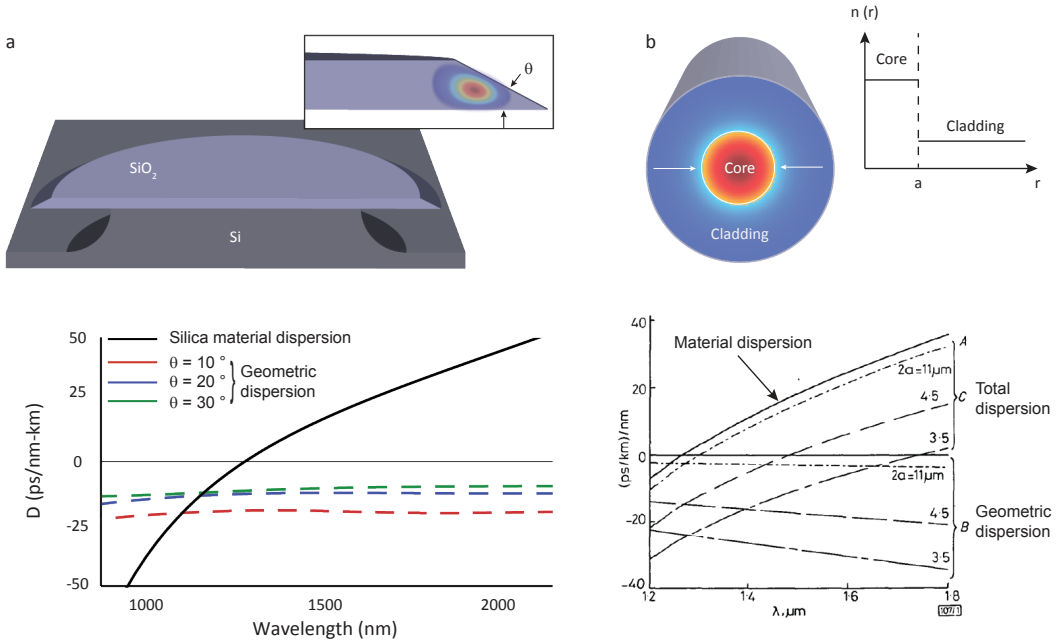

Figure 3.6: **Dispersion control in single-wedge disk and single-cladding fiber** (**a**) Geometric dispersion control schematic in wedge disk resonator using wedge angle (θ). Top: silica wedge resonator is illustrated and the inset shows optical mode profile on the wedge structure. Bottom: material and geometric dispersion is presented as a function of wavelength. (**b**) Geometric dispersion management scheme in single cladding fiber using core diameter control. Optical mode profile is super-imposed on the fiber schematic, and core layer is defined with radius "a" and higher index (n) material than cladding layer. The bottom dispersion chart is from Ref [109].

Fig.3.6 shows dispersion control of single-cladding fiber, and the analogous method of single-wedge disk. In a single-cladding fiber with higher core refractive index than the refractive index of the cladding (usually about 1 percent), the index contrast causes total internal reflection at the boundary and confines the optical wave along the length of fiber. The propagated optical waves are mainly confined in the core layer, and the mode partially spreads to cladding layer which has distinct refractive index. The distribution of the optical wave through the fiber cross-section is a function of wavelength even assuming zero material

dispersion, and the wavelength dependent distribution leads to different optical pathlengths that electromagnetic waves experience depending on the wavelength – this is the definition of geometric dispersion. Core radius "a" adjusts the geometric dispersion (commonly called as "waveguide dispersion" in fiber optics), and the bottom panel of Fig.3.6b shows the geometric dispersion contribution as a function of core radius. As optical mode extends over lower index cladding layer in longer wavelength, the group velocity (group index) increases (decreases) and it corresponds to normal dispersion[4]. Thus, by changing the index profile of the fiber, geometric dispersion can be used to offset the fixed material dispersion (see total dispersion curves in the bottom panel), so it can shift the overall dispersion (dispersion-shifted fiber).

Fig.3.6a shows the geometric dispersion control of single-wedge disk using wedge angle (θ). Here, the silica wedge structure confines optical waves by total internal reflection at the boundary of silica and air, and the optical mode partially extends over air cladding. Here, the wedge angle (analogue of core diameter "a") controls the distribution of optical mode over silica (analogue of fiber core) and air (analogue of fiber cladding). As shown in bottom panel in Fig.3.6a, geometric dispersion becomes stronger as wedge angle decreases, and this is analogous to the geometric dispersion adjustment using core diameter in panel b. Besides WGM mode moves inwards (outward) in longer (shorter) wavelength, and the path length of the WGM mode becomes shorter (longer). The optical mode shifts further in lower wedge angle, and the path length is additional variable that we need to consider when understand WGM resonator dispersion (see the following sections).

[4] $v_g = \frac{c}{n_g}$, GVD = $\frac{d}{d\omega}(\frac{1}{v_g}) = \frac{dn_g}{d\omega}$ and dispersion parameter D has opposite sign of GVD.

3.4.1.2 Single-wedge dispersion control – Numerical analysis

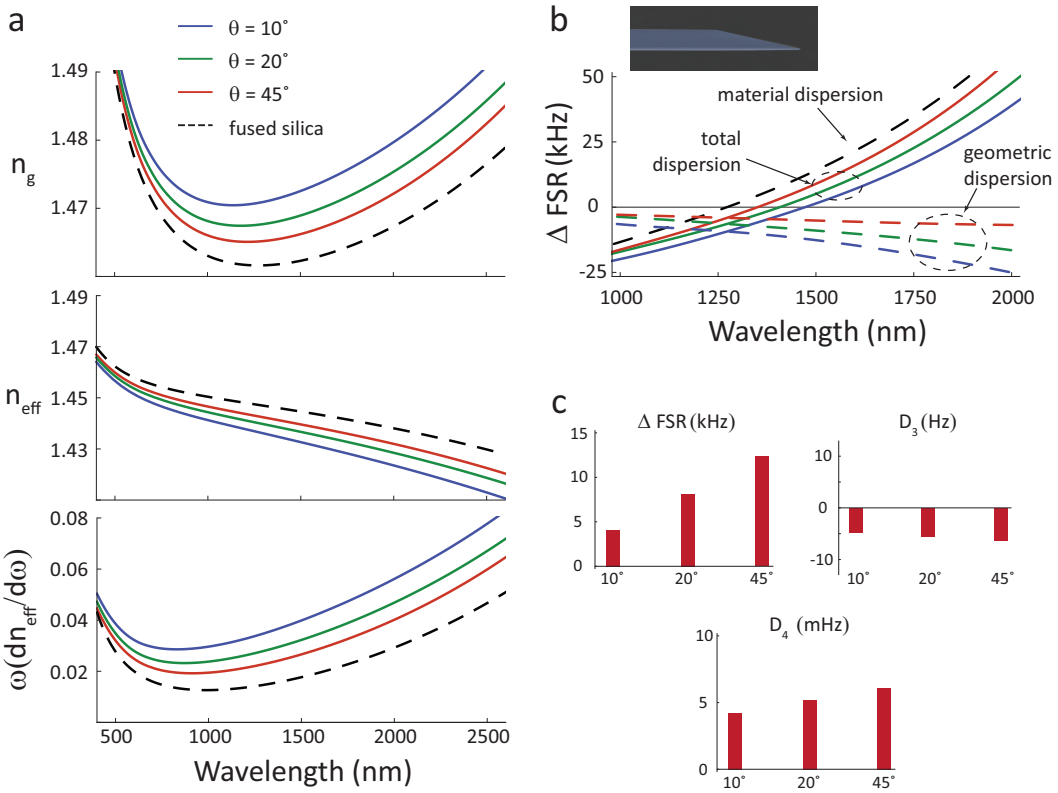

Figure 3.7: **Single-wedge dispersion control** (**a**) n_g, n_{eff}, and $\omega\frac{dn_{eff}}{d\omega}$ of the optical mode at the single-wedge disks. Black dashed lines are plotting n_g, n_{eff}, and $\omega\frac{dn_{eff}}{d\omega}$ of fused silica, respectively. (**b**) Calculated D_2 of single-wedge disks ($\theta = 10, 20, 45°$). Black dashed line, colored solid lines, and colored dashed lines are plotting total dispersion, material dispersion, and geometric dispersion, respectively. (**c**) Calculated ΔFSR, D_3, and D_4 of single-wedge shown in **a**-**b**. Dispersion coefficients are calculated at 1550 nm

Fig.3.7 shows the group index (n_g), effective index (n_{eff}), and $\omega\frac{dn_{eff}}{d\omega}$ of single-wedge disks. In lower θ-wedge, the optical mode spreads further into an air cladding and it results in effective index drop. Here, the effective index of lower θ-wedge decreases faster in longer wavelength, hence $\omega\frac{dn_{eff}}{d\omega}$ component in group index increases and the rise is even larger than n_{eff} drop. Therefore, the group index becomes larger even though the optical mode spreads out and effective index drops quickly – usually group index increases when the effective index is larger in fiber optics. Single-wedge can control the group index by 0.01 (θ= 10°), 0.007 (θ= 20°), and 0.004 (θ= 45°) over 1.46 (material group index at 1550 nm), and doped silica in commercial optical fiber has variation on the group index with the similar level of variation in wedge disks[71]. Therefore, controllable geometric confinement (using wedge angle) can efficiently change the group index of the optical mode as a single mode fiber does using different doping concentration on the core layer.

Fig.3.7b shows calculated ΔFSR (= D_2) of single-wedge, and it also illustrates material

dispersion (black dashed line) and geometric dispersion (colored dashed lines) separately. Single wedge disks have almost constant geometric dispersion offset with different strengths depending on θ, the contribution of geometric dispersion becomes larger as geometric confinement is stronger. The zero dispersion wavelength moves from 1300 nm to 1500 nm as wedge angle drops and simultaneously geometric dispersion (normal dispersion) becomes stronger. Dispersion coefficients are also displayed on Fig.3.7c for more information.

Here there is one note on ΔFSR: in a WGM resonator, FSR is determined with frequency-dependent $n_g(\omega)$ and $R(\omega)$ (see eqn.3.12)– R is the radial location where mode is confined [32]. ΔFSR isn't simply expressed as inversely proportional to the group index, as it is in fact affected by $R(\omega)$ too.

$$FSR = \frac{c}{L(\omega)} = \frac{c}{2\pi n_g(\omega) R(\omega)} \tag{3.12}$$

3.4.1.3 Single-wedge dispersion control – equation model

Frequency (ω_ν) of the optical fundamental mode in single-wedge resonator (assuming no material dispersion) is numerically modeled with Eqn. (1) of Ref [110, 111]

$$\frac{n_0}{c}\omega_\nu \approx \frac{\nu}{R}\left[1 + \frac{\alpha}{\nu^{2/3}}\right]. \tag{3.13}$$

where $\nu \gg 1$ is mode number, R is the radius, and α (= 10.23, 6.78, 4.08 for $10, 20, 45°$ wedge angle) is constant. Fig 3.8 a-b compare the approximated model (solid lines) with finite-element-simulation (dots) of single-wedge disk (geometric dispersion only), and Fig 3.8 shows the dispersion parameter calculated from Eqn.(12) of Ref [110] with finite-element-simulation (dots) which includes material dispersion. Single-wedge resonator defined light-guiding boundary and modified the magnitude of geometric contribution on dispersion using a wedge angle which is a wavelength-independent parameter.

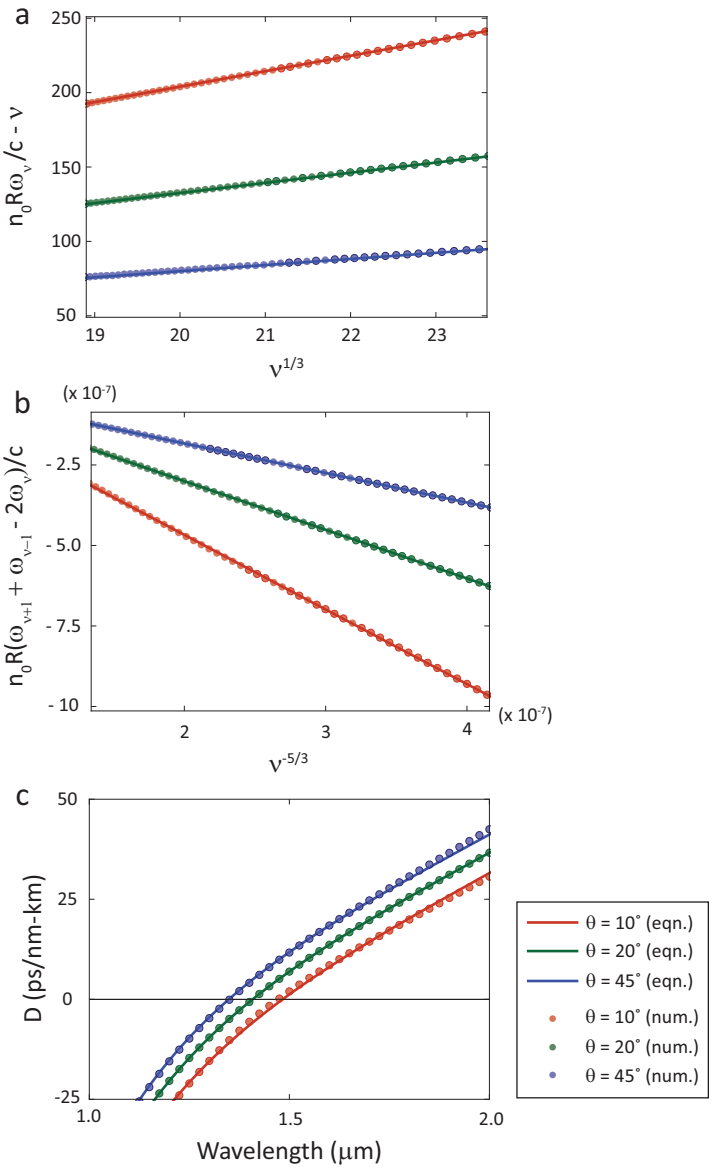

Figure 3.8: **Single-wedge dispersion in equation model** (**a**) $n_0R\omega_\nu/c - \nu$ for single wedge disks ($\theta = 10°, 20°, 45°$; solid lines) are plotted against $\nu^{1/3}$. Numerical simulation (finite-element-method; dots) results are plotted for comparison. (**b**) $n_0R(\omega_{\nu+1} + \omega_{\nu-1} - 2\omega_\nu)/c$ for single wedge disks are plotted against $\nu^{-5/3}$. Solid lines are from Eqn. (3) of Ref [110]; dots are finite-element-simulation results. (**c**) Dispersion parameter is plotted using both asymptotic expansion (solid lines, Eqn. (12) of Ref [110]) and numerical simulation (circular dots) which take material/ geometric dispersion into account.

3.4.1.4 Single-wedge dispersion characterization

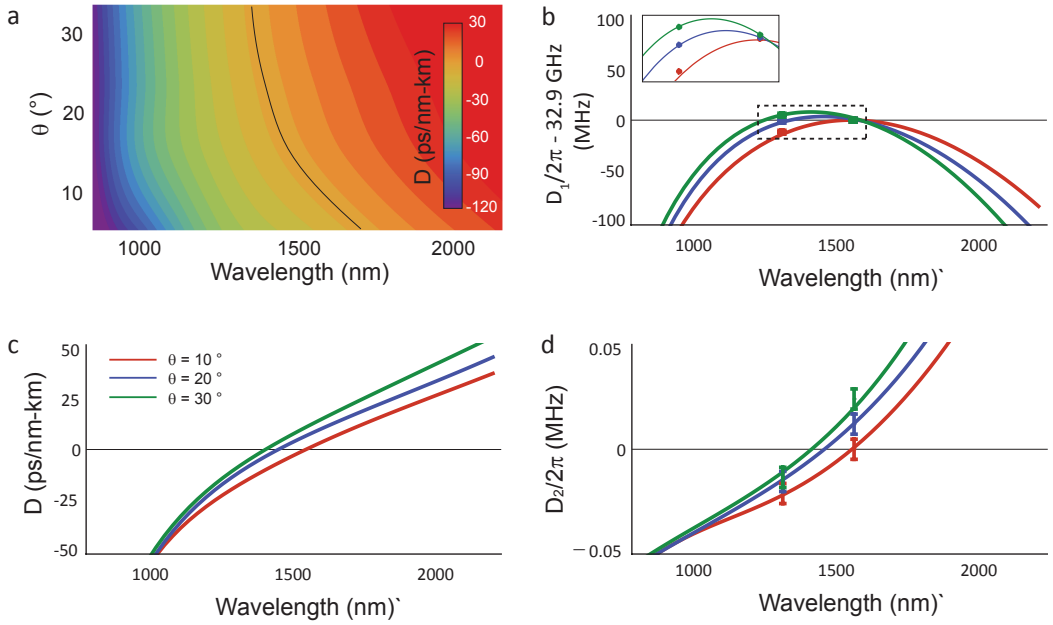

Figure 3.9: **Dispersion control in single wedge resonator** (**a**) Numerical calculation of single wedge disk as a function of wedge angle θ. Here, the diameter of resonator is 2 mm (corresponds to 33 GHz) and the black solid curve indicates the wavelength where dispersion is zero (zero dispersion wavelength). (**b**) Measured (colored makers) FSR of 2-mm-diameter single-wedge resonator. The finite-element-simulation results are solid line, and the inset shows the zoom-in around 1300 and 1550 nm spectral range. (**c**) Dispersion parameter converted from numerical simulations. It shows close agreement with Fig.3.8. (**d**) Measured D_2 of single-wedge disks. In order to measure deviation of FSR ($D_2 \sim$ 1 - 20 kHz per FSR), FSR was measured over 120 FSR modes in order to accumulate the changes over measurement error (usually 100 kHz level).

Fig.3.9a shows finite-element-simulation of single wedge disks as a function of wedge angle (θ). The diameter of disk is 2 mm, and the oxide thickness is 8 μm. As wedge angle decreases, the geometric dispersion (normal dispersion contribution) becomes stronger and as a result the zero dispersion wavelength shifts from $\sim$ 1300 nm (close to material dispersion[23]) to $\sim$ 1500 nm.

Single-wedge dispersion is measured using sideband spectroscopy[98] in order to confirm the dispersion model and numerical prediction. The FSR of fundamental mode is measured over 100×FSR-wide-spectral range, and Q-factors of the modes are between 150 and 250 million (varies because of different wedge angle as shown in Fig.2.11). Usually the deviation of FSR ($\Delta FSR = FSR_m - FSR_{m-1}$) is in the order of 1 - 20 kHz/ FSR, so it is necessary to measure over multiple FSRs in order that accumulated $m \times \Delta FSR > \delta FSR$ (δFSR is the uncertainty of FSR which is defined in subsection3.3.2). For example, the blue dot with error bar at 1550 nm shows a dispersion of 12.2 kHz/ FSR in Fig.3.9d, and this is in

good agreement with finite element simulation (12.8 kHz/ FSR) of the fabricated resonator structure and the rms error of the FSR measurement is 180 kHz. This δFSR is also in the consistent level of the one in subsection3.3.2.

Fig.3.9b shows measured FSR from different wedge angle disks at two distinct wavelengths (1300 nm and 1550 nm). Colored dots represent experimental measurement with error bars, and the solid lines are from the numerical simulation results. Considering measurement variation ($\sim$ 100 kHz for FSR measurement) with respect to FSR variation over wavelength, measurements at widely separated wavelength can give larger FSR changes and the confidence of the measurement results becomes higher. FSR measurements at separated wavelength points are conducted at this work for the first time. Each experimental points represent average FSR over 100×FSR-wide-spectral span at each wavelengths, and it shows a close agreement with the numerical prediction.

Fig.3.9c shows GVD dispersion parameters (eqn.3.2&3.8) as a function of wavelength, and the solid lines are converted from the calculated FSR in Fig.3.9b. Here, the material dispersion of silica (D_M) is common on wedge disks with different wedge angle, and the total dispersion curves show (normal) geometric dispersion contribution as a function of wedge angle. Fig.3.9d shows D_2 (related to GVD) from wedge disks, and the values can be fitted from FSR measurements over 100×FSR-wide-spectral span at both 1300 and 1550 nm wavelength.

Wedge angle	Wavelength (nm)	ΔFSR (kHz/FSR)	D (ps/nm/km)
10°	1300	-21.98	-18.5
	1550	1.20	0.67
20°	1300	-16.08	-13.4
	1550	12.2	6.75
30°	1300	-12.68	-10.5
	1550	25.01	13.8

Table 3.2: **Single wedge disk dispersion** The mode spectra were measured from single wedge disks ($\theta = 10°, 20°, 30°$, FSR $\approx$ 33 GHz), and fitted dispersion parameters from the measured mode spectra.

3.4.2 Mode spectrum engineering

The anomalous GVD is requirement for the ignition of parametric oscillation and frequency comb[6, 20], furthermore soliton formation has an additional requirement on the mode spectrum[21] – the soliton forming mode family must have anomalous dispersion near the pump frequency and be relatively free of avoided mode interaction from other mode families. Microresonator typically supports multiple mode families (cf. Fig.3.10), and the coupling between mode families additionally modifies the mode frequencies[112]. The avoided mode crossings alter the dispersion properties locally. The modified dispersion properties produce perturbation on the soliton forming process, and prevent the soliton generation if the crossing is close to the pump mode. Therefore, soliton formation additionally needs the mode spectrum without strong dispersion perturbation around the soliton spectrum[21].

3.4.2.1 Mode spectrum of microresonators

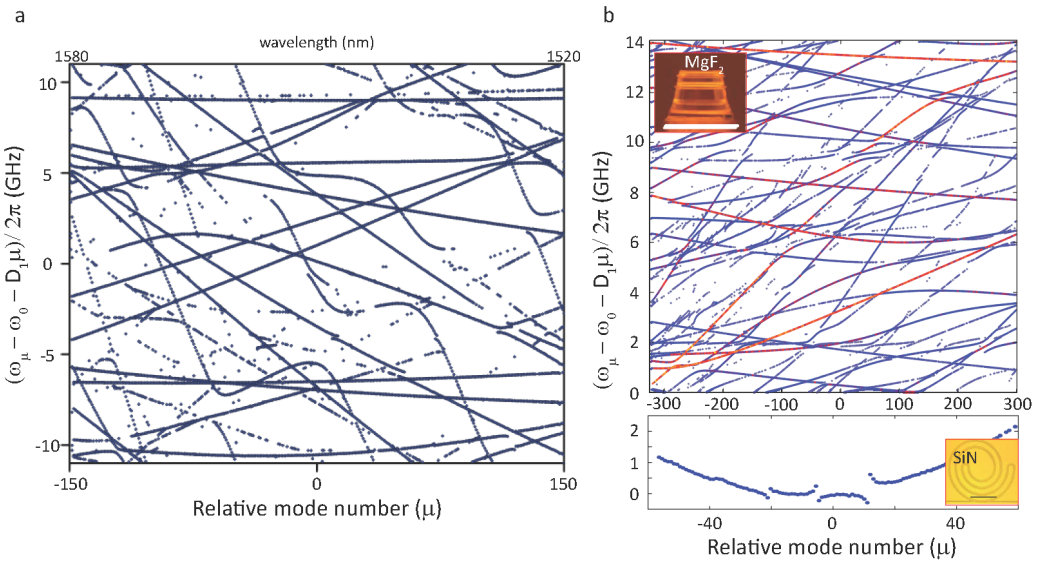

Figure 3.10: **Mode spectra of SiO_2, MgF_2 and SiN resonators** (**a**) Mode structure of silica wedge disk with an approximate FSR of 22 GHz. Dots represent resonance dips of transverse modes those are coupled with tapered fiber, and the group of dots forming continuous line represent particular mode family. (**b**) Mode structure of MgF_2 crystalline resonator with an approximate FSR of 14.09 GHz and linewidths in the range of 50 - 500 kHz. (**c**) Specific mode structure (TM fundamental mode) of SiN resonator with an approximate FSR of 76 GHz and linewidths in the range of 350 MHz. Panel **b-c** are edited from Herr, et al.[21]

Fig.3.10 shows mode spectra of silica, MgF_2, and SiN resonators. The mode frequencies are measured using a calibrated MZI (panel a), reference comb (panel b), and scanning diode laser (cf.section 3.3.1). The mode frequencies are offset by absolute frequencies (ω_0) and

the first order term ($\tilde{D}_1\mu$) in Taylor expansion (cf. eqn.3.7 and eqn.3.14).

$$\begin{aligned}\omega_\mu - \omega_0 - \tilde{D}_1\mu &= \omega_0' + D_1\mu + \frac{D_2}{2}\mu^2 - \omega_0 - \tilde{D}_1\mu \\ &= \omega_0' - \omega_0 + (D_1 - \tilde{D}_1)\mu + \frac{D_2}{2}\mu^2\end{aligned} \tag{3.14}$$

Here the spacing of frequency grid ($\tilde{D}_1$) is arbitrarily determined (close to the approximate average FSR), and dots forming a continuous line represent specific mode family. Different FSR shows distinct slopes of the continuous lines and curvature of the curves represents GVD dispersion including higher order dispersion. In addition, modified dispersion due to avoided mode crossings are presented in both **a** and **b**.

WGM resonators typically support multiple mode families as shown in Fig.3.10. Specifically silica and MgF_2 supports over 20 distinct transverse modes within one FSR and the mode structure is complicated. The mode spectrum of SiN resonator only shows the one of TM fundamental mode, but the mode interactions are apparently shown within measurement bandwidth several times. In order to achieve soliton generation from the one of transverse modes in WGM resonator, it is required to find the modes that feature anomalous dispersion and also that have minimal distortion of the dispersion caused by other mode families from the mode spectrum. The mode spectrum shows both mode family dispersion and avoided-mode-crossing behavior, so this method can be useful to screen the soliton-forming mode families.

Previous sections explained dispersion control in single-wedge disk (zero dispersion wavelength shift, dispersion control in pump wavelength), and the following sections will discuss the methods to adjust avoided-mode-crossing behavior – (i) intermodal FSR difference control and (ii) intermodal resonance frequency seperation control.

3.4.2.2 Intermodal FSR (D_1) difference control

In WGM resonator, multiple mode families have distinct FSR as a result of modal dispersion[98]. As seen in Fig.3.10, the slopes of continuous mode frequency lines represent relative FSR with respect to the frequency grid spacing ($\tilde{D}_1$) and multiple mode lines have different slopes as long as they have distinct modal dispersion. It is practically impossible to make every transverse mode in WGM resonator have the same FSR (if then, the mode lines are all parallel in the mode spectrum), and have no mode line crossing. Otherwise, each mode lines should have crossing points with other mode lines and the crossing points induce the mode interactions which perturb the dispersion properties. In this section, we will discuss the method to control the number of mode interactions that occur around 1550 nm band and also show that the mode crossing happens more often as resonator diameter increases (FSR rate decreases).

Rate of mode crossing occurrence It is interesting to note that the rate of mode crossing occurrence depends on FSR differences between distinct mode families. First we can consider

mode crossing occurrence between only two distinct mode families (mode$_{A,B}$ with FSR$_{A,B}$ in this discussion). Here, we assume that FSR$_A$ >FSR$_B$ and chromatic dispersion, which deviates FSR value with respect to wavelength, is negligible compared to FSR difference between two mode families.

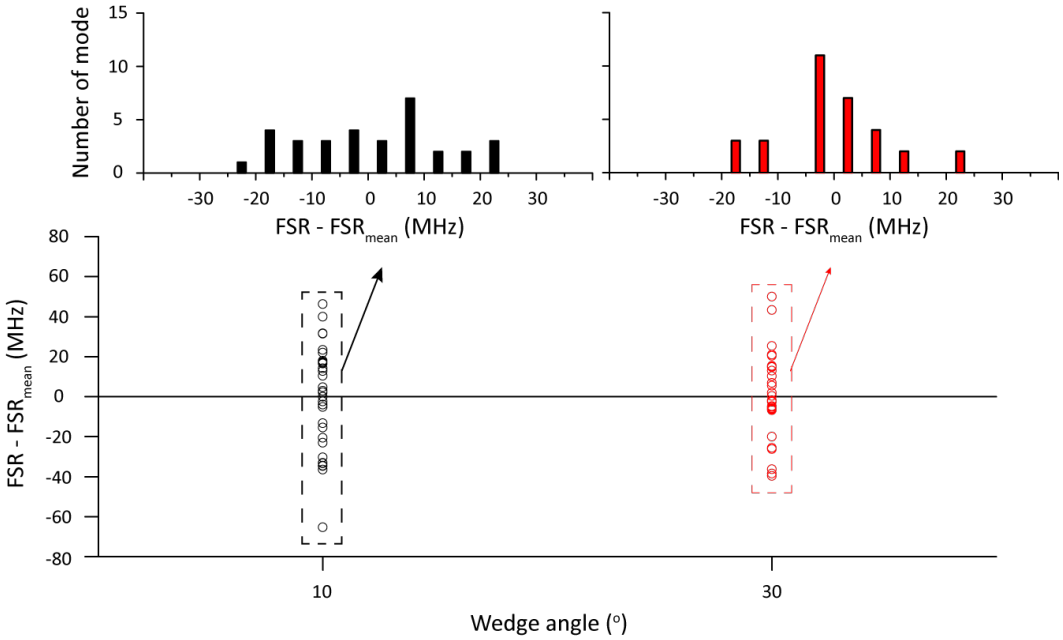

Figure 3.11: **Relative FSR distributions in 10° and 30° wedge** Top panels (left: 10°, right: 30°) show the distribution of FSR measured at 1550 nm wavelength (polarization: TE). FSRs were measured from different mode families. The horizontal axis depicts relative FSR with respect to FSR_{mean} (average of the distribution), and the vertical axis shows the number of mode families. Bottom panel shows measured FSR distribution as a function of wedge angle.

If two mode lines are crossing at mode number μ_0, then the separation between two mode families is given as $\Delta_{A-B}(\mu) = (FSR_A - FSR_B) \times (\mu - \mu_0)$ at any mode number μ. Two mode lines will be crossing at certain μ if $|\Delta_{A-B}(\mu) - FSR_B| < \Delta f$ (Δf is linewidth of modes)[5], and approximately two distinct modes are crossing every $\frac{FSR_B}{FSR_A - FSR_B}$ modes. When the FSR difference ($FSR_A - FSR_B$) is small, the mode crossing occurs less often. This might not be a method to completely remove mode crossings but can be the realistic method to avoid the mode interaction at specific spectral domain as required for soliton frequency comb operation.

Let's discuss how to reduce the FSR difference ($FSR_A - FSR_B$). Mode families have their own spatial mode distribution within a cavity structure, and the deviation of the modal distribution causes different amount of geometric dispersion contribution. If the cavity geometry contributes stronger on total dispersion, the total dispersions of mode families

[5]This only consider the case of weak mode interaction.

depend more on the spatial mode distribution, and the FSR distribution have larger variation – otherwise, the FSR distribution converges as geometric dispersion decrease. Fig.3.11 shows the measured FSR of several mode families in single-wedge disk (diameter = 3 mm; oxide thickness = 8 μm). The FSR was measured at 1550 nm, and tapered fiber was used to monitor the mode spectrum and measured the FSR. It is also important to note that various taper thicknesses were used to measure the FSR in order to measure mode families as much as possible. As wedge angle (θ) increases, the FSR difference decreases as shown in the distribution plot (then possibly the occurrence of mode crossing may drop). In higher wedge angle structure, the cavity geometry contributes less on the total dispersion and the total dispersion almost follows the material dispersion (the material dispersion is same to every mode family). This is the reason that the FSR difference is smaller in higher wedge angle, and generally the FSR difference increases as geometric dispersion increases[6].

Diameter dependent occurrence rate The mode crossing tends to be more often in lower FSR (larger diameter) than in higher FSR (smaller diameter)[113], and this should be outstanding challenge for cavity platforms to achieve detectable (lower) repetition rate soliton frequency comb. Here we would like to systematically understand the mode crossing occurrence as a function of cavity diameter. For simplicity's sake, let's consider constant group index and dispersion (indeed it is reasonable assumption as the dispersion is not strongly dependent on the diameter), then FSR is simply scaled by resonator diameter and the FSR difference is also following the same scale rule. Then the ratio between FSR and FSR difference can be approximately constant regardless resonator diameter ($\frac{FSR_A - FSR_B}{FSR_B} \sim constant$), and it consequently provide constant occurrence rate in mode number (μ) domain. It is interesting to note that mode spacing is inversely proportion to resonator diameter so the rate of crossing occurrence becomes proportional to resonator diameter (inverse proportional to FSR) in spectral domain.

Fig.3.12 shows the avoided mode crossings in SiN resonator ($\sim$ 725 nm $\times$ 1700 nm cross section) with different resonator diameter (200, 570 μm). According to Ref.[113], there are two types of mode crossing occurred on this resonators – (TYPE I) mode crossing between differently polarized fundamental modes, and (TYPE II) mode crossing with higher order modes (same polarization). 220-GHz-FSR SiN resonator has one TYPE I and one TYPE II mode crossings while 80-GHz-FSR SiN resonator has three TYPE I and eight TYPE II mode crossings (measurement wavelength: 1500 - 1560 nm). Because TYPE II mode crossing counts the mode interaction with several mode families which are not clearly defined in this reference, it might be more precise to compare the rate of TYPE I mode crossing occurrence (between fundamental modes with TM and TE polarizations). TYPE I mode crossing occurs once in 220-GHz-FSR and three times in 80 GHz-FSR – this increase

[6] Wedge angle around 30 to 50° is high enough to reduce the FSR variations. It was experimentally turned out that wedge angle higher than 30 - 50° (i.e. 70°) doesn't help more but mode interaction becomes little stronger once the mode lines are crossing as the mode overlap increases.

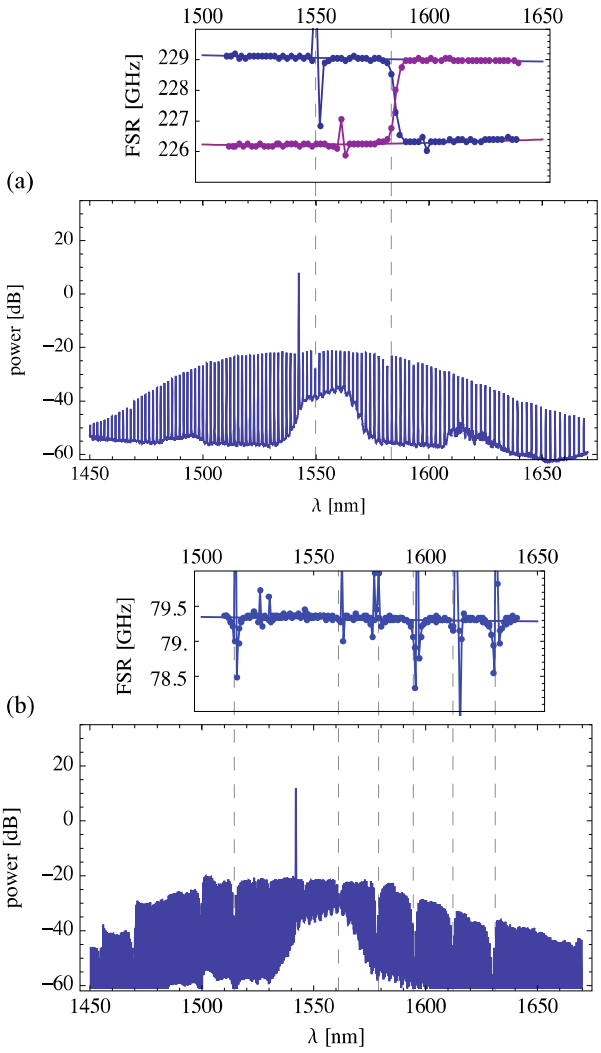

Figure 3.12: **Avoided mode crossing and generated frequency comb spectra in SiN resonator with distinct FSR** (**a**) Measured FSR (top) and comb spectrum (bottom) in 220 GHz FSR SiN resonator (725 nm × 1650 nm cross section, 200 μm diameter, effective index = 1.8). Dashed lines indicate the avoided mode crossing wavelengths. (**b**) same as **a** but in 80 GHz FSR SiN resonator (725 nm × 1700 nm cross section, 570 μm diameter, effective index = 1.8). Panel **a-b** are edited from Ramelow, et al.[113]

(×3) approximately corresponds to FSR decrease (×1/3). Therefore, the occurrence rate of avoided mode crossing can be higher in smaller mode spacing (FSR, corresponds to repetition rate of comb) and it is outstanding challenge with electronic-rates (< 20 GHz) soliton frequency comb generation.

Solutions in SiN microresonators

The mode confinement is relative strong in nitride waveguide (considering the thickness of resonator), so effective indices of distinct mode families have relative difference over

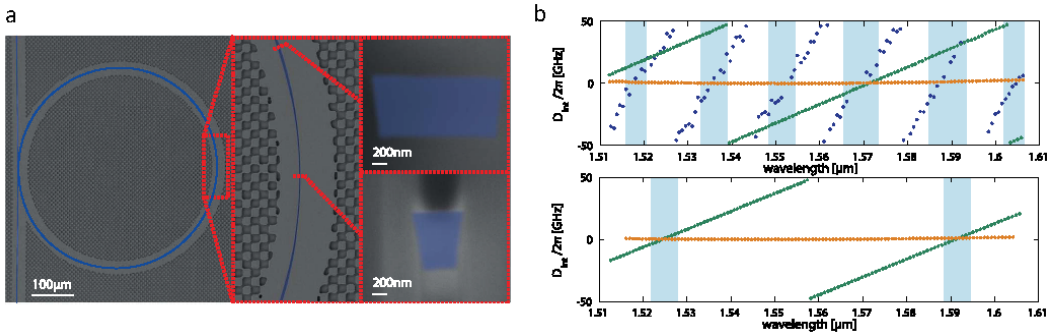

Figure 3.13: **Higher transverse mode suppression in nitride microresonator** (**a**) SEM image of higher mode suppressed nitride microresonator. Mode filtering section is shown in lower right panel (dimension: 0.8 × 0.6 μm), and the ring resonator cross section is shown in upper right panel (dimension: 0.8 × 1.65 μm) (**b**) Characterization of a resonator with constant waveguide width (upper panel) and the one including the mode filtering section (lower panel). Panel **a-b** are edited from Kordts, et al.[114]

10 % even with wider waveguide width (> 2 μm)(see Fig.2 of Ref[114]). As a result, it is very challenging to avoid the mode crossing unless the resonator supports only single mode family. The upper panel of Fig.3.13b is a good example. FSR is approximately 100 GHz and three distinct mode families exist in the resonator at 1550 nm. Because the FSR difference is still quite large, the occurrence rate of the mode crossing is high so the avoided mode crossings might occur with 20 nm interval. It is expected that the rate of mode crossing becomes even higher (few nanometer wavelength interval) if FSR is reduced (e.g. 20 GHz).

On the other hand, the nitride resonator in Fig.3.13a features mode filtering section with an adiabatic tapered section through the rim (tapering length: 130 μm). The dimension of the mode filtering section is 0.8 × 0.6 μm, so as to filter out the higher mode that formed the serious mode crossing with the TE0 mode. The lower panel shows the measured mode spectrum of the nitride resonator featuring mode filtering section, and the spectrum shows very clean mode profile with anomalous dispersion around pump wavelength.

Solutions in Silica wedge disk Compared to nitride waveguide, silica resonators confine the optical mode weakly (dimension: 8 μm thickness). The FSR difference is thereby quite small, and the difference is in a level of 1:1000 with respect to resonator FSR. As nitride resonator features the mode filtering section[114], the geometric structure of silica resonator can be engineered to reduce the total mode number but might cause scattering loss. Instead, the mode spectrum can be engineered by adjusting resonator diameter in a level of few microns. The technique to engineer the mode spectrum will be discussed in the next section and soliton generation will be demonstrated from the mode-spectrum-engineered resonator.

3.4.2.3 Intermodal resonance frequency (ω) separation control

Engineered FSR difference can reduce the rate of mode crossing occurrence, however in practice it is almost impossible not to have any mode crossing over 50 - 100 nm wavelength span with 10 - 20 GHz level repetition rate – this condition requests that FSR of all transverse modes should be within ~ 10 - 80 MHz. Even if the requirement is fulfilled, the mode crossing point might be within measurement bandwidth accidentally. This section will discuss the method that can shift the mode crossing point by changing resonator diameter. The resonance frequencies of the microresonator are determined as eqn.3.4. In this equation,

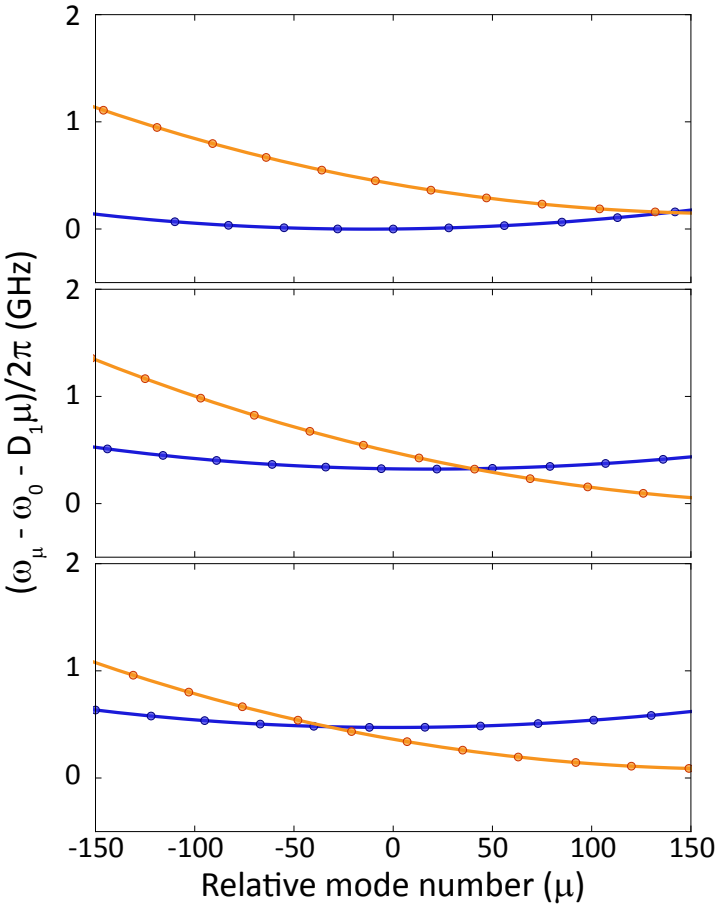

Figure 3.14: **Simulated mode spectrum of distinct mode families and the relative mode location control** Two distinct mode frequencies are calculated around 1550 nm wavelength in silica wedge disk (wedge angle = 30°, oxide thickness = 8 μm). The diameter of microresonator was adjusted in the finite-element-simulations from the top to the bottom panels (top: 3000 μm, center: 2998 μm, bottom: 2996 μm). Numerical simulation was conducted with 25 mode number grids (dots) and solid lines are interpolation curve using the numerical simulation.

the effective index and the effective radius of optical mode change the resonance frequencies with respect to mode number (μ). When the resonator diameter changes in this equation,

distinct mode families have different resonance frequency shift caused by discrete effective index of optical modes (see eqn.3.15).

$$\frac{df_{\mu}}{dR} = -\frac{\mu \cdot c}{(2\pi \cdot R \cdot n_{eff})^2} \times (2\pi \cdot n_{eff} + 2\pi \cdot R\frac{dn_{eff}}{dR}) \tag{3.15}$$

Here, dn_{eff}/dR is negligible (approximately less than 0.05% per micron) and the mode radius deviation directly follow the fabricated resonator radius adjustment (in microns-level-radius control)[7]. In addition, it is interesting to note that relative mode frequencies shift more significantly as two distinct mode families have larger effective index difference. Therefore, the mode crossing between fundamental mode and higher order mode might be adjusted with just few microns diameter adjustment while the one between similar index mode might not. Fig.3.14 shows the simulated mode frequencies of two distinct modes in Silica wedge disk with different resonator diameter (adjusted from 3000 (top) to 2996 μm (bottom)). Here, the wedge angle is 30° and the oxide thickness is 8 μm. As a result of diameter adjustment, the mode crossing point between two distinct modes shifts approximately 200 mode number from short wavelength to longer wavelength.

Fig.3.15 shows the measured mode frequencies of TE0 and TE2 modes in silica wedge disk (wedge angle = 30°, oxide thickness = 8 μm). Here, the diameter of disk resonator was controlled in order to shift the mode crossing wavelength and the resonator diameter changes by $\sim$ 2 μm from the top to the bottom panel. As discussed and confirmed numerically, the mode crossing wavelength between TE0 and TE2 modes is experimentally confirmed to shift as resonator diameter changes. It is worth to note that the structural parameters (e.g. wedge angle, wedge thickness) are identical over the disks from the top to the bottom except the diameter. In order to reduce the uncertainty of fabricated structural parameters, the disks are fabricated from the same wafer (oxide thickness) with the identical photo-lithography conditions (photoresist thickness, exposure time, develop condition). The diameter was adjusted using the wet etch duration (etch speed is approximately 100 nm/ min).

In addition, it is important to note that the relative mode shift becomes larger with respect to the same amount of diameter adjustment as FSR difference increases. Therefore, the shift amount between TE0 and TE2 in Fig.3.15 (diameter change: $\sim$ 2 μm) is larger than the predicted amount between TE0 and TE1 in Fig.3.14 (diameter change: $\sim$ 4 μm).

3.4.3 Electronics-rate soliton source in mode-spectrum-engineered resonator

3.4.3.1 Mode engineering for soliton frequency comb generation

As discussed in Ref.[21], the mode families that form the soliton frequency comb needs to feature anomalous dispersion and minimal distortion from the anomalous dispersion. In

[7] 10 - 50 nm level deviation occurs over few microns radius adjustment (few percent), but it is below minimum mesh unit.

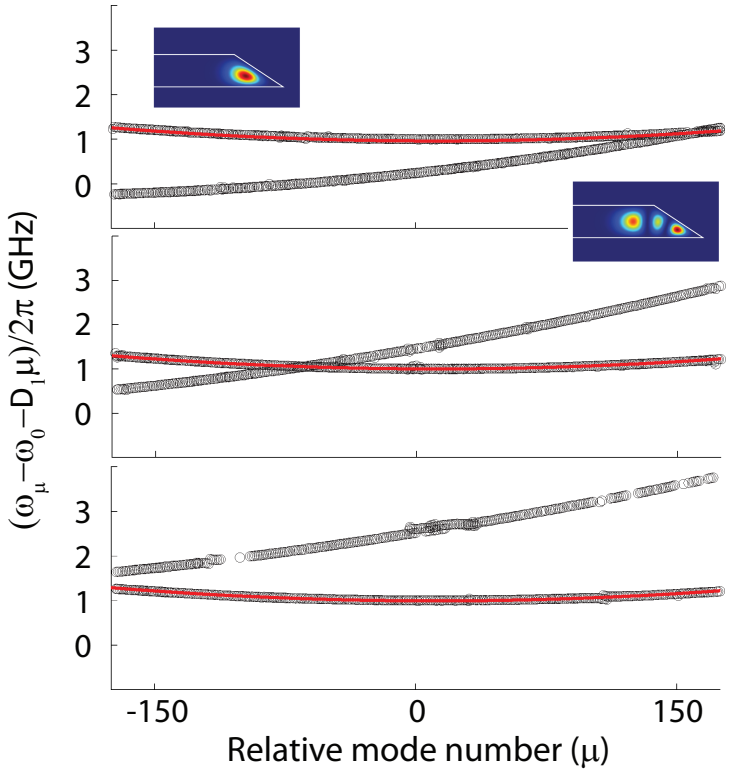

Figure 3.15: **Mode structure of TE0 and TE2 modes in silica wedge disk** In silica wedge disk (wedge angle = 30°, oxide thicknes = 8 μm, diameter ~ 3 mm), the mode frequencies of TE0 and TE2 modes (calculated mode profiles are shown as inset) are measured in 1520 - 1580 nm. From the top panel to the bottom, the resonator diameter changes by ~ 2 μm and consequently the mode crossing position shifted from shorter wavelength (μ > 150; top panel) to longer wavelength (μ < -150; bottom panel).

single-wedge resonator, group velocity dispersion around 1550 nm wavelength is generally anomalous in wedge angles from 10° to 30° as shown in Table.3.2. Furthermore, FSR difference in distinct mode families decreases as wedge angle increases so as to reduce the occurrence rate of mode crossing. Therefore, we decided to use 30° wedge angle with 22 GHz repetition rate for this experiment. Q factor tends to increase as wedge angle is higher– the optical mode experiences etched surface less (see Fig.2.11 and 2.12). In addition, the set of different wet etch time have been applied to wedge disk fabrication in order to shift mode crossing (radius interval ~ 1 μm).

3.4.3.2 Required operating power as a function of Q-factor and repetition rate

As discussed in Chapter 1, the threshold power for parametric oscillation can be obtained from coupled mode equation[20, 49]:

$$P_{th} = \frac{\pi n \omega_0 A_{eff}}{4\eta n_2} \frac{1}{FSR \cdot Q^2} \tag{3.16}$$

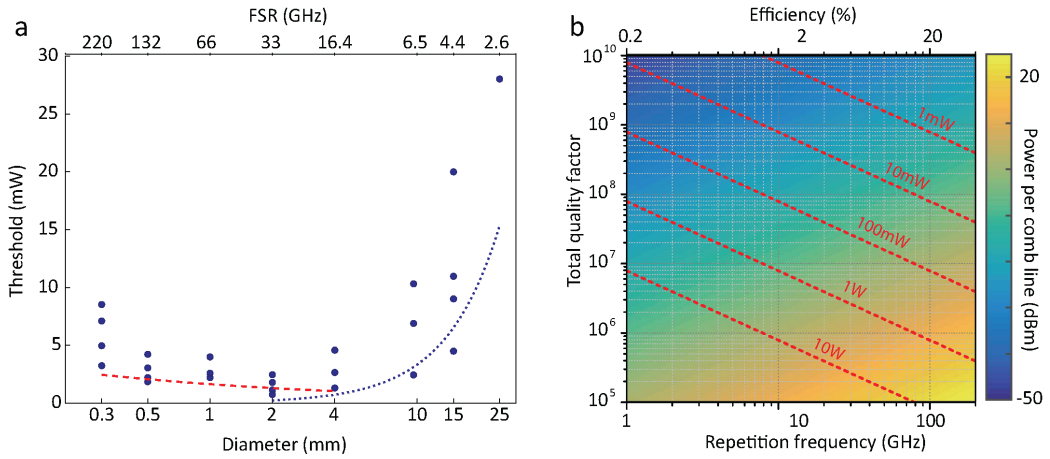

Figure 3.16: **Parametric oscillation threshold power and soliton operating power** (**a**) Parametric oscillation threshold versus resonator diameter (D). The trend curves of threshold are shown (red: $D^{-1/3}$, blue: $D^{5/3}$). This figure is from Li et al.[50]. (**b**) Soliton operating power and maximum power per comb line. Red lines represent the minimum pump power for 200 fs soliton existence in silica resonator. $\eta = Q/Q_{ext}$ is assumed to be 0.7 in making the plot. This figure is from Yi et al.[55].

where A_{eff} is mode area, n is refractive index of microresonator, n_2 is the Kerr coefficient, ω_0 is the pump frequency, and $\eta = Q/Q_{ext}$ is the waveguide to resonator loading (Q_{ext} is coupling Q-factor, and Q is total Q-factor). Fig.3.16a shows measured parametric threshold power versus diameter from silica wedge resonators. P_{th} is inverse proportional to FSR, so the threshold power increases as repetition rate decreases (Diameter increases). However, silica wedge resonators have diameter dependent Q value as discussed in section 3.4.1, and the threshold power is proportional to the inverse of Q^2. If the resonator diameter is less than 4 mm, the optical mode experiences sidewall and bottom surface roughness and the Q factor increases in larger diameter because mode shifts inwards (and experience the sidewall roughness less). However, with resonator diameter larger than 4 mm, the optical mode experiences the top and bottom surface roughness instead of the sidewall roughness. Q factor is saturated, so threshold becomes larger as FSR increases. It is also interesting to note that the mode area scales like $D^{2/3}$, so the trend curves on the Fig.3.16a follow $D^{-1/3}$ and $D^{5/3}$ accordingly[50]. Table.3.3 illustrates the comparison of chip-based microcomb sources including non-soliton platforms.

The soliton power (P_{sol}) and pulse width (τ) are given by[47, 53, 54]:

$$\begin{aligned} P_{sol} &= \frac{2\eta A_{eff}}{n_2 Q}\sqrt{-2nc\beta_2\delta\omega} \\ \tau &= \sqrt{-\frac{c\beta_2}{2n\delta\omega}} \end{aligned} \tag{3.17}$$

where $\beta_2 = -nD_2/cFSR^2$ is GVD as defined earlier, and $\delta\omega$ is the amount of detuning. When

Materials	n_2 $(10^{-20}m^2/W)$	A_{eff} (μm^2)	FSR (GHz)	Q $(\times 10^6)$	$P_{th}(mW)$
$Hydex$	12	1.45×1.50	200	1	50
AlN	23	0.65×3.50	435	0.8	200
$Diamond$	8.2	0.95×0.85	925	1	20
$AlGaAs$	2600	0.32×0.62	995	0.1	3
Si_3N_4	25	0.60×3.00	25	17	2.7
SiO_2	2.2	~ 40	33	270	2

Table 3.3: **Comparison of chip-based microcomb sources (including non-soliton platforms)** Hydex[115], AlN[116], Diamond[12], AlGaAs[117], Si_3N_4[91], SiO_2[50].

we fix the pulse width (τ_0) of soliton, the amount of detuning is determined correspondingly as $\delta\omega = c(-\beta_2)/2n\tau_0^2$ and the input power determines the maximum detuning range for soliton existence as $\delta\omega/2\pi\kappa \leq \pi^2 P_{in}/16P_{th}$ (κ is the resonance linewidth)[47, 53, 54]. In order to form soliton with pulse width τ_0, the minimum operating power is given as:

$$\begin{aligned} -16c\beta_2 P_{th}/4n\tau_0^2\pi^3\kappa &\leq P_{in} \\ P_{in}^{min} = -\frac{2c\beta_2}{\pi\eta} \cdot \frac{A_{eff}}{n_2 \cdot Q \cdot FSR} &\cdot \frac{1}{\tau^2} \end{aligned} \tag{3.18}$$

In the top row of eqn.3.18, the scaling factor ($-16c\beta_2/4n\tau_0^2\pi^3\kappa$) is around 5 - 20 assuming 200 fs pulse width, silica material dispersion (-28ps^2/km), and Q factor of 100 - 300 M – it means that operating power is about 5 - 20 times of parametric threshold power. Fig.3.16b shows soliton operating power versus repetition rate and Q factor of optical mode, and the minimum pump power is required for 200 fs soliton existence in silica resonator[22] which is used for microcomb[50] and soliton[118] generations.

3.4.3.3 Characterization of soliton frequency comb

Fig.3.17a shows measured mode spectrum of soliton-forming mode families from 1520 nm to 1580 nm. The solid lines are finite-element-simulation results, and the numerical calculations used the SEM scan of the wedge resonator. The fitted dispersion curve shows $D_1/2\pi$ = 21.92 GHz, and $D_2/2\pi$ = 17 kHz. Numerical simulation confirmed that the mode is TE1 mode, and also identified the nonsoliton-forming mode families perturbing the parabolic shape (but not seriously). The measured Q factor of the mode was around 300 million, and typical measured threshold power were around 2.5 mW.

Single soliton was triggered and locked[118] from the mode spectrum engineered resonator, and the measured optical spectrum is shown in Fig.3.17b. Solitons form when the pump frequency is red detuned with respect to an optical mode, and further detail on the locking process is in Ref[118]. The square of a hyperbolic secant function is overlaid onto the spectrum to verify the single soliton characteristic. The presence of small spurs corresponds to the minor mode crossing points in the mode spectrum. Direct confirmation of pulse

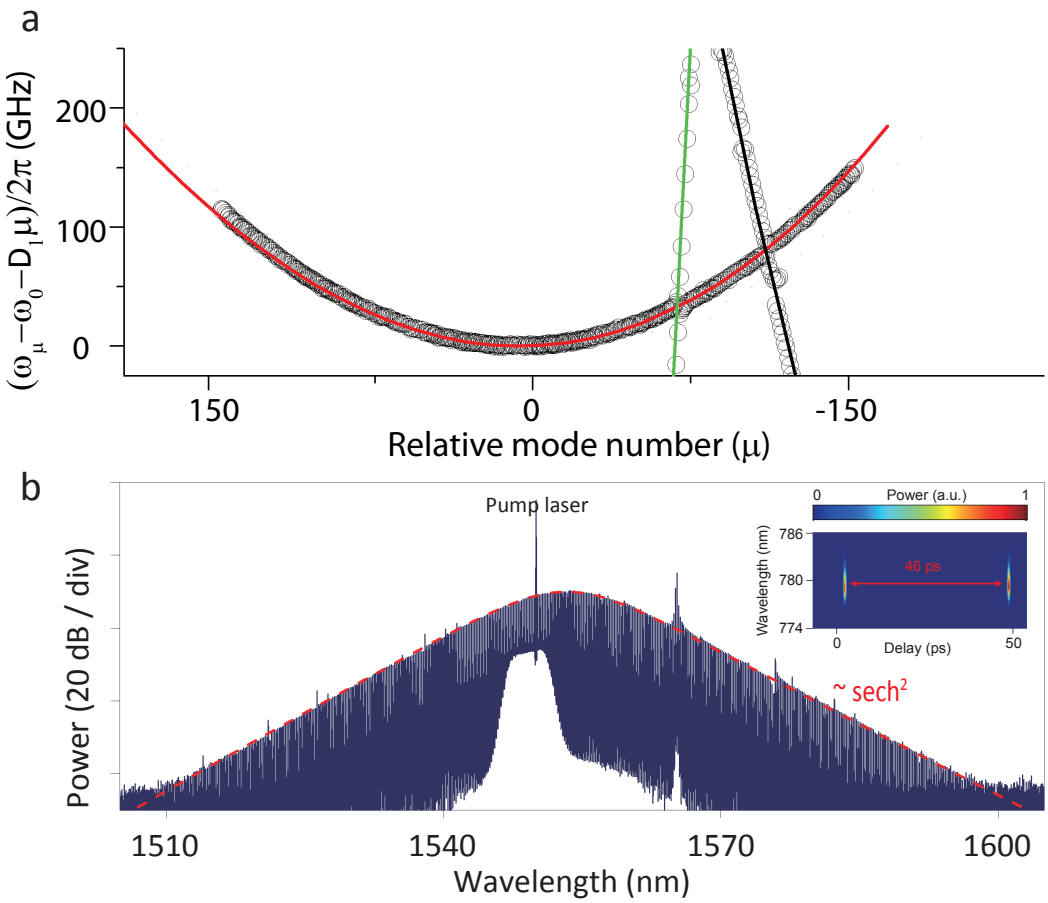

Figure 3.17: **Soliton mode family dispersion, optical spectrum, and FROG** (**a**) Measured frequency dispersion (black points) of the soliton-forming mode family (Measured modes span from 1520 nm to 1580 nm. μ_0 corresponds to a wavelength close to 1550 nm). Red curve is a fit using $D_1/2\pi = 21.92$ GHz and $D_2/2\pi = 17$ kHz. The nonsoliton-forming mode families are also shown and the avoided mode crossings perturb the parabolic shape. (**b**) The optical spectrum of a single soliton state with a $sech^2$ envelope (red dashed line). Inset: FROG of the soliton state. The optical pulse period is 46 ps and the fitted pulse width is 250 fs. **a-b** are edited from Yi, et al.[55].

generation is provided by frequency-resolved optical gating (FROG)[47]. The pump laser was suppressed by fiber Bragg-grating filter, the waveshaper (programmable optical filter) adjusted dispersion compensation, and then the output signal is amplified using optical amplifier (EDFA). The measured date shows the pulse generation in the microresonator, and the fitted pulsewidth is 250 fs, which is limited by amplifier bandwidth.

Active capture and stabilization of soliton allows to dramatically reduce the soliton operating range using detuning locking. By adjusting soliton power set-point (P_{sol}) as well as pump power (P_{in}), it was feasible to closely match cavity-pump detuning with soliton existence range. As a result, the operating power of a single soliton in wedge disk was recorded as low as 22 mW[118].

3.5 Broadband dispersion-engineered UHQ resonator

In previous section, the geometric dispersion control on single-wedge disk was introduced and the discussion was further developed towards mode spectrum engineering for soliton frequency comb generation. The chromatic dispersion and mode spectrum have been lithographically defined using cavity structural parameter (e.g. wedge angle and diameter), so the dispersion engineering has realized to shift zero dispersion wavelength and to reduce avoided-mode-crossing. However, a couple of structural parameters has limitations on the level-of-control, and cannot compensate material dispersion over broadband span. In this section, design and fabrication technique that allows dispersion control over wide bandwidth will be introduced. Broadband dispersion control can be applied for wideband frequency comb generation[8], soliton generation from visible to mid-infrared wavelength pump[119], dispersive wave generation[120, 121], and second- or third-harmonic generations[122].

3.5.1 Geometric dispersion control

Travel speed of optical wave in microcavity is determined by combined contribution from cavity material and geometry. As discussed earlier, the material dispersion has significant contribution on the dispersion properties and can easily modify broadband dispersion by combining heterogeneous materials[101]. However, it might be challenging to maintain high-Q factor during extra material process that can easily degrade the microcavity quality and the Q factor is essential for efficient nonlinear oscillation. Therefore, this section will mainly discuss geometric dispersion design that systematically tailors cavity structure with higher-level-control for broadband dispersion engineering.

3.5.1.1 Geometric dispersion control – principle

Fiber dispersion design Optical fiber designers use multiple cladding layers to control both the magnitude, sign and spectral profile of the combined material and waveguide dispersion[123, 124]. Fig.3.18a shows the dispersion of a single-clad optical fiber. The core layer is surrounded by single cladding layer which has lower refractive index. Top panel shows finite-element-simulation of fundamental mode in single-clad fiber; the index contrast and core diameter have been set to Δn = 0.0028 and 4.5 μm so as to make the variation in mode profile with wavelength more readily observable. In fiber optics, the control of Δn is primary method to adjust group index of optical mode[125], and the corresponding group index spectrum is shown in bottom panel. In addition, it is interesting to note that the fundamental mode spreads over lower-index cladding layer in longer wavelength while the shorter wavelength mode is mainly confined in core layer.

[8]The octave spanning frequency comb with detectable repetition rate is directly used for self-referenced comb[5], but also it doesn't need to be always octave span for other specific applications such as dual-comb spectroscopy[14] and comb-based telecommunications[16]

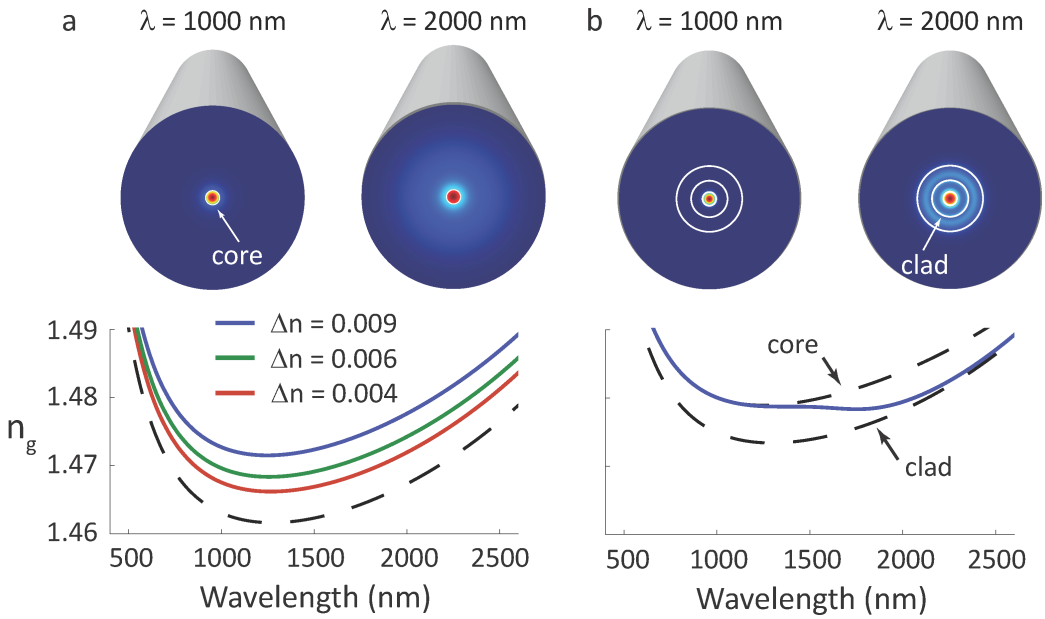

Figure 3.18: **Dispersion engineering in multi-clad fiber** (**a**) Upper panel depicts finite-element-simulation of the fundamental mode in single-clad fiber at the wavelengths 1000 and 2000 nm. Lower panel illustrates the corresponding group index spectra of HE_{11} mode. Here Δn is core-cladding refractive index difference. (**b**) Dispersion control using multi-cladding layers. Upper panel shows finite-element-simulation of HE_{11} mode in multiple cladding fiber at wavelengths 1000 and 2000 nm. Bottom panel is the group index spectra of fundamental mode in multi-cladding fiber. The dashed lines in the group index spectra give the single core and clad cases for the fiber. Fiber refractive index profile is provided as insets. Fig.**a-b** are edited from Yang, et al[71].

Fig.3.18b shows the dispersion of multiple-cladding optical fiber. The multi-clad fibre can be understood by analyzing the dispersion in short and long-wavelength cases[123]. Short wavelength modes are confined primarily by the core region and experience a group index that is similar to a corresponding single core fibre. Longer wavelength modes are primarily confined by the secondary cladding layer. The corresponding spectral dependence of the group index can be understood as a transition between these two extreme cases (see spectrum for multi-clad fibre in Fig. 1c). The wavelength at which the transition occurs can be correspondingly engineered[126, 127]. For example, by placing the outer, higher index region closer to the inner core, the transition will occur at shorter wavelengths.

Cavity dispersion design Fig.3.19a shows the group index control method using cavity geometry (left) as discussed in section 3.4.1.2. The group index spectra of three resonators that differ only in wedge angles are shown in the panel, and the index of bulk silica is also provided for comparison[23, 128]. The wedge angle introduces normal dispersion offset (material dispersion: anomalous dispersion in 1550 nm) that is stronger for smaller wedge angles[98], and raises the group index from the material index as wedge angle decreases.

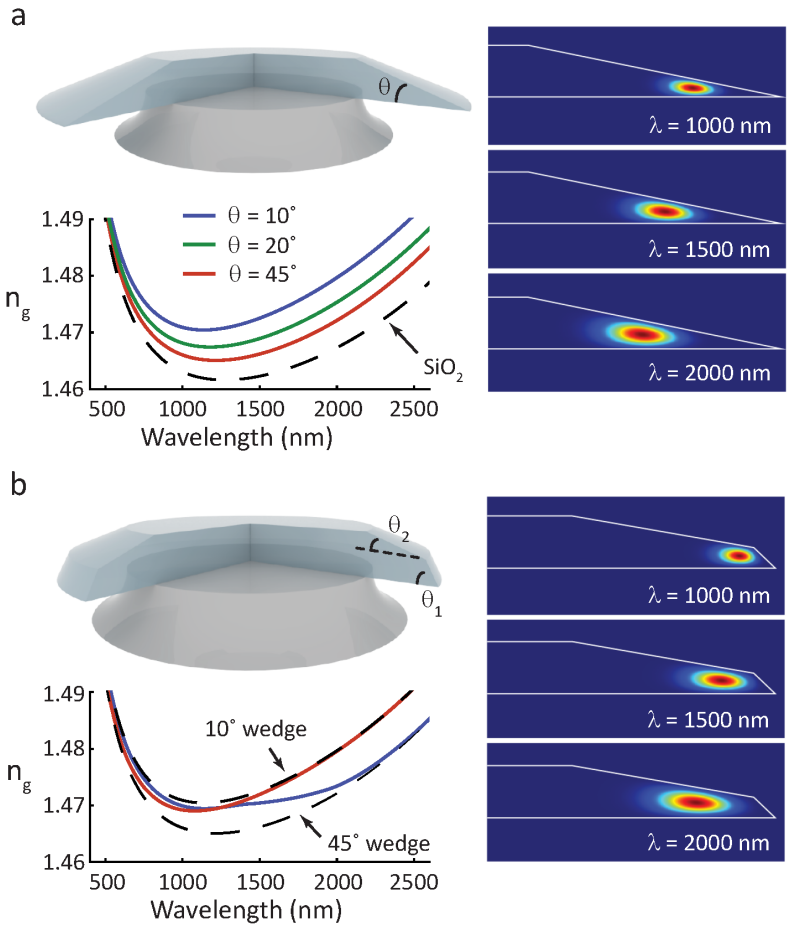

Figure 3.19: **Fiber-inspired cavity dispersion design** (**a**) Upper panels depict single-wedge resonator schematic; and lower panel give the corresponding group-index spectrum of the fundamental modes in the single-wedge disk (left panel). Here, θ is the wedge angle of the resonator, and the dashed curves give the bulk group index of silica. Calculations assume a resonator diameter of 3 mm. Finite element simulation of the fundamental mode in a single-wedge disk at the wavelengths 1000, 1500, and 2000 nm (right panel). (**b**) As in (*a*), but for double-wedge disk. The dashed lines in group index spectrum give the single-wedge results (10° and 45° cases). The blue and red curves in the lower left panel indicate the multi-wedge resonator where the angle ordering is red (45° (outer) → 10° (inner)) and blue (10° (outer) → 45° (inner)). Fig.**a-b** are edited from Yang et al.[71].

For comparison, single-clad fiber adjusts the group index of the mode through control of Δn and usually Δn modifies the group index in a level of $\sim$ 1%[125]. It is interesting to note that the magnitude of geometric dispersion in single-wedge disk is almost comparable with the level in fiber optics.

The right panel in Fig.3.19a shows the finite-element-simulations of the fundamental mode in single-wedge disks, and the wedge angle is 10° with 3-mm-diameter. In the resonator, longer wavelength mode has smaller radii while shorter wavelength mode see their centroid

of motion around the resonator outwards. The effective optical path becomes smaller as wavelength increases, and it corresponds to normal dispersion[22, 98]. This is analogous with that longer wavelength modes have greater spatial overlap with the lower-index cladding, and the greater overlap strengthens normal dispersion contribution in fiber optics.

The similarity between the resonator and fiber cases suggests a method to engineer dispersion in the resonator that is illustrated in the Fig.3.19. In double-wedge resonator, the shorter wavelength modes experience the outer wedge angle (θ= 10° in blue curve; 45° in red curve) while the longer wavelength modes mainly experience the inner wedge angle (θ= 45° in blue curve; 10° in red curve). The spectral dependence of the group index have a transition between these two cases. In analogy with the multi-clad fiber, the thickness of the wedge-angle transition allows control of the wavelength band over which the group index transitions between these two limits. This concept can be extended to design the group index of quadruple-wedge disk, which provides more flexibility in dispersion control over a wider range of wavelengths.

3.5.1.2 Geometric dispersion control – numerical analysis

In this section, dispersion engineering method using wedge angle transition was studied using finite-element-simulation and the numerical study will provide how to independently tailor (i) magnitude, (ii) sign, and (iii) spectral profile of geometric dispersion.

Magnitude of geometric dispersion Fig.3.20a shows the double-wedge group index spectra that transitions between the group index spectra of single-wedge disks (red = 10°, green = 20°). The group index spectra exclude material dispersion in order to confirm the geometric contribution clearly. Blue dots are calculated group index of double-wedge that has 20° outer wedge (θ_1) and 10° inner wedge (θ_2), while red dots represent the group index of double-wedge with 10° outer wedge and 20° inner wedge. The transition in group index spectra makes either normal or anomalous dispersion contribution in group velocity dispersion spectra, as shown in Fig.3.20b. The first derivative of the group index curve determines the magnitude of geometric dispersion, and the magnitude increases as the group index difference between two wedges are larger. The wedge angles (θ_1 and θ_2) thereby control the magnitude of geometric dispersion at transition wavelength.

Sign of geometric dispersion Fig.3.20b shows that transition from lower angle (higher group index) to higher angle (lower group index) creates normal dispersion (upper panel) while the inverse transition (from higher angle to lower angle) form anomalous dispersion (lower panel). Silica material dispersion is normal in wavelengths shorter than 1.3 μm, and anomalous otherwise. The tunable sign of geometric dispersion can thereby compensate for the material dispersion with more flexibility.

Spectral profile of geometric dispersion Fig.3.20b also shows that the wedge angle transition thickness (t) can control the spectral position that group index transitions and form

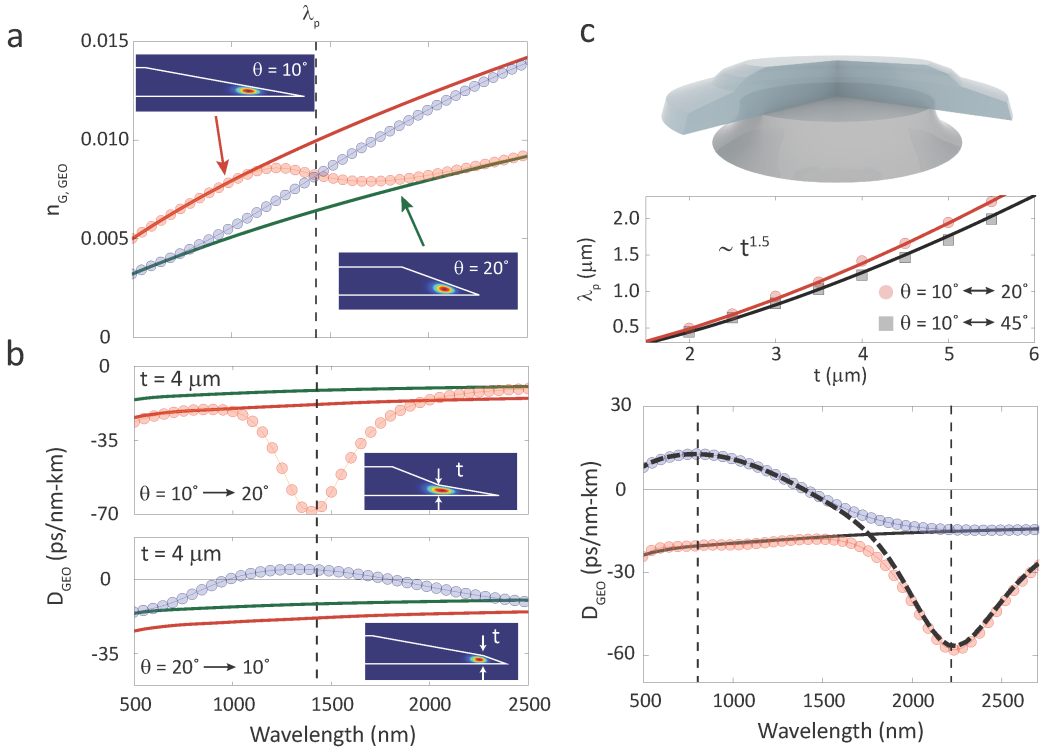

Figure 3.20: **Geometric dispersion control in multi-wedge disk** (**a**) The group-index spectra ($n_{G,GEO}$ = n_G - $n_{G,MAT}$; n_G: group index of mode; $n_{G,MAT}$: group index of material[23]) of the single-wedge (solid lines; red=10°, green=20°) and the double-wedge (dots) are shown. (**b**) Top and bottom panels depict the geometric dispersion of each lines in **a**. (**c**) Dispersion of multi-wedge (θ_1=45°, θ_2=10°, θ_3=20°; dashed line) transits from the one of double-wedge (θ_1=45°, θ_2=10°; blue dots) to another (θ_1=10°, θ_2=20°; red dots). Black solid line is the geometric dispersion of single-wedge (θ=10°). Inset shows λ_p, the wavelength where the additional dispersion of double-wedge is maximum (dots).

either normal or anomalous dispersion. At t = 4 μm, both double-wedges in upper and lower panels have common λ_p that geometric dispersion is maximized in wedge angle transition. As long as the transition thickness is determined, the geometric dispersion is formed at the same spectral location regardless the sign of the dispersion. In addition, Fig.3.21c shows that λ_p is approximately proportional to $t^{3/2}$. In addition, wedge angles can be defined without limitation on the number of transitions, and the geometric dispersion from one angle transition is simply superpose on the dispersion of the other angle transition in spectral domain without strong perturbation (almost linearly). The lower panel in Fig.3.20c shows the geometric dispersion of multi-wedge disk (θ_1 = 45°, θ_2 = 10°, θ_3 = 20°; dashed line) with geometric dispersion spectra of two double-wedge disks (blue dots:θ_1 = 45° and θ_2 = 10°, red dots: θ_1 = 10° and θ_2 = 20°). Each double-wedge disks have λ_p at 800 nm (blue dots) and 2200 nm (red dots), and geometric dispersion of multiple-wedge transits from the blue dot double-wedge spectrum to red dot double-wedge spectrum. The geometric dispersion

of multiple-wedge can compensate normal material dispersion at shorter wavelength and anomalous material dispersion at longer wavelength.

3.5.1.3 Geometric dispersion control – equation model

The dispersion of double-wedge resonator (θ_1: outer wedge angle; θ_2: inner wedge angle) can be understood by separately analyzing the θ_1-single-wedge in short- and θ_2-single-wedge in long-wavelengths. Fig.3.21a shows the optical mode profiles of double-wedge and two single-wedges. The vertex at the bottom of the double-wedge has the same coordinate as the one at the bottom of the θ_1-single-wedge, while the vertex at the top of the double-wedge has the same coordinate as the one at the top of the θ_2-single-wedge. The radius of each single-wedge is determined as a function of t:

$$R_2 - R_1 = t\cot(\theta_2) - t\cot(\theta_1) \tag{3.19}$$

where R_1, R_2 are the radius of each single-wedge, t is the outer wedge height of double-wedge, and the radius of double-wedge is the same with R_1. The lower panel of Fig. 3.21b shows that the resonance frequency of double-wedge (dots) is the result of transition from the θ_1-single-wedge to the θ_2-single-wedge, and the upper panel depicts that the magnitude of geometric dispersion is maximized at the mode number (ν_p in eqn 3.21) where the two single-wedge curves intersect – the mode number (ν_p) is a function of t (see eqn 3.20 and 3.21).

$$\frac{\nu_p}{R_1}\left[1 + \frac{\alpha_1}{{\nu_p}^{2/3}}\right] = \frac{\nu_p}{R_2}\left[1 + \frac{\alpha_2}{{\nu_p}^{2/3}}\right] \tag{3.20}$$

$$\nu_p \approx \left[\frac{(\alpha_2 - \alpha_1)R}{\cot(\theta_2) - \cot(\theta_1)}\right]^{\frac{3}{2}} t^{-1.5} \tag{3.21}$$

Fig.3.21c shows that the double-wedge dispersion is following the same relation at different t, and Fig.3.21d-f show the dispersion at different wedge angles ($\theta_1 = 10°$, $\theta_2 = 20°$). The additional dispersion is generated through wedge angle transition, and the bandwidth of additional dispersion generation is fairly wide (> hundreds nm wavelength) so as to enable wideband dispersion control with a couple of wedge angle transitions. Wedge angles can be ordered in any sequence along the radial direction, and the geometric dispersion contributions of the angle transitions are then placed in order along the spectral domain. There have been reports that a dual-ring resonator (silicon nitride) can also produce additional dispersion by strong mode coupling[129, 130]. This is a good example to show that additional geometric parameter (gap between ring resonators) makes the degree of dispersion control higher, as we used the wedge angle transition height.

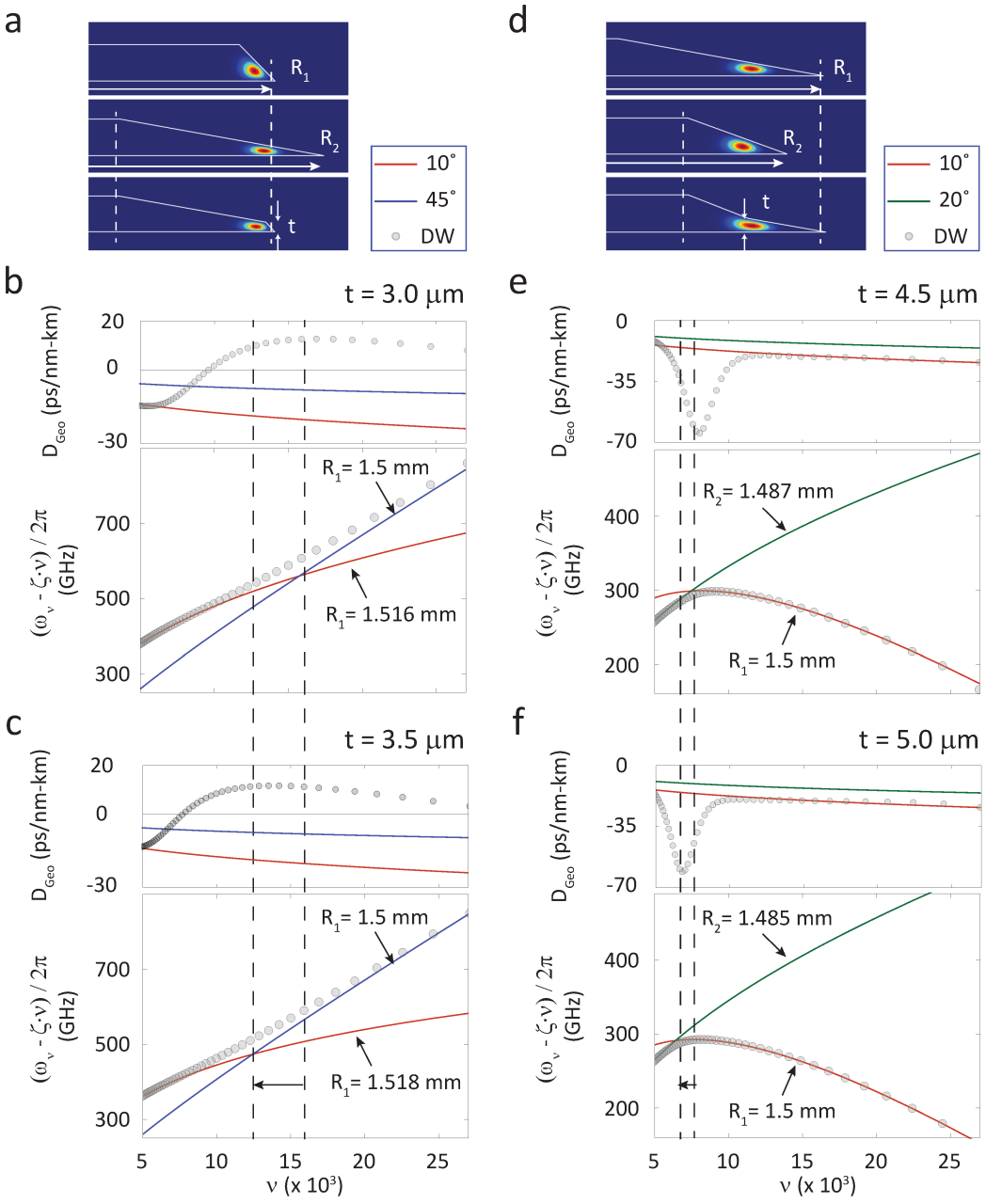

Figure 3.21: **Multi-wedge dispersion in equation model** (**a**) Finite-element-simulation of optical modes in single-wedge ($\theta = 45°$ (Top), 10° (Center)) and double-wedge (Bottom: t=3 μm) disks. Outer wedge angle is 45°, and inner wedge angle is 10°. (**b**) Upper panel depicts the geometric dispersion, and lower panel shows the resonance frequencies as a function of mode number ν. t = 3 μm, R_1=1.5 mm, and R_2=1.516 mm. Solid lines illustrate the dispersion of single-wedge (eqn (S1)), and dots are numerical results from finite-element simulations. In the plot, the mode frequencies are offset by the linear line with constant slope ζ so as to show dispersion more readily observable. (**c**) Same as (**b**), but for t = 3.5 μm, R_1=1.5 mm, R_2=1.518 mm. (**d**) Finite-element-simulation of optical modes in single-wedge ($\theta = 10°$ (Top), 20° (Center)) and double-wedge (Bottom: t=5 μm) disks. Outer wedge angle is 10°, and inner wedge angle is 20°. (**e**) Same as (**b**), but for t = 4.5 μm, R_1=1.5 mm, R_2=1.487 mm. (**f**) Same as (**b**), but for t = 5.0 μm, R_1=1.5 mm, R_2=1.485 mm.

3.5.2 Multi-wedge fabrication process

Fiber-inspired cavity dispersion design allows broadband dispersion control, and the design can avoid heterogeneous material process which easily degrades Q factor of resonator. Q factor is critical for efficient nonlinear process and this section will discuss microfabrication method that tailor cavity structure while maintaining Q factor in ultra-high-Q regime. In addition, imprecision of micro-fabrication will be discussed as well as its effect on dispersion properties.

3.5.2.1 Overview of process flow

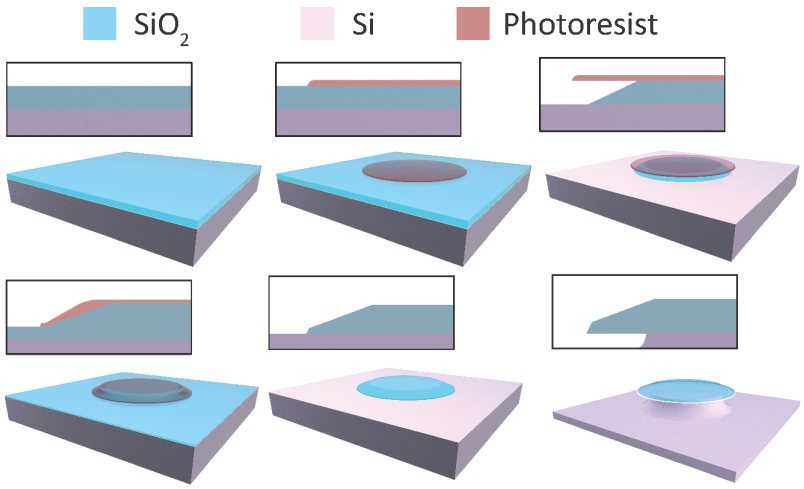

Figure 3.22: **Multi-wedge structure fabrication** SiO_2 film is grown on *Si* wafer by thermal oxidation. SiO_2 single-wedge disk is formed by photolithography and wet etching (Upper panels). An additional wedge is created through another cycle of thermal oxidation, photolithography, and wet etching. XeF_2 dry etch is applied to etch Si after removing photoresist and residues (lower panels). This figure is edited from Yang et al. [71]

Fig.3.22 shows the microfabrication process of double-wedge disk. Microfabrication begins with thermally grown SiO_2 on Si, which is then processed with photolithography and wet etching into single-wedge shaped disks (see top row in Fig.3.22) in which the wedge angle can be controlled from 8° to 55° (see Fig.2.8). Hexamethyldisilazane (HMDS) was additionally deposited prior to photoresist coating for wedge angles larger than 20° (right column of Fig.2.8). For wedge angles in a range of 8°−20°, photoresist was spin-coated on the oxide layer without HMDS (left column of Fig.2.8). Photoresist thickness was used to adjust the wedge angle. The photoresist pattern acted as an etch mask during immersion in a buffered hydrofluoric acid (HF) solution, and the resist was removed once wet etching was completed. The second SiO_2 layer was grown at the same temperature as the etched wedge disk, and the thickness of the oxide was accurately controlled via duration of thermal oxidation. Again, the photoresist was patterned on the oxide layer and the wet etch proceeded

to create additional wedge angles. After cleaning to remove photoresist and residues, XeF_2 dry etch was applied to etch the Si. The multi-wedge disk process is an extension of the techniques developed for the original single-wedge disk resonator[22]. During this second cycle, the angle of the additional wedge is adjusted as before and its height is controlled through the duration of etching. Calibrations have shown that the height increases at a rate of ~ 10 nm/min, resulting in the following spectral rates: FSR ~ 400 kHz/min and D_2 ~ 300 Hz/min. The process can be repeated to add additional wedges.

3.5.2.2 Additional wedge process

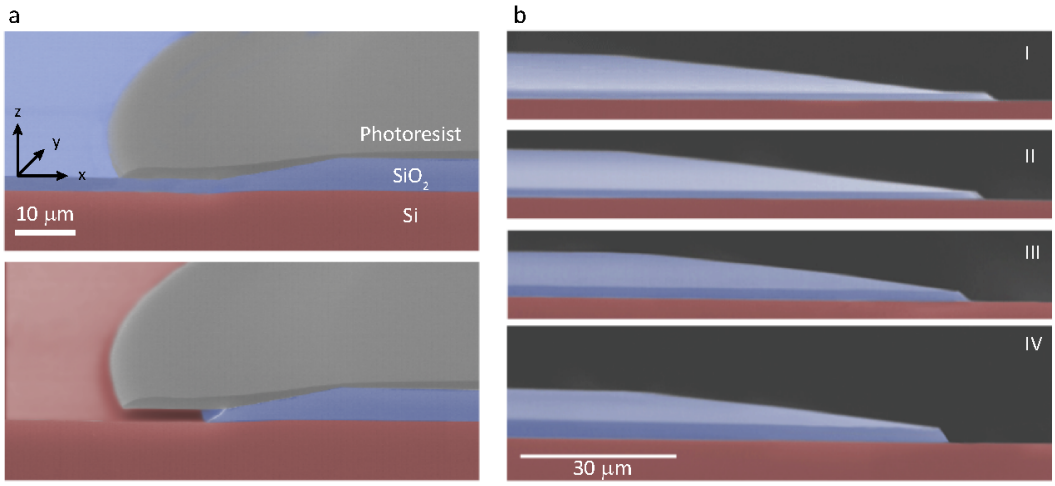

Figure 3.23: **Additional wedge process using photolithography and wet etch** (**a**) Extra wedge addition to the sigle-wedge structure. The photoresist was patterned on the oxide layer, and the photoresist pattern covers over the entire surface of etched wedge with an additional μm radius (Top). Then wet etch is proceeded, and it made an additional wedge once the undercut proceeded all the way up to the original wedge (Bottom). (**b**) The outermost wedge height as a function of wet etch time. The height is kept as the original thickness of second oxide layer, and it starts to increase once the BHF undercut proceeded all the way up to the original wedge. (**c**) False-colored SEM image of the progression towards double-wedge structure.

Multi-wedge structure can be precisely fabricated using CMOS-compatible process, and the overall procedure is explained in Method. Fig. 3.23 shows detailed process steps through Fig. 3.22, and an additional wedge is fabricated with desired wedge angle and height. The photoresist is patterned on the silica layer which the additional oxide layer is thermally grown under chemically etched single-wedge silica disk. Buffered hydrofluoric acid (BHF) undercut a silica layer covered by photoresist, and make an additional wedge once the undercut reaches to the original wedge. Fig.3.23a shows false colored SEM images of sample which is proceeding BHF etching, and the outermost wedge (additional wedge) height is controlled as a function of etch duration[71]. The height is keeping its original layer thickness of second oxide layer (Fig.3.23b I) until the etch duration that an additional

wedge reaches the original wedge (Fig.3.23b II). Undercut is then proceeded through the original wedge (Fig.3.23b III), and its height keep increasing as etch is proceeding longer (Fig.3.23b IV). Etch rate varies depending on an adhesion between photoresist and silica layer, and it is approximately able to adjust the outermost height by tens of nm per minute. Additional oxidation step can be avoided if etch steps repeat to only carve out certain depth of silica[131], instead of etching all the way up to the silicon surface and growing an oxide again. However it empirically gives the best smoothness of wedge surface by removing 'foot' region[22], and makes Q factor comparable to the single-wedge disk.

The oxide thickness empirically controls the etching speed; thicker oxide layer lowers the speed of additional wedge height increment (Fig. R3b), so as to improve the process accuracy. The height of additional wedge can be controlled as a function of etch time, and the angle can be adjusted by the thickness of photoresist (Fig. R3a) with the same experimental condition as the one for single-wedge angle control.

3.5.2.3 Imprecision of micro-fabrication

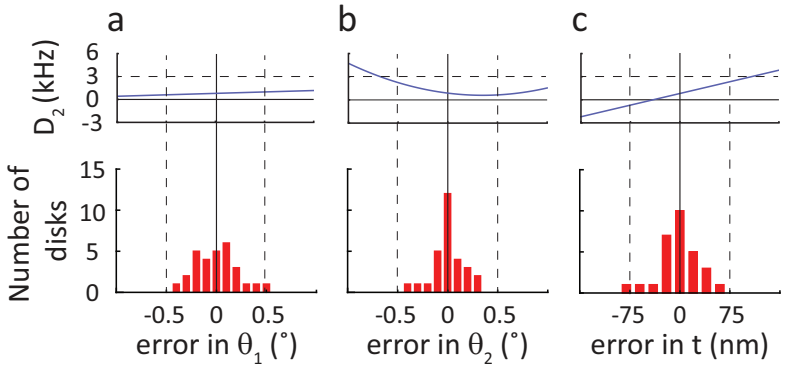

Figure 3.24: **Analyzed fabrication imprecision and dispersion inaccuracy**(**a**) Colormap of chromatic dispersion of double-wedge disk as a function of the outermost wedge height (t). Black solid line indicates the zero dispersion wavelength (λ_{ZDW})− $D_2 > 0$ corresponds to anomalous dispersion, and $D_2 < 0$ corresponds to normal dispersion. Inset shows the SEM image of double-wedge and indicates the height of double-wedge. (**b**) Measured D_2 of double-wedge as a function of the height of outermost wedge. Blue line is the result of finite element simulation (I). (**c**) Measured FSR and D_2 with 2.93 (II), 2.87 (III), and 2.81 (IV) μm of the height of outermost wedge. Each II, III, and IV correspond to the black dashed line on the (**a**). This figure is from supplementary information of Yang et al.[71]

The imprecision of micro-fabrication[22, 114] might lower the repeatability of dispersion in fabricated disks. It can also impact the repeatability of resonator geometry design to achieve specifed dispersion coefficients. As a preliminary test of process accuracy, double-wedge disks (29 EA) were identically fabricated from multiple wafers (4 EA) and structural parameters were measured using an AFM (see Fig.3.24). The measurements show 30.4 nm,

0.21°, and 0.15° standard deviations in t, θ_1, and θ_2, respectively(actual values are 2.92 μm, 43.5°, and 10.5° for t, θ_1, and θ_2). In order to understand how this imprecision in the process impacts the dispersion of the resonator, we have run a set of simulations on double-wedge disks and independently varied t and $\theta_{1,2}$ by ± 150 nm and 1°, respectively. Based on numerical simulation, the standard deviations of t, θ_1, and θ_2 approximately cause 0.8, 0.01, 0.3 kHz of D_2 variations from the designed dispersion parameter, respectively. For simplicity, D_2 variation was calculated as function of a single parameter (one of t, θ_1, and θ_2) assuming other geometric parameters constant.

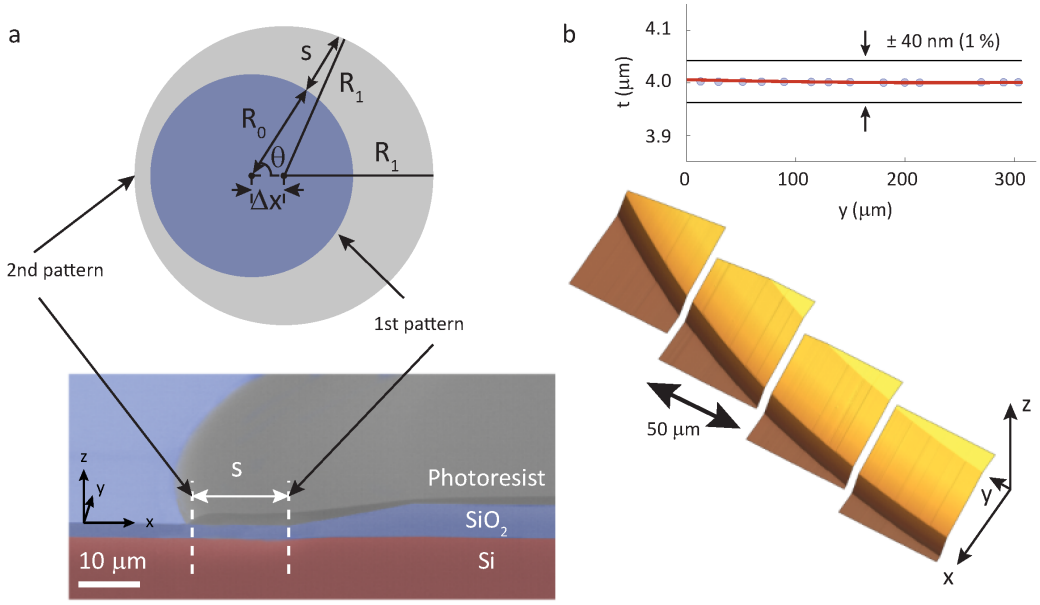

Figure 3.25: **Variation of fabricated geometric parameters regarding to the lithographic alignment** (**a**) Photoresist (2nd pattern) is covering the silica single-wedge (1st pattern) on the oxidized layer. Lithographic misalignment (Δx) makes the variation of *s* (see the lower panel) through the circumference of the circle, and consequently changes the height of additional wedge. (**b**) The height of additional wedge (1-mm-diameter) is measured using AFM. The upper panel shows the measured height of additional wedge through the y-axis on the lower panel, and the lower panel shows the AFM image of the double-wedge.

The double-wedge resonator is formed using a pair of lithography + etch steps in order to pattern the each wedges, respectively. Mask aligner (KarlSuss MA-6 aligner) has 0.5 μm of an alignment accuracy with 99.7 % confidence[132], and the stepper (GCA 6300 DSW) has 0.25 μm accuracy[133]. The misalignment makes the variations of *s* in Fig.3.25a. The variation of gap "s", additional wedge height "t", and D_2 follow eqn.3.22.

$$
\begin{aligned}
s = \Delta x \cos\theta + \sqrt{R_1^2 - \Delta x^2 \sin^2\theta} - R_0 \\
\Delta s \sim \Delta x \cos\theta \\
\Delta t \sim \Delta s \tan(10^\circ) \\
\Delta D_2 \sim 30 Hz/nm \times \Delta t
\end{aligned}
\tag{3.22}
$$

Fig.3.25b shows the measured outer wedge height (t) of fabricated double-wedge disks (1-mm-diameter), and the lower panel shows the AFM image of the measured disk. Fig.3.26 shows estimated s, Δt, and ΔD_2 as a function of θ and misalignment Δx. The measured data in Fig.3.25b is fitted as $\Delta x \sim 85$ nm and $\Delta t \sim 15$ nm for comparison. In addition, net cavity dispersion[134], integrated dispersion through one round trip of the resonator, is calculated as a function of Δx, and $\Delta D_{2,net}$ is the net cavity dispersion divided by one round trip length (see Fig.3.26).

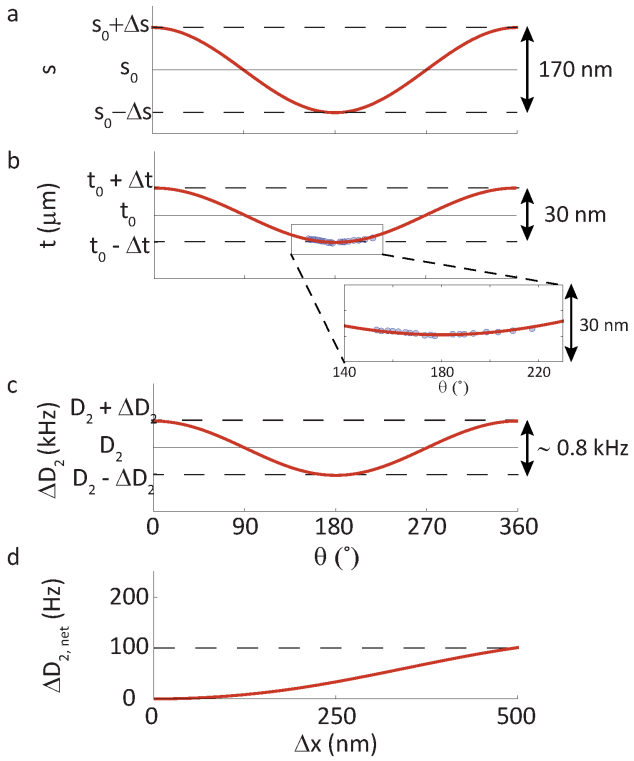

Figure 3.26: **Variation of fabricated geometric parameters regarding to the lithographic alignment** (**a**) Photoresist (2nd pattern) is covering the silica single-wedge (1st pattern) on the oxidized layer. Lithographic misalignment (Δx) makes the variation of s (see the lower panel) through the circumference of the circle, and consequently changes the height of additional wedge. (**b**) The height of additional wedge (1-mm-diameter) is measured using AFM. The upper panel shows the measured height of additional wedge through the y-axis on the lower panel, and the lower panel shows the AFM image of the double-wedge.

3.5.3 Dispersion-engineered resonator characterization

3.5.3.1 Multi-wedge resonator structure

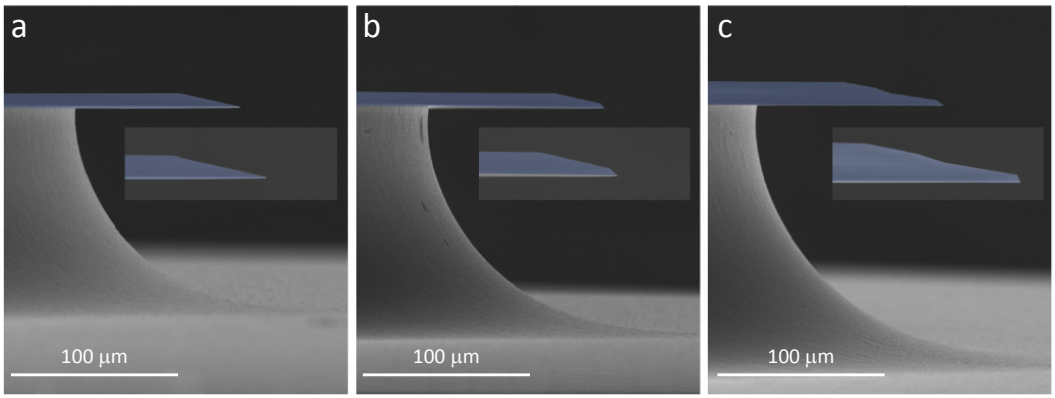

Figure 3.27: **Electron micrographs of dispersion-engineered resonators** Scanning electron micrographs (SEM) of side-views for (**a**) single, (**b**) double and (**c**) quadruple wedge resonators. Inset shows zoom-in images. Fig.**a-c** are edited from Yang et al.[71]

Fig.3.27 shows SEM image of single-, double-, and quadruple-wedge disk resonators. In the device of Fig.3.27c, the additional oxidation, photolithography, and wet etch steps were followed in order to define more wedge angles from the double-wedge process. Diameter of the resonators are approximately 22 GHz, and the oxide thicknesses are around 8 μm. Insets show high resolution zoom-in scan of wedge disks; single wedge angle = 10°, double wedge angle = 45°/ 10°, and quadruple wedge angle = 45°/10°/20°/10° (from outward to inward wedge).

3.5.3.2 Multi-wedge resonator Q factor characterization

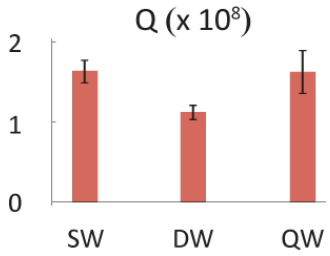

Figure 3.28: **Q factor characteristics of dispersion-engineered resonators** (**a**) Measured Q factor (intrinsic Q factor) of TM0 mode in single-, double-, and quadruple-wedge disks. This figure is edited from Yang et al.[71]

As has been discussed earlier, the Q factor of microresonator is critical for efficient nonlinear operation. Therefore, maintaining Q factor in ultra-high-Q regime is another important feature that needs to be achieved in dispersion-engineered resonator. Fig.3.28 shows sum-

marized measured Q factor of single-, double-, and quadruple-wedge resonators (diameter = 3 mm, FSR = 22 GHz). The developed microfabrication process achieved average Q factors (intrinsic Q factor) of 1.6×10^8, 1.1×10^8, and 1.6×10^8 for single-, double-, and quadruple-wedge disks (TM0 mode). Here error bars indicates the variation of measured Q factors from set of devices.

It is also worth to note that taper fiber coupling easily achieved critical and over-coupling with the fundamental mode of dispersion-engineered resonator (see Fig.2 in Ref[135]). Because dispersion-engineered resonator also adjusts the optical mode distribution using cavity geometry, there might be possibilities that the spatial mode shifts inward and the mode shift causes less evanescent field coupling with tapered fiber.

3.5.3.3 Multi-wedge resonator dispersion characterization

Dispersion comparison in single-, double-, and quadruple-wedge is shown for demonstration of additional wedge angle effect. To characterize dispersion in the resonator we measure FSR_μ (μ is mode index) in several wavelength bands and calculate $D_2(\mu) = \partial FSR_{\mu'}/\partial\mu'|_{\mu'=\mu}$ which is related to the GVD parameter through the following expression:[32]

$$\beta_2(\mu) = \left.\frac{\partial^2\beta}{\partial\omega^2}\right|_{\omega=\omega_\mu} \approx -\frac{1}{4\pi^2 R}\cdot\frac{D_2(\mu)}{FSR_\mu^3} \tag{3.23}$$

where R is a resonator radius. Here, we define dispersion coefficients as

$$f_\mu = f_0 + D_1\cdot\mu + \frac{D_2}{2!}\mu^2 + \frac{D_3}{3!}\mu^3 + \cdots \tag{3.24}$$

where f_0 is the frequency at which the dispersion is measured and D_1, D_2, D_3 correspond to FSR, ΔFSR per mode, and the third order dispersion parameter[21, 43, 47, 136]. Controllability of broadband dispersion will be followed using structural parameter adjustment in dispersion-engineered resonator.

Dispersion parameter fitting The resonance frequencies of one mode family can be described as a Taylor series (cf.eqn.3.7), and the coefficients of the series correspond to dispersion parameters at $\mu = 0$. Fig.3.29 shows the measured FSR of single-, double-, quadruple-wedge resonators. FSR is measured using both EOM-assisted (300-nm-bandwidth; cf. Fig.3.5a)/ sideband (70-nm-bandwidth; cf. Fig.3.4) spectroscopy, and both methods show precise agreement. It is important to note that higher-order dispersion fitting (e.g. D_3 in a level of Hz/ mode) needs wideband measurement.

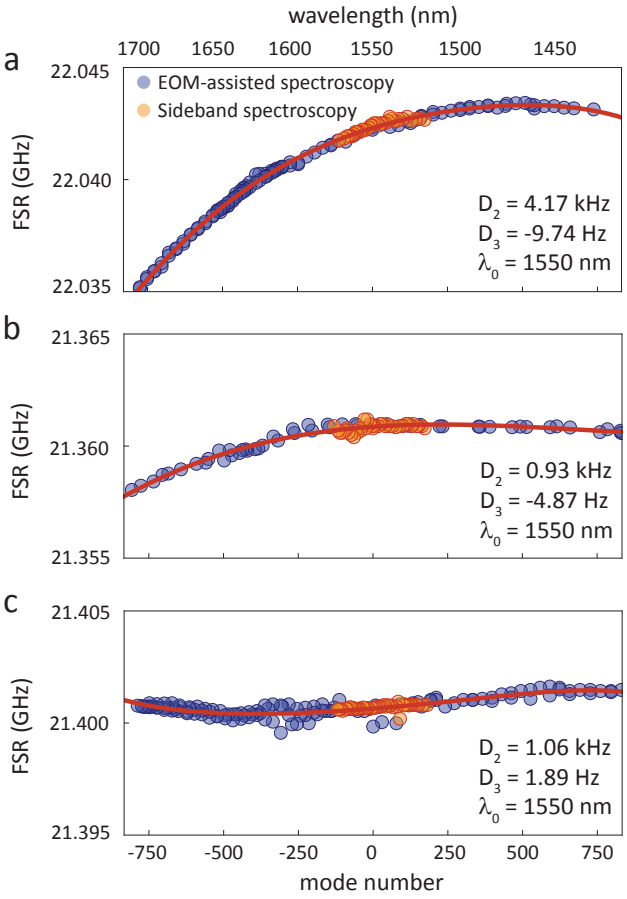

Figure 3.29: **Higher order dispersion parameter fitting** (**a**) Measured FSR of single-wedge disk and the Taylor series fit (solid line). Blue dots are measured by the EOM comb method (Fig.3.5a), and red dots are measured by sideband spectroscopy (Fig.3.4) for comparison. The FSR is 22.042 GHz at 1550 nm. (b-c) Same as panel a, but for quadruple-wedge disks. FSR: 21.36 GHz for (b), 21.40 GHz for (c) at 1550 nm. This figure is from supplementary information of Yang, et al.[71]

Dispersion measurement results in single-, double-, and quadruple-wedge disks

Fig.3.30 shows measured FSR, D_2, D_3 and the results of simulations for the device structures provided in the insets. As has been noted in Ref [98], a single-wedge contributes geometrical dispersion that is both normal and approximately spectrally flat. In the upper panel of Fig.3.30a, the zero dispersion wavelength (λ_{ZDW}), has been shifted by this effect to 1.5 μm[22, 98] (material dispersion has a λ_{ZDW} near 1.3 μm). The bottom panel shows D_3 of single-wedge disk, and the dots represent fitted value from wideband measurement (> 300 nm spectral span). In the double-wedge resonator (Fig.3.30b) there is a gradual onset (anomalous) of the geometrical dispersion around 1200 - 1500 nm wavelength as a result of mode transition from 45° wedge to 10° wedge. The overall effect is to provide a flattening of group velocity dispersion on wavelength over a broad range of wavelengths. The dispersion

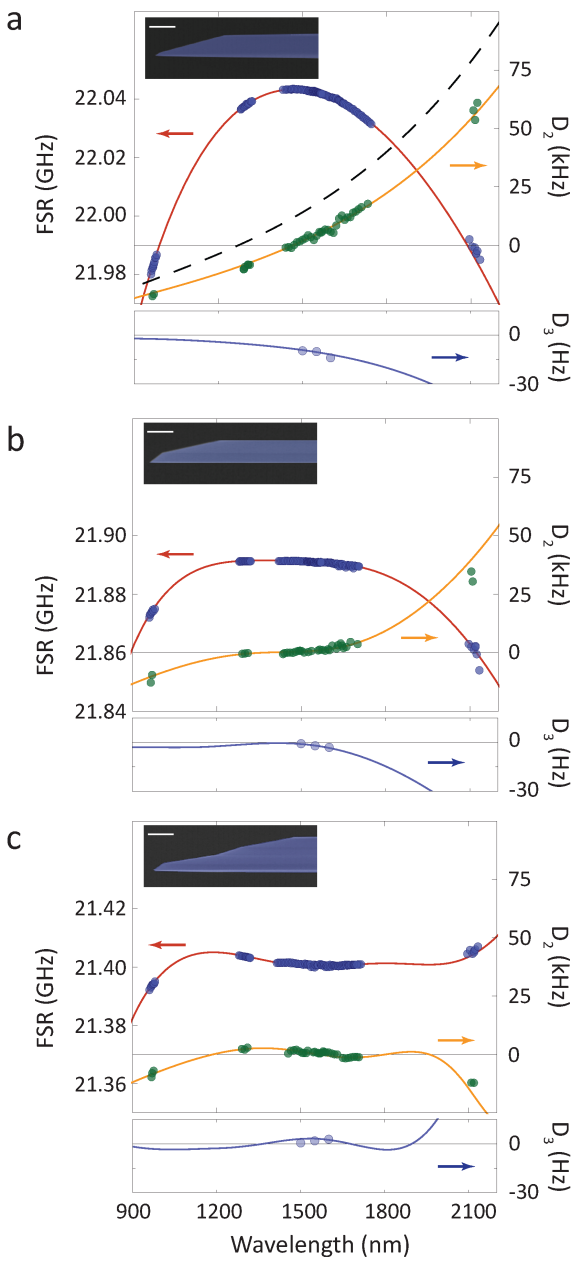

Figure 3.30: **Dispersion characteristics of single-, double-, and quadruple-wedge disks** (**a**) FSR and D_2 of single-wedge disk (wedge angle = 10°). Green and blue dots are measured D_2 and FSR, respectively; Orange and red lines are numerical results. The resonator geometry was scanned using both SEM (inset; scale bar = 10 μm) and AFM for finite-element-simulation. Dashed line shows silica material dispersion[23, 128]. Bottom panel represents D_3 of single-wedge disk. Dots shows experimental fitting data from wideband measurement, and line represents numerical results. (**b-c**) As in (**a**) but for double-, and quadruple-wedge disk, respectively. This figure is edited from Yang, et al.[71]

in the transition is therefore reduced. The addition of further wedges can be used to extend this control to longer wavelengths. In the quadruple-wedge design the third wedge provides control out to 2,000 nm (Fig.3.30c).

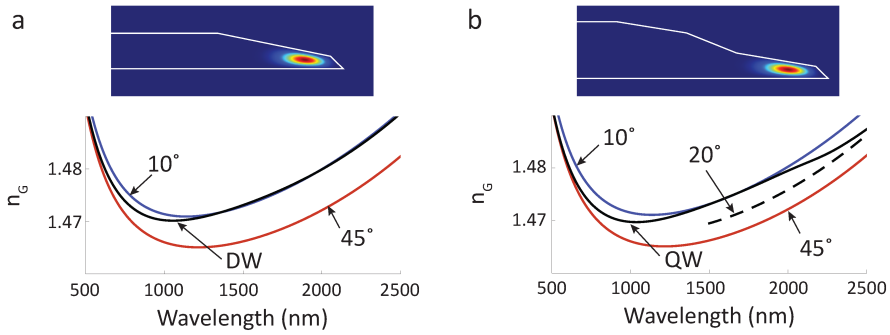

Figure 3.31: **Group index spectra of double- and quadruple-wedge disks** (**a**) Group index spectra of double-wedge disk. The simulated geometric structure is from the resonator in Fig. 3.30b. Blue line shows the group index of 10° single-wedge disk, and red line represents the group index of 45° single-wedge disk. (**b**) Same as (**a**), but for quadruple-wedge disk. The calculated resonator profile is from Fig.3.30c. Dashed line represents 20° single-wedge group index.

Fig.3.31 shows calculated group index spectra of double- and quadruple-wedge disks (Here finite-element-simulation used AFM-scanned resonator profiles in Fig.3.30). Upper panel of Fig.3.31a shows fundamental mode profile in double-wedge resonator. The blue and red lines represent the group index of 45° and 10° single-wedges, respectively. Double-wedge group index was extracted from solid curves in Fig.3.30b – calculated FSR and D_1 are in good agreement with measurement results (cf. Fig.3.30). Fig.3.31b shows group index spectra of quadruple-wedge disk, and it shows clear group index spectra from outer wedge to inner wedge (45° $\rightarrow$ 10° $\rightarrow$ 20°) as wavelength increases.

Double-wedge dispersion – anomalous geometric dispersion for material dispersion compensation in shorter wavelength

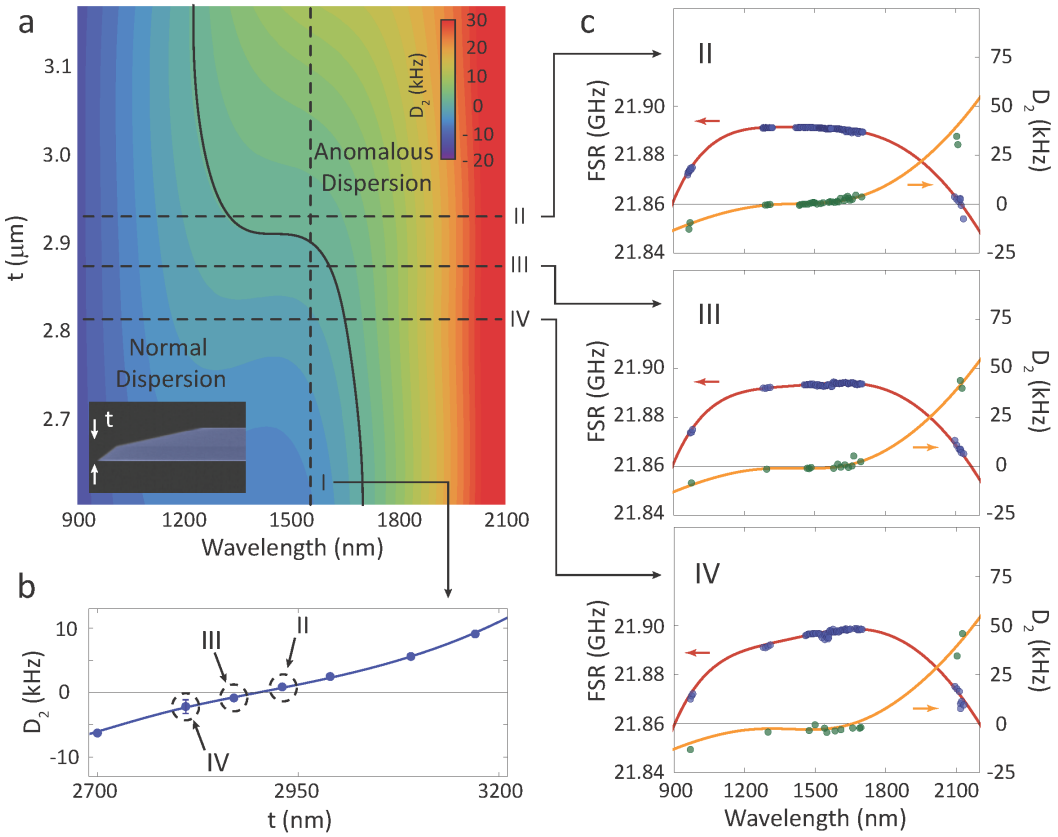

Figure 3.32: **Double-wedge dispersion control** (**a**) Colormap of chromatic dispersion of double-wedge disk as a function of the outermost wedge height (t). Black solid line indicates the zero dispersion wavelength (λ_{ZDW})– $D_2 > 0$ corresponds to anomalous dispersion, and $D_2 < 0$ corresponds to normal dispersion. Inset shows the SEM image of double-wedge and indicates the height of double-wedge. (**b**) Measured D_2 of double-wedge as a function of the height of outermost wedge. Blue line is the result of finite element simulation (I). (**c**) Measured FSR and D_2 with 2.93 (II), 2.87 (III), and 2.81 (IV) μm of the height of outermost wedge. Each II, III, and IV correspond to the black dashed line on the (**a**).

In double-wedge resonator, the group index of the mode transitions between the group index of outer wedge (θ_1; shorter wavelength) and inner wedge (θ_2; longer wavelength). As has been discussed, the geometric dispersion becomes anomalous when the optical mode transitions from higher θ_1 to lower θ_2 ($\theta_1 > \theta_2$ in Fig.3.32). Otherwise the geometric dispersion from the transition becomes normal – lower θ_1 to higher θ_2. In addition, the outer wedge height ("t" shown in Fig.3.32a inset) determines the spectral location at which the mode transitions from θ_1 to θ_2, and it corresponds to determine λ_p in Fig.3.20. In Fig.3.32, a set of double-wedge disks were measured and double-wedge dispersion control is shown using outer wedge height "t"– here other structural parameters are fixed (θ_1 =

45°, θ_2 = 10°, D = 3 mm). Because $\theta_1 > \theta_2$, the mode transition between two wedge angles creates anomalous geometric dispersion. The anomalous geometric dispersion can compensate material dispersion and D_2 became relatively flat if the spectral location of mode transition is around 1000 - 1300 nm (silica material dispersion is normal at wavelengths < 1.3 μm). Fig.3.32a shows simulated double-wedge dispersion as a function of wavelength and the outermost wedge height "t". It clearly shows that the flat dispersion regime can move from shorter wavelength to longer wavelength as "t" increases. Fig.3.32b-c compare the measurement values with finite element simulation plotted on Fig.3.32a, and dashed lines (I - IV) correspond to Fig.3.32b - c, respectively. It is interesting to note that D_2 at 1550 nm is approximately given as linear function of "t" in Fig.3.32, and it corresponds to variable curvature of parabolic mode curve in mode spectra as shown in Fig.3.33.

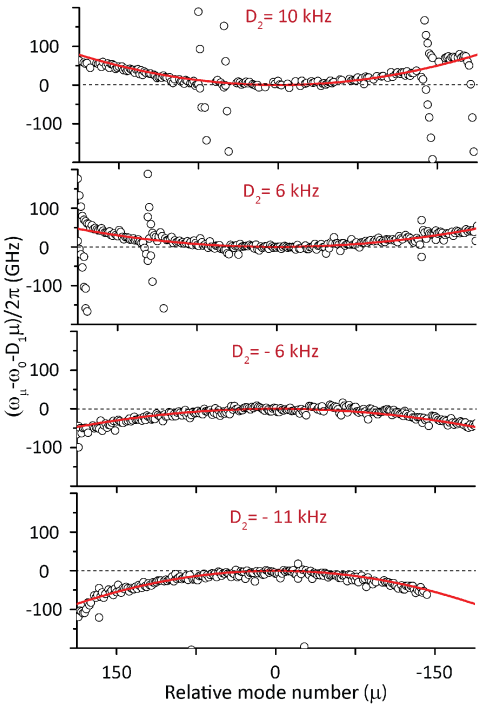

Figure 3.33: **Double-wedge mode spectrum** Measure mode spectra of double-wedge disks. TM fundamental mode was measured from 1520 to 1580 nm, and the outer wedge thicknesses are 2.58, 2.70, 3.09, and 3.17 μm from lower to upper panels. Measured D_2 correspond to -10.9, -6.27, 5.61, and 10 kHz/ FSR

Quadruple-wedge dispersion – normal geometric dispersion for material dispersion compensation in longer wavelength

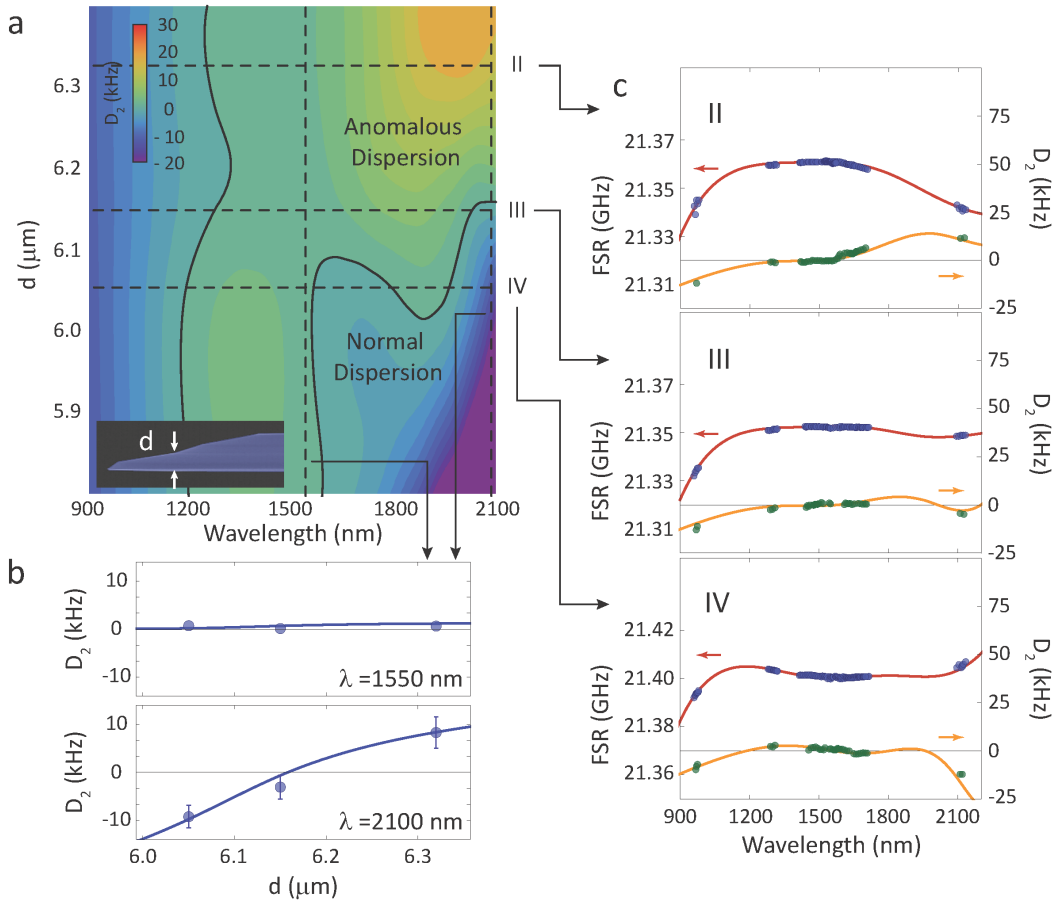

Figure 3.34: **Quadruple-wedge dispersion control** (**a**) Colormap of chromatic dispersion of quadruple-wedge disk as a function of the third wedge height (d, see inset). Black solid line indicates the zero dispersion wavelength (λ_{ZDW}). Inset shows the SEM image of quadruple-wedge and indicates the height of third wedge. (**c**) Measured FSR and D_2 of quadruple-wedge disks which have 6.32 (II), 6.15 (III), and 6.05 (IV) μm of d. Each II,III, and IV correspond to the black dashed line on the **a**.

In this section, the additional third wedge was added to double-wedge structure in Fig.3.32 – θ_1, and θ_2 are same and "t" is fixed. The group index transitions from θ_1 to θ_2 in shorter wavelength, and the third wedge (θ_3) introduces additional mode transition in longer wavelength from θ_2 to θ_3. The wedge transition thickness ("d" seen in the inset of Fig.3.35) between θ_2 and θ_3 determines the spectral location at which the the centroid of motion shifts from θ_2 to θ_3 as "t" does in double-wedge structure – it corresponds to determine λ_p. Because "d">"t" in this quadruple-wedge disk, λ_p of mode transition between θ_2 and θ_3 is thereby longer than the one between θ_1 and θ_2. In addition, θ_2 and θ_3 are 10° and 20°. Therefore, the geometric dispersion at this transition should be normal dispersion. Fig.3.35a shows finite-element-simulation results of quadruple-wedge dispersion as a function of wavelength and

"d". It is important to note that chromatic dispersion at longer wavelength (cf. Lower panel of Fig.3.35b) becomes normal dispersion from anomalous dispersion as the additional wedge approaches to the optical mode ("d" decreases). Then the normal geometric dispersion shifts from far longer wavelength to $\sim 2\ \mu m$, so the total dispersion at 2100 nm becomes normal dispersion as a result of material dispersion compensation. It is also interesting to note that D_2 at 1550 nm is almost constant while D_2 at 2100 nm varies from 10 to -10 kHz/ FSR (Upper panel of Fig.3.35b) – this is because θ_1, θ_2, and "t" are fixed. Fig.3.35b-c compare the measurement values with finite element simulation plotted on Fig. 3.35a, and dashed lines (I - IV) correspond to Fig.3.35b-c, respectively.

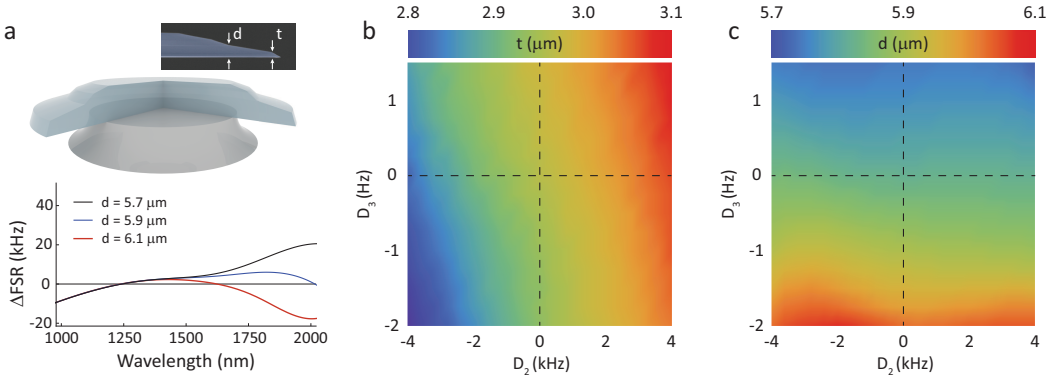

Figure 3.35: **Higher-order dispersion control using quadruple-wedge geometry** (**a**) Colormap of chromatic dispersion of quadruple-wedge disk as a function of the third wedge height (d, see inset). Black solid line indicates the zero dispersion wavelength (λ_{ZDW}). Inset shows the SEM image of quadruple-wedge and indicates the height of third wedge. (**c**) Measured FSR and D_2 of quadruple-wedge disks which have 6.32 (II), 6.15 (III), and 6.05 (IV) μm of d. Each II, III, and IV correspond to the black dashed line on the **a**.

Dispersion in different mode families

As preliminary tests of dispersion in higher order- and TE-polarized modes, the FSR and D_2 were additionally measured from TM1 and TE0 modes. The same resonators in Fig.3.30 were used for the additional measurements. The simulation results are from the same resonator geometry without extra tuning, and the results also show the group index transition as shown in Fig.3.19 (see Fig.3.37).

Intermodal dispersion Fig.3.36a-b show the dispersion of the TM0 and TM1 modes. The higher order mode (TM1) similarly shows an adjustable dispersion in multi-wedge structures (see middle and bottom panels in Fig.3.36b), but the compensated dispersion shows different magnitude and spectral dependency with those in TM0 because of different mode distribution and location. Generally, higher order mode has stronger geometric dispersion.

Polarization effect Fig.3.36c shows the dispersion of the TE0 mode. TE mode, which the transverse electric field is parallel to the flat oxide surface in wedge disk[22], extends into air

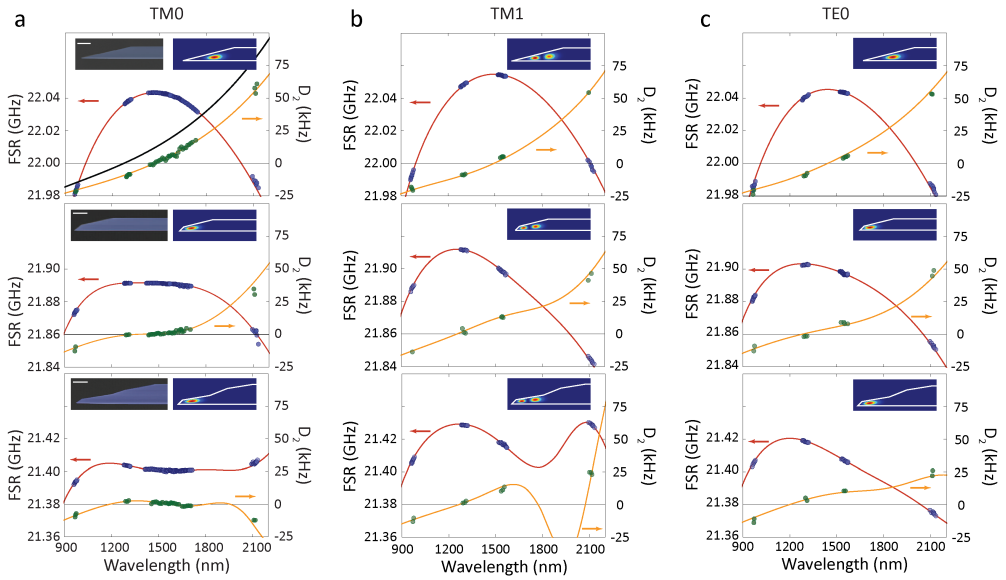

Figure 3.36: **Higher-order mode dispersion engineering** (**a**) FSR and D_2 of TM0 (fundamental) mode for single- (top). double- (middle), and quadruple-wedge (bottom) disk. Blue and green data points are measured FSR and D_2, respectively; red and orange lines are numerical results. The cavity geometry is imported from SEM image (left inset, bar: 10 μm) for finite element simulations, and the simulated mode profile is shown in the right inset. (**b-c**) Same as (**a**), but for (**b**) TM1 (higher order) and (**c**) TE0 (different polarization) mode. TM1 and TE0 modes were measured from the same resonator in Fig. 3, and the simulation is also conducted in the same resonator geometry without extra tuning.

cladding less than TM mode, so that the TE polarization has weaker geometric dispersion. The multi-wedge measurement results show the modified dispersion from the single-wedge dispersion, but the magnitude of dispersion compensation tends to be less than the one of TM0.

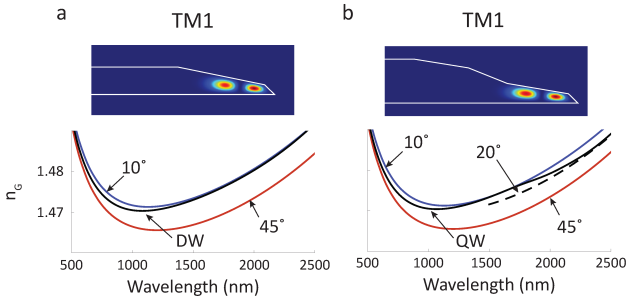

Figure 3.37: **Group index spectra of TM1 mode in double- and quadruple-wedge disks** (**a**) Group index spectra of TM1 mode in double-wedge disk. The simulated resonator structure is from Fig.3.36. Blue line shows the group index of TM1 in 10° single-wedge, and red line represents the group index of TM1 in 45° single-wedge. (**b**) Same as (**a**), but for TM1 in quadruple-wedge disk. Dashed line represents the group index of TM1 in 20° single-wedge.

3.5.4 Frequency comb generation in dispersion-engineered resonator

In this section, frequency comb generation in dispersion-engineered resonator will be discussed. Phase-locked frequency comb will be introduced with a comparison with the one in single-wedge resonator. Then wideband frequency comb generation will be further discussed.

3.5.4.1 Mode-locked frequency comb

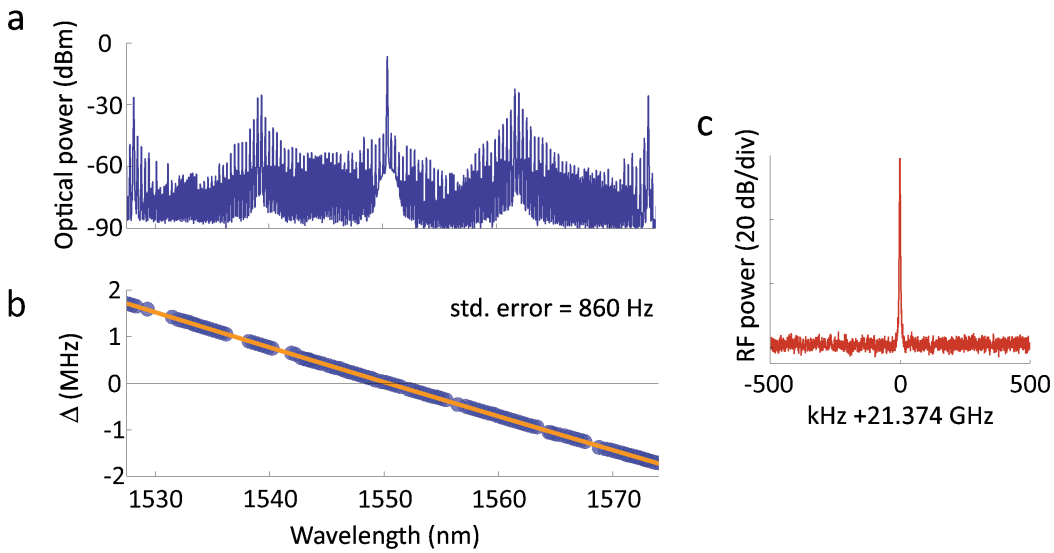

Figure 3.38: **Phase locked state comb (non-soliton) in dispersion-engineered resonator** (**a**) Optical spectrum of phase locked state comb in quadruple wedge resonator. The frequency comb envelope seems similar with the one in Ref[136]. (**b**) RF beatnotes between microcomb and reference comb. Pump laser is locked with the one of reference comb lines (offset $\Delta = 0$), and the repetition rate of the reference comb is slightly different with the one of the microcomb. (**c**) RF beat note shown here from the optical spectrum (red, RBW = 1 kHz).

In order to confirm the feasibility as a nonlinear optical cavity, frequency comb is demonstrated in dispersion-engineered microresonator (quadruple wedge disk, 21 GHz FSR). Fig.3.38a shows the optical spectrum of frequency comb generated in quadruple wedge disk. The threshold power was below 10 mW, and the operating power was around 100 mW in Fig.3.38. The comb envelope shape is similar with the one in Ref[136], and the microwave scan from the microcomb showed only single beat note. In order to confirm the spacing of frequency comb more carefully, the heterodyne beat note experiment was conducted using highly stable reference comb. The pump of the microcomb is locked to one of the reference comb lines, so Δ (heterodyne beat note frequency between microcomb and nearest reference comb) is zero at the pump. The repetition rate of the reference comb is slightly different with the one of microcomb, so the offset needs to linearly increase as the mode is separated

from the pump further. The linear line of the offset frequency shows standard error of 860 Hz, and it shows that the microcomb lines have a common repetition rate as well as no offset frequency[46, 136].

Fig.3.39 shows bandwidth engineering of the phase-locked frequency comb. As shown in measured FSR and predicted mode spectra, the quadruple-wedge disk has flat dispersion (low D_2 and D_3) at 1550 nm wavelength and the bandwidth consequently increases from ≈ 50 nm to 200 nm. Both frequency comb showed clean RF beatnote as well as low phase noise. It is worth noting that (i) frequency comb is generated in dispersion-engineered resonator with comparable threshold power as well as comb properties, and (ii) the bandwidth was

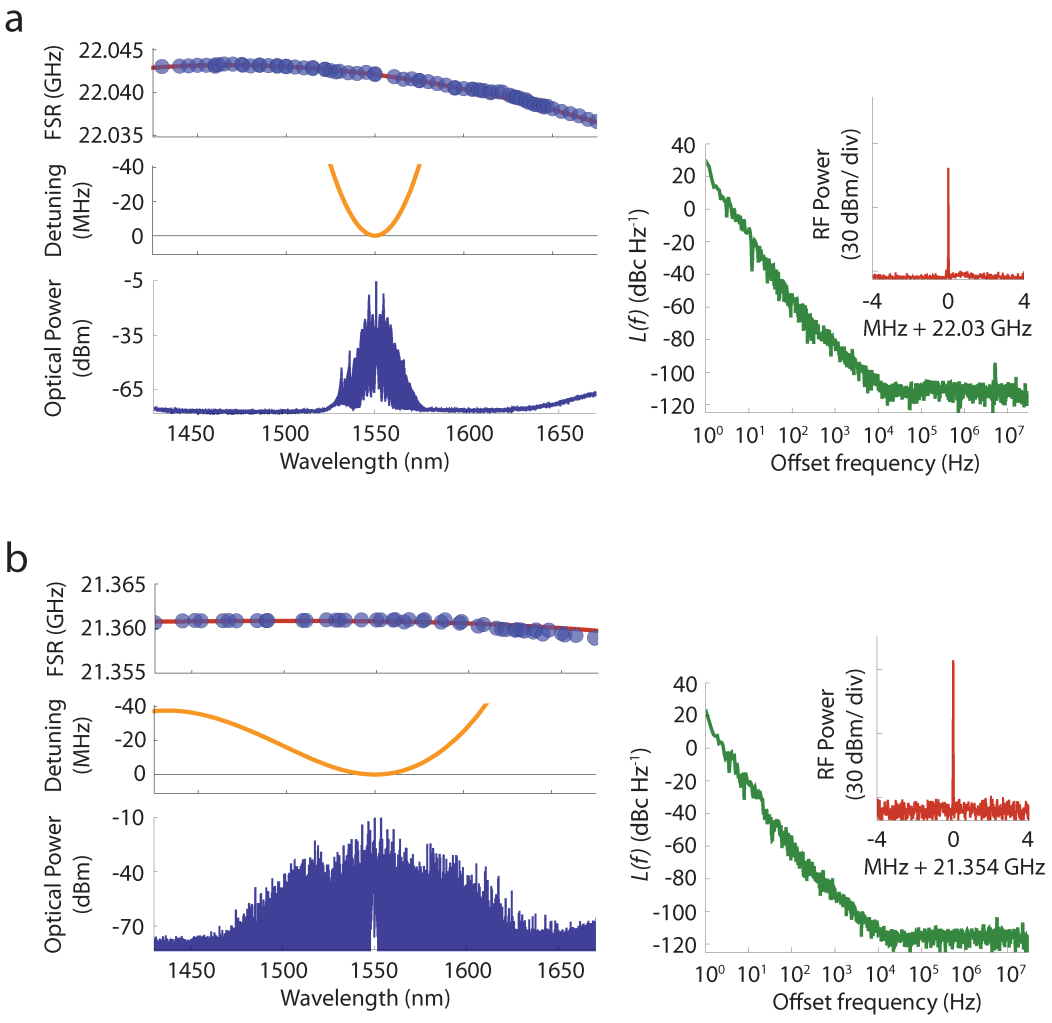

Figure 3.39: **Bandwidth shaping of phase-locked state comb** (**a**) Left Panel: Measured FSR, calculated detuning ($\omega_\mu - \omega_0 - D_1 \cdot \mu$), and optical spectrum of phase-locked comb in single-wedge disk. Right Panel: Phase noise of RF beatnote from the comb in left panel, and inset shows RF beatnote measured by ESA. (**b**) Same as (**a**), but in quadrupled-wedge disk.

confirmed to be engineered using the dispersion of microresonator.

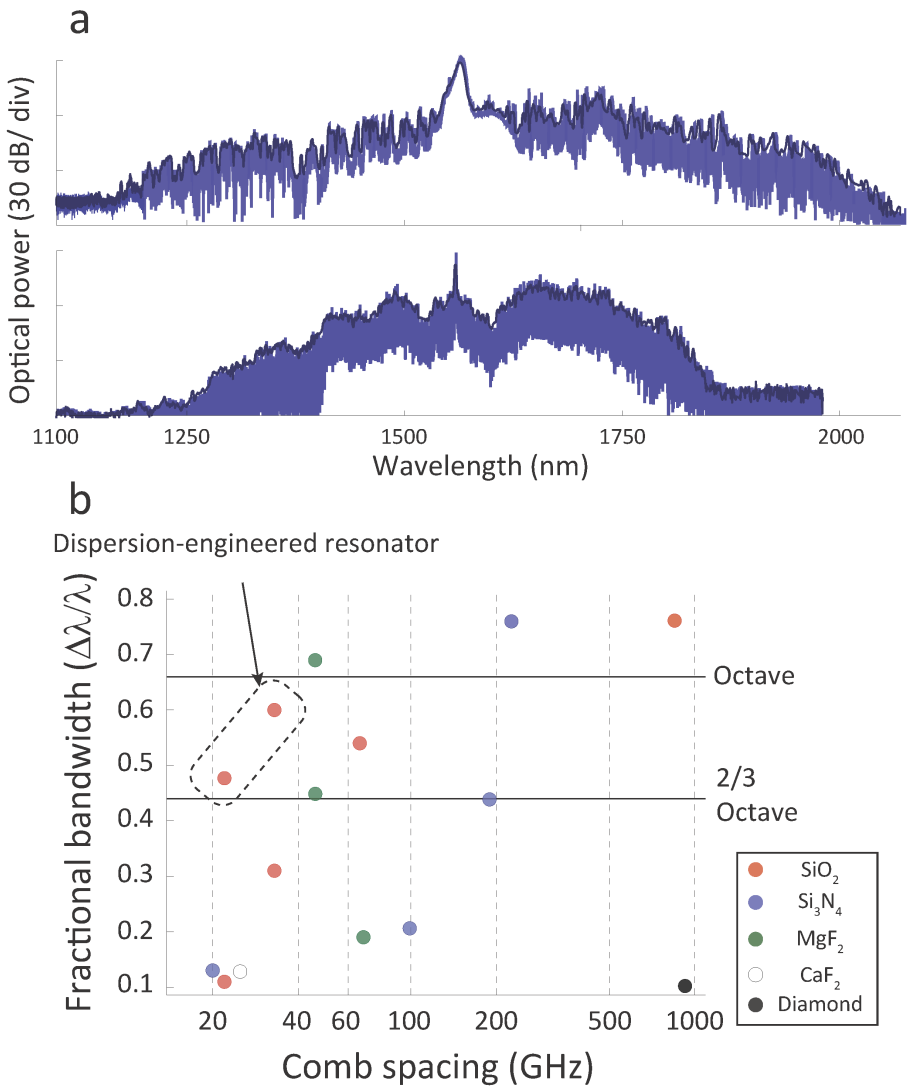

Figure 3.40: **Wideband frequency comb generation**(**a**) Dispersion engineered resonator generates broadband frequency comb which has over two-third of octave span. Upper panel: Span = 930 nm, Comb spacing = 33 GHz, Coupled pump power = 250 mW. Lower panel: Span = 740 nm, Comb spacing = 22 GHz, Coupled pump power = 60 mW. (**b**) Microresonator-based frequency comb technologies as a function of comb spacing and fractional bandwidth. This includes silica microresonator[50], silica toroidal microresonator[96], silicon nitride[43, 95, 137, 138], crystalline MgF_2 resonator[46, 139], crystalline CaF_2 resonator[140], and diamond microresonators[12].

3.5.4.2 Broadband frequency comb in detectable repetition rate – towards octave span frequency comb

Increasing the resonator size lowers the repetition rate towards detectable microwave rate. Optical finesse decreases under the similar level of Q factor, and hence parametric oscillation needs to be more efficient in order to attain the same level of comb bandwidth[5, 51, 141]. One of approaches to control the comb bandwidth at detectable microwave rate, might be dispersion-engineered resonator[139]. As a preliminary test of frequency comb generation in dispersion-engineered resonator, multi-wedge disks are fabricated with 2-mm- (33 GHz FSR), and 3-mm-diameter (22 GHz FSR). Multiple wedge resonators achieved 930-nm-span (120 THz) comb at 33-GHz-spacing (Upper panel of Fig.3.40a), and 760-nm-span (100 THz) at 22-GHz-spacing (Lower panel of Fig.3.40a). It is also important to note that the RF beat note was neither clean nor single tone in these wideband frequency comb. However, it is promising to achieve the wide span frequency comb in electronic-compatible rate and the device can be further developed towards wideband soliton generation.

3.6 Discussion

The nonlinear optics in microcavities has created lots of new, interesting problems on dispersion control (i.e. chromatic dispersion control[71, 139, 142], mode spectrum engineering[21, 55, 114], strong mode interaction[113, 120, 143, 144]) that many researchers haven't thought before. This chapter introduced the cavity design method to tailor the dispersion property while maintaining UHQ for efficient nonlinear operation. As a result, we demonstrated low-repetition-rate, and low-operating-power soliton generation using mode-spectrum-engineered resonator[55], and broadband frequency comb generation using dispersion-engineered resonator[71]. Not shown in this thesis, but dispersion engineering cooperated with many interesting physics in microcavities and demonstrated exciting results in other literatures[105, 120, 143]. Furthermore, dispersion-engineered UHQ platform can be directly transferred to the fully integrated platform which will be discussed in Chapter 5.

Chapter 4

CHIP-INTEGRATED NANOPHOTONIC WAVEGUIDES

4.1 Abstract[1]

Ultrashort pulses of light can extend its spectral width when propagating through highly nonlinear optical devices. In this thesis, silica nanophotonic waveguides can provide the engineered nonlinearity, dispersion control, and excellent waveguide transmission from ultra-violet to mid-infrared[2]. The continuum generation process (pulse broadening) can cooperates with the formation of dispersive waves (optical analogue to Cherenkov radiation), and the engineered nonlinear properties can precisely control the emission frequencies of the dispersive wave. This new capability is used to simplify offset frequency measurements of a mode-locked frequency comb. The nanophotonic waveguides can also enable mode-locked lasers to attain tunable spectral reach from ultraviolet to mid-infrared.

[1] Section 4.3-4.7 have appeared in Nature Communications 8, 13922, 2017

[2] Silicon dioxide has transmission window in wavelength from 200 nm to 2 micron. Furthermore, material dispersion is relatively low compared to other chip-based materials[143], so this platform has an advantage to apply nonlinear cavity study (chapter 3) to the broad transmission window (discussion with Prof. Harry Atwater). This chapter only shows the waveguide results, but after then this work was extended over visible soliton generation in nonlinear cavities[143].

4.2 Introduction to on-chip nanophotonic waveguides for nonlinear optics

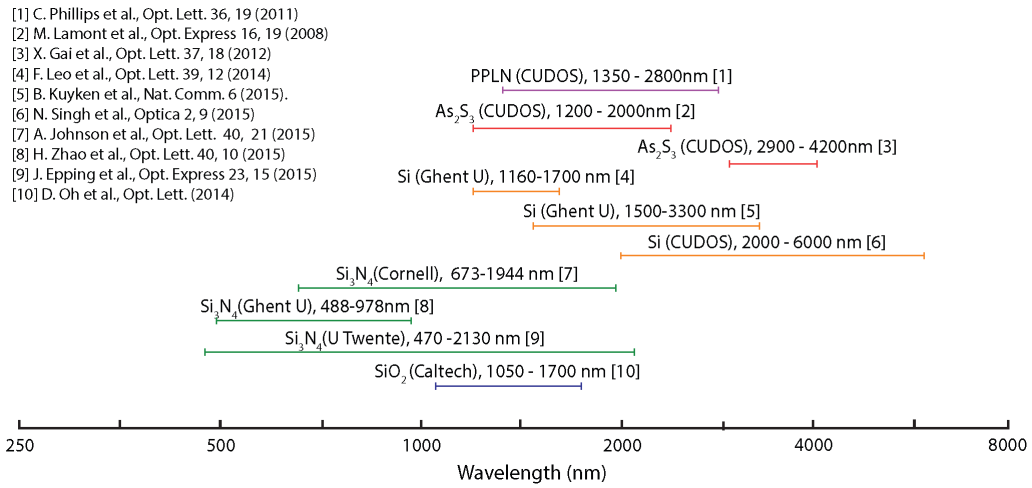

Figure 4.1: **Review of on-chip nanophotonic waveguides for nonlinear optics** State-of-the-art nanophotonic waveguide comparison of spectral coverage. Waveguide platforms in PPLN[145], As_2S_3[146, 147], Si[148–150], Si_3N_4[151–153], and SiO_2[154] are presented, and the spectral coverages are from visible to several microns wavelength.

Continuum generation in optical fiber[68] has been actively investigated for the applications in optical frequency combs[39, 56] as well as spectroscopy and optical coherence tomography. The advent of microcomb has focused attention on this technology for on-chip system. Beginning with studies of Raman and four-wave-mixing in monolithic waveguides[10, 155], numerous material platforms has been investigated towards low-threshold, broadband supercontinuum generation[145–154]. Low threshold power for efficient broadening have been demonstrated with nano-scale waveguide cross sections[153, 156]; the device also operates in the mid-infrared[149, 157]; the self-referencing has been achieved using silicon nitride waveguide[158]. Fig.4.1 shows the nanophotonic waveguides from various material platform in the spectral domain. PPLN, As_2S_3, and silicon have been generally used for mid-infrared wavelengths while nitride and silica have been used for relatively shorter wavelength (from visible to infrared wavelengths).

4.3 Ridge waveguide dispersion design

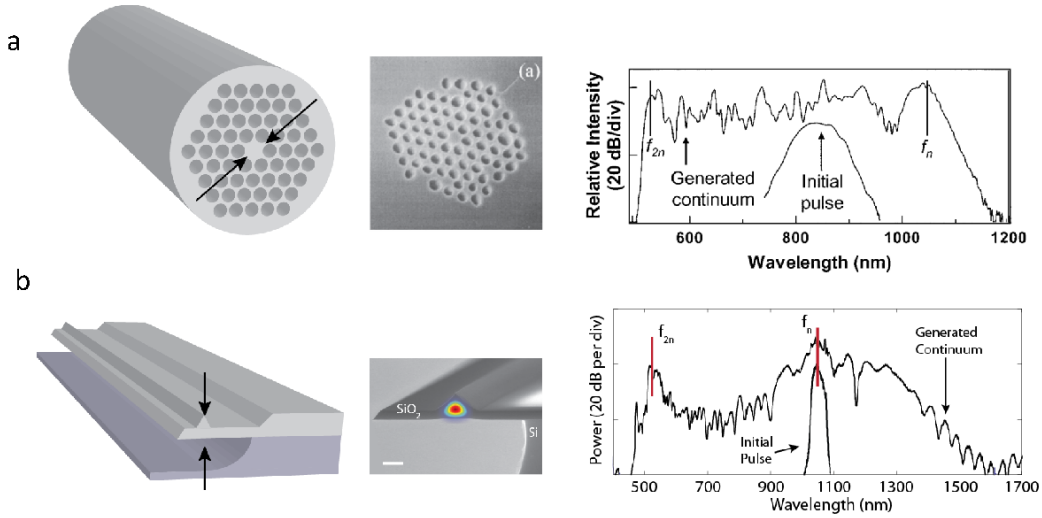

Figure 4.2: **Pulse broadening in photonic crystal fiber and analogous approach on-a-chip** (**a**) The schematic illustration of photonic crystal fiber with SEM image of cross section. The core defined by surrounding holes confines the optical mode for propagation. The control of core area allows dispersion control from visible to mid infrared, so as to achieve octave span supercontinuum which enable self-referencing of frequency comb. (**b**) The core size control in photonic crystal fiber is analogous to ridge size control in chip-integrated waveguide. The nanophotonic waveguide can function as photonic crystal fiber in self-referenced comb. The SEM image in **a** is from Ranka, et al.[68] ; the optical spectrum in **a** is from Jones, et al.[39]; SEM and the optical spectrum in **b** are edited from Oh, et al.[72].

Fig.4.2a shows the schematic illustration of photonic crystal fiber structure with cross-sectional SEM image[68], and one of the applications used for spectral broadening in frequency comb self-referencing[39, 56]. The photonic crystal fiber leveraged enhanced nonlinearity and controlled dispersion properties by modifying the optical mode confinement in core structure. The near-infrared input pulse was thereby spectrally broadened, so the comb lines cover from visible to mid-infrared wavelengths. Supercontinuum generation has been widely developed from deep ultraviolet to mid-infrared, and specifically ultraviolet and visible wavelength covers several optical clock transition lines[58] as well as the optical sources for biomedical imaging[159]. There has been remarkable progress on visible and ultraviolet continuum generation in microstructured optical fibers[160–164].

Fig.4.2b shows analogous approach in chip-integrated waveguide platform. As the size of fiber core engineered the mode confinement as well as dispersion, the silica ridge dimension can tailor the mode area and chromatic dispersion. The SEM image and optical spectrum will be introduced in following discussions, and those are for presenting the feasibility of the analogous approach.

4.3.1 Geometric dispersion control – principle

As discussed, the photonic crystal fiber compensates significant amount of material dispersion at visible wavelength using strong modal confinement[68] – the core primarily confines the optical mode[3], and air acts as cladding layer in this device. In strongly confined waveguide structure, the optical mode easily transitions from the core to the cladding layer and larger index contrast requires smaller core layer radius (see egn.4.1):

$$V = k_0 a (n_1^2 - n_c^2)^{1/2} \tag{4.1}$$

Here, V is normalized frequency parameter of fiber (called as "V number"), a is a radius of the core layer, n_1 is the refractive index of the core layer, and n_c is the refractive index of the cladding layer[23]. This equation comes from the eigenmode equation in step-index fiber and defines the single mode condition ($V = V_c = 2.405$) as below:

$$2a = 2 \times \frac{V_c}{(n_1^2 - n_c^2)^{1/2}} \times \frac{\lambda}{2\pi} \approx 0.76\lambda \tag{4.2}$$

n_1 is 1.45 (silica) and n_c is 1.0 (air) for the approximation in this equation. The core diameter needs to be proportional to the wavelength where we want to make a modal transition between the core and the cladding layer. The core of photonic crystal fiber needs to be tiny in order to drag the cut-off frequency around shorter wavelength (visible), and the index contrast needs to be maximized in order to compensate stronger material dispersion at shorter wavelength. It is worth reviewing the equation of the group index in order to see how the geometric dispersion collaborates with the modal transition[23]:

$$n_g = n_{eff} + \omega \frac{dn_{eff}}{d\omega} \tag{4.3}$$

Here n_g, n_{eff}, and ω are the group index, effective index, and frequency. At the modal transition wavelength, strong index contrast produces rapid effective index changes as a function of frequency ($\frac{dn_{eff}}{d\omega}$), and the second term on the right hand side has positive sign as n_{eff} decreases. When the contribution of the second term is larger than n_{eff} decrease, then the total dispersion becomes anomalous. Fig.4.3 shows the geometric dispersion of a step-index fiber, and the geometric dispersion is anomalous once the modal transition occurs (the transition wavelength scales proportional with the core diameter).

It is also worth discussing the multi-wedge dispersion design[71] using eqn.4.1. In contrast to the photonic crystal fiber, the index contrast in multi-wedge resonator (or multi-cladding

[3] Here we will only consider fundamental mode (TE_{00} or TM_{00}).

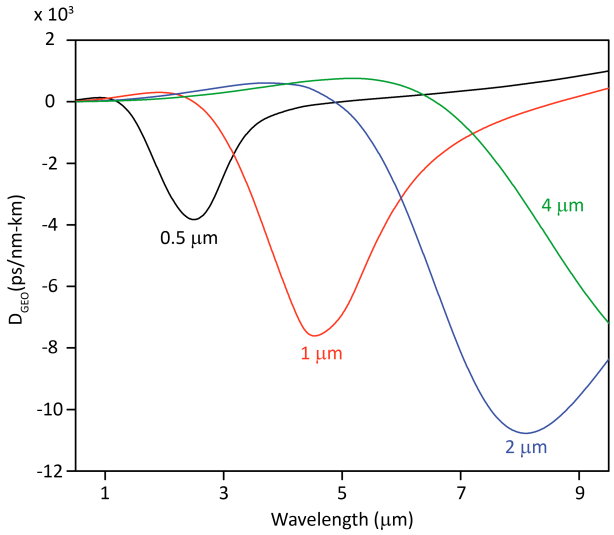

Figure 4.3: **Geometric dispersion versus core diameter** Numerical simulation of the step-index fiber geometric dispersion as a function of core diameter. Here the cladding layer is air (n = 1), and the core layer is fused silica[23]. As core diameter increases, the cut-off wavelength increases and the maximum geometric dispersion wavelength increases.

fiber) is comparably small (generally < 1%), so that the required core diameter doesn't need to be small (weaker modal confinement) in order to make the mode transition between the core and the cladding. In addition, the additional geometric dispersion is not strong as the index contrast is smaller, so the multi-wedge dispersion design was thereby used to tailor the chromatic dispersion at the wavelength where the material dispersion isn't too strong.

In the next subsection (4.3.2), we will discuss numerical simulation of silica ridge dispersion. The silica ridge structure has thickness around 600 - 900 nm (triangular shape with angle of 30 - 45 °) in order to confine an optical wave strongly. The ridge structure can be microfabricated as shown in the next section (4.4), and the design will show the feasibility to control zero dispersion wavelength as well as dispersive wave frequencies.

4.3.2 Geometric dispersion control – numerical analysis

Fig.4.4 shows numerical simulation of ridge waveguide dispersion. As has been discussed in previous section, the optical mode transitions from the waveguide core to the air cladding as wavelength increases. Because the group index mismatch between waveguide core and air cladding is relatively high[4], the mode transition creates significant amount of geometric dispersion and the sign of the geometric dispersion is anomalous at the beginning of the transition (then goes to strong normal geometric dispersion).

In this thesis, the nanophotonic waveguide is designed to generate supercontinuum from

[4]Generally fiber has approximately 1 % index difference between core and cladding.

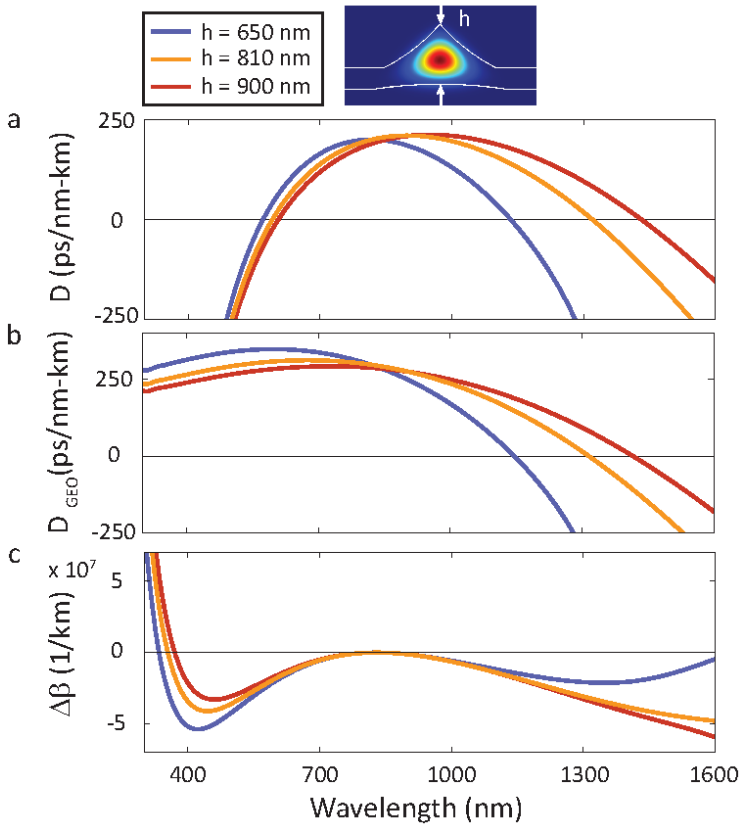

Figure 4.4: **Geometric dispersion control in ridge waveguide structure** (**a**) Numerical simulation of ridge waveguide total dispersion. The ridge thicknesses ("h") of 650, 810, and 900 nm were calculated, and the inset depicts the calculated ridge structure. The sidewall angles are approximately 30°. (**b**) Calculated geometric dispersion of ridge waveguide structure. (**c**) Calculated phase matching parameter $\Delta\beta = \beta(\omega) - \beta(\omega_s) - (\omega - \omega_s)/v_g$ where ω_s corresponds to the center frequency of input pulse in section 4.5 (830 nm), v_g is group velocity at ω_s. $\Delta\beta \approx 0$ corresponds to the phase matching condition for dispersive wave generation[72].

830 nm pump and therefore the total dispersion at 830 nm needs to be anomalous. However, the material dispersion is strongly normal at the wavelength regime[23], and the geometric dispersion control using strong confinement waveguide needs to be used in order to form comparable geometric dispersion[5]. As predicted in previous discussion, the optical mode (from the waveguide to air cladding) transitions in shorter wavelength as waveguide dimension decreases (from h = 650 nm to h = 900 nm). Then the anomalous geometric dispersion is induced by the mode transition in shorter wavelength, and the additional geometric dispersion can compensate the normal material dispersion in shorter wavelength. Therefore, the zero dispersion wavelength becomes shorter as the ridge thickness decreases (see Fig.4.4a).

[5]Multiple wedge structure in previous chapter can also adjust the dispersion property of nanophotonic waveguides[71], however the total amount of geometric dispersion is only comparable with the one from mode transition between 1 % index difference and might not be strong enough in shorter wavelength (< 1 micron).

In order to discuss the contribution from the waveguide geometry more precisely, Fig.4.4b shows calculated geometric dispersion of ridge waveguide structures. The geometric dispersion is given as the subtraction of the material dispersion[23, 128] from the total dispersion (Fig.4.4a), and it is interesting to note that the geometric dispersion transitions from anomalous to normal dispersion as wavelength increases. In addition, the maximum geometric dispersion is induced at shorter wavelength as the waveguide geometry confines the optical mode stronger; the magnitude of the geometric dispersion is also dependent on the waveguide dimension.

The waveguide dispersion control modifies not only zero dispersion wavelength but also the phase-matching condition of dispersive wave generation. The dispersive wave frequency can be thereby controlled using waveguide dimension. As has been discussed in Chapter 1, the phase-matching condition of dispersive wave generation is:

$$\begin{aligned} \phi(\omega_s, z) &= \phi(\omega_{DW}, z) \\ \omega_s t - \beta(\omega_s) z + \gamma P z/2 &= \omega_{DW} t - \beta(\omega_{DW}) z \end{aligned} \tag{4.4}$$

4.4 Ridge waveguide fabrication process

4.4.1 Overview of process flow

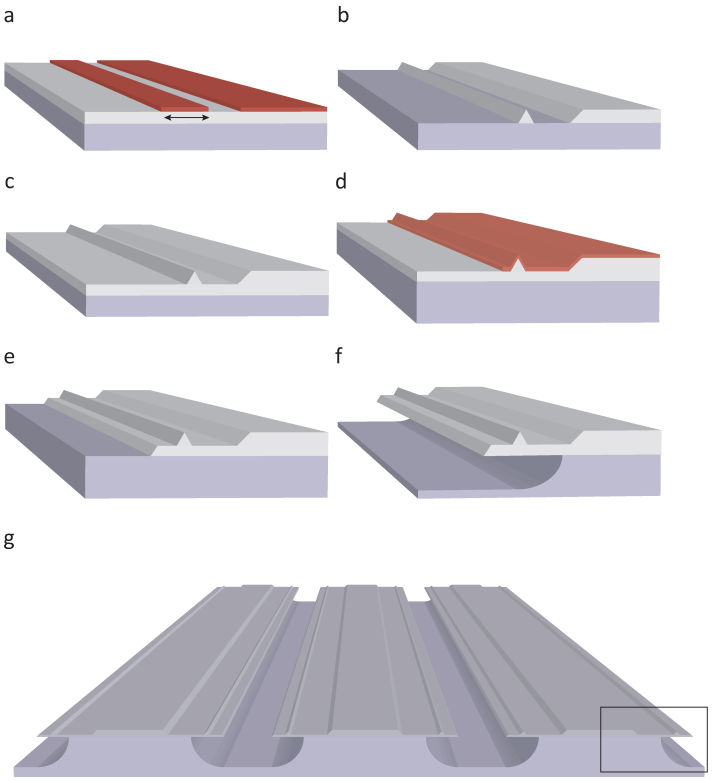

Figure 4.5: **Microfabrication process of ridge waveguide structure and schematic illustrationi of ridge waveguide arrays** (**a - f**) Microfabrication process flow of waveguide arrays on a chip. (**a**) First the waveguide pattern (arrow indicates the mask width on Fig.4.7) is defined in the oxide layer of an oxidized silicon wafer by photolithography and (**b**) HF wet-etching. (**c**) Additional oxide layer is grown by thermal oxidation, and the supporting structure is patterned by (**d**) photolithography (**e**) and HF wet-etching. (**f**) Isotropic silicon etch is applied as a final step. (**g**) Schematic of ridge waveguide arrays. This figure is from Oh, et al.[72].

Waveguide arrays are fabricated on (100) prime-grade float-zone silicon wafers. The initial oxide layer is thermally grown at 1000 °C with 2 μm thickness. The photoresist is patterned on the oxide layer (Fig.4.5a), and acts as etch mask during hydrofluoric acid (HF) immersion. HF wet-etching creates the wedge surfaces at the edge of the photoresist pattern, and the further wet-etching results in the triangular-cross-section ridge stripe of silica as the two angled wedge surfaces meet each other (Fig.4.5b). The wet-etching duration is around 45 min. Then, an additional thermal oxidation creates an under-layer of silica (Fig.4.5c). The waveguide chips used for data in the manuscript had the under-layer thickness of either 310 nm or 450 nm. Striped openings (Fig.4.5d) are etched after a second lithography step (Fig.4.5e). As a final step, silicon under oxide structure is isotropically etched to lower scat-

tering of fundamental guided mode by silicon structure to levels below that caused by silica surface scattering (Fig.4.5f). Both numerical calculation[6] and measurement confirmed that an undercut of 10 μm is sufficient to eliminate the silicon structure interaction as a result of modal confinement. The average spacing between two waveguides is about 35 μm, and 725 waveguides per inch can be fabricated in an array.

4.4.2 Lithographic ridge dimension control

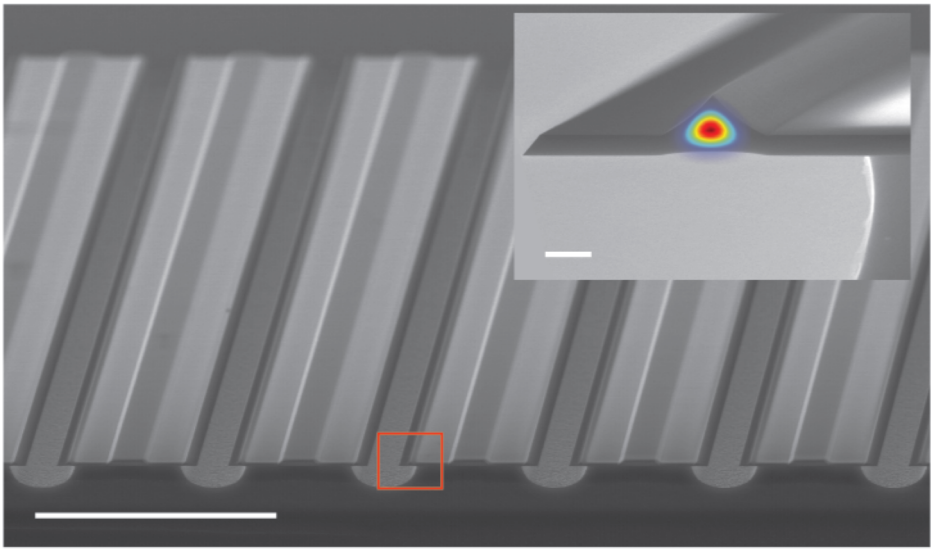

Figure 4.6: **Fabricated ridge waveguide array** Perspective view of SEM image of fabricated ridge waveguide array on-a-chip (bar: 100 μm). The average spacing between two waveguides is about 35 μm and it corresponds to 725 waveguide per inch. The inset shows zoom-in cross section of ridge waveguide (bar: 1 μm). Simulated mode profile is superimposed on the cross section image (wavelength = 830 nm). This image is edited from Oh, et al.[72].

Fig.4.6 shows the SEM image of fabricated ridge waveguide array on silicon chip. The average spacing between two waveguides is about 35 μm, so 725 waveguides can be fabricated within one inch. Also high resolution zoom-in scan is shows as inset, and red box is indicated the zoom-in position. Ridge structure is confined on the thin supporting layer, and the supporting layer is holding the ridge structure from silicon pillar with 10 μm undercut. The calculated optical mode profile is superimposed on the cross-section image.

The ability to lithographically define ridge dimension enables precise control of waveguide dispersion, and it allows a tunability on dispersive wave frequencies. Fig.4.7 shows the dependence of the ridge dimension parameters(H,w) on the mask width. Here, the mask width is the width of the red rectangular strip patterned on photoresist in Fig. 4.5a (see

[6]The numerical calculation will be discussed in following section.

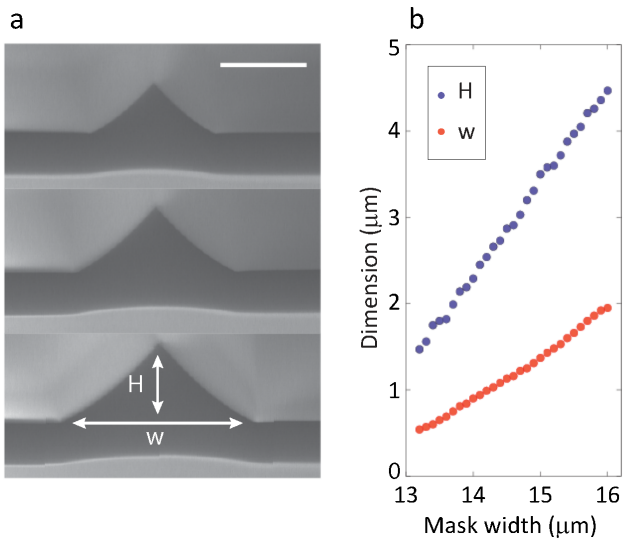

Figure 4.7: **Dependence of ridge dimension on mask width** (**a**) SEM images of a series of ridges in a fabricated silica waveguide array. The thickness of the base silica layer is 0.31 μm. Scale bar is 1μm. The definition of ridge height(H) and ridge width(w) is shown in the panel. (**b**) Measured ridge dimension based on SEM images as a function of mask width

arrow). The ridge height (H) and width (w) increase by about 0.5 μm and 1 μm, respectively, as the mask width increases by 1 μm.

4.4.3 Transmission loss characterization

In order to characterize the transmission loss of ridge waveguide structure, the Q factors of ridge resonator with the same waveguide dimension were measured (mode area $\approx$ 2.5 μm^2). Low-loss waveguide device requires longer waveguide length for apparent attenuation through the propagation[165]. Otherwise, the extra losses are caused from experiment (i.e. waveguide input coupling loss, facet reflection) and the waveguide attenuation might not be clear enough to measure. In contrast, resonator doesn't require longer propagation length as long as cross-section dimensions are same. The extra losses involved from the experiment is also negligible as taper fiber coupling caused minimal scattering loss[83].

Not clear in this thesis, but it is also worth discussing the possible differences between straight waveguide and ring resonator. There might be distinct optical properties caused by waveguide bending, because resonator has to experience stronger bending loss (few mm radius) than the waveguide (infinite radius). Furthermore, the centroid of the motion would shift towards outer radial direction as a result of the bending effect, and the greater portion of spatial mode experiences surface roughness from outward sidewall while experiencing less scattering from inwards sidewall as well as silicon pillar structure.

Fig.4.8b shows transmission scan of TE1 mode at 772 nm wavelength, and the mode

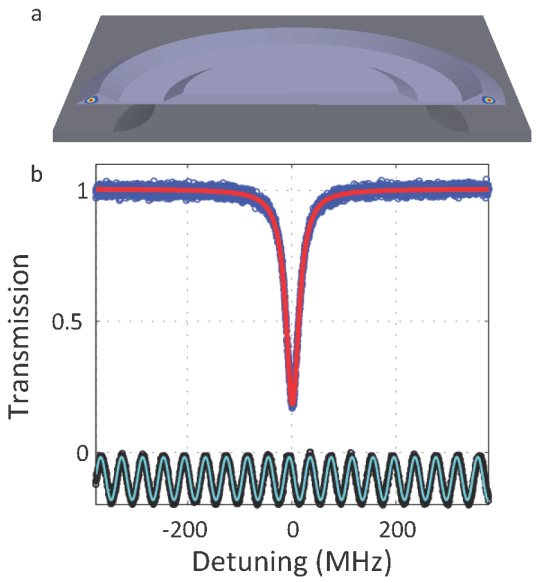

Figure 4.8: **Ridge waveguide transmission loss characterization** (**a**) Schematic illustration of ridge ring resonator in order to characterize transmission loss of waveguide. (**b**) Zoom-in spectral scan of TE fundamental mode (measured wavelength = 772 nm). The scanning wavelength is calibrated using fiber interferometer (black dots: measured interferometer signal; green: fitted sinusoidal curve). The resonance dip in transmission spectrum is fitted with Lorentzian curve. Intrinsic Q factor is 18 million, and it corresponds to 0.028 dB/cm propagation loss.

families were identified by comparing the mode spectrum with numerical simulation. The scanning frequency was calibrated using fiber interferometer at 772 nm wavelength, and fitted Lorentzian gives an intrinsic Q factor as high as 18 million. This Q factor corresponds to 0.028 dB/cm, and the length of the waveguide can be extended over few meters (loss will still be < 10 dB).

4.5 Dispersive wave generation in silica ridge waveguide

4.5.1 Lithographic control of dispersive wave frequency

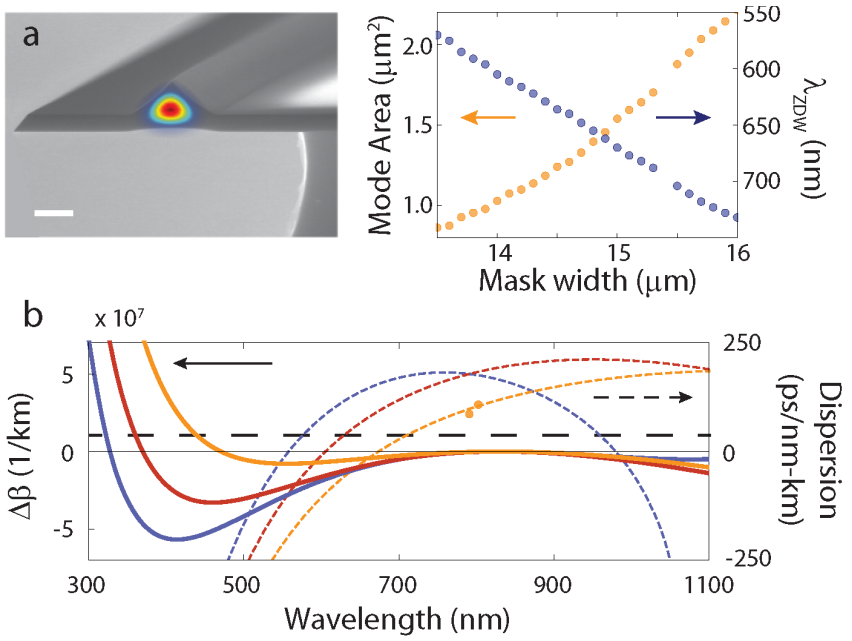

Figure 4.9: **Lithographic control of waveguide dispersion and phase matching parameter for dispersive wave generation** (**a**) SEM images of a cross section of silica ridge waveguide. The calculated mode profile of the TM mode at 830 nm is superimposed on the cross section. The thickness of the base silica layer is 0.31 μm. Scale bar is 1μm. In the right panel, calculated mode area and zero dispersion wavelength (λ_{zero}) are plotted versus mask width.(**b**) Calculated GVD (dashed lines) and phase matching parameter $\Delta\beta$ (solid lines) for dispersive wave generation in TM fundamental mode. This figure is edited from Oh et al.[72].

The phase matching condition for the dispersive wave generation satisfies the following equation[44]:

$$\begin{aligned} \phi(\omega_s, z) &= \phi(\omega_{DW}, z) \\ \omega_s t - \beta(\omega_s) z + \gamma P z/2 &= \omega_{DW} t - \beta(\omega_{DW}) z \end{aligned} \tag{4.5}$$

where $\beta(\omega_s)$ and $\beta(\omega_{DW})$ are the propagation constant at the pump soliton frequency (ω_s) and the dispersive wave frequency (ω_{DW}); P is the peak power of the pulse once dispersive wave is generated; γ is the nonlinearity of the waveguide at pump frequency ($\gamma = \omega_p n_2/(cA_{eff})$); t and z are travel time and length from the waveguide input to the point that dispersive wave is generated and group velocity is $v_g = z/t$. Here we define $\Delta\beta(\omega) = \beta(\omega) - \beta(\omega_s) - (\omega - \omega_s)/v_g$, and the dispersive wave phase matching condition

is given by $\Delta\beta(\omega_{DW}) = \gamma P/2$. The following equation expresses $\Delta\beta$ in terms of dispersion parameters and frequencies:

$$\Delta\beta(\omega) = \frac{\beta_2}{2}(\omega - \omega_s)^2 + \frac{\beta_3}{6}(\omega - \omega_s)^3 + \frac{\beta_4}{24}(\omega - \omega_s)^4 \tag{4.6}$$

In general, we can approximately find the dispersive wave frequency at $\Delta\beta(\omega) = 0$ as $\gamma P/2$ is negligible compared to dispersion terms. Then we can obtain the dispersive wave frequency[7] as:

$$\omega_{DW} = \omega_s - \frac{2\beta_3}{\beta_4} \pm \sqrt{(\frac{2\beta_3}{\beta_4})^2 - \frac{12\beta_2}{\beta_4}} \tag{4.7}$$

If we neglect β_4, then we can obtain:

$$\omega_{DW} = \omega_s - \frac{3\beta_2}{\beta_3} \tag{4.8}$$

Fig.4.9 shows lithographic dispersion control of ridge resonator and the phase matching condition for dispersive wave generation. As has been discussed, the ridge geometry adjusts the confinement of optical mode and consequently shifts group velocity dispersion in shorter wavelength ($\lambda <$ 700 nm). The ridge dimension (height and width) can be modified using lithographic mask width (cf. Fig.4.9b), and the calculated zero dispersion wavelengths (λ_{ZDW}) varies from 550 nm to 750 nm in TM polarization. Fig.4.9b presents calculated GVD and $\Delta\beta$ in ridge waveguide structure. Blue, red, and yellow lines correspond to mode areas of 0.83, 1.03, 1.69 μm^2; Solid line presents $\Delta\beta$ and dashed line indicates GVD. The effective mode area were determined by input of SEM waveguide cross sections to finite-element-method solver. The points with error bars are measured dispersion values obtained from sets of ten scans of spectral fringes measured using a Mach-Zehnder interferometer. The measurement plots show close agreement with numerical simulation results. In addition, it is interesting to note that GVD becomes larger at pump frequency in smaller ridge mode area (ridge height and width decreases) and dispersive wave frequency shifts blue. As the pump wavelength of 830 nm, the phase matching wavelength can be engineered to vary from 310 to 576 nm in TM polarization – TE mode also provides dispersive wave generation at longer wavelength.

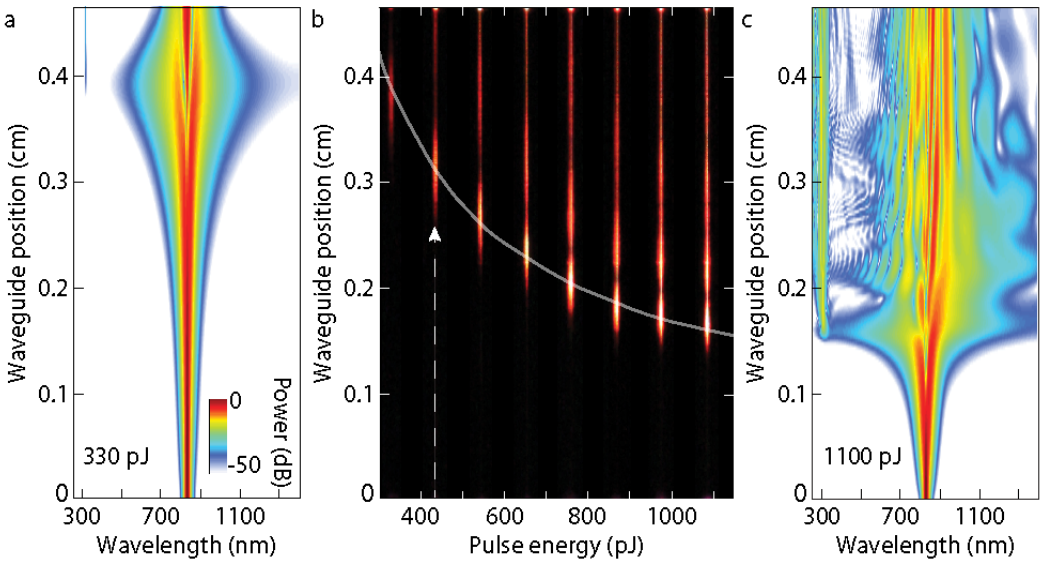

Figure 4.10: **Numerical simulation of pulse propagation in the waveguide** (**a**) Calculated supercontinuum spectra as a function of waveguide position. The TM-polarized pulse is launched into waveguide with 0.76 μm^2 mode area, and the coupled power is 330 pJ. (**b**) Photograph (Top view) of scattered light from the waveguide. The pulse energies ranging 330 to 1100 pJ (left to right) were launched and the pulse travels in the waveguide from the bottom to the top of the image (indicated by the dashed line with arrow). The grey line indicates the length at which dispersive wave generation occurs as predicted by numerical simulation. (**c**) Calculated supercontinuum spectra at a pulse energy og 1100 pJ. **a-c** are edited from Oh et al.[72].

4.5.2 Numerical analysis of pulse propagation and dispersive wave generation in ridge waveguides

As discussed in Chapter 1, numerical calculation of the pulse propagation in the optical media were performed using a nonlinear Schrodinger equation as below:

$$\begin{aligned}\frac{\partial \tilde{A}}{\partial z} = &\left(i(\beta(\omega)-\beta(\omega_p)-\frac{1}{v_g}[\omega-\omega_p])-\frac{\alpha(\omega)}{2}\right)\tilde{A}(z,\omega)\\ &+i\bar{\gamma}(\omega)\mathcal{F}\{\bar{A}(z,T)\int_{-\infty}^{\infty}R(T')|\bar{A}(z,T-T')|^2dT'\}\end{aligned} \tag{4.9}$$

where $\tilde{A}(z,\omega)$ is the complex spectral envelope of the pulse as a function of waveguide position z and frequency (ω), $\bar{A}(z,T)$ is defined as $\mathcal{F}^{-1}\{\tilde{A}(z,\omega)/A_{eff}^{1/4}(\omega)\}$, $\alpha(\omega)$ is the linear loss, and R(T) is the Raman response function. $\bar{\gamma}(\omega)$ is the parameter related to the nonlinear response[40, 41]:

[7] It was also discussed in Ref.[43] for dispersive wave generation in microcavity.

$$\bar{\gamma}(\omega) = \frac{n_2(\omega_0)n_0\omega}{cn_{eff}(\omega)A_{eff}^{1/4}(\omega)} \tag{4.10}$$

The propagation constant ($\beta(\omega)$), effective mode index ($n_{eff}(\omega)$), and mode area (A_{eff}) were calcualted from finite-element-simulation; $n_2(\omega_0)$ is the nonlinear refractive index.

Fig.4.10a and c are the calculated supercontinuumm spectra plotted versus propagation length for pulse energies of 330 pJ (a) and 1100 pJ (c). In the calculation, input pulse center wavelength is 830 nm, and the pulse width is 60 fs which is directly measured by an autocorrelator. The input pulse propagates as a higher-order soliton, and the dispersion of waveguide causes temporal compression and spectral broadening until the pulse experience soliton fission and dispersive wave generation at the fission length. According to numerical simulation, the fission length depends on the pulse energy and the fission length decreases as input pulse energy increases (330 pJ; 0.39 cm; 1100 pJ: 0.16 cm). This prediction is observable in Fig.4.10b. The composite of photographs of the waveguide is shown at coupled power from 330 pJ to 1100 pJ. The waveguide where pulse propagates is identical from the left to the right of the picture, and the mode area of the ridge structure is 0.76 μm^2 at pump wavelength (830 nm). It is also important to note that dispersive wavelength frequency is consistent in distinct pulse energies at the same mode area. This is because $\gamma P/2$ term in phase matching condition is almost negligible comparing to the scale of dispersion changes. Thus, the dispersive wave frequencies at soliton fission point are thereby controllable using resonator geometry which dominantly mediates the mode area and dispersion condition.

4.5.3 Dispersive wave generation in ridge waveguide

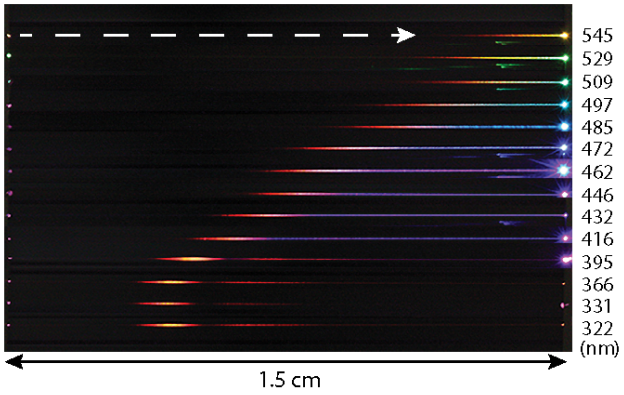

Figure 4.11: **Ultraviolet-visible dispersive wave generation in a silicon chip** Multiple photographs of scattered light taken from 1.5 cm long chip. Infrared pulses are launched at the left side facet, and the initial spectral broadening can be seen as the orange-red emission. This figure is edited from Oh et al.[72].

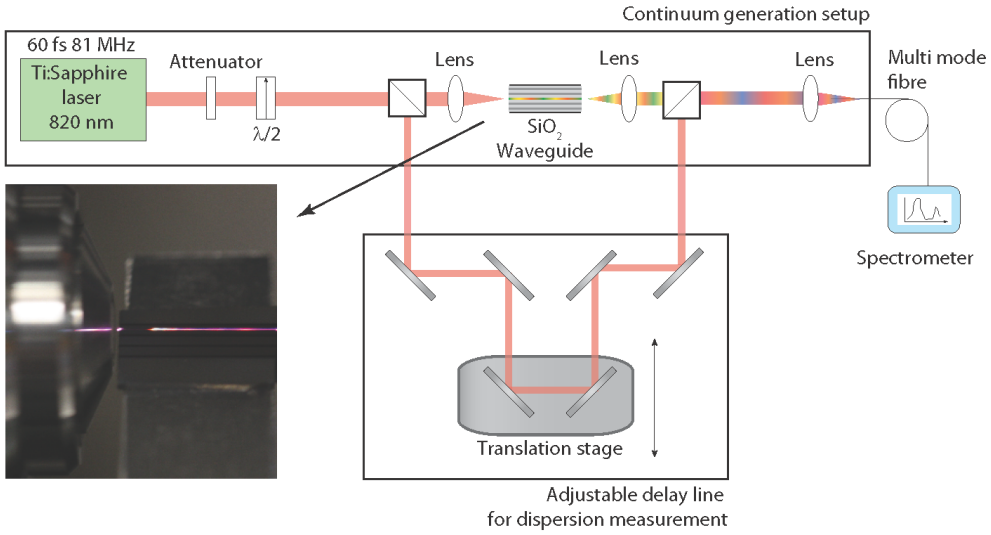

Figure 4.12: **Experimental setup for supercontinuum generation and waveguide dispersion measurement** (**a**) SEM images of a series of ridges in a fabricated silica waveguide array. The thickness of the base silica layer is 0.31 μm. Scale bar is 1μm. The definition of ridge height(H) and ridge width(w) is shown in the panel. (**b**) Measured ridge dimension based on SEM images as a function of mask width

Fig.4.11 shows the combined photographs of pumped ridge waveguide on a single chip. The laser pulse is provided by a mode-locked titanium-sapphire laser (830 nm) and the input is launched into the ridge waveguide using an objective lens. The average coupling efficiency is estimated to be 25 - 35 %. As input pulse propagates along the waveguide from the left to the right (arrow), the infrared pulse undergoes temporal compression and spectral broadening as a result of self-phase modulation and anomalous dispersion of the guide[23]. At the broadening position, soliton fission and dispersive wave generation occur at a bright spot on the figure (shown as the orange-red emission that gradually shifts diagonally upward right). As has been discussed, decreasing mode areas[8] shift the phase matching condition to shorter wavelength so the dispersive wave transitions from the visible wavelength to ultraviolet from the top to the bottom waveguide – the dispersive wave is invisible in the photograph for wavelengths below 400 nm. The colour emission at the left side of the image is the dispersive wave emission which is reflected at the right facet of the guide, and the majority of the light is forward propagating and collected into a multimode fiber.

To further probe the behavior of the dispersive wave generation, the spectral measurements were performed at varying waveguide cross section area (Fig.4.13a) as well as launched input power (Fig.4.13b). For the measurement, the titanium sapphire laser (830 nm pump, 60 fs pulse width, 81 MHz repetition rate) launched the pulse into waveguide input facet

[8] 332 nm emission has 0.83 μm^2 while 545 nm emission has area of 2.09 μm^2.

using objective lens. The experimental setup included an attenuator and a half-wave plate to control the input pulse energy and polarization. The light output is endfire coupled to multimode fiber, and the coupled light was analyzed using a Yokogawa OSA (AQ6370D, 600 - 1700 nm) and an Ocean Optics spectrometer (HR4000, 200 - 900 nm). The conversion of pump light in near infrared to either visible or ultraviolet wavelength is apparent in each spectrum, and the dispersive wave generation frequency varies from 310 to 515 nm in this figure.

Fig.4.14a shows measured supercontinuum spectra for TM and TE polarized mode launched into waveguides varying mode area at pump wavelength. Conversion light from 830 nm pulse to visible and ultraviolet wavelength dispersive waves is presented, and the corresponding mode areas are indicated on the panel (Red: TE, Blue: TM). Controlled tuning of the dispersive wave from 310 to 576 nm is demonstrated in TM polarized pulse and from 475 to 613 nm in TE polarized mode. In addition, Fig.4.14b shows the predicted dispersive wave frequencies using the phase matching condition with calculated dispersion from finite-element-simulation. The numerical prediction (solid line) shows close agreement with the measured frequencies (dots), and the tuning was recorded with an average 8 nm intervals.

4.5.4 Discussion on coherence of dispersive wave

The dispersive wave initially overlaps with the soliton pulse. However, the dispersive wave walks off from the soliton and is temporally stretched as it propagates in the waveguide. The

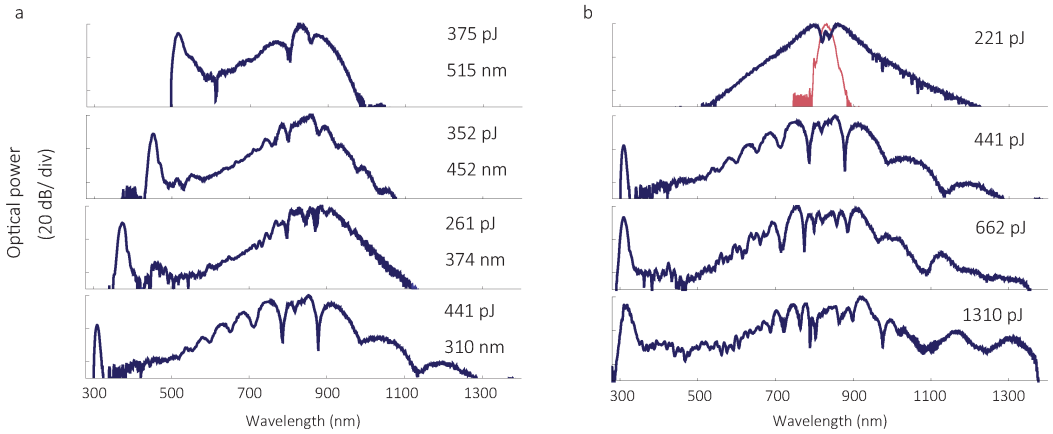

Figure 4.13: **Supercontinuum spectra for a series of dispersive wave frequencies and its power dependence** (**a**) Measured supercontinuum spectra for the TM mode at a series of dispersive wave generation frequencies: from top to bottom, 515, 452, 374, 310 nm. Here the spectra were taken for a pulse energy at the dispersive wave generation threshold (indicated in the panel). (**b**) Supercontinuum spectra for the TM mode at a series of launched powers: from top to bottom, 221, 441, 662, 1310 pJ (input coupling efficiency $\sim$ 26 - 27 %). As launched power increases, the supercontinuum spectra was flattened and extended from 300 nm to 1400 nm.

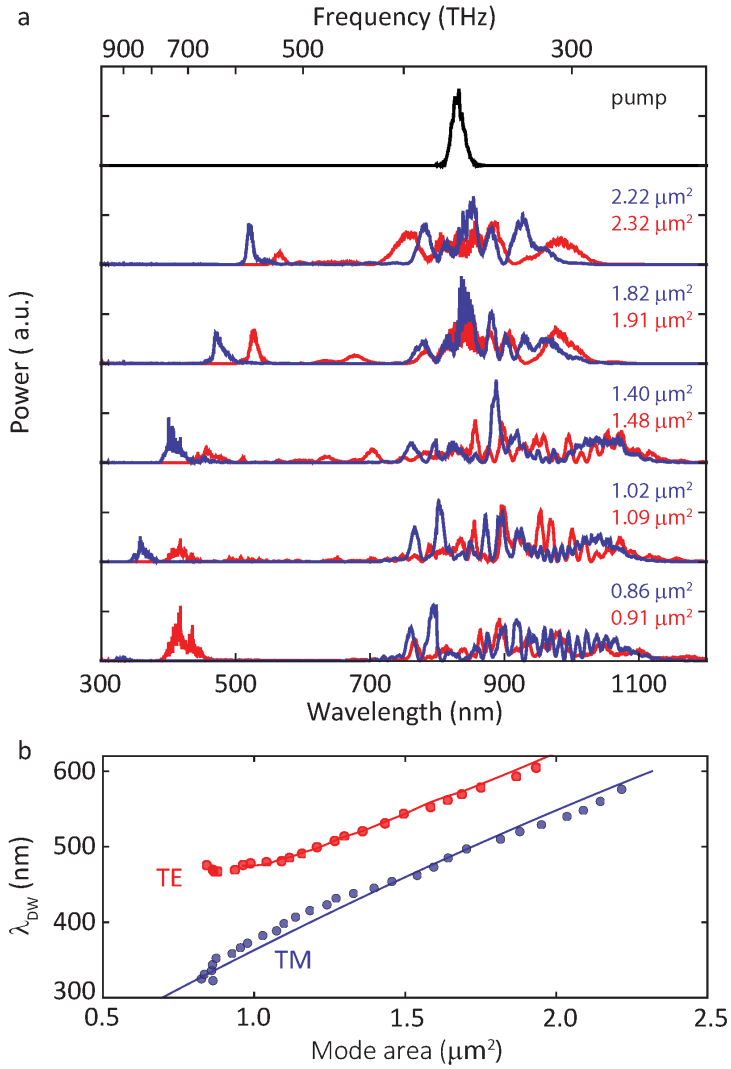

Figure 4.14: **Controlled tuning of the dispersive wave using ridge waveguide dimension** (**a**) Measured supercontinuum spectra for a series of ridge waveguides on a single waveguide array (with distinct ridge cross section dimension). The coupled pulse energy is 1000 pJ, and the wavelength is 830 nm. The mode area of the waveguide is indicated in the panel, and varies from 0.86 to 2.32 μm^2 by lithographic control. The supercontinuum spectra from both TE mode (red) and TM mode (blue) are measured. (**b**) Measured tuning of the dispersive wave peak wavelength (λ_{DW}). The data are taken for a pulse energy at dispersive wave generation threshold, and the solid lines are from phase matching condition obtained from finite-element-simulation. This figure is edited from Oh, et al.[72].

walk-off is from group velocity mismatch, and the stretch is from normal dispersion at dispersive wave frequency. Fig.4.15 shows the calculated spectrogram of the propagating pulse, and the launched power is 1100 pJ. As shown in **b**, the spectral components at dispersive wave frequencies has same temporal delay with soliton pulse and then the dispersive-wave pulse starts to walk off from the soliton pulse with continued propagation (**c**).

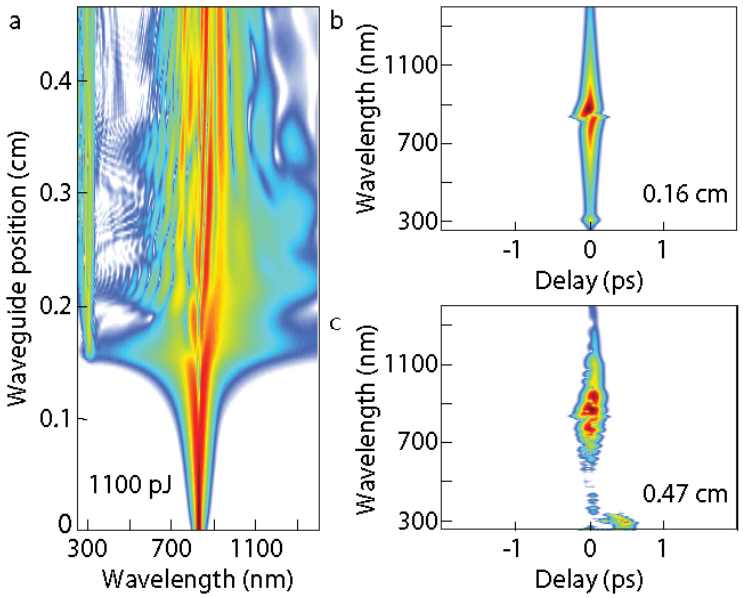

Figure 4.15: **Calculated spectrograms of the optical pulse propagating in the waveguide** (**a**) Calculated supercontinuum spectra as a function of propagation length at a pulse energy of 1100 pJ. This result is also presented in Fig.4.10c. (**b-c**) Calculated spectrogram of the optical pulse at waveguide position 0.16 cm (**b**; where dispersive wave is generated) and at waveguide output (**c**) This figure is edited from Oh, et al.[72].

4.6 Walk-off-free dispersive-wave-enhanced octave generation and self-referencing a Yb fiber laser frequency comb

Waveguide length can be adjusted to optimize the overlap between dispersive wave pulse and pump soliton mode, so as to simplify self-referencing setup that generally requires delay line to maximize the mode overlap. In addition, geometric dispersion control allows tuning dispersive wave pulse peak frequency with an average 8 nm interval, and the peak wavelength can vary from ultraviolet to visible using infrared pulse. Using the Yb fiber laser emission at 1064 nm (100 MHz repetition rate), it was possible to generate even deeper ultraviolet dispersive wave generation below 300 nm[72] – it was also consistent with numerical prediction on phase matching condition. The precise dispersive-wave engineering can be applied to simplify the setup for detection of the carrier-envelope offset frequency of Yb laser frequency comb[39, 56]. The waveguide has 3.13 μm^2 mode area at the pump wavelength, and the length is 1.5 cm. The dispersion of the ridge waveguide is engineered so as to generate dispersive wave at twice the frequency of the Yb laser pump. Then, the $f - 2f$ offset frequency generation[39, 56] of Yb fiber laser can be performed using the comb lines from pump and dispersive wave.

Fig.4.16a shows the experimental setup. Yb laser emits 90 fs pulses, and half-wave plate rotates the polarization (80 % TE and 20 % TM; total coupled pulse energy = 2300 pJ). The

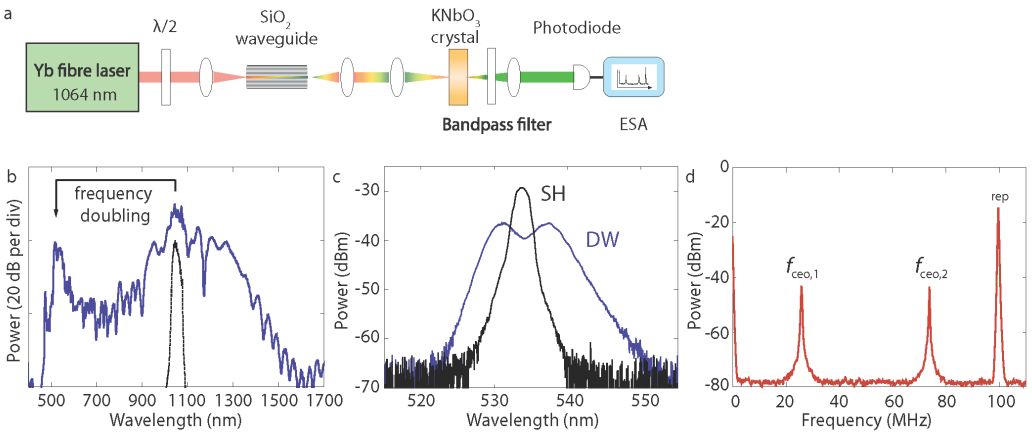

Figure 4.16: **Self-referencing a Yb fiber laser frequency comb** (**a**) Yb fiber laser is coupled to the ridge waveguide (mode area = 3.13 μm^2; length = 1.5 cm), and $KNbO_3$ crystal is used for frequency doubling. f_{ceo} is measured from ESA (electrical spectrum analyzer). (**b**) Measured optical spectrum of the collimated beam at the output facet of the waveguide. The input spectrum is shown in black, and the coupled pulse energy is 2300 pJ. (**c**) Spectra of dispersive wave (DW) and second harmonic light (SH) filtered by a bandpass filter. (**d**) RF spectrum measured with ESA (f_{rep}: pulse repetition rate; $f_{ceo,1}$, $f_{ceo,2}$: the carrier-envelope-offset beat frequency; resolution bandwidth: 300 kHz). This figure is from Oh, et al.[72].

TE wave creates the dispersive wave near 532 nm, and both polarization modes are coupled to $KNbO_3$ crystal where the TM wave is phase matched for second harmonic generation. The second harmonics are aligned with the TE polarized dispersive mode, so those two modes can make interference. The measured second harmonic spectrum and dispersive wave spectrum are shown in Fig.4.16c, and the two waves are mixed on a photodiode for offset frequency beatnote generation (**d**). $f_{ceo,1}$ = 25.8 MHz, $f_{ceo,2} = f_{rep} - f_{ceo,1}$ = 73.8MHz are shown, and the signal-to-noise ratio is over 34 dB at resolution bandwidth of 300 kHz. It is important to note that the coherence nature of dispersive wave is confirmed by the interference with second harmonic of pump laser, and the signal-to-noise ratio is sufficient for subsequent self-referenced servo control of the comb.

4.7 Discussion

Broadband supercontinuum generation can be one of good examples that we can discuss further in this section. The dispersive wave generally defines the shorter (or longer) wavelength boundary of supercontinuum spectral span, and the spectrum can grow as pulse propagates more. Fig.4.17 shows measured supercontinuum spectra in TE mode of the ridge waveguide. The mode area of the waveguide is 1.1 μm^2 at pump wavelength (830 nm), and the launched input power increases from the top to the bottom panels. As has been discussed in Fig.4.13, the pulse spectra at output facet shows the radiation of dispersive wave in the normal dis-

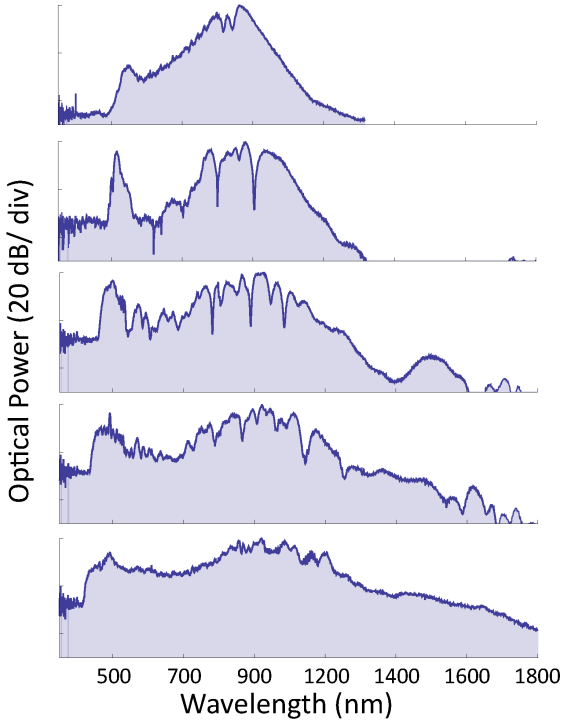

Figure 4.17: **Broadband supercontinuum generation in ridge waveguide** Measured supercontinuum spectra for a series of pulse energies. The mode area of the waveguide is 1.1 μm^2, and all the continuum spectra are measured from the same device. Dispersive wave was generated around 500 nm wavelength, and the supercontinuum spectra was broadened over a couple of octave.

persion regime with lower pump power. As the input pulse energy increases, the soliton fission length decreases and the supercontinuum spectra were broadened at the output facet. As shown in lower panel, the supercontinuum covers the spectral region from 500 nm over 1800 nm, which spans more than an octave.

Silica ridge waveguide platform can readily extend its waveguide length over few meters as shown in the attenuation measurement (section 4.4). The launched pulse starts to have a progression on nonlinear process as the pulse is propagating over nonlinear length $L_{NL} = \frac{1}{\gamma P}$ where γ and P are nonlinearity and peak power[23]. Thus, certain waveguide length determines minimum threshold power and the threshold power becomes lower as waveguide length increases (if the attenuation can be acceptable through the propagation length). Fig.4.18 shows supercontinuum generation in spiral ridge waveguide structure. As preliminary studies (the spiral waveguide lengths are approximately 40 - 60 cm), the pulse broadening started at the power level of 50 - 60 pJ and the octave span was achieved at the power level of 1 nJ.

Silica is a transparent material in wavelength from 200 nm to 2 microns (> 90 % trans-

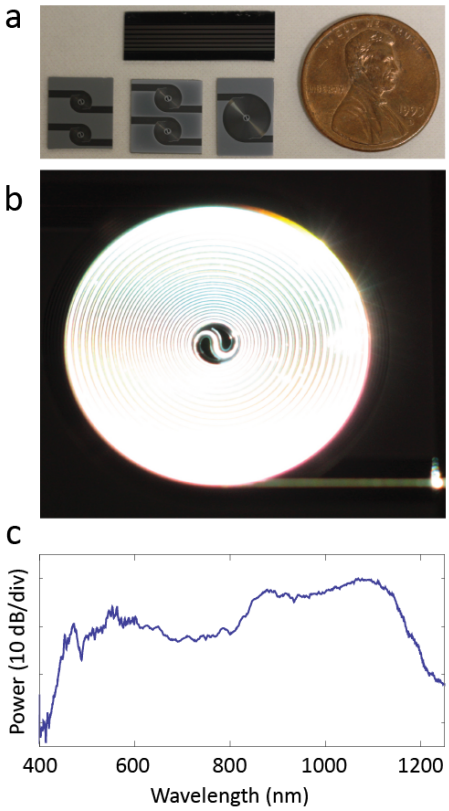

Figure 4.18: **Supercontinuum generation in spiral ridge waveguide** (**a**) Photograph of spiral ridge waveguide (Lower left: spiral waveguide, Upper left: straight waveguide) (**b**) Photograph of supercontinuum generation in spiral waveguide (**c**) Supercontinuum spectrum.

mission), therefore this material platform can provide versatile nonlinear devices in the transparent window. In this chapter, we demonstrated silica nanophotonic waveguide operation in short wavelength, so we experimentally proved the functionality of silica platform over the wavelength regime. Furthermore, the device engineering allows to compensate strong material dispersion, so demonstrated soliton broadening and dispersive wave generation which renewed the shortest wavelength record that chip-based waveguide have ever worked.

Chapter 5

INTEGRATED UHQ PHOTONIC RESONATOR PLATFORM

5.1 Abstract[1]

Optical microcavities[1] are compact, often chip-based devices, that are essential in technologies spanning frequency metrology[5, 13] to biosensing[166–168]. They have also enabled new science in quantum information[169] and cavity optomechanics[170]. Key performance metrics often scale as a function of cavity Q factor and the ultra-high-Q (UHQ) performance even can utilize new functionalities in wide applications. There have been several demonstrations of ultra-high-Q cavities, however the UHQ performance with monolithic integration hasn't been achieved yet in any place. An array of system-on-a-chip applications have recently emerged and the applications require the integrated UHQ performance[14, 171–173]. Here, we demonstrate a silicon-chip-based microcavity that combines high-Q performance with monolithic integration. Q factors over 200 million are achieved, and an integrable soliton microcomb having a detectable repetition rate is demonstrated.

[1] Section 5.2-5.6 have appeared in Arxiv 1702.05076, 2017. Section 5.7 has appeared in Arxiv 1708.05228.

5.2 Introduction to integrated high-Q resonators

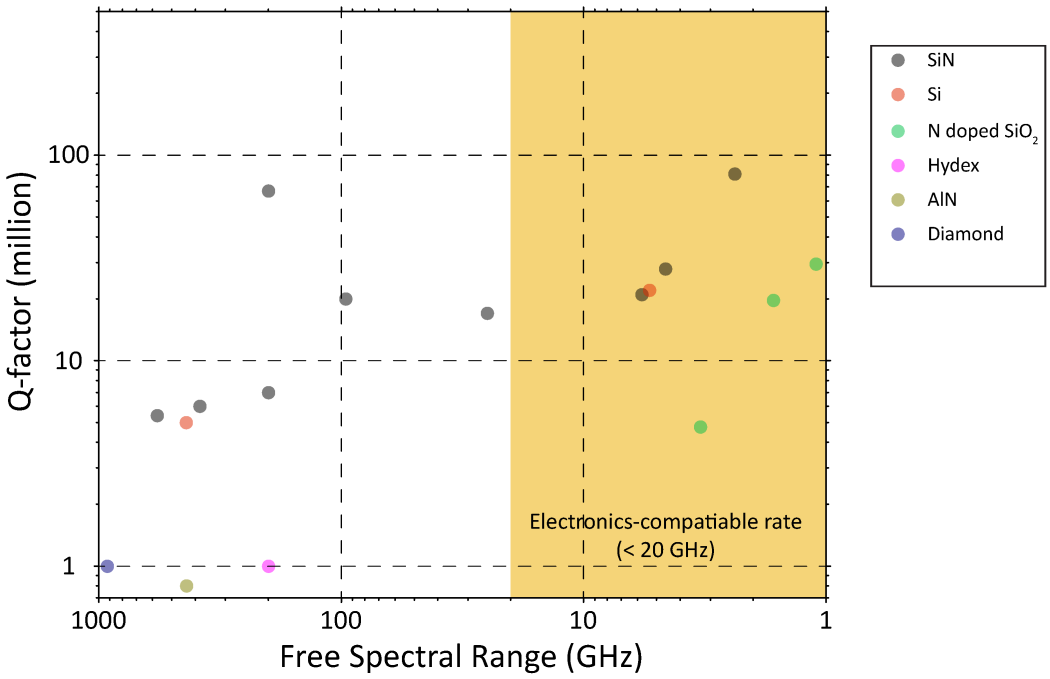

Figure 5.1: **Planar integrated resonator platforms and Q factor versus FSR of the resonators** The state of the art in planar integrated resonator performance. Q_0 are presented as a function of FSR, and the plots are from several platforms using SiN[4, 90, 91, 174–177], Si[178, 179], doped silica[180, 181], Hydex[94, 115], aluminum nitride[116], and diamond[12].

A monolithically integrated high-Q resonator can build the photonic system with lithographic method, and allow integration with other optical components in the liner optics[182–187]. Specifically, the high-Q resonators works for MHz-level narrow filters as well as oscillators with lower noise performance in the microwave frequencies[75, 187–189]. The coherent Doppler radars can be also benefit from the high Q performance, so the detection sensitivity on the moving targets can be improved[190].

In the nonlinear optics, boosted Q factor and small mode volume can enable wide range of applications. The high-Q resonators increased the Sagnac effect and boost sensitivity[191, 192] to achieve Earth-rotation-rate gyroscope. The soliton frequency comb can be generated using the Kerr effect of the optical media, and high Q resonator enables mW-level threshold[20, 50, 90, 91] and chip-compatible operating power[70, 193, 194]. Furthermore, stimulated Brillouin scattering can create low-threshold and narrow linewidth microlaser out of high-Q resonator[22, 195, 196].

Key performance metrics scale at least as 1/Q and frequently as $1/Q^2$ across all applications areas and there has been remarkable progress on boosting Q factor of chip-based microres-

onators. Recently several distinct material platforms were developed and enabled to build the optical system. Fig.5.1 shows the state of the art in planar integrated resonator performance, and the Q factors are displayed with FSR of resonator platforms.

Among these systems are those in inertial optical sensors[172, 191, 192] and microcomb-related applications[5]. The critical challenge is the need for centimeter-scale resonators required to either improve rotation sensitivity or to match mode-locking rates of the frequency comb with electronics bandwidths (generally < 20 GHz). The larger cavity mode volume requires higher pumping power, so high Q factors (> 10^8) are necessary to avoid impractically high pumping power. Chip-based ultra-high-Q (~ 875 million) silica resonators[22] were already discussed in Chapter 2. But still tapered fiber was only method[2] to couple the light into the device, and it is challenging to be fully-integrated.

5.3 Silica ridge resonator design & characterization

In this section, silica ridge resonator design will be discussed. The silica-only structure will be considered at this section, and the designed structure will feature planar integration, ultra-high-Q, and optimized mode spectrum.

5.3.1 Exterior ridge structure for planar integration

In silica exterior wedge disk (Fig.5.2a), silicon supports silica disk structure. The silicon undercut reduces coupling between optical mode (air-cladding) and silicon structure, and the silicon pillar makes silica disk mechanically stable. The optical mode is thereby supported in silica wedge disk with extremely high Q, and tapered fiber is the method to couple light into the cavity[22]. However, as shown in Fig.5.2a, silica wedge structure doesn't provide any possible space that planar waveguide can exist around cavity, so it has been challenging to achieve planar waveguide integration.

Fig.5.2b shows exterior WGM resonator structure for planar waveguide integration. First, the optical mode is confined at silica ridge structure. Thin silica layer covers the whole silicon layer except the hole at the center of ridge ring. The thin layer is holing the silica ridge ring structure, and silicon structure support the silica structure from outside of the ring. Because the silica layer is holding the exterior ridge with uniform thickness, it is feasible to form the planar waveguide next to the ridge resonator for optical mode coupling.

It is necessary to optimize the ridge thickness (T), the supporting silica layer thickness (t), and the required silicon undercut depth (d). The ratio between T and t determines the strength of optical mode confinement. Here, the supporting layer thickness (t) determines the optical mode confinement strength within ridge structure – the mode will be weakly

[2]Other crystalline-based microcavities[3, 197] have routinely exceeded Q factor over 100 million, but also full integration with waveguide is challenging

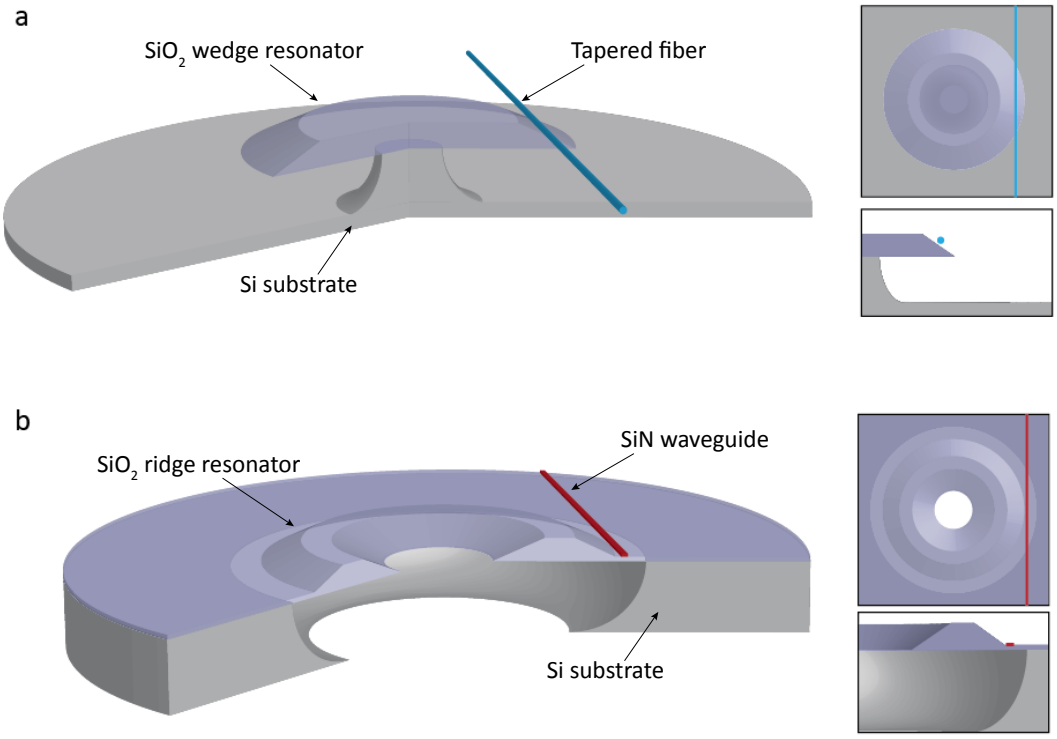

Figure 5.2: **Interior and exterior WGM resonators** (**a**) Silica microdisk structure on silicon pillar (interior WGM resonator). Insets illustrate top and cross-sectional view of the structure. Silicon undercut reduces optical mode coupling with silicon structure, and tapered fiber can couple photon into the resonator via near field coupling. (**b**) Silica exterior ridge resonator structure with silicon nitride planar waveguide. The optical mode can be confined within ridge ring structure.

confined and lossy if t is too thick. In addition, mechanical stability of the structure needs to be considered with optical properties – the silica structure is easily buckled with thin oxide thickness[87], so lower t can make whole structure mechanically unstable.

It is also important to note that the supporting silica layer thickness (t) needs to consider the condition for transmission of nitride waveguide. The refractive index of nitride is approximately 2 at 1550 nm wavelength, while the refractive index of silicon is around 3.5. Silicon oxide layer is thereby needed to isolate nitride waveguide from silicon substrate. This requirement can set minimum thickness of supporting silica layer as shown in Fig.5.3. The dimension of waveguide cross-section is 250 nm × 3000 nm, and the fraction of mode energy in silicon layer was numerically calculated as[198]:

$$\Gamma_i = \frac{Re\int_i (E \times H^*) \cdot z dx}{Re\int_{-\infty}^{\infty} (E \times H^*) \cdot z dx}, i = 1, 2, 3, 4 \tag{5.1}$$

where Γ_i is the fraction of power flowing in the medium i (i=1,2,3,4; air, nitride, silica,

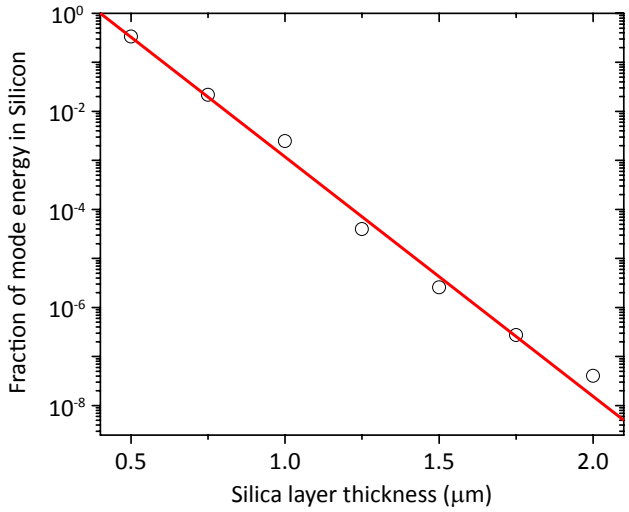

Figure 5.3: **Fraction of mode energy in silicon versus supporting silica layer thickness** The fraction of mode field (TE fundamental mode) in silicon layer is numerically calculated as a function of supporting silica layer thickness. The waveguide dimension in this calculation is 250 nm × 3000 nm.

silicon).

5.3.2 Q-factor engineering – numerical design

In the ridge structure, there are additional geometric features that the wedge resonator doesn't have; an outward supporting layer, and inward sidewall. **(i)** The supporting silica layer is holding the ridge ring structure, and entire structure becomes stable as the the layer becomes thicker. However, then the optical modes start to be leaky and Q factor might drop. **(ii)** Inward sidewall defines the ridge structure, and enable to open the silica aperture at the center for XeF_2 etch. The ridge width is defined as the distance between inward sidewall and outward sidewall, and Q-factor of fundamental mode becomes higher when the mode experiences the surface roughness less from both sidewalls. In this section, numerical studies on those structural features will be discussed. In order to consider the surface roughness of sidewalls, the results of previous AFM studies (cf. Chapt.2) were implemented on this numerical study. The thickness of ridge structure (T) is 8.5 μm in this chapter, because the Q was proven to be optimal at the level of thickness (cf. Fig.2.11).

Supporting silica layer thickness The supporting silica layer needs to be optimized for Q factor of fundamental mode. The additional geometric structure introduces an additional scattering and leakage loss. The Q factor of the mode thereby drops from the Q-level of wedge disk as the thickness of the layer increases (approximately 2.5 μm in Fig.5.4). However, the silica layer needs to have thickness at least thicker than 2.0 μm, as has been discussed in Fig.5.3.

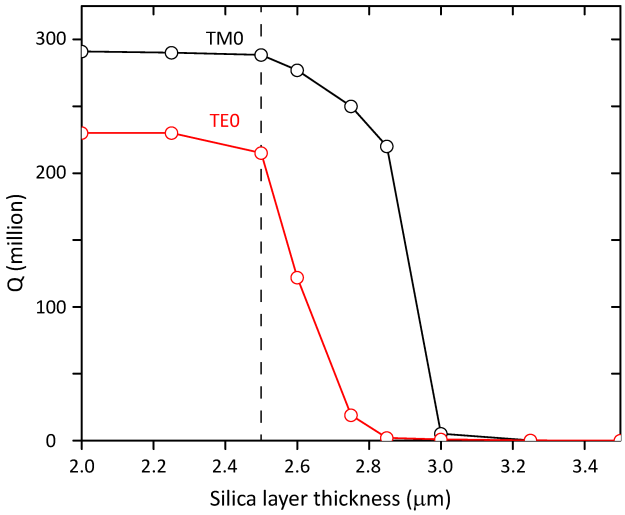

Figure 5.4: **Calculated Q factors of TM0 and TE0 versus silica layer thickness** Q factors of TM0 and TE0 modes were numerically calculated as a function of supporting silica layer thickness. The ridge resonator has 8.5 μm thickness and 10 μm width. The outward sidewall angle is 30°, while the inward sidewall angle is 25°. The structural parameters were based on a preliminary fabrication test.

Ridge structure width – separation between inward and outward sidewalls[3] In order to form the silica aperture for XeF_2 etch, the inward sidewall needs to be defined. If the inward sidewall is so close to optical mode, then the surface roughness of the sidewall causes additional scattering loss. On the other hand, the Q factor of the mode isn't degraded with larger ridge width but deeper XeF_2 etch is needed and it easily causes buckling of silica structure[87]. Fig.5.5 shows numerical studies that investigated the minimum ridge width (approximately 10 μm) that the inner sidewall doesn't degrade Q factor of fundamental mode. In addition, it is worth discussing Q factor sensitivity with respect to the ridge width. The sidewalls of the ridge structure are defined at separated lithography process, thus the misalignment between those lithography can cause the variation of ridge width through the cavity circumference (we will overview the microfabrication process in following sections). Interestingly, the simulated Q factors of fundamental mode are nearly constant if ridge width is larger than 10 μm and the misalignment is less than 250 nm using stepper process[133].

[3]Misalignment issue was discussed with Prof. Axel Scherer, and the discussion was added here.

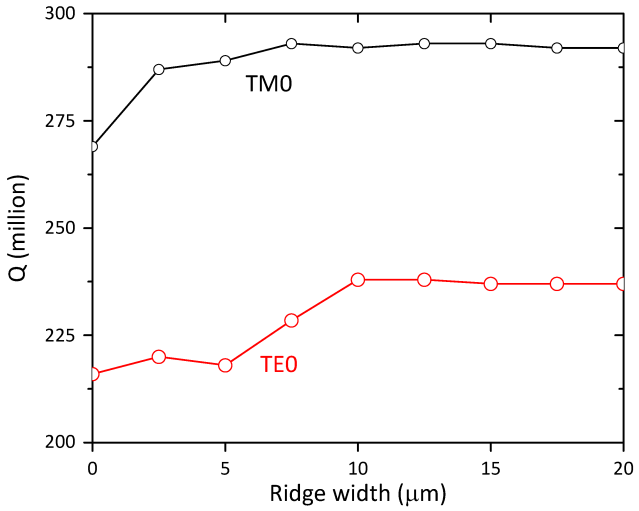

Figure 5.5: **Calculated Q factors of TM0 and TE0 versus ridge width** Q factors of TM0 and TE0 modes were numerically calculated as a function of ridge width (separation between inward and outward sidewall). The ridge resonator has 8.5 μm thickness and 2.5-μm-thick supporting layer. The outward sidewall angle is 30°, while the inward sidewall angle is 25°. The structural parameters were based on a preliminary fabrication test.

5.3.3 Q factor of silica ridge resonator – characterization

5.3.3.1 Silica ridge resonator fabrication

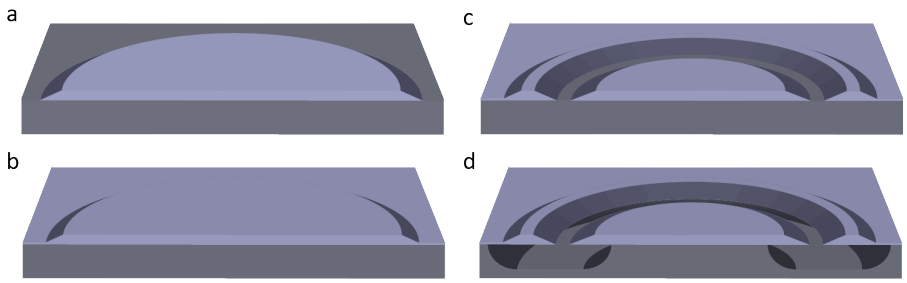

Figure 5.6: **Silica ridge resonator microfabrication procedures** (**a**) Silica wedge structure is defined on silicon substrate by photolithography and wet etch[22, 71]. (**b**) The additional oxide layer is grown at the interface between silican and silicon. (**c**) Lithography and wet etch of the silica defines an aperture to the silicon substrate. (**d**) XeF_2 etch is applied to remove silicon around ridge structure.

Fig.5.6 shows microfabrication process flow of silica ridge resonator. The process starts from high purity silicon wafer with thermally grown oxide. The silica wedge structure is defined by photolithography and buffered hydrofluoric acid (BHF) etch[22, 71]. An additional oxidation process is followed, and the oxide layer thickness can be adjusted by oxidation time. The additional oxide layer forms the silica supporting layer which can make entire structure stable as well as compatible with planar waveguide integration. Lithography and wet etch

on the silica layer defines an ring aperture to the silicon substrate, and uncovered silicon is etched during XeF_2 dry etch. The diameter of ring aperture determines the width of ridge structure.

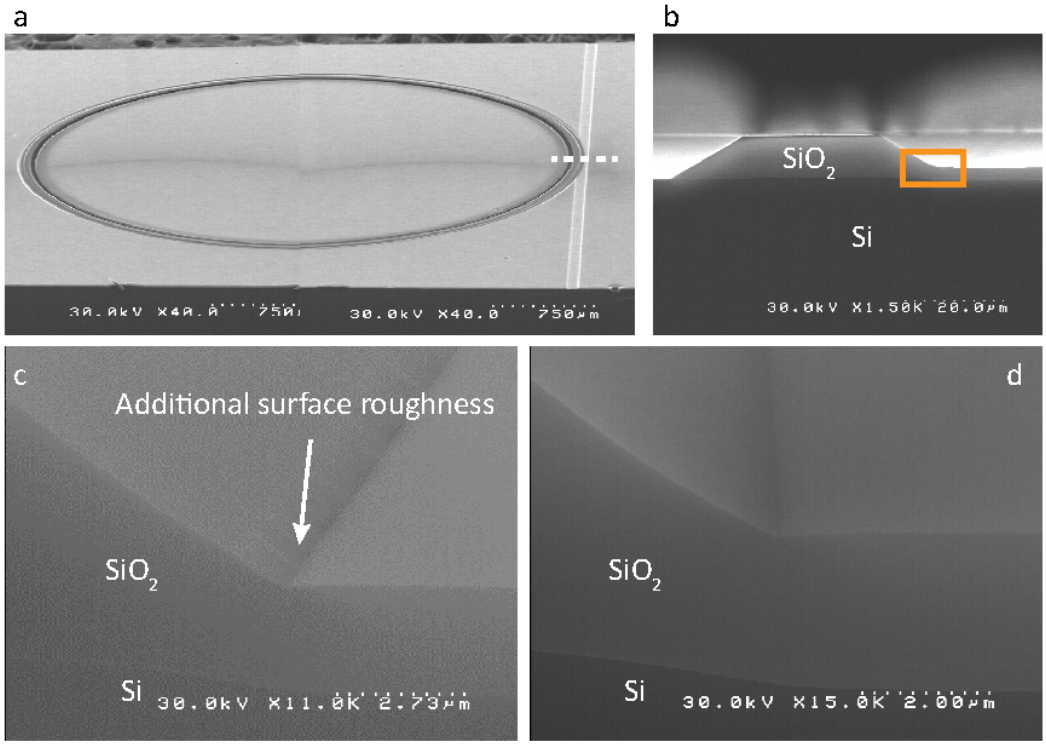

Figure 5.7: **SEM image of silica ridge resonator and "Foot region" on the additional oxide layer** (**a**) SEM image of fabricated silica ridge resonator. In this sample, nitride waveguide is already featured but this image is just for demonstrating ridge resonator structure at this section. This figure is edited from Yang et al.[199] (**b**) Cross-section SEM image of silica ridge structure. XeF_2 etch wasn't applied in this image. (**c**) Zoom-in scan of outward sidewall of ridge and supporting silica layer. As a result of additional oxidation, the surface roughness ("Foot region") was caused at the intersection line between sidewall and silica film. (**d**) Zoom-in scan of outward sidewall without the "Foot region."

Fig.5.7a shows SEM image of fabricated silica ridge resonator, and resonator diameter is 4.3 mm (corresponds to 15.2 GHz FSR). The dashed line segment gives the location of cleavage plan in Fig.5.7b. XeF_2 etch wasn't applied for the samples in Fig.5.7b-d. Interestingly, Fig.5.7c shows an additional surface roughness ("Foot region") at the intersection line between ridge outward sidewall and supporting silica film. In order to understand the origin of the "Foot region", the additional SEM image was taken from the sample in Fig.5.6c (silica wedge disk on silicon wafer), and it is confirmed that the "Foot region" was occurred during additional oxidation process. Fig.5.6d shows zoom-in scan of outward sidewall without "Foot region." It is still unknown how unpredicted roughness was occurred, but empirical observation demonstrated that (i) "Foot region" disappears as grown oxide film is thicker,

and (ii) the thicker oxide layer is required as sidewall angle increases. Because the optical mode is defined close to the intersection line between sidewall and supporting silica film, the "Foot region" may cause higher scatter loss as has been discussed in Ref.[22].

5.3.3.2 Q factor characterization

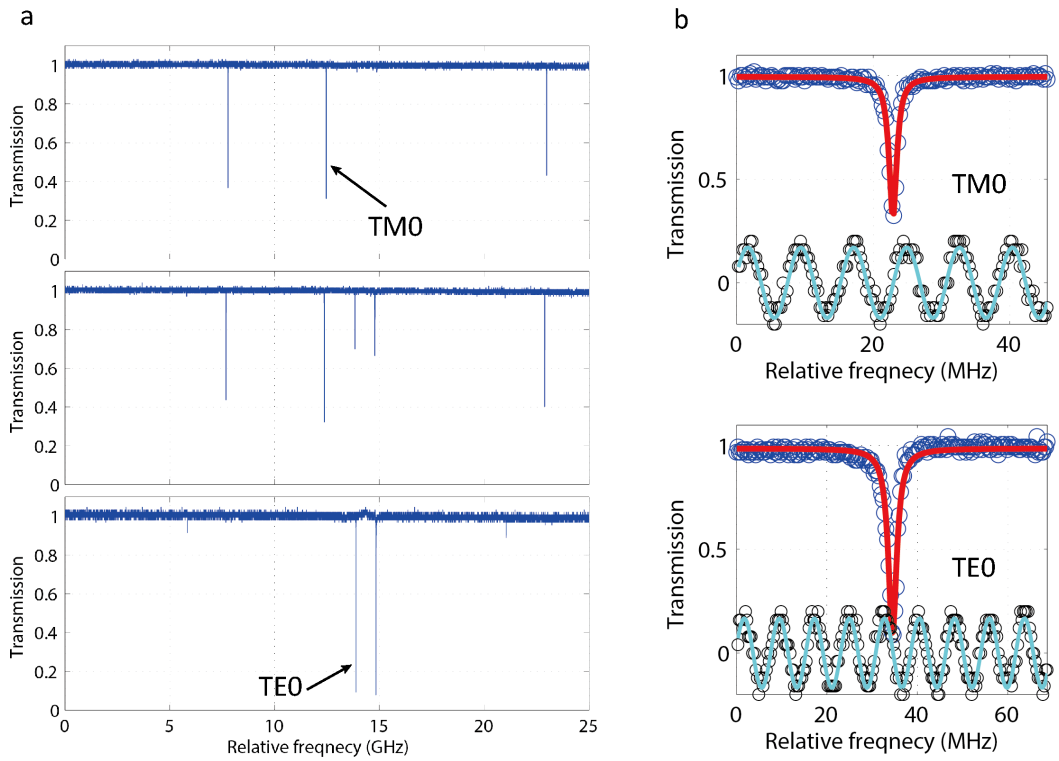

Figure 5.8: **Q factor characterization in silica ridge resonator (FSR = 15.2 GHz)** (**a**) Measured spectral scan of TM- (upper), TE- (lower), mixed (middle) polarized mode families in silica ridge resonator. Tapered fiber was used for the measurement, and fundamental modes are indicated using arrows. Mode family was identified using wide scan of mode spectrum and its comparison with numerical simulation[55, 71] (**b**) Zoom-in spectral scan of TM0 (upper) and TE0 (lower) mode in 1560 nm. Q_0 of TM0 is 208 million, while Q_0 of TE0 is 150 million.

Fig.5.8a shows spectral scans of TM-, TE-, and mixed polarization mode families in upper, lower, and middle panel. From the previous discussion in fabrication, the "Foot region" was totally removed from the intersection line between ridge and supporting film. Tapered fiber was used for the mode coupling, and scanning frequencies were calibrated using fiber interferometer[22]. The mode families were identified from the comparison between wide scan of mode spectrum and finite-element-simulation based on SEM profile of the sample[55, 71]. In order to couple with every transverse mode existing in the resonator, several positions in tapered fiber were used for the measurement. Fig.5.8b shows zoom-in scans of TM0 (upper panel) and TE0 (lower panel) modes in 1560 nm. The linewidth of the

resonance dip is fitted to Lorentzian model, and the fitted linewidth was converted to Q_0 using transmission at resonance frequency. Here, it is necessary to confirm that the resonator is undercoupled by changing fiber location and gap with ridge resonator[22].

5.4 SiN waveguide design & characterization

This section will discuss nitride waveguide design and characteristics. Above all, there are a couple of considerations needed for nitride waveguide : (i) single-mode operation and (ii) polarization of waveguide propagation mode. Single mode operation generally requires strong waveguide confinement, so it is unavoidable that optical mode experiences the waveguide boundary. The top and bottom boundaries of nitride waveguide is defined by intrinsic silica and nitride layer roughness while side boundaries of nitride wavegude are defined by RIE (reactive ion etch) roughness. TE mode, which the transverse electric field is parallel to top and bottom boundaries of waveguide, requires wider width and thin thickness waveguide cross-section dimension for single mode operation, and the structure experience sidewall roughness relatively less than narrower width and thick thickness waveguide. In order to achieve high transmission[4, 90, 91] as well as compatibility with other photonic devices[200], SiN waveguide is designed for TE-polarized mode in this work. Tapering and pulley waveguide design will be also discussed and utilized on the integrated resonator platform.

5.4.1 Design requirements for nitride waveguide dimension

We need to consider two criteria when we design the nitride waveguide dimension: (i) single mode operation, and (ii) phase matching condition. Single mode operation can prevent an additional parasitic loss, and phase-matching condition allows the evanescent field tunneling between resonator and waveguide.

Single mode operation Fig.5.9 shows calculated effective index of nitride waveguide mode as a function of waveguide width (The thickness of guide is 250 nm). It is also important to note that silicon layer is removed from the silica layer bottom in this numerical study because the resonator coupling region has silicon undercut (see Fig.5.10 for more detail). As waveguide width increases from 900 nm to 1.4 μm, the effective index of TE0 mode quickly increases from 1.43 to 1.53. In addition, higher order TE modes are neither well confined within waveguide structure nor existing. From the width of 1.4 μm, TE0 mode starts to be confined within the nitride structure and the effective index of the mode increases quickly. It is important to operate the single mode waveguide coupler in order to prevent parasitic loss caused by multiple waveguide mode coupling with resonance mode[201].

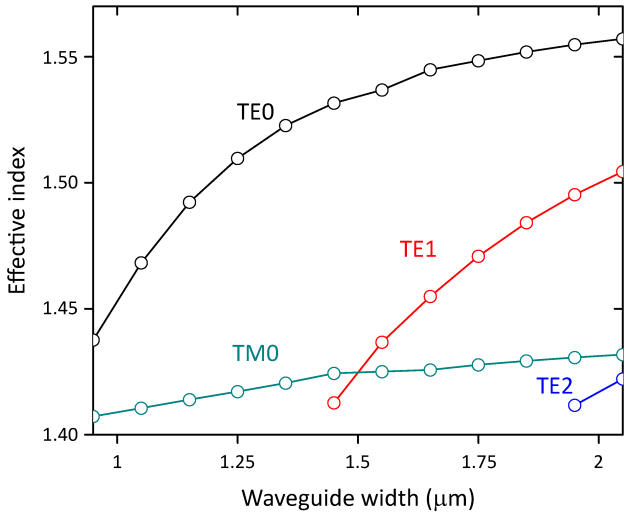

Figure 5.9: **Effective index of waveguide mode versus waveguide width** Calculated effective index of nitride waveguide modes (TE0, TE1, TE2, and TM0) versus waveguide width. Numerical simulation searched over 100 mode solutions, and the thickness of waveguide is 250 nm. Waveguide width narrower than 1.4 μm shows single mode operation in TE polarization. Significant amount of TM0 mode field is confined in silica layer, so the effective index is quite low even with wider width.

Phase-matching condition Fig.5.9 simultaneously shows the phase-matching condition between nitride waveguide and silica ridge resonator. According to numerical studies on ridge structure, the effective index of resonator modes (both TM0 and TE0) is approximately the silica material index (1.444 at 1550 nm wavelength). 900-nm-wide nitride waveguide supports TE0 mode which has a similar phase velocity with the one of resonance mode. TE0 mode also has similar effective index at 1.6 μm-width waveguide. However, as has been discussed earlier, the waveguide only needs to support a single transverse mode in the coupling region with resonator. 900×250 nm dimension is thereby one of good candidates for the process.

5.4.2 Tapered waveguide design

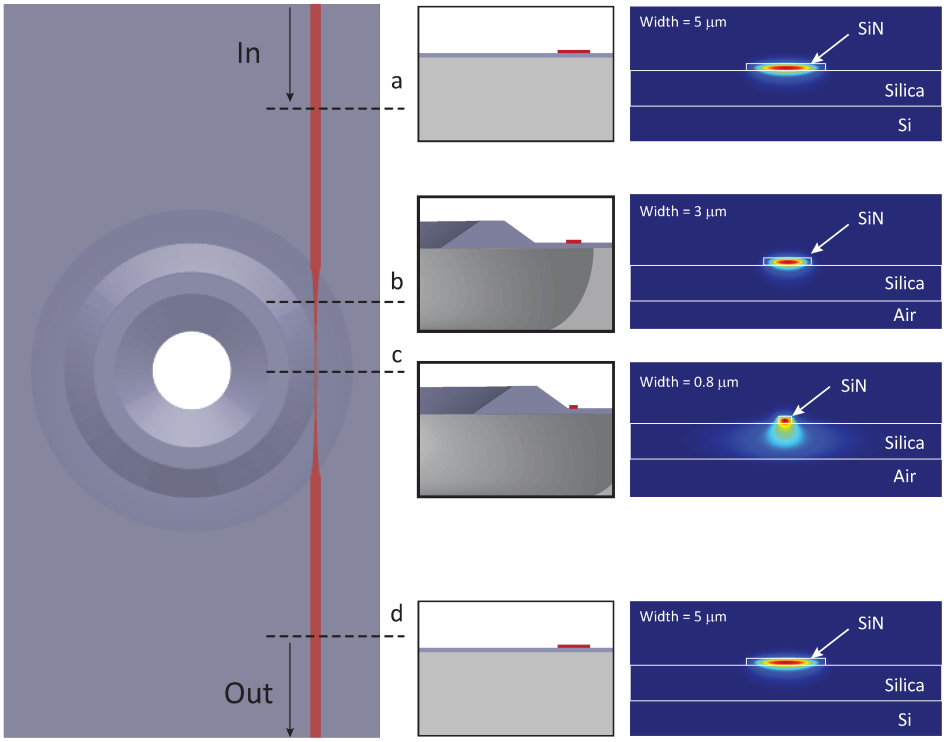

Figure 5.10: **Tapered SiN waveguide structure with integrated silica ridge resonator** Top view of integrated resonator and waveguide. The optical wave can propagates from the top (indicated as "In") to the bottom ("Out"), and the tapered waveguide structure is designed around resonator for phase matching. Dashed lines correspond to cross-section schematics with mode profile in the right panel (Left panel). Waveguide has 250 nm $\times$ 3 μm dimension at the input facet, and the propagating mode is almost confined in nitride structure with 2.5 μm thick oxide layer. As waveguide approaches the resonator, waveguide has narrow width with constant thickness. Then mode extends over silica and air layer but transmission doesn't droup because silicon is removed at the bottom of silica layer. As the coupling region, waveguide has 250 nm $\times$ 900 nm dimension for phase matching as discussed in previous section. The waveguide width becomes wider again, and propagates the optical mode to output facet.

As has been discussed, SiN waveguide has optimal phase-matching condition if effective index of propagation mode is similar with silica refractive index. Then the propagation mode should extends more over silica thin layer as well as air cladding, and the mode thereby becomes highly lossy if silicon is not removed at the bottom of silica structure. However, it is practically challenging to undercut silicon anywhere nitride waveguide exists (complex undercut causes mechanical issue on silica film).

Tapered waveguide structure is thereby required for both waveguide transmission and phase matching with silica ridge resonator – narrow waveguide (w_{narrow}) in cavity-waveguide coupling region, and wider waveguide (w_{wide}) elsewhere. Waveguide width needs to be as

narrow as 900 nm for mode coupling with resonator, and the waveguide transmission can be maintained because the silicon is undercut around ridge resonator. And then waveguide needs to be wider adiabatically once the waveguide approach the area that has silicon layer at the bottom. In order to find minimum w_{wide}, the set of waveguide dimension was tested using finite-element-simulation as shown below:

The waveguide tapering region was designed using the following equation:

$$w(x) = w_1 + (w_2 - w_1) \cdot \frac{(x/d)^n}{1 + (x/d)^n} \tag{5.2}$$

where x is along the waveguide propagation direction, w_1 and w_2 are desired waveguide width (e.g. w_1 is tapered width and w_2 is width without tapering), d and n are controllable parameters[202]. Here, n defines the steepness of tapering rate, $n \geq 3$ is required for $w'(0) = w''(0) = 0$. d gives the scale of tapering region, and the scale depends on silicon undercut region as shown in Fig.5.11. In this work, n = 6 is used for taper profile design and more detail requirements for design are shown in Table.5.1.

d (μm)	w_{narrow} (nm)	w_{wide} (nm)	Thickness (nm)
120	880	3000	250

Table 5.1: **Requirements on nitride waveguide taper**

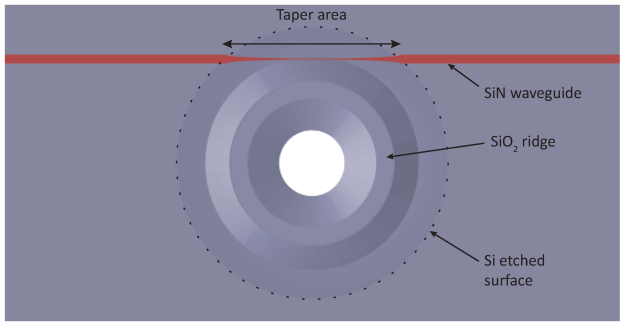

Figure 5.11: **Silicon etched area dependent taper length scale** Schematic view of integrated resonator with waveguide coupler. Silicon undercut depth determines allowed taper length scale (arrow).

5.4.3 Pulley waveguide design

The ability to lithographic coupling control allows another advantage of fully integration other than system compactness and stability. The waveguide dimension can be designed to target coupling mode (phase-matching condition); the gap and pulley region length[4]

[4]Pulley structure can be interpreted as tapered gap[4]

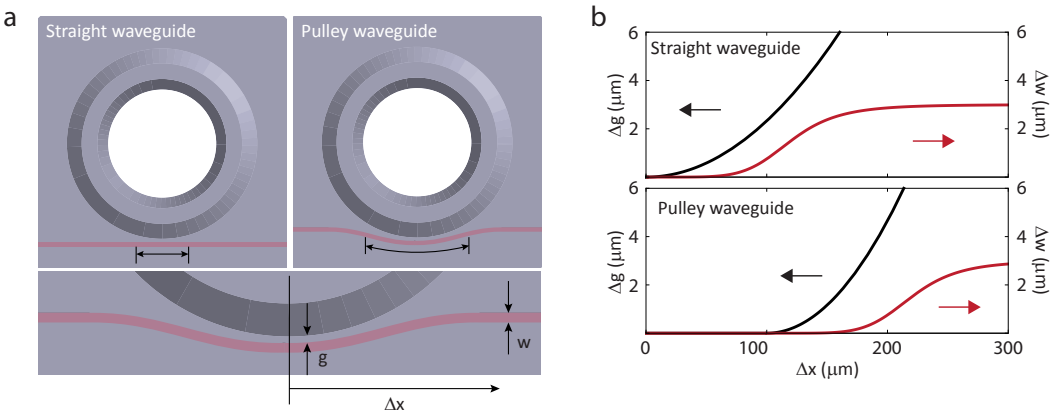

Figure 5.12: **Pulley waveguide structure** (**a**) Top view of resonator-waveguide schematics (upper left: straight SiN waveguide, upper right: pully SiN waveguide, arrow: effective interaction region). Lower panel depicts zoom-in of pulley waveguide structure. (**b**) Comparison between straight waveguide and pulley waveguide (deviation of g and ω as a function of Δx).

can determines the external coupling rate with the specific mode families. As an example, Fig.5.12a shows a schematic of pulley waveguide structure on integrated silica ridge resonator. The arrows on upper panels show effective mode coupling region, and the gap on the other region are too separated to make enough mode overlap. The lower panel shows the zoom-in schematic on the coupling region. Fig.5.12b shows quantitative comparison between straight and pulley waveguide. Nitride waveguide width is presented as a function of Δx; the gap between resonator and waveguide coupler is adjusted in pulley structure.

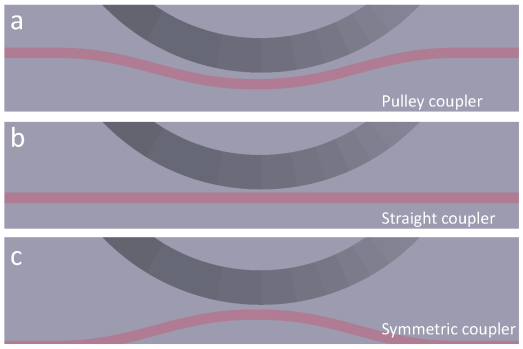

Figure 5.13: **Directional coupler layouts** (**a**) Pulley coupler (**b**) straight coupler, (**c**) symmetric coupler. This figure is adopted from D.T.Spencer et al.[4].

Fig.5.13 shows directional coupler layouts for integrated resonator. As shown in those schematics, the bending direction in symmetric coupler is opposite to the ring resonator while the direction in pulley coupler has the same direction. Pulley structure thereby increases the interaction length by tapering the gap while symmetric coupler decrease the interaction region[4]. According to Ref.[203], the straight waveguide caused excess loss associated with

a decrease in gap and yielded the increment of cavity internal loss rate. In order to reduce the excess loss, the waveguide can be apart from the resonator. However, then the coupling efficiency may drop. Alternatively, pulley waveguide structure can compensate the reduced external coupling rate from the decrease in gap[4].

The external coupling rate (κ_{ext}) is given as:

$$\kappa_{ext} = \kappa_{sc} L_c \frac{sin(L_c\sqrt{(\Delta\beta)^2 + \kappa_{sc}^2})}{L_c\sqrt{(\Delta\beta)^2 + \kappa_{sc}^2}} \tag{5.3}$$

where κ_{sc} is the field overlap in the waveguide-resonator cross section, $\Delta\beta$ is phase mismatch between waveguide and resonator, and L_c is the coupling length. Assuming $\Delta\beta$ is negligible as a result of phase matching, then the external coupling rate becomes $\kappa_{ext} = sin(\kappa_{sc} L_c)$.

5.4.4 SiN waveguide characterization

The basic properties of nitride waveguide needs to be characterized in order to utilize the material for further development towards full integration with resonator. First, the material index of nitride film needs to be confirmed because all numerical calculations and structural designs are based on the material characteristic. Second, the transmission loss of nitride structure also needs to be characterized in order to function for efficient nonlinear platform.

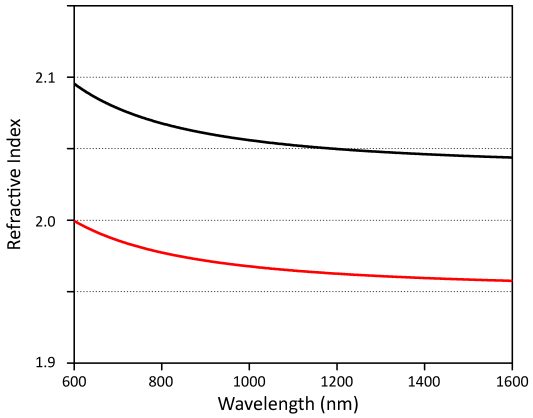

Figure 5.14: **Refractive index of PECVD nitride film** Refractive index of PECVD nitride film was measured using Ellipsometry from 600 nm to 1600 nm. Red line indicates the refractive index of PECVD nitride film prior to annealing, and black line indicates the refractive index of nitride film after annealing ($1000°C$ in N_2 ambient).

Nitride refractive index characterization The refractive index of PECVD nitride was measured using Ellipsometry from 600 nm to 1600 nm. Imaginary index was also measured from the sample, but it is not shown because the value is negligible. It is interesting to note that the index of nitride film increases by 5 % after N_2 annealing process while the measured thickness decreases by 10 %. Because waveguide integrated resonator needs few annealing

steps, the refractive index of annealed nitride film was thereby used for all modeling and numerical design work.

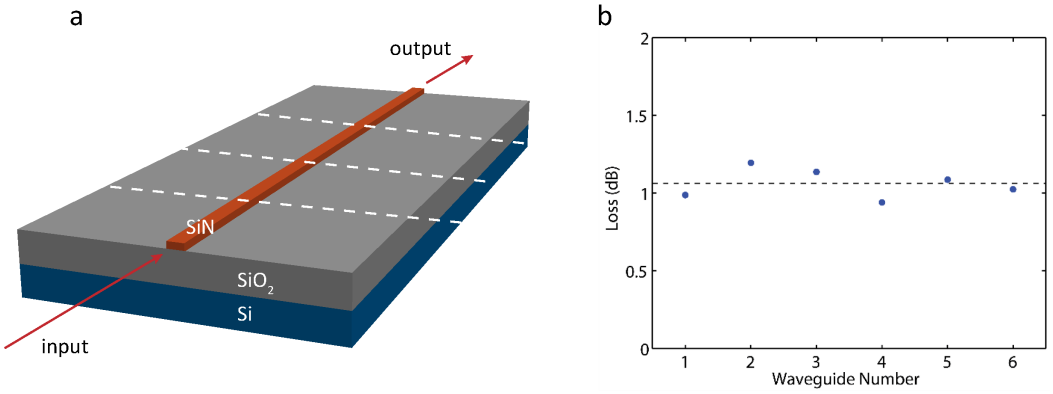

Figure 5.15: **Nitride waveguide characterization** (**a**) Schematic illustration of nitride waveguide on silica and silicon. Nitride waveguide is on 2.5-μm silica layer, and waveguide dimension is 2300 × 250 nm. Dashed line indicates chip cut line in order to proceed cut-back measurement method. Then multiple measurement of transmission share common input facet, so the coupling rate is constant over the measurements. (**b**) Measued transmission loss of nitride waveguide (waveguide dimension: 2300 × 600 nm).

Nitride transmission characterization In order to test the transmission property, the nitride waveguide (straight, constant waveguide dimension) was fabricated on 2.5-μm thick silica on silicon. The thickness of silica film is identical with the one of silica supporting layer, and a fully integrated resonator will be utilized with this thickness in the next section. Here two different waveguide dimensions (2300 × 600 nm, 3500 × 250 nm) were tested.

The transmission measurements have been made using the cut-back method and at the same time the fiber-to-waveguide coupling coefficient can be separately estimated[204, 205]. Waveguide input coupling was achieved using lensed fiber, and output transmission was collected by aspheric lens. As the first step, the transmission through long length of waveguide is performed, and here the transmission includes lensed fiber-waveguide coupling rate and waveguide-aspheric lens coupling. Then the waveguide chip was cut at a point near the output facet, and another transmission measurement was followed. Here both measurements share common input fiber-waveguide coupling coefficient and we assume that the coupling at output facet is the same. By repeating the measurements on the shorter length of the chip (as indicated using dashed lines in Fig.5.15a), the unit length transmission can be characterized more precisely.

Fig.5.15b shows the measured transmission loss, and the waveguide dimension is 2300 × 600 nm. Total 6 waveguides were tested for the transmission characterization. The measurement shows approximately 1.06 ± 0.10 dB/cm transmission loss, and approximately corresponds to 0.2 - 0.3 million Q factor. This dimension wasn't used in waveguide integrated resonator

platform, but the dimension is comparable with the one used for nitride ring resonators. In addition, the transmission loss of 3500 $\times$ 250 nm dimension was also investigated using the cut back method. The nitride waveguide was fabricated on the 2.5-μm thick silica layer, and total 5 EA waveguide chips were tested. The measured transmission is 1.8 $\pm$ 0.9 dB/cm as a result of lower waveguide thickness.

5.5 Fully-integrated ultra-high-Q resonator

New resonator structure was proposed for monolithic integration, and designed to support high Q optical mode in 5.3. The planar silicon nitride waveguide design was followed, and tapered waveguide structure was utilized in 5.4. In this section, resonator-waveguide integration will be discussed – microfabrication process (5.5.1), Q factor characterization (5.5.2), and engineering mode spectrum (5.5.3). The fully-integrated resonator featured ultra-high-Q (> 200 million), and mode spectrum engineering was demonstrated for nonlinear optic applications.

5.5.1 Microfabrication process

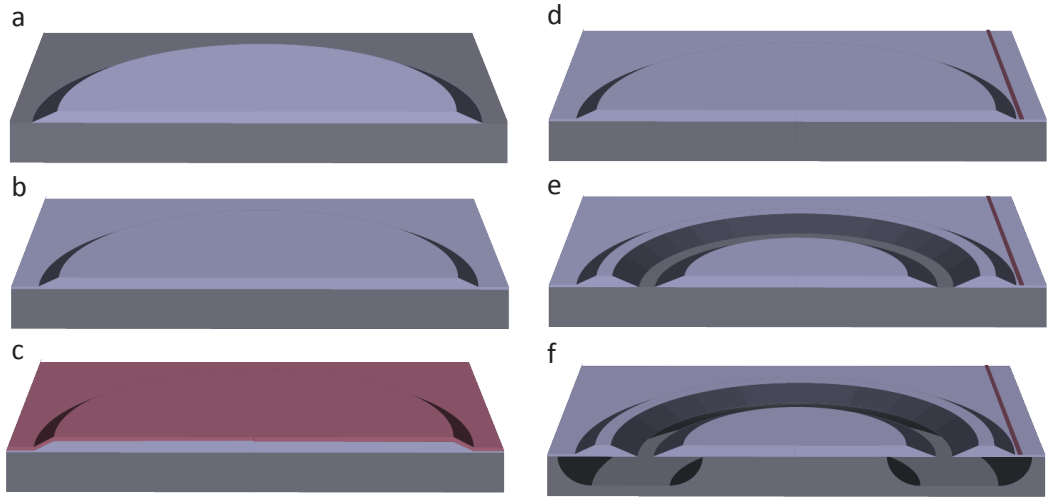

Figure 5.16: **Fabrication process for integrated ultra-high-Q microresonator** (**a**) Silica disk is defined on silicon by photolithography and HF etching of an initial silica layer. (**b**) Thermal oxidation grows a second oxide layer beneath the etched silica disk. (**c**) PECVD silicon nitride is deposited. (**d**) Silicon nitride waveguide is defined on silica layer by lithography and etching. (**e**) Lithography and wet etch of the silica define a ring aperture on the silicon substrate. (**f**) XeF_2 etches the silicon through the ring aperture. This figure is from Yang et al.[70].

Overview of microfabrication process The fabrication process begins by growing a thermal silica layer (thickness: 8 μm) on a high-purity float-zone silicon wafer. This layer is then patterned and wet etched using buffered hydrofluoric acid (BHF) according to a process used to create wedge resonators[22]. The resulting etched oxide forms a circular disk structure that defines the exterior sidewall of a resonator (Fig.5.16a). A subsequent thermal oxidation grows the oxide layer under the bottom of the oxide disk (Fig.5.16b). The oxidation is followed by deposition of 500 nm of PECVD silicon nitride (Fig.5.16c). Lithography and a shallow ICP RIE are then applied to partially etch the silicon nitride. Phosphoric acid is

used to fully define the silicon nitride waveguide (Fig.5.16d)[5]. A thin layer (20 nm) of silica is applied by atomic layer deposition[6] to protect the silicon nitride waveguide during the xenon difluoride (XeF_2) etch step below. A lithography/wet-etch step is then used to open an interior, ring aperture to the silicon substrate (Fig.5.16e). In the final step, XeF_2 etches the silicon through the interior ring aperture so as to create an optical cavity (Fig.5.16f).

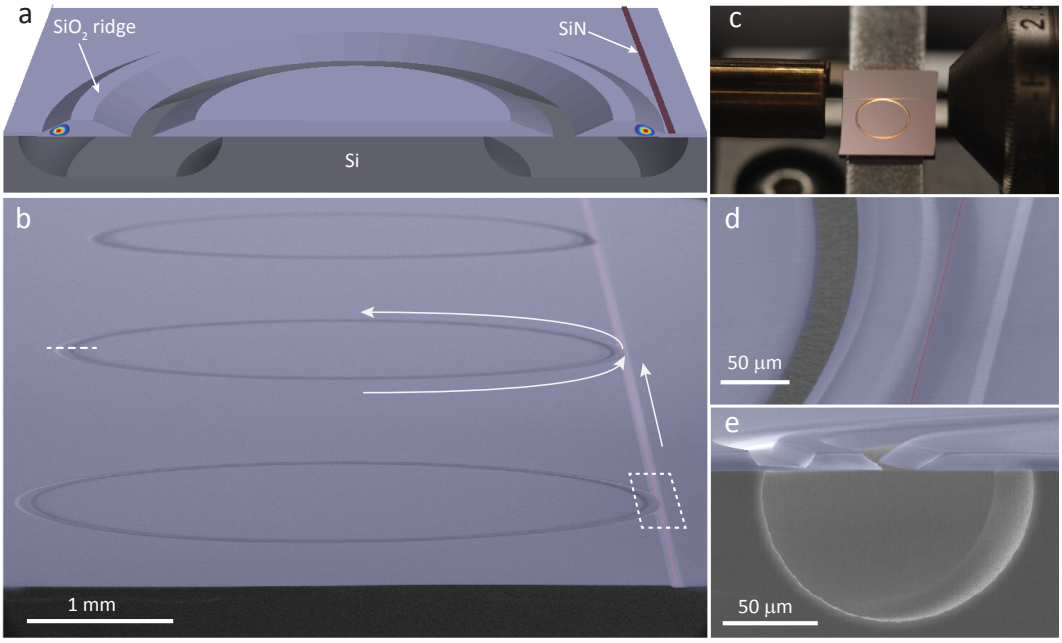

Figure 5.17: **Integrated ultra-high-Q microresonator** (**a**) Schematic illustration of monolithic integrated silica resonator. The SiN waveguide mode is coupling to fundamental mode of silica resonator illustrated in color. (**b**) SEM image of resonator array with a common silicon nitride waveguide (false red color). White arrows show the direction of circulation within the resonator for the corresponding direction of coupling from the waveguide. Dashed white box corresponds to the region for the zoom-in image in **d**. Dashed white line segment gives the location of cleavage plane used for preparation of the SEM image in **e**. (**c**) Photograph of a integrated resonator with endfire coupling provided by a lensed fiber (left) and aspheric lens (right). (**d**) SEM zoom-in image of the waveguide-resonator coupling region shown within the dashed white box in **b**. (**e**) SEM image of resonator cross section prepared by cleaving at the dashed white line in **b**. This figure is from Yang et al.[70].

Illustration of integrated resonator structure Fig.5.17b shows SEM image of integrated resonator array (3 resonators with 1 common waveguide). The nitride waveguide is illustrated with false red color, and the resonators are coupled with the common nitride waveguide. The resonator diameter is approximately 4.3 mm (corresponds to 15.2 GHz FSR); the ridge thickness is 8.5 μm; the nitride waveguide thickness is 250 nm. The lensed fiber (Fig.5.17c)

[5]RIE on silica structure degrades the surface roughness of resonator, so the RIE should be applied for partial removal of nitride film.

[6]Lin Chang in UCSB kindly helped to characterize the refractive index of the silicon oxide ALD film – 1.471 at 1550 nm

is used to couple the light to the silicon nitride waveguide facet (see the cleaved cross-section in Fig.5.17b), and approximately 25 % of the power could be coupled. No attempt to improve coupling was made, but in the future a tapered waveguide end can be introduced to improve the coupling efficiency[206]. The silicon nitride initially has a width of 3 to 3.5 μm with 250 nm thickness, and it is tapered to about 900 nm width as approaching to silica ridge resonator. Both straight (cf. section 5.5.2.2) and pulley version (cf. section 5.5.2.2) of nitride waveguide were designed and fabricated in order to vary coupling strength. The transmitted power is re-collected through the aspheric lens and the spectral scan is recorded through fiber coupled photodiode.

Structural parameter adjustment There are several structural parameters that modify the device characteristics, and each parameters are adjusted by multi-step of microfabrication:
- Diameter of circular pattern in Fig.5.16a: The effective radius of ridge ring is determined by this step, and it corresponds to FSR.
- Additional oxidation duration in Fig.5.16b: The supporting silica layer thickness is determined in this step, and the thickness of the layer determines the number of existing mode families as well as Q factor of fundamental mode.
- Alignment between nitride waveguide pattern and resonator in Fig.5.16d: The gap between resonator and waveguide determines the strength of mode coupling.
- Diameter of ring pattern in Fig.5.16e: The diameter of ring pattern determines the width of ridge structure.

5.5.2 Q-factor characterization

5.5.2.1 Intrinsic Q-factor of silica ridge resonator

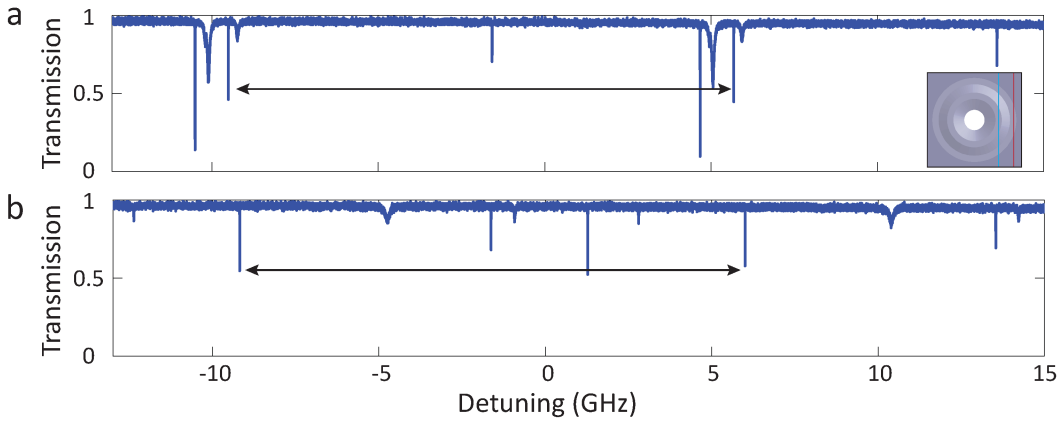

Figure 5.18: **Spectral scan of ridge resonator using taper fiber coupling** Measured transmission spectral scan of (**a**) TE- and (**b**) TM-polarized mode families. Tapered fiber was using to couple the light to silica ridge resonator, and laser was scanned over one FSR (> 15 GHz) to find all resonance modes that exist in resonator. Nitride waveguide was featured on the resonator with the gap less than 1 μm; however, it is fabricated for non phase-matching in order to measure the intrinsic quality of resonator using tapered fiber.

In this section, the intrinsic Q factor of silica ridge resonator will be discussed and the silica ridge structure also features nitride waveguide with planar integration. However, the nitride waveguide has wider width (> 1.5μm) for non-phase matching condition and the external coupling loss of resonance mode is thereby negligible. The measured Q factor in this system is determined by:

$$1/Q = 1/Q_0 + 1/Q_{ext} + 1/Q_p \tag{5.4}$$

where Q, Q_0, Q_{ext}, and Q_p are total, intrinsic, external coupling, and parasitic Q factors, respectively[4, 49]. Because nitride waveguide dimension is in non-phase matching condition, Q_{ext} is only determined by tapered fiber coupling. In addition, Q_p still contains the parasitic loss caused by SiN surface scattering (gap between silica ridge and nitride waveguide < 1μm), so this approach allows to estimate the intrinsic Q factor of resonator when the resonator is coupled to nitride waveguide. It is also important to note that parasitic loss can be also caused by additional coupling loss between multi-mode waveguide and resonator[201]. Because the waveguide mode doesn't have phase-matching condition with resonance mode in this experiment, the multi-mode coupling issue doesn't need to be considered.

Fig.5.18a-b show the measurement results from TE-, and TM-polarized mode families, and the coupling strength can be easily adjusted by taper thickness and spacing between resonator and tapered fiber. The spectral scan shows that (i) approximately 4 - 6 mode families per

polarization exits in the ridge resonator, and (ii) FSR is approximately 15 GHz as designed. In addition, it is important to confirm that quasi-TM fundamental mode has max 200 M intrinsic Q factor while quasi-TE fundamental mode has max 120 - 130 M intrinsic Q factor. As has been discussed, the nitride waveguide is designed for TE polarized mode propagation with single mode operation. The mode coupling between TE-polarized waveguide mode and quasi-TE, TM polarized resonance mode will be discussed in the following sections.

5.5.2.2 Q-factor of straight SiN waveguide coupled resonator

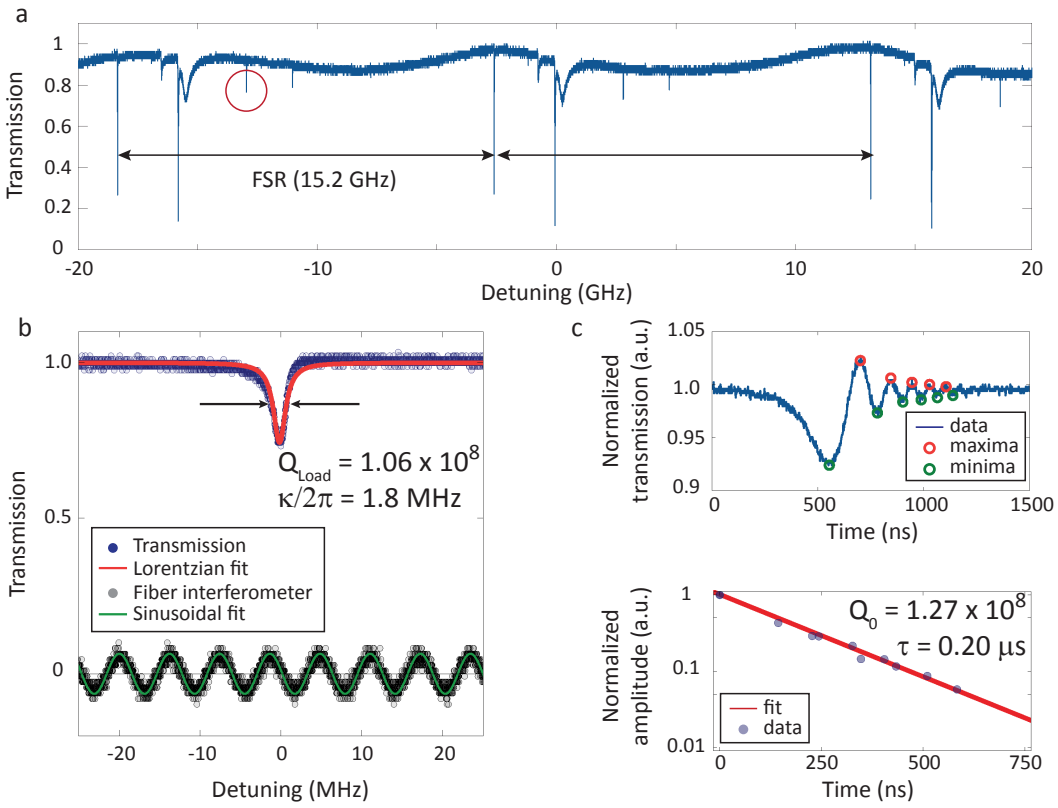

Figure 5.19: **Spectral scan of integrated ridge resonator (straight SiN waveguide coupling) and ring down measurement** (**a**) Spectral scan containing over 2 FSR (λ = 1570 nm). Several transverse modes appear in scan including TE0 mode, and the red-circled mode recorded Q factor over 100 million. (**b**) High-resolution zoom in scan of the highest Q mode (TE0). The sinusoidal signal is a frequency calibration scan using a fiber Mach–Zehnder inteferometer with a free-spectral range of 5.979 MHz (**c**) Cavity ring down measurement for the TE0 mode (Top: Transmission spectra of the ring down signal, Bottom: Exponential fits (red line) of the minima and maxima dataset (blue dots)). This figure is edited from Yang et al.[199].

In following sections, spectral measurements of the integrated resonator were performed by endfire coupling to a tunable external cavity laser (λ = 1520 - 1580 nm) and monitoring of the transmission through the waveguide-coupled device as the laser is scanned. Straight

silicon nitride waveguide (width = 880 nm, thickness = 250 nm; see detail phase-matching condition in 5.4.1) is fabricated with silica ridge resonator, and waveguide is tapered for higher transmission. The devices tested had a free-spectral-range (FSR) of approximately 15 GHz (ridge ring diameter of approximately 4.3 mm).

Fig.5.19a presents a spectral scan containing over two FSRs (>30 GHz). Approximately 6 - 7 distinct mode families appear in the spectral scan, and one of them is almost critical-coupled with nitride waveguide. A high-resolution scan (red-circled mode in Fig.5.19a) is presented in Fig.5.19b and shows TE0 mode in the full scan having a total Q factor of 106 million. The transverse mode families were identified by collecting mode frequencies scan for coupled spatial mode families and comparing numerical modeling[55, 71]. The measured mode spectrum will be shown in following discussions.

Here, the linewidth measurements are only a reliable measure in the case of either weak cavity-coupled power or wide cavity linewidth (low Q). Specifically, the poor thermal conductivity of silica constitutes the inaccuracy of Q measurement via transmission linewidth more[49]. To overcome inaccuracy in linewidth measurement, resonator ring-down measurement[197] was performed as shown in Fig.5.19c-d. Resonator ring-down measurement directly records the photon lifetime in time domain. The laser scans across the resonance frequencies with a shorter duration than cavity lifetime. Then the oscillation appears on the transmission spectra as a result of the interference between laser source and build-up power that decays into fiber (Fig.5.19c). The oscillation envelope depends on the cavity lifetime, and the phase of the oscillation depends on the wavelength difference between cavity resonance and scanning laser – scanning speed can change the duration of oscillation. The ring down oscillation was analyzed from the transmission spectra, and its theoretical fit gives a measured amplitude decay of 0.2 μs corresponding to an intrinsic Q factor 127 million (assuming no parasitic loss)[7].

It is important to note that estimated Q_0 (127 million; assuming no parasitic loss) through nitride waveguide is similar with intrinsic Q factor of silica ridge resonator through tapered fiber (120 - 130 million). As discussed, the loaded Q factor is determined by Q_0, Q_{ext}, and Q_p. Parasitic loss of TM-, and TE-polarized fundamental modes in silica ridge resonator were negligible as discussed in section 5.5.2.1. However, the SiN waveguide mode coupling with silica resonator mode may cause an additional parasitic loss (Q_p) in case that resonance mode couples to multi waveguide modes. Q_0 of TE-polarized fundamental mode in silica ridge resonator was measured, and Q_{ext} can be estimated from transmission at the resonance dip. Parasitic loss is confirmed to be negligible by following equation:

$$1/Q_p = 1/Q - 1/Q_0 - 1/Q_{ext} \tag{5.5}$$

[7] Q_0 becomes even higher unless assume no parasitic loss from the equation: $1/Q_0 = 1/Q - 1/Q_{ext} - 1/Q_p$

Ideality of modal coupling is thereby 1, and we don't need to assume no parasitic loss in following discussions – measured Q_0 also becomes 127 million in Fig.5.19 without any assumption.

Only 25 % of propagation power is coupled to TE0 resonator mode while higher order TE mode has stronger mode coupling. This is because lower order mode tends to shift the centroid of motion around ridge resonator inwards and the mode overlap with waveguide mode drops. Stronger mode coupling with TE fundamental mode will be discussed using the pulley waveguide structure in the following sections.

5.5.2.3 Q-factor of pulley SiN waveguide coupled resonator

In this section, pulley nitride waveguide was featured on integrated resonator and the mode coupling trend will be discussed with corresponding pulley designs.

	TM0	TE0
$Q_{0,taper}$	200 - 250 M	120 - 130 M
$Q_{0,SiN}$	N/A	127 M
$P_{coupled}$	0	0.25

Table 5.2: **Mode coupling and measured Q in straight nitride waveguide**

Table.5.2 summarizes the mode coupling and measured Q_0 of straight nitride waveguide structure. As has been discussed, TE0 mode was measured using straight nitride waveguide and the measured Q_0 was 127 million without suffering from parasitic loss caused in multi-mode waveguide coupler. However, the mode coupling is only 25 % level so that might not be sufficient to use the coupling for nonlinear optics application – generally coupling strength also determines operating power of both frequency comb and lasers[22, 55]. Besides, TM0 mode has higher Q_0, but it is even not coupled with straight nitride waveguide because of insufficient field overlap between TE waveguide mode and quasi-TM resonator mode.

In order to strengthen the mode coupling with fundamental modes, cavity-waveguide gap can be one of methods that adjust the magnitude of field overlap. This approach corresponds to the gap adjustment between taper fiber and WGM resonator, and it can cause an additional scattering loss because then waveguide needs to be on the outward sidewall of the ridge resonator. Pulley waveguide structure[4] is also another approach, and this method can avoid an additional scattering loss caused in narrower gap. Fig.5.20 shows optical microscope image of pulley nitride waveguide featured on integrated resonator system. As has been discussed in 5.4.3, the width of nitride waveguide is constant in the bending region so as to keep the same phase-matching condition with longer interaction length. The designed waveguide dimension is same with the straight waveguide (900 nm $\times$ 250 nm).

Fig.5.21 shows the transmission scan of TE fundamental mode coupled with pulley waveguide structures, and the measurement result in straight waveguide (Fig.5.19) is also shown

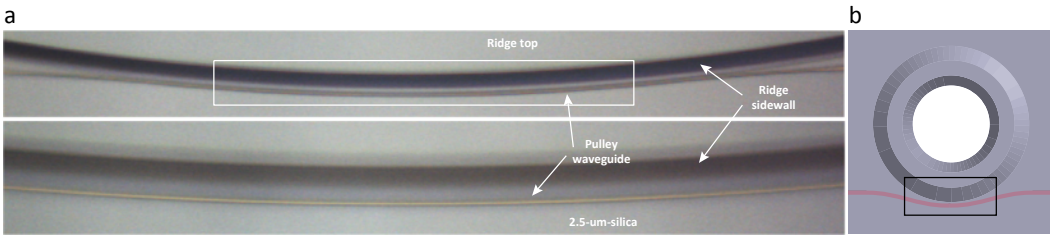

Figure 5.20: **Optical microscope image of pulley waveguide structure on integrated resonator** (**a**) Top view of pulley waveguide structure on integrated resonator. Upper panel is the image with lower magnification which has wider field of view. Nitride waveguide has bending radius in order to increase interaction length at the coupling regime, and the waveguide width is tapered simultaneously. Lower panel shows zoom-in optical microscope image. (**b**) Schematic illustration of pulley waveguide on integrated resonator. Square box corresponds to the microscope view field in upper panel of **a**.

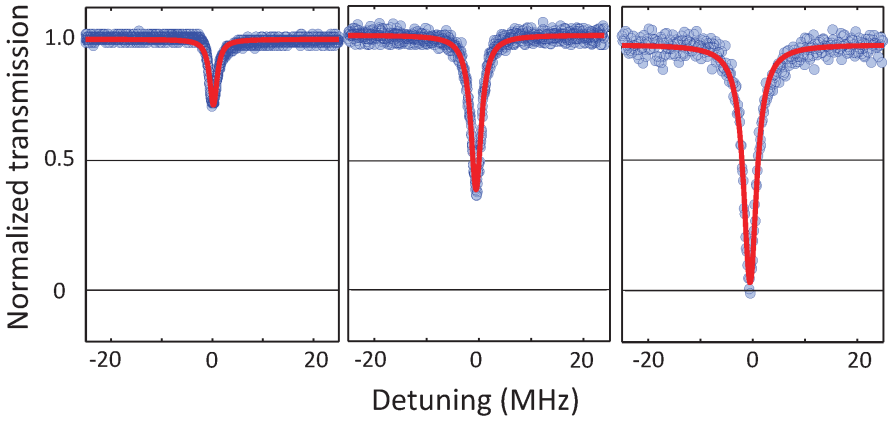

Figure 5.21: **TE0 mode coupling in distinct pulley lengths** High resolution zoom-in spectral scan of TE0 mode in straight (left panel) and pulley nitride waveguide. The power coupling to the resonance mode increases from 25 % to 100 % as a function of interaction length. Red curve represents Lorentzian fitting, and blue dots are measured transmission. The fiber interferometer was calibrated the laser detuning. The left panel is edited from Yang et al.[199].

for comparison (left panel). The measured mode families on the transmission scan were identified using comparison between broadband mode spectrum and numerical simulation – measured FSR and fitted D_2 are generally used for comparison with numerical simulation[55, 71]. Tapered fiber was used for mode spectrum measurement, and the taper can find all transverse mode families existing in silica resonator – nitride waveguide may not couple to every transverse mode families in resonator. According to the measurement results, it is confirmed that Q_0 of TE0 mode from different waveguide structures are consistent (120 M, 25 %; 110 M, 60 %; 130 M, 100 %), and it thereby shows that there is no unpredicted issue that cause an additional parasitic loss in pulley waveguide coupler. In addition, it is interesting to note that the critical coupling condition (right panel; 200 μm pulley length)

was maintained over 100 nm spectral span.

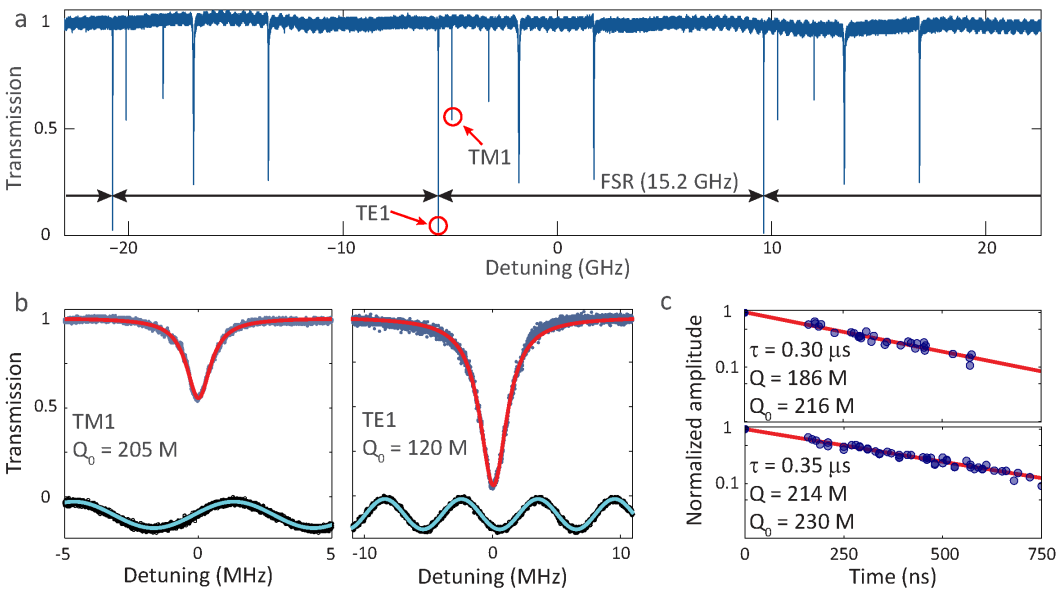

Figure 5.22: **Spectral scan of integrated ridge resonator (200-μm long Pulley SiN waveguide coupling) and ring down measurement** (**a**) Spectral scan encompassing two free-spectral-ranges. (**b**) High resolution zoom-in scan for the TM0 and TE0 modes with intrinsic (Q_o) and loaded (Q) quality factors (M = million). The green sinusoidal signal is a frequency calibration scan using a radio-frequency calibrated fiber Mach-Zehnder interferometer (free-spectral range is 5.979 MHz), and the red line is Lorentzian fitting. (**c**) Superposition of 10 cavity-ringdown signal scans for the TM0 mode with the corresponding decay time and the loaded and intrinsic Q factors. Upper panel was measured from the wavelength of **b**, and lower panel shows the ring down measurement featuring 230 M at 1560 nm wavelength. This figure is edited from Yang et al.[70].

Fig.5.22a shows a spectral scan of integrated resonator with pulley nitride waveguide. The spectral scan encompasses over two FSRs and the pulley length is 200 μm in this measurement. The device tested had a FSR of approximately 15.2 GHz (corresponds to 4.3-mm-diameter), and several mode families appear within one FSR in the scan. High-resolution scans of the TE and TM fundamental mode families are presented in Fig.5.22b. The detuning frequency are calibrated using Mach-Zehnder fiber interferometer (green sinusoidal curve at the lower half of each panel). A linewidth fitting gives Q_0 of 120 million for the TE fundamental mode and 205 million for the TM fundamental mode. Cavity ring dwon was performed[197] to further confirm the Q factor of TM fundamental mode. The ring down scans were conducted over 10 times with different scan speed, and the superposition of the traces is presented in Fig.5.22c. Upper panel shows the ring down trace from the mode in **b**, and gives Q_0 of 216 million in close agreement with the linewidth date. Furthermore, the lower panel shows the ring down trace from the same mode family in different wavelength (1560 nm). A superposition of ring down traces gives fitted Q_0 of 230 million. It is important

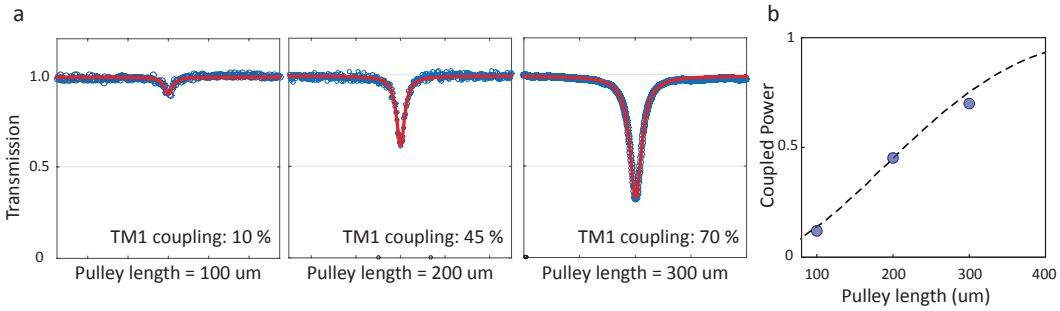

Figure 5.23: **TM0 mode coupling in distinct pulley lengths** (**a**) High resolution zoom-in spectral scan of TM0 mode in pulley lengths from 100 to 300 μm. The power coupling to the resonance mode increases from 10 % to 70 % as pulley length increases. (**b**) TM0 power coupling versus pulley length. Dots are measurement results, and dashed line is the predicted trend from numerical simulations.

to note that coupled TM0 mode was observed in spectral scan[8], and estimated Q_0 is in close agreement with the Q_0 measured with tapered fiber – it proves that there is no additional parasitic loss and ideality of the coupling is close to one.

Fig.5.23 shows TM0 mode coupling in distinct pulley lengths (pulley length = 100, 200, 300 μm from the left to the right panel in **a**). Only 10 % of power was coupled to TM0 mode with 100 μm pulley length, while 70 % of power was coupled to the same mode if the pulley length is 300 μm. The mode coupling trend shows close agreement with numerical prediction, and it prospects higher coupling strength (TM0 resonance mode with TE waveguide mode) with longer pulley length. Table.5.3 is summarized results discussed here.

	TM0	TE0
$Q_{0,taper}$	200 - 250 M	120 - 130 M
$Q_{0,SiN}$	230 M	130 M
$P_{coupled}$	0.7	1

Table 5.3: **Mode coupling and measured Q in pulley nitride waveguide**

[8]TM0 wasn't observed in the spectral scan from straight nitride waveguide.

5.5.2.4 Prospects for higher mode coupling

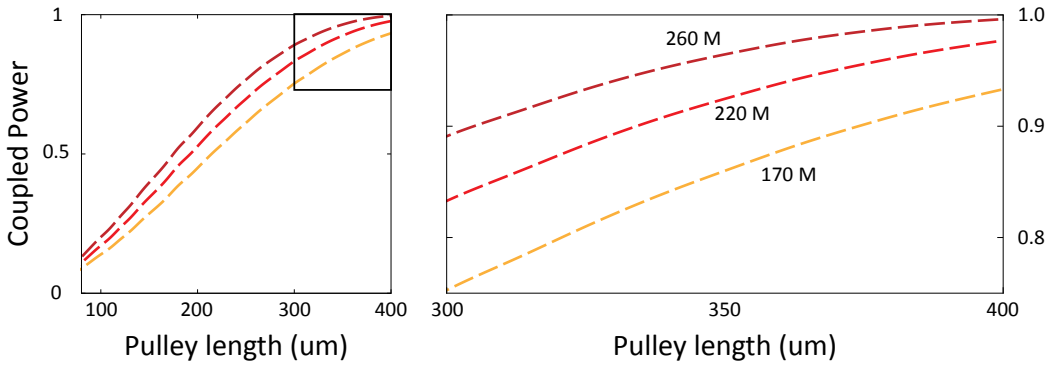

Figure 5.24: **Resonator-coupler design towards higher coupling strength on TM0 mode** The predicted power coupling is shown as a function of pulley length and Q_0 of TM0 mode. Here, the waveguide dimension is 900 nm × 250 nm.

Fig.5.24 shows the prediction of TM0 mode coupling as a function of pulley length and Q_0. The waveguide dimension is 900 nm × 250 nm, and the gap between the waveguide coupler and resonator is 0 μm. The mode coupling (represented using device power transmission T) is mediated using two parameters – pulley length and Q_0. Pulley length mediates external coupling rate (κ_{ext}), and Q_0 modifies the internal cavity loss rate (κ_0) as shown below:

$$T = (1 - \frac{2}{(\kappa_{ext}/\kappa_0)^{-1} + (\kappa_{ext}/(\kappa_{ext} + \kappa_p))^{-1}})^2 \tag{5.6}$$

where κ_p is parasitic loss rate, but it is negligible in the system. In specific waveguide dimension and gap, the external coupling rate per unit length ($\Delta\kappa_{ext}$) is determined, and the external coupling rate (κ_{ext}) is $sin(\Delta\kappa_{ext} \times l)$ (l is pulley length, and assuming phase mismatch is zero) – longer pulley induces higher external coupling rate. Q_0 of TM0 mode corresponds to internal cavity loss rate (κ_0) – higher Q_0 cavity needs less external coupling rate to achieve critical coupling ($\kappa_0 = \kappa_{ext}$). The numerical results show device power coupling which increases as either pulley length or Q_o increases. Further efforts on those parameters are thereby anticipated to increase modal coupling toward critical coupling (pulley length = 400 μm and Q_0 ~260 M).

5.5.3 Mode spectrum characteristics

5.5.3.1 Mode spectrum engineering of exterior ridge ring resonators

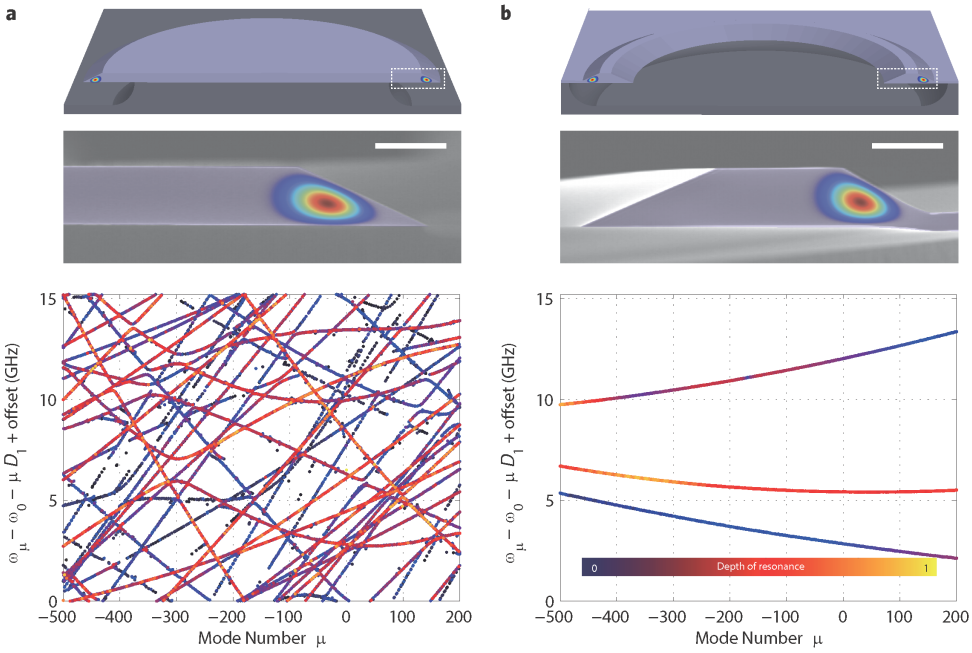

Figure 5.25: **Mode spectra of interior wedge disk- and exterior ridge ring-resonator** (**a**) Upper panel depicts side-view schematic illustration of interior silica wedge resonator (top), and cross-section SEM image (bottom). Mode profile of fundamental mode is overlapped on both rendering and SEM image. The white scale bar indicates 10 μm. The lower panel shows measured mode spectrum using a fiber taper. The laser was scanned from 1520 nm to 1620 nm to find all resonance peaks at single polarization condition. The wavelength at $\mu = 0$ is 1550 nm. FSR of the resonator designed to be 15.2 GHz. (**b**) As (**a**) but for exterior silica ridge resonator. Here, only 3 mode families (TE) were observed without avoided mode crossing in the entire scan range.

Fig.5.25 shows measured mode spectra of interior- and exterior- resonator[9]. In order to compare the mode spectra, both interior- and exterior-resonators are designed to have 15.2 GHz FSR. Wedge angle of interior-resonator is approximately same with the angle of outward sidewall of exterior-resonator ($\theta = 27°$). Tapered fiber was used to measure mode spectra of both interior- and exterior-resonators, and the laser was scanned from 1520 nm to 1620 nm to find all resonance peaks at single polarization condition (TE). The color scale on mode spectra indicates the depth of resonance coupled to taper fiber.

It is interesting to note that only three mode families exist in the exterior ridge ring resonator while interior resonator has over 20 distinct mode families. As shown in SEM images of

[9]Interior resonator is single-wedge and exterior resonator is ridge structure. The oxide thickness is 8 μm, the ridge supporting layer thickness is 2.55 μm, and the ridge width (top surface) is approximately 20 μm

Fig.5.25, the resonator dimensions (e.g. oxide thickness and ridge width) are similar and the ridge structure doesn't confine the optical mode strongly. The outward supporting layer filters out lower-index, higher-order modes. Higher-order modes thereby no longer exist in the exterior ridge structure, or have lower Q factor as a result of the supporting layer. The thickness of supporting layer can adjust the number of existing mode families in the exterior ridge structure. It is also important to note that the mode families have similar FSR in the exterior ridge structure. As a result of similar FSR, mode families don't have either mode line crossing or avoided mode crossing over 700 mode number and 100 nm wavelength span (1520 - 1620 nm).

5.5.3.2 SiN coupled mode spectrum

Fig.5.26 shows the measured mode spectrum from waveguide integrated resonator. Nitride waveguide was used to monitor the transmission spectrum of silica ridge resonator, and silica ridge structure confined less number of mode families than wedge resonator as discussed earlier. TE polarized waveguide was fabricated with pulley length of 200 μm (waveguide dimension: 250 $\times$ 900 nm). According to the spectrum, TE0 mode (Q_0 = 130 M) is almost critical coupled over the whole measurement span, and TM0 mode (Q_0 = 230 M) is under-coupled with 25 - 50 % of contrast. Mode families were identified by comparing the dispersion measurement with finite-element-simulation result. Specifically, the fundamental mode families are indicated on the panel and it is interesting to note that the FSR of fundamental modes are higher than FSR of other mode families[10].

[10] In conventional wedge disk, the fundamental modes have either the lowest or lower FSR than higher order mode[55, 98] Here, the supporting layer adjusts the FSRs of mode families and the fundamental mode has the highest FSR in ridge structure.

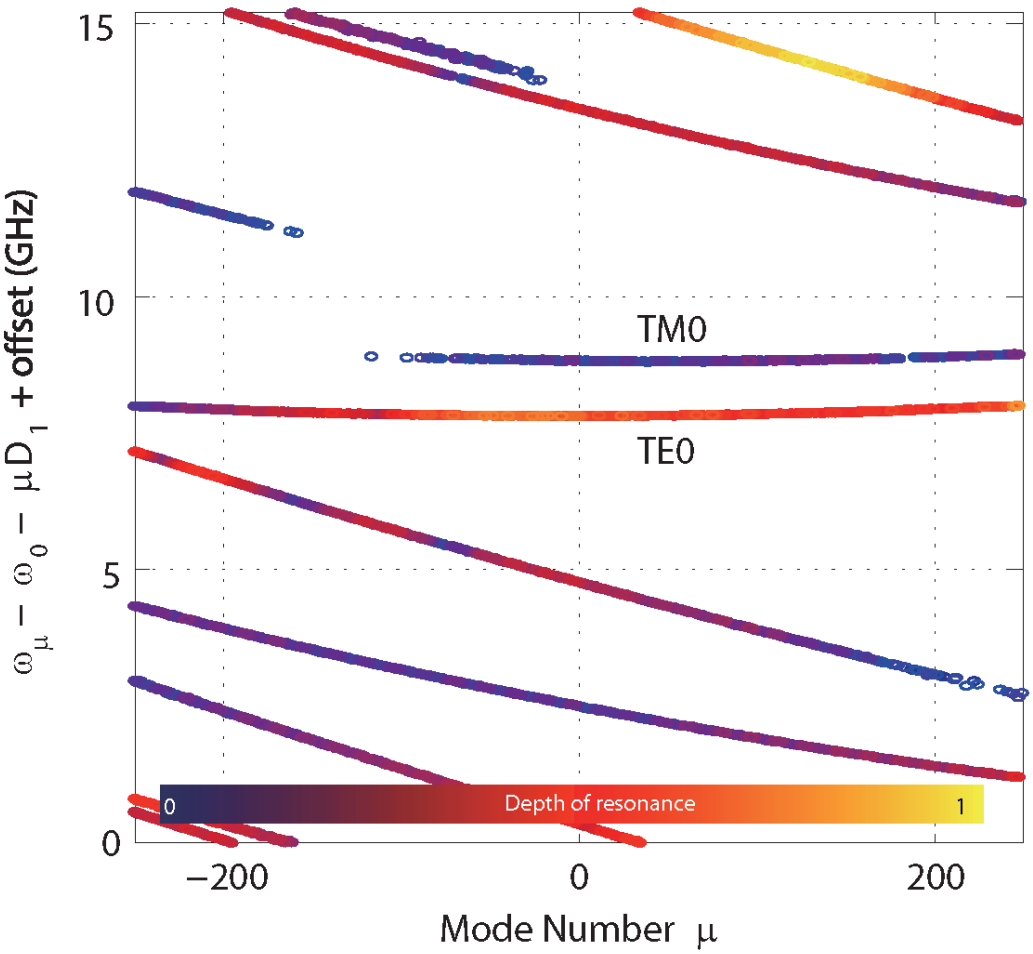

Figure 5.26: **Mode spectrum of nitride waveguide integrated ridge resonator** Measured mode spectrum of fully integrated silica ridge resonator (pulley length = 200 μm). The transmission spectrum was measured through nitride waveguide, so the depth of resonance (color scale) is a function of the external coupling rate between nitride waveguide and the transverse mode family. TM0 and TE0 modes are indicated on the panel, and the modes were identified by comparing the mode spectrum with numerical simulations[55, 71].

5.6 Integrable soliton frequency comb generation

Soliton frequency microcombs [43, 47, 55, 207, 208] can potentially miniaturize optical clocks, frequency synthesizers and precision spectroscopy systems into chip scale systems. To date, integrated soliton microcombs have achieved remarkable performance including highly reproducible optical spectra with 2/3 and full octave span coverage at THz repetition rates [43, 193]. However, in order to self-reference a comb it is essential that the repetition rate be detectable. To attain detectable repetition rates in a microcomb, the cavity mode volume must be substantially increased to reduce the resonator free-spectral-range to microwave rates[50]. To avoid impractically-high pumping power, the greatly increased stored energy

of the larger mode volumes must be accommodated by stronger resonant build-up and hence a more stringent requirement on high Q factor. To date, only non-integrable crystalline and silica resonators have been used[47, 55]. Furthermore, to maintain low pump power in an octave-spanning, self-referenced microcomb system, the comb formation can be broken down into a THz-rate comb (micrometer-scale resonator diameter), and an electronics-rate comb (centimeter-scale resonator diameter)[171]. While the octave-span THz-rate soliton microcomb has been realized[193, 194], the electronics-rate soliton microcomb has not so far been possible in a waveguide-integrated form, because it requires ultra-high-Q factors to avoid excessive pump power.

In this section, an integrable soliton microcomb having a detectable repetition rate of 15 GHz is demonstrated in an ultra-high-Q silica ridge-ring resonator. The Q factors of the integrated resonator are greater than 200 million as discussed in previous section, and the 200 million mode was identified as TM0 mode which has fulfilled the requirements for soliton generation – (i) anomalous dispersion and (ii) minimized avoided mode crossing. Besides, TE0 mode also recorded Q factor over 100 million with soliton forming requirements. The transverse mode family has higher external coupling rate with nitride waveguide, so it achieved critical coupling around 1550 nm. Soliton generation in both polarized mode will be discussed, and the investigation on minimum operating power will be followed.

The integrable electronic rate soliton source represents a critical advance that can be used in newly proposed miniature optical-synthesizers [171], secondary time standards [173], and compact spectroscopy systems [14], all of which require electronic-compatible rate, integrable microcombs.

5.6.1 Soliton frequency comb generation in silica ridge resonator

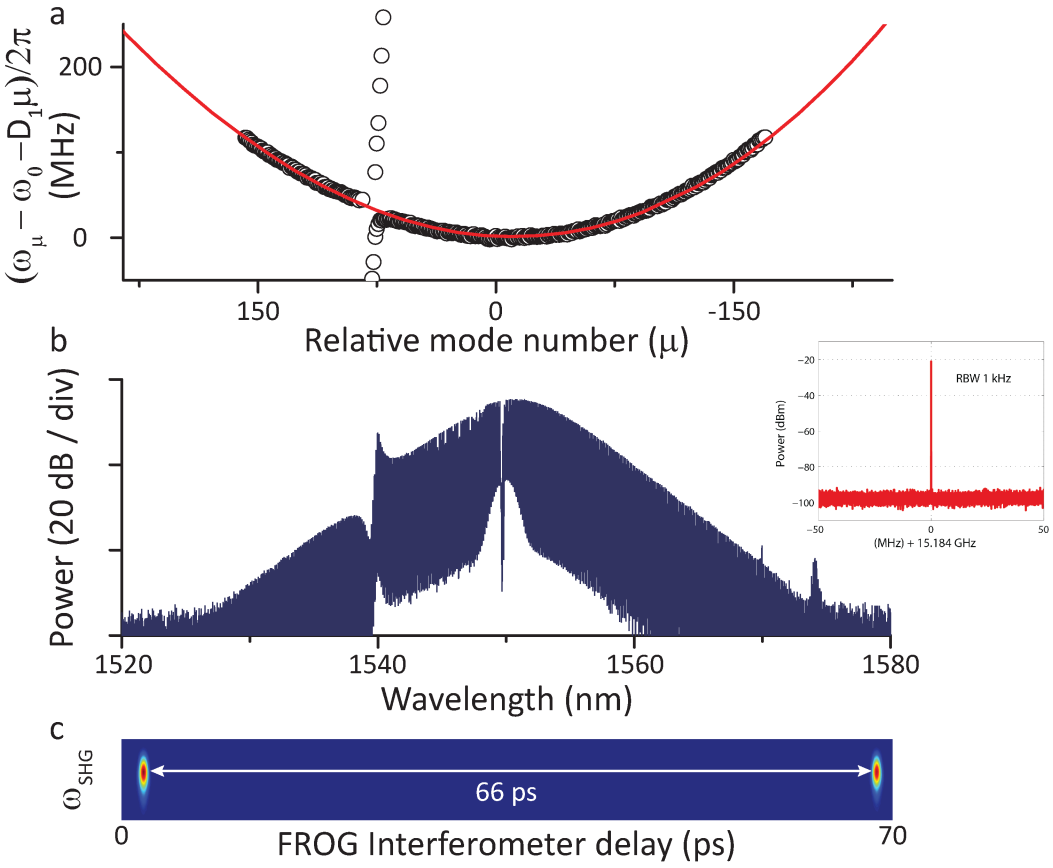

Figure 5.27: **Soliton frequency comb generation in silica ridge resonator (taper coupled)** (**a**) Measured mode spectrum of TM0 in silica ridge structure. Tapered fiber is used to find all TM0 resonance peak from 1520 nm to 1580 nm. Fitted D_1 = 15.1854 GHz, D_2 = 9 kHz/FSR. (**b**) Optical spectrum of soliton microcomb in silica ridge resonator. The presence of small spurs in the spectrum correlate with the appearance of avoided mode crossing in **a**. Inset shows the electrical spectrum of the detected soliton pulse stream. (**c**) frequency resolved optical gating (FROG) scan of single soliton state in **b** showing the single pulse signal. The pulse period is 66 ps.

As preliminary test, soliton frequency comb was demonstrated in silica ridge resonator using taper fiber coupler. The silica ridge resonator doesn't feature the nitride waveguide on a chip, so there is no external coupling loss from other than taper fiber coupler. Q_0 of TM0 mode is approximately 200 million, and the measured mode spectrum is shown in Fig.5.27a. The mode number $\mu = 0$ corresponds to approximately 1550 nm, and the mode spectrum was measured from 1520 nm to 1580 nm using scanning diode laser[55]. There is one minor mode crossing around at $\mu = 70$ with higher order mode, and group velocity dispersion is anomalous ($D_2 = 9kHz/FSR$) around 1550 nm. Using the power kick and active capture technique[118], solitons were triggered and stabilized at continuous wave pump. Fig.5.27b

shows an optical spectrum of a single soliton state, and the frequency resolved optical gate (FROG)[47] method was used to confirm the soliton pulse stream in Fig.5.27c. The pulse period is 66.5 ps corresponding to the resonator round-trip time, and it corresponds to the repetition rate of the comb (15.2 GHz). In addition, threshold power of parametric oscillation is around 8 mW and the measured soliton power is around 10 μm.

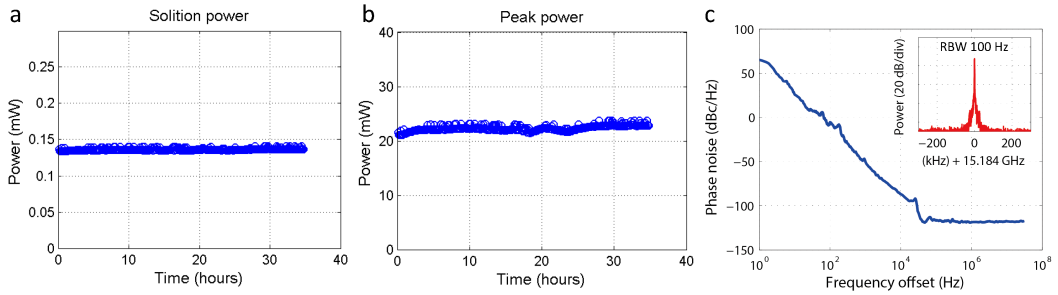

Figure 5.28: **Soliton frequency comb stability and phase noise performance** (**a-b**) Continuous soliton measurement over 30 hours. The soliton power (**a**) and the peak power (**b**) are plotted versus time in hours. The soliton power experiences a slow drift which is attributed to a slow variation in power set point and detected power. (**c**) Detected phase noise and electrical spectra. Inset shows the electrical spectrum of the soliton repetition frequency (15.2 GHz) from silica ridge resonator (taper coupled).

Fig.5.28 shows further investigations on generated soliton comb – stability of soliton power and phase noise of RF beatnote. As has been already demonstrated in Ref[55], the soliton in silica disk performs highly stable over long time operation as well as low phase noise performance. Panel **a-b** show soliton total power and peak power versus operating time, and interestingly the operation was continued over 30 hours without serious variations. Panel **c** shows the measured phase noise spectrum from detected RF beatnote. Inset shows zoom-in RF beatnote scan from the optical spectrum in Fig.5.27 (resolution bandwidth = 100 Hz; Span = 500 kHz).

5.6.2 Integrated soliton comb generation

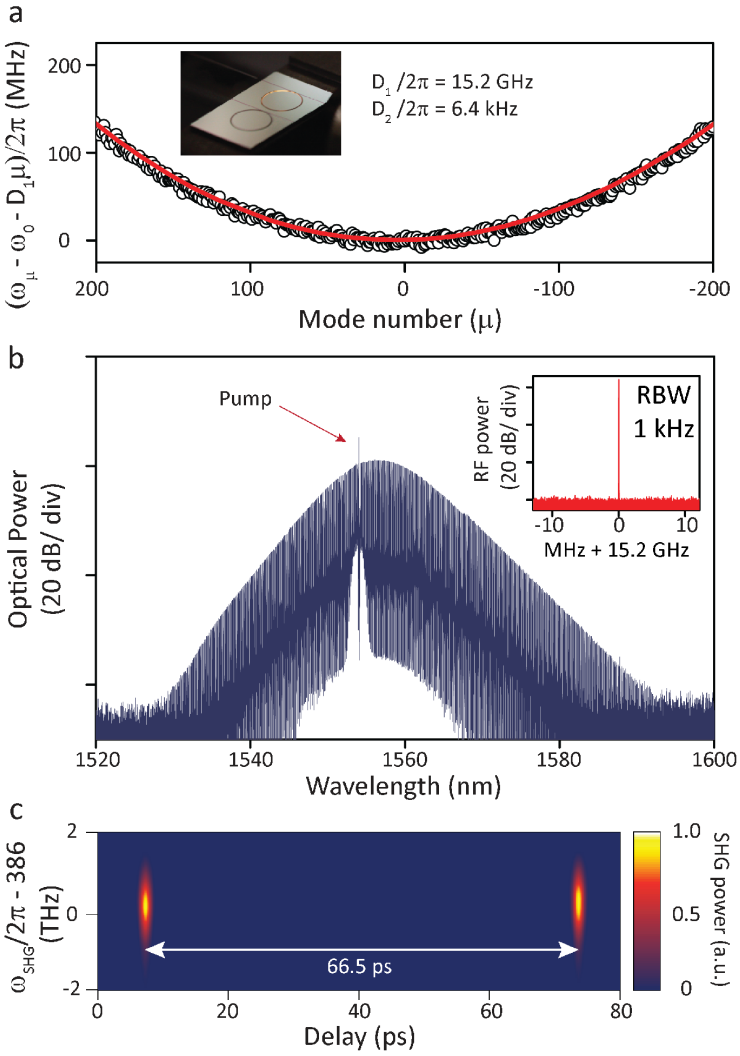

Figure 5.29: **Soliton frequency comb generation (TE0, Q = 100 M) in integrated resonator (SiN coupled)** (**a**) Measured mode spectrum for the TE0 mode family with linear dispersion offset. The red line is a parabola fitting on the mode frequencies over 400 modes. (**b**) Optical spectrum of single soliton. Inset shows the electrical spectrum of the detected soliton pulse. (**c**) FROG scan of single soliton state. This figure is from Yang, et al.[70]

As a preliminary test, a critically coupled TE0 mode was used for soliton generation. The critical coupling was achieved over 50 nm span around 1550 nm, and intrinsic Q factor of the TE0 mode was around 100 - 110 million over the measurement bandwidth. Fig.5.29a shows measured mode spectrum of TE0 mode with linear dispersion offset. The mode frequencies were measured from 1520 nm to 1580 nm, and surprisingly the mode spectrum doesn't show any avoided crossing with other mode families. The red line us a parabola fitting on the mode spectrum, and fitted dispersion is $D_1/2\pi$ = 15.2 GHz and $D_2/2\pi$ = 6.4 kHz. The active capture technique [118] was used to trigger and stabilize solitons at continuous wave

(CW) pump. Fig.5.29b shows an optical spectrum of a single soliton state, and the soliton was directly detected and analyzed on an electrical spectrum analyzer in order to confirm the detectable repetition rate. The inset shows RF beatnote scan near 15.2 GHz (resolution bandwidth: 1kHz), and the beatnote shows narrow and high signal-to-noise ratio single tone. To confirm the soliton state as well as pulse-like nature of the solitons, FROG was used (Fig.5.29c). The pulse period were measured to be 66.5 ps corresponding to the resonator round-trip time. In the same device, TM0 mode was also coupled to nitride waveguide through transmission scan and the intrinsic Q factor of the mode was as high as 180 million. However, the power coupling rate was around 10% so that higher pump power needs to be loaded through nitride waveguide in order to couple sufficient energy to the mode.

Soliton in Fig.5.30 and 5.31 were generated in different device with slight modification on waveguide-resonator coupling – the intrinsic Q factor of the mode were improved too. First, Fig.5.30 shows single soliton generated in TE0 mode and the intrinsic Q factor of the mode was improved from 100 million in Fig.5.29 to 130 million while maintaining the critical coupling. Mode spectrum of this device is shown in Fig.5.26, and the spectrum confirmed that dispersion of TE0 mode is D_1 = 15.2 GHz D_2 = 6.5 kHz (almost consistent with the previous device in Fig.5.29). RF beatnotes and FROG traces were confirmed for clarifying the state of soliton as well as microwave signal quality.

It is worth to note that this soliton was triggered and stabilized using active capturing with operating power as low as 61 mW. It is promising result considering maximum power level of integrated semiconductor optical amplifier (SOA)[209, 210] and on-chip lasers[211, 212].

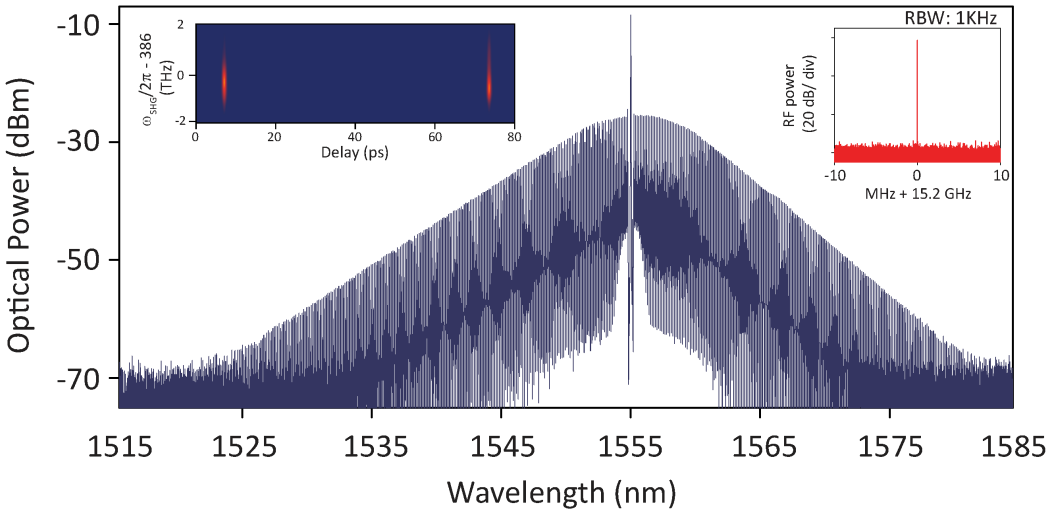

Figure 5.30: **Soliton frequency comb generation (TE0, Q = 130 M) in integrated resonator (SiN coupled)** Measured optical spectrum of single soliton from TE0 mode. Left inset shows FROG trace from the single soliton state and the pulse duration corresponds to cavity round trip time. Right inset shows RF beatnote near 15.2 GHz.

Further investigation on operating power will be discussed in following section.

Fig.5.31 shows soliton generation in TM0 mode. The intrinsic Q factor of TM fundamental mode was as high as 230 million, and also the Q factor was 210 million around 1550 nm. Coupled power was around 25 % at 1550 nm, yet it is not sufficient to trigger soliton efficiently. However, it was possible for soliton generation because of high Q factor. Mode spectrum of the TM0 mode was provided in Fig.5.26, and the spectrum confirmed that dispersion of TM0 mode is approximately D_1 = 15.2 GHz D_2 = 6.0 kHz. One minor mode

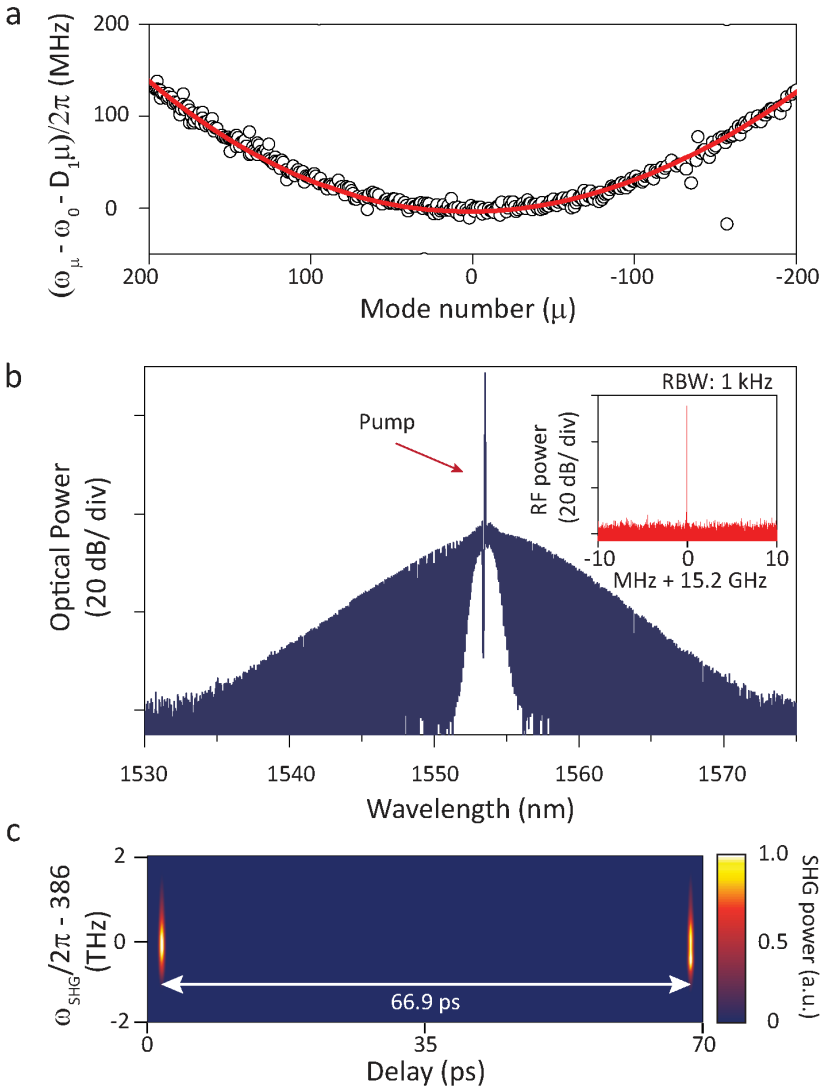

Figure 5.31: **Soliton frequency comb generation (TM0, Q = 210 M) in integrated resonator (SiN coupled)** (**a**) Measured mode spectrum for the TM0 mode family with linear dispersion offset. The red line is a parabola fitting on the mode frequencies over 400 modes. (**b**) Optical spectrum of single soliton. Inset shows the electrical spectrum of the detected soliton pulse. (**c**) FROG scan of single soliton state.

crossing was observed around μ = -150, however the strength is not strong enough and far enough from the pump mode. Panel **b** and **c** shows optical spectrum, RF beatnote, and FROG trace in order to confirm the soliton state.

5.6.3 Discussion on soliton operating power

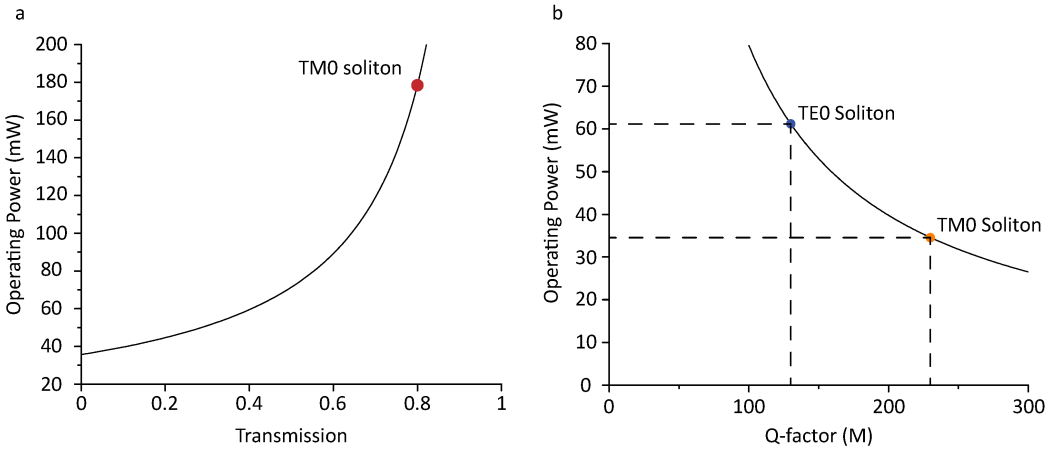

Figure 5.32: **Soliton operating power** (**a**) Operating power versus coupled power. Unity transmission means zero power coupling, and zero transmission corresponds to 100 % power coupling. For the calculation, Q_0 = 210 million was used. (**b**) Operating power versus intrinsic Q factor (Q_0). Critical coupling was assumed for this calculation, and experimental value from TE0 (61 mW) is indicated on the panel with predicted value from TM0 ($\approx$ 35 mW)

Fig.5.32 shows operating power as a function of either resonator-waveguide coupling or intrinsic Q factor of the resonator (assuming critical coupling). As discussed in eqn.3.18, the soliton operating power is given as a function of multiple variables including waveguide-resonator coupling (η), Q factor, mode volume (A_{eff}), dispersion (β_2), and pulse width (τ)[47, 55]. Here, mode volume and dispersion are inherently given with silica ridge resonator and let's fix the frequency comb bandwidth (corresponds to pulsewidth) for simplicity. Then the operating power is inverse proportional to $\eta = Q/Q_{ext}$ and total Q factor.

Fig.5.32a shows the operating power versus waveguide-resonator coupling. The TM0 mode dots in the panel was from the result in Fig.5.31, and it shows rapid power drop at critical coupling point (as low as 39 mW). Fig.5.32b shows operating power versus intrinsic Q factor. The operating power equation is indeed following total Q factor, but we fixed the η at critical coupling in this calculation. It is predicted that the TM0 mode can operate soliton with the power as low as 35 mW in critical coupling point, and further improvement of Q factor can decrease the power level below 30 mW. It is also interesting to note that the estimated power level with Q of 300 million is in the similar level with the power level in Ref[118] (300 million 21 GHz soliton with 22 mW operating power).

5.6.4 Integrated soliton frequency comb technologies

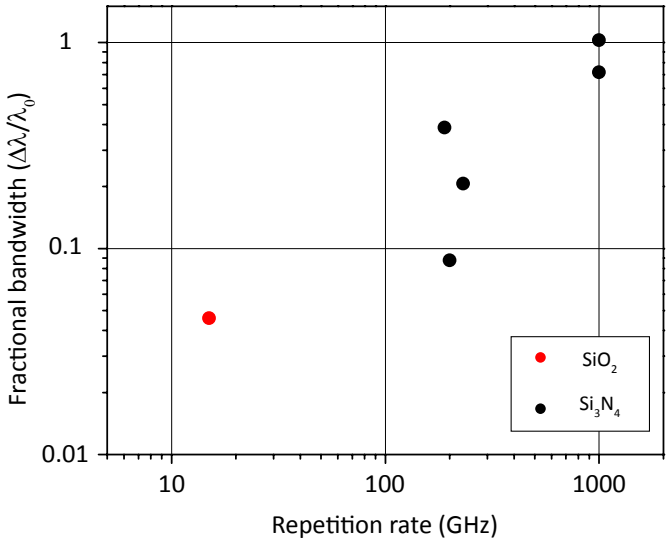

Figure 5.33: **Integrated soliton frequency comb technologies as a function of repetition rate and fractional bandwdith** Chip-integrated soliton technologies are represented as a function of repetition rate and their fractional bandwidth(the definition is from Kippenberg, et al.[5]). The dots denote recently developed integrated soliton sources with corresponding material choice of the platform. This includes silicon nitride[43, 193, 194, 207, 208] and silica integrated resonators[70].

Fig.5.33 reviews integrable soliton frequency combs on nitride[43, 193, 194, 207, 208] and silica platforms[70]. Horizontal axis represents the repetition rate of soliton comb, and vertical axis represents the fractional bandwidth given as $\Delta\lambda/\lambda_0$ ($\Delta\lambda$ is comb bandwidth, and λ_0 is pump wavelength). Li, et al.[194] and Pfeiffer, et al.[193] separately demonstrated octave spanning soliton comb with 1 THz repetition rate. It is remarkable to operate the octave span comb with sub 100 mW power level[194], and those platform can be used for $f-2f$ self-referencing. There have been also several demonstration in 200 GHz repetition rate from different groups.

However, as noted above, a electronics-compatible rate (<20 - 30 GHz repetition rate) soliton comb using an integrable device platform has not yet been realized and this is one of essential gear to realize direct control of optical frequencies using electronics – THz octave comb can detect carrier offset frequency and estimate the repetition rate, but not directly detect and stabilize the repetition rate[11]. Therefore, as a demonstration of the new performance capability provided by the integrated resonator, the 15 GHz soliton stream was generated with chip-compatible operating power.

[11]The octave span comb is another essential component to detect and stabilize the offset frequency[5], but the lower-repetition-rate comb has challenges on the broadband operation under chip-compatible power consumption. The alternative solution will be discussed in the next section.

5.7 Discussion

This section will discuss the applications of the integrated UHQ resonators towards photonic system-on-a-chip, and we have been participating on the collaboration with multi-institutes and industry under the support of Defense Advanced Research Projects Agency (DARPA). In addition, the integrated UHQ resonator demonstrated high coherence Brillouin lasing action[70] but more detail and discussion are not included in this thesis.

5.7.1 Chip-integrated self-referenced soliton comb[12]

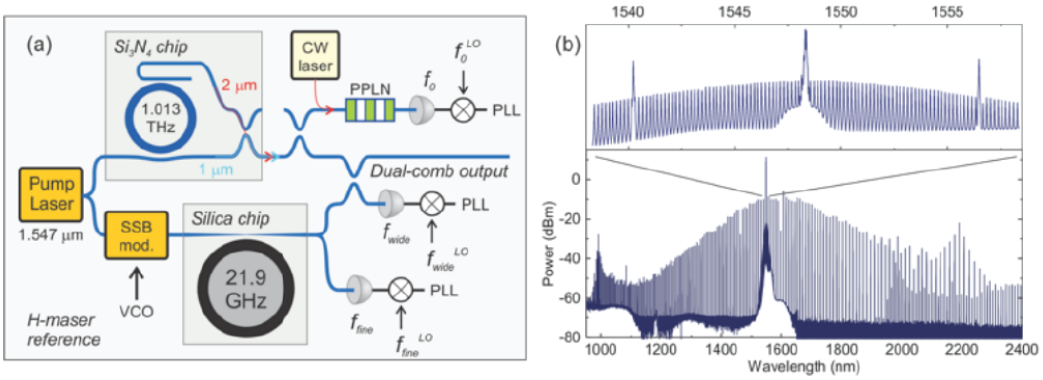

Figure 5.34: **Microresonator-based self-referenced soliton frequency comb** (**a**) Self-referenced comb system illustration. The self-referenced comb is stabilized using three PLL setpoints (f_{fine}^{LO} for 21.9 GHz comb spacing, f_{wide}^{LO} for 1.013 THz comb spacing, and f_0^{LO} for offset frequency). (**b**) Optical spectrum of the dual frequency combs (1.013 THz comb and 21.9 GHz comb). The upper panel shows c-band comb spectrum (stronger sidebands are 1 THz comb signals, and weaker fine combs are 21.9 GHz comb signals), and the lower panel shows octave spanning THz comb with overlapped 21.9 GHz comb. Dual dispersive waves are also appeared at 992 nm and 2190 nm. This schematic is from Briles, et al.[213].

Frequency comb can provide numerous applications, and the photonic integration of soliton combs with pump laser, modulators, $f-2f$ stabilization, and photodiodes offers the possibility of chip-integrated frequency comb system. One outstanding challenge is detection and stabilization of carrier offset frequency (f_{CEO} in Chapter 1). Here, the system complexity and power consumption should be chip-compatible. The previous demonstration of self-referenced microcomb requires external spectral broadening that brings the necessity of additional amplifiers and extra power consumption[214].

One unique feature that microresonators solely can provide is a high repetition rate (i.e. 1 THz repetition rate) soliton frequency comb[5, 193, 194] – this is very challenging with other photonic system. Interestingly, the repetition rate scales inverse with spectral bandwidth and power consumption. The octave-span, high repetition rate soliton comb was demonstrated with chip compatible power consumption level[194]. This feature can alter the external

[12]This section added more detail after discussion with Prof. Emami in thesis defense.

spectral broadening when the comb is locked with stable detectable rate frequency comb (21.9 GHz comb in Fig.5.34a) that can detect and stabilize the spacing of 1 THz comb (1.013 THz comb in Fig.5.34a)[13].

It is worth tracking the comb stabilization steps using microwave system clock[73]. First, microwave-repetition-rate silica comb signal is photo-detected and phase-locked to clock signal ($f_{fine} = 2190 \times f_{fine}^{LO}$ and let's set $f_{fine}^{LO} = f_{wide}^{LO} = f_0^{LO} = 10$ MHz and they are phase-locked). Second, 1 THz comb spacing is detected using the heterodyne beat note between nitride comb line which is 1 THz away from pump and the nearest silica comb line (46th relative comb). The heterodyne beat note can be given as $f_{wide} = \alpha f_{wide}^{LO}$ where α is the ratio of two integers, and the 1 THz comb spacing can be expressed as $46 \times (2190 \times f_{fine}^{LO}) + \alpha f_{wide}^{LO}$. The next step is detecting and stabilizing the offset frequency. Here, we have independent laser at 1998 nm where one of dispersive waves are appeared (Fig.5.34b), and we define the heterodyne beat note between the laser and comb line as f_{1998}. The independent laser is doubled using periodically poled Lithium Niobate (PPLN), and the frequency-doubled light generates another beatnote (f_{999}) with comb line at 999 nm. Then, the offset frequency is $f_0 = f_{999} - 2 \times f_{1998}$, and the signal can be processed using electronics and phase-locked with system clock[73]. Here, the monolithic second harmonic generation has been demonstrated[215, 216], and the technologies can be potentially integrated with the frequency comb system. In addition, the advanced dispersion engineering[43, 71, 142] can improve the signal intensities of dispersive waves at 999 nm and 1998 nm, so can eliminate the external laser from the system.

As discussed, the monolithic low-repetition-rate soliton source detects and stabilizes 1-THz-comb spacing. The low-repetition-rate comb transfers the stability of microwave reference to 1-THz-comb lines over octave span (i.e. 130 THz to 300 THz [73]), however hasn't been demonstrated in any integrated platform. First, low-repetition-rate requires larger mode volume (i.e. 10-GHz-comb needs 100X mode volume assuming same mode area) and the operating power of frequency comb scales linear with the mode volume. Second, soliton frequency comb requires additional dispersion engineering[14] but the cavity design interplays with not only dispersion but also Q factor of microresonator. It is very challenging to control dispersion properties while maintaining Q factor. Integrated UHQ resonator discussed in this chapter can be perfect solution for integrated comb system.

5.7.2 Optical frequency synthesizer

The phase-coherent synthesize of optical frequencies can have impact on numerous applications, as the electronics revolution that began in the mid-20 century was partly driven by the synthesize of radio and microwave synthesize[73]. Here, the stabilized frequency comb

[13] The integrated low-repetition-rate soliton comb has also remained elusive prior to the work in this thesis.

[14] Dispersion engineering includes not only chromatic dispersion control but also mode-spectrum-engineering that we have discussed in Chapter 3.

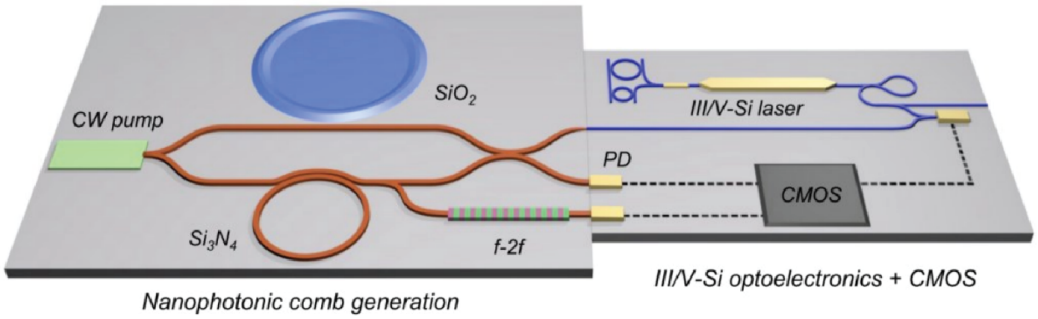

Figure 5.35: **Integrated photonic frequency synthesizer system** The conceptual schematic of integrated optical frequency synthesizer. Nanophotonic comb generator consists of GHz comb (SiO_2), THz comb (Si_3N_4), CW pump, and $f-2f$ stabilization; III/V optoelectronics + CMOS consists of III/V silicon laser, photodiodes, and CMOS circuits. Both comb generator and optoelectronic chip share 10 MHz system clock. This schematic is from Spencer, et al.[73].

serve as the backbone to guide the tunable laser to arbitrary frequencies across the spectral span that lower-repetition-rate comb can cover. The comb system can provide the frequency uncertainty of Hz level over hundreds THz absolute frequencies[213]. The III/V silicon-ring-resonator laser[217] is the synthesizer output, and is phase-coherent with frequency comb system. The wide frequency tuning can be achieved through heaters on the two ring resonators and intracavity phase section (modulation speed: upto 10 kHz)[15], and low-loss Si waveguide can reduce the linewidths to 300 kHz.

Biased heater of III/V-Si laser shifts the lasing frequency for initial alignment to comb lines (the comb line location is addressed from the system input, and CMOS circuits control the initial heater settings). Then the combined optical spectra of low-repetition-rate comb and integrated laser produces the heterodyne beatnote which can be stabilized using a FPGA based phase-locked-loop (PLL) with system clock[73]. The final synthesizer output (f_{output}) can be expressed[73]:

$$\begin{aligned} f_{output} &= 192 \times f_{rep,THz} + m \times f_{rep,GHz} + f_{laser} \\ &= f_{clk}[192(46 \times 2197 + \alpha) - 64 \times \beta + m \times 2197 + 512 \times \gamma] \end{aligned} \tag{5.7}$$

where $f_{rep,THz}$, $f_{rep,GHz}$, f_{laser}, f_{clk} are the repetition rate of THz comb (1.019 THz), the repetition rate of GHz comb (21.97 GHz), the heterodyne beatnote between GHz comb and integrated Si laser, and the system clock frequency (10 MHz), respectively. Here, the offset frequency is divided by 64 and phase-locked to f_{clk} with the factor β; the heterodyne beatnote between laser and comb is divided by 512 and phase-locked to f_{clk} with the factor

[15] Fine, high-speed feedback control can be achieve through semiconductor optical amplifier (SOA) current (modulation speed: GHz)[171].

γ. As discussed in previous subsection, the THz comb spacing was detected using the heterodyne beatnote between GHz comb and THz comb, and the signal is phase-locked to f_{clk} with the factor α. The frequency output is defined relative to input clock in terms of integer m and the control factors (α, β, γ).

5.7.3 Chip-integrated optical clock

The frequency comb system can directly phase-link microwave with optical wave[39, 56]. The optical atomic transitions have been recognized as the most advanced technology for precision time keeping due to enhanced line quality factor as well as its stability[57]. The two-photon Rubidium transition at 778 nm (385 THz) has the 330 kHz natural linewidth which corresponds to 10^9 Q factor. The splitting the line to part in 10^4 can achieve 10^{-13} retrace and environment stability[218]. The atomic transition at optical domain can be used to synthesize microwave signal by using frequency comb system. The Rubidium atom can be confined in microfabricated vapor cell and the chip-integrated frequency comb (c.f. subsection 5.7.1) can perform optical frequency division[173].

BIBLIOGRAPHY

[1]K. J. Vahala, "Optical microcavities", Nature **424**, 839–846 (2003).

[2]D. Armani, T. Kippenberg, S. Spillane, and K. Vahala, "Ultra-high-Q toroid microcavity on a chip", Nature **421**, 925–928 (2003).

[3]I. S. Grudinin, V. S. Ilchenko, and L. Maleki, "Ultrahigh optical Q factors of crystalline resonators in the linear regime", Physical Review A **74**, 063806 (2006).

[4]D. T. Spencer, J. F. Bauters, M. J. Heck, and J. E. Bowers, "Integrated waveguide coupled Si_3N_4 resonators in the ultrahigh-q regime", Optica **1**, 153–157 (2014).

[5]T. J. Kippenberg, R. Holzwarth, and S. A. Diddams, "Microresonator-based optical frequency combs", Science **332**, 555–559 (2011).

[6]P. Del'Haye, A. Schliesser, O. Arcizet, T. Wilken, R. Holzwarth, and T. J. Kippenberg, "Optical frequency comb generation from a monolithic microresonator", Nature **450**, 1214–1217 (2007).

[7]T. Carmon, and K. J. Vahala, "Visible continuous emission from a silica microphotonic device by third-harmonic generation", Nature Phys. **3**, 430–435 (2007).

[8]S. Spillane, T. Kippenberg, and K. Vahala, "Ultralow-threshold raman laser using a spherical dielectric microcavity", Nature **415**, 621 (2002).

[9]J. Li, H. Lee, and K. J. Vahala, "Microwave synthesizer using an on-chip brillouin oscillator", Nature communications **4** (2013).

[10]M. A. Foster, A. C. Turner, J. E. Sharping, B. S. Schmidt, M. Lipson, and A. L. Gaeta, "Broad-band optical parametric gain on a silicon photonic chip", Nature **441**, 960–963 (2006).

[11]J. S. Levy, A. Gondarenko, M. A. Foster, A. C. Turner-Foster, A. L. Gaeta, and M. Lipson, "CMOS-compatible multiple-wavelength oscillator for on-chip optical interconnects", Nature photonics **4**, 37–40 (2010).

[12]B. Hausmann, I. Bulu, V. Venkataraman, P. Deotare, and M. Lončar, "Diamond nonlinear photonics", Nature Photon. **8**, 369–374 (2014) 10.1038/nphoton.2014.72.

[13]S. B. Papp, K. Beha, P. Del'Haye, F. Quinlan, H. Lee, K. J. Vahala, and S. A. Diddams, "Microresonator frequency comb optical clock", Optica **1**, 10–14 (2014).

[14]M.-G. Suh, Q.-F. Yang, K. Y. Yang, X. Yi, and K. J. Vahala, "Microresonator soliton dual-comb spectroscopy", Science **354**, 600–603 (2016).

[15]P. Marin-Palomo, J. N. Kemal, M. Karpov, A. Kordts, J. Pfeifle, M. H. Pfeiffer, P. Trocha, S. Wolf, V. Brasch, M. H. Anderson, et al., "Microresonator-based solitons for massively parallel coherent optical communications", Nature **546**, 274–279 (2017).

[16]J. Pfeifle, V. Brasch, M. Lauermann, Y. Yu, D. Wegner, T. Herr, K. Hartinger, P. Schindler, J. Li, D. Hillerkuss, et al., "Coherent terabit communications with microresonator kerr frequency combs", Nature photonics **8**, 375–380 (2014).

[17]M. Kues, C. Reimer, P. Roztocki, L. R. Cortés, S. Sciara, B. Wetzel, Y. Zhang, A. Cino, S. T. Chu, B. E. Little, et al., "On-chip generation of high-dimensional entangled quantum states and their coherent control", Nature **546**, 622–626 (2017).

[18]A. González-Tudela, C.-L. Hung, D. E. Chang, J. I. Cirac, and H. Kimble, "Subwavelength vacuum lattices and atom–atom interactions in two-dimensional photonic crystals", Nature Photonics **9**, 320–325 (2015).

[19]A. Goban, C.-L. Hung, S.-P. Yu, J. Hood, J. Muniz, J. Lee, M. Martin, A. McClung, K. Choi, D. E. Chang, et al., "Atom–light interactions in photonic crystals", Nature communications **5** (2014).

[20]T. Kippenberg, S. Spillane, and K. Vahala, "Kerr-nonlinearity optical parametric oscillation in an ultrahigh-q toroid microcavity", Physical review letters **93**, 083904 (2004).

[21]T. Herr, V. Brasch, J. D. Jost, I. Mirgorodskiy, G. Lihachev, M. L. Gorodetsky, and T. J. Kippenberg, "Mode spectrum and temporal soliton formation in optical microresonators", Phys. Rev. Lett. **113**, 123901 (2014) 10.1103/PhysRevLett.113.123901.

[22]H. Lee, T. Chen, J. Li, K. Y. Yang, S. Jeon, O. Painter, and K. J. Vahala, "Chemically etched ultrahigh-Q wedge-resonator on a silicon chip", Nature Photonics **6**, 369–373 (2012).

[23]G. P. Agrawal, *Nonlinear fiber optics* (Academic press, 2007).

[24]Y. K. Chembo, and N. Yu, "Modal expansion approach to optical-frequency-comb generation with monolithic whispering-gallery-mode resonators", Physical Review A **82**, 033801 (2010).

[25]A. N. Oraevsky, "Whispering-gallery waves", Quantum Electronics **32**, 377–400 (2002).

[26]S. Schiller, "Asymptotic expansion of morphological resonance frequencies in mie scattering", Applied Optics **32**, 2181–2185 (1993).

[27]C. A. Fletcher, "Computational galerkin methods", in *Computational galerkin methods* (Springer, 1984), pp. 72–85.

[28]M. Oxborrow, "Traceable 2-d finite-element simulation of the whispering-gallery modes of axisymmetric electromagnetic resonators", IEEE Transactions on Microwave Theory and Techniques **55**, 1209–1218 (2007).

[29]M. Koshiba, K. Hayata, and M. Suzuki, "Improved finite-element formulation in terms of the magnetic field vector for dielectric waveguides", IEEE transactions on microwave theory and techniques **33**, 227–233 (1985).

[30]A. Konrad, "High-order triangular finite elements for electromagnetic waves in anisotropic media", IEEE Transactions on Microwave Theory and Techniques **25**, 353–360 (1977).

[31]M. Hara, T. Wada, T. Fukasawa, and F. Kikuchi, "A three dimensional analysis of rf electromagnetic fields by the finite element method", IEEE Transactions on Magnetics **19**, 2417–2420 (1983).

[32]P. Del'Haye, O. Arcizet, M. Gorodetsky, R. Holzwarth, and T. Kippenberg, "Frequency comb assisted diode laser spectroscopy for measurement of microcavity dispersion", Nature Photonics **3**, 529–533 (2009).

[33]P. Del'Haye, "Optical frequency comb generation in monolithic microresonators", PhD thesis (Ludwig-Maximilians-Universitat Munchen, 2011).

[34]R. W. Boyd, *Nonlinear optics* (Academic press, 2003).

[35]K. Tai, A. Tomita, J. Jewell, and A. Hasegawa, "Generation of subpicosecond solitonlike optical pulses at 0.3 thz repetition rate by induced modulational instability", Applied physics letters **49**, 236–238 (1986).

[36]E. Greer, D. Patrick, P. Wigley, and J. Taylor, "Generation of 2 thz repetition rate pulse trains through induced modulational instability", Electronics Letters **25**, 1246–1248 (1989).

[37]L. F. Mollenauer, R. H. Stolen, and J. P. Gordon, "Experimental observation of picosecond pulse narrowing and solitons in optical fibers", Physical Review Letters **45**, 1095 (1980).

[38]T. Birks, W. Wadsworth, and P. S. J. Russell, "Supercontinuum generation in tapered fibers", Optics letters **25**, 1415–1417 (2000).

[39]D. J. Jones, S. A. Diddams, J. K. Ranka, A. Stentz, R. S. Windeler, J. L. Hall, and S. T. Cundiff, "Carrier-envelope phase control of femtosecond mode-locked lasers and direct optical frequency synthesis", Science **288**, 635–639 (2000).

[40]J. M. Dudley, G. Genty, and S. Coen, "Supercontinuum generation in photonic crystal fiber", Reviews of modern physics **78**, 1135 (2006).

[41]J. M. Dudley, and J. R. Taylor, *Supercontinuum generation in optical fibers* (Cambridge University Press, 2010).

[42]N. Akhmediev, and M. Karlsson, "Cherenkov radiation emitted by solitons in optical fibers", Physical Review A **51**, 2602 (1995).

[43]V. Brasch, M. Geiselmann, T. Herr, G. Lihachev, M. H. Pfeiffer, M. L. Gorodetsky, and T. J. Kippenberg, "Photonic chip–based optical frequency comb using soliton cherenkov radiation", Science **351**, 357–360 (2016).

[44]A. Husakou, and J. Herrmann, "Supercontinuum generation of higher-order solitons by fission in photonic crystal fibers", Physical Review Letters **87**, 203901 (2001).

[45]Y. K. Chembo, D. V. Strekalov, and N. Yu, "Spectrum and dynamics of optical frequency combs generated with monolithic whispering gallery mode resonators", Physical review letters **104**, 103902 (2010).

[46]T. Herr, K. Hartinger, J. mensberger, C. Wang, E. Gavartin, R. Holzwarth, M. Gorodetsky, and T. Kippenberg, "Universal formation dynamics and noise of kerr-frequency combs in microresonators", Nature Photonics **6**, 480–487 (2012).

[47]T. Herr, V. Brasch, J. D. Jost, C. Y. Wang, N. M. Kondratiev, M. L. Gorodetsky, and T. J. Kippenberg, "Temporal solitons in optical microresonators", Nature Photonics **8**, 145–152 (2014).

[48]A. B. Matsko, A. A. Savchenkov, D. Strekalov, V. S. Ilchenko, and L. Maleki, "Optical hyperparametric oscillations in a whispering-gallery-mode resonator: threshold and phase diffusion", Physical Review A **71**, 033804 (2005).

[49]T. J. A. Kippenberg, "Nonlinear optics in ultra-high-Q whispering-gallery optical microcavities", PhD thesis (California Institute of Technology, 2004).

[50]J. Li, H. Lee, T. Chen, and K. J. Vahala, "Low-pump-power, low-phase-noise, and microwave to millimeter-wave repetition rate operation in microcombs", Physical review letters **109**, 233901 (2012).

[51]S. Coen, H. G. Randle, T. Sylvestre, and M. Erkintalo, "Modeling of octave-spanning kerr frequency combs using a generalized mean-field lugiato–lefever model", Optics letters **38**, 37–39 (2013).

[52]L. A. Lugiato, and R. Lefever, "Spatial dissipative structures in passive optical systems", Physical review letters **58**, 2209 (1987).

[53]A. B. Matsko, and L. Maleki, "On timing jitter of mode locked kerr frequency combs", Optics express **21**, 28862–28876 (2013).

[54]S. Wabnitz, "Suppression of interactions in a phase-locked soliton optical memory", Optics letters **18**, 601–603 (1993).

[55]X. Yi, Q.-F. Yang, K. Y. Yang, M.-G. Suh, and K. Vahala, "Soliton frequency comb at microwave rates in a high-Q silica microresonator", Optica **2**, 1078–1085 (2015).

[56]S. A. Diddams, D. J. Jones, J. Ye, S. T. Cundiff, J. L. Hall, J. K. Ranka, R. S. Windeler, R. Holzwarth, T. Udem, and T. Hänsch, "Direct link between microwave and optical frequencies with a 300 thz femtosecond laser comb", Physical Review Letters **84**, 5102 (2000).

[57]S. Diddams, T. Udem, J. Bergquist, E. Curtis, R. Drullinger, L. Hollberg, W. Itano, W. Lee, C. Oates, K. Vogel, et al., "An optical clock based on a single trapped 199hg+ ion", Science **293**, 825–828 (2001).

[58]T. Rosenband, D. Hume, P. Schmidt, C.-W. Chou, A. Brusch, L. Lorini, W. Oskay, R. E. Drullinger, T. M. Fortier, J. Stalnaker, et al., "Frequency ratio of al+ and hg+ single-ion optical clocks; metrology at the 17th decimal place", Science **319**, 1808–1812 (2008).

[59]C. Gohle, T. Udem, M. Herrmann, J. Rauschenberger, R. Holzwarth, H. A. Schuessler, F. Krausz, and T. W. Hänsch, "A frequency comb in the extreme ultraviolet", Nature **436**, 234–237 (2005).

[60]S. A. Diddams, L. Hollberg, and V. Mbele, "Molecular fingerprinting with the resolved modes of a femtosecond laser frequency comb", Nature **445**, 627–630 (2007).

[61]R. J. Jones, K. D. Moll, M. J. Thorpe, and J. Ye, "Phase-coherent frequency combs in the vacuum ultraviolet via high-harmonic generation inside a femtosecond enhancement cavity", Physical Review Letters **94**, 193201 (2005).

[62]I. Coddington, W. Swann, L. Nenadovic, and N. Newbury, "Rapid and precise absolute distance measurements at long range", Nature photonics **3**, 351–356 (2009).

[63]C.-H. Li, A. J. Benedick, P. Fendel, A. G. Glenday, F. X. Kärtner, D. F. Phillips, D. Sasselov, A. Szentgyorgyi, and R. L. Walsworth, "A laser frequency comb that enables radial velocity measurements with a precision of 1 cm s-1", Nature **452**, 610–612 (2008).

[64]T. Steinmetz, T. Wilken, C. Araujo-Hauck, R. Holzwarth, T. W. Hänsch, L. Pasquini, A. Manescau, S. D'odorico, M. T. Murphy, T. Kentischer, et al., "Laser frequency combs for astronomical observations", Science **321**, 1335–1337 (2008).

[65]C.-B. Huang, Z. Jiang, D. Leaird, J. Caraquitena, and A. Weiner, "Spectral line-by-line shaping for optical and microwave arbitrary waveform generations", Laser & Photonics Reviews **2**, 227–248 (2008).

[66]J. J. McFerran, E. N. Ivanov, A. Bartels, G. Wilpers, C. W. Oates, S. A. Diddams, and L. Hollberg, "Low-noise synthesis of microwave signals from an optical source", Electronics Letters **41**, 650–651 (2005).

[67]W. E. Lamb, "Theory of an optical maser", Phys. Rev. **134**, A1429–A1450 (1964) 10.1103/PhysRev.134.A1429.

[68]J. K. Ranka, R. S. Windeler, and A. J. Stentz, "Visible continuum generation in air-silica microstructure optical fibers with anomalous dispersion at 800 nm", Opt. Lett. **25**, 25–27 (2000).

[69]J. Reichert, R. Holzwarth, T. Udem, and T. W. Haensch, "Measuring the frequency of light with mode-locked lasers", Optics communications **172**, 59–68 (1999).

[70]K. Yang, et al., "Bridging ultrahigh-Q devices and photonic circuits", Nature Photonics (2018) 10.1038/s41566-018-0132-5.

[71]K. Y. Yang, K. Beha, D. C. Cole, X. Yi, P. Del'Haye, H. Lee, J. Li, D. Y. Oh, S. A. Diddams, S. B. Papp, et al., "Broadband dispersion-engineered microresonator on a chip", Nature Photonics **10**, 316–320 (2016) 10.1038/nphoton.2016.36.

[72]D. Y. Oh, K. Y. Yang, C. Fredrick, G. Ycas, S. A. Diddams, and K. J. Vahala, "Coherent ultra-violet to near-infrared generation in silica ridge waveguides", Nature Communications **8**, 13922 (2017).

[73]D. T. Spencer, et al., "An optical-frequency synthesizer using integrated photonics", **Nature** (2018) 10.1038/s41586-018-0065-7,

[74]D. Vernooy, V. S. Ilchenko, H. Mabuchi, E. Streed, and H. Kimble, "High-q measurements of fused-silica microspheres in the near infrared", Optics Letters **23**, 247–249 (1998).

[75]H. Lee, M.-G. Suh, T. Chen, J. Li, S. A. Diddams, and K. J. Vahala, "Spiral resonators for on-chip laser frequency stabilization", Nature communications **4** (2013).

[76]S. Wolf, *Silicon processing for the vlsi era* (1995), pp. 559–581.

[77]O. Humbach, H. Fabian, U. Grzesik, U. Haken, and W. Heitmann, "Analysis of oh absorption bands in synthetic silica", Journal of non-crystalline solids **203**, 19–26 (1996).

[78]D. K. Armani, "Ultra-high-q planar microcavities and applications", PhD thesis (California Institute of Technology, 2005).

[79]M. Cai, O. Painter, and K. J. Vahala, "Observation of critical coupling in a fiber taper to a silica-microsphere whispering-gallery mode system", Physical review letters **85**, 74 (2000).

[80]V. Braginsky, M. Gorodetsky, and V. Ilchenko, "Quality-factor and nonlinear properties of optical whispering-gallery modes", Physics Letters A **137**, 393–397 (1989).

[81]V. S. Ilchenko, X. S. Yao, and L. Maleki, "Pigtailing the high-q microsphere cavity: a simple fiber coupler for optical whispering-gallery modes", Optics Letters **24**, 723–725 (1999).

[82]H. A. Haus, *Waves and fields in optoelectronics* (Prentice-Hall, 1984).

[83]Y.-H. Lai, **K.Y. Yang**, M.-G. Suh, and K. J. Vahala, "Fiber taper characterization by optical backscattering reflectometry", **Optics Express 25**, 22312 (2017) 10.1364/OE.25.022312.

[84]P. Michler, A. Kiraz, L. Zhang, C. Becher, E. Hu, and A. Imamoglu, "Laser emission from quantum dots in microdisk structures", Applied Physics Letters **77**, 184–186 (2000).

[85]B. Gayral, J. Gérard, A. Lemaıtre, C. Dupuis, L. Manin, and J. Pelouard, "High-q wet-etched gaas microdisks containing inas quantum boxes", Applied physics letters **75**, 1908–1910 (1999).

[86]X. Zhang, H. S. Choi, and A. M. Armani, "Ultimate quality factor of silica microtoroid resonant cavities", Applied physics letters **96**, 77 (2010).

[87]T. Chen, H. Lee, and K. J. Vahala, "Thermal stress in silica-on-silicon disk resonators", Applied Physics Letters **102**, 031113 (2013).

[88]P. E. Barclay, K. Srinivasan, O. Painter, B. Lev, and H. Mabuchi, "Integration of fiber-coupled high-q sinx microdisks with atom chips", Applied physics letters **89**, 131108 (2006).

[89]J. F. Bauters, M. J. Heck, D. John, D. Dai, M.-C. Tien, J. S. Barton, A. Leinse, R. G. Heideman, D. J. Blumenthal, and J. E. Bowers, "Ultra-low-loss high-aspect-ratio si3n4 waveguides", Optics express **19**, 3163–3174 (2011).

[90]X. Ji, F. A. Barbosa, S. P. Roberts, A. Dutt, J. Cardenas, Y. Okawachi, A. Bryant, A. L. Gaeta, and M. Lipson, "Breaking the loss limitation of on-chip high-confinement resonators", arXiv preprint arXiv:1609.08699 (2016).

[91]Y. Xuan, Y. Liu, L. T. Varghese, A. J. Metcalf, X. Xue, P.-H. Wang, K. Han, J. A. Jaramillo-Villegas, A. Al Noman, C. Wang, et al., "High-q silicon nitride microresonators exhibiting low-power frequency comb initiation", Optica **3**, 1171–1180 (2016).

[92]B. Min, L. Yang, and K. Vahala, "Controlled transition between parametric and raman oscillations in ultrahigh-q silica toroidal microcavities", Applied Physics Letters **87**, 181109 (2005).

[93]T. Carmon, T. J. Kippenberg, L. Yang, H. Rokhsari, S. Spillane, and K. J. Vahala, "Feedback control of ultra-high-Q microcavities: application to micro-raman lasers and micro-parametric oscillators", Optics Express **13**, 3558–3566 (2005).

[94]D. J. Moss, R. Morandotti, A. L. Gaeta, and M. Lipson, "New CMOS-compatible platforms based on silicon nitride and hydex for nonlinear optics", Nature Photonics **7**, 597–607 (2013).

[95]Y. Okawachi, K. Saha, J. S. Levy, Y. H. Wen, M. Lipson, and A. L. Gaeta, "Octave-spanning frequency comb generation in a silicon nitride chip", Optics letters **36**, 3398–3400 (2011).

[96]P. Del'Haye, T. Herr, E. Gavartin, M. Gorodetsky, R. Holzwarth, and T. Kippenberg, "Octave spanning tunable frequency comb from a microresonator", Physical review letters **107**, 063901 (2011).

[97]K. Saha, Y. Okawachi, J. S. Levy, R. K. Lau, K. Luke, M. A. Foster, M. Lipson, and A. L. Gaeta, "Broadband parametric frequency comb generation with a 1-μm pump source", Opt. Express **20**, 26935–26941 (2012) 10.1364/OE.20.026935.

[98]J. Li, H. Lee, K. Y. Yang, and K. J. Vahala, "Sideband spectroscopy and dispersion measurement in microcavities", Opt. Express **20**, 26337–26344 (2012).

[99]L. G. Cohen, and C. Lin, "Pulse delay measurements in the zero material dispersion wavelength region for optical fibers", Applied optics **16**, 3136–3139 (1977).

[100]D. Y. Oh†, **K.Y. Yang**†, C. Fredrick†, G. Ycas, S. A. Diddams, and K. J. Vahala, "Coherent ultra-violet to near-infrared generation in silica ridge waveguides", **Nature Communications 8**, 13922 (2017) 10.1038/ncomms13922,

[101]J. Riemensberger, K. Hartinger, T. Herr, V. Brasch, R. Holzwarth, and T. J. Kippenberg, "Dispersion engineering of thick high-Q silicon nitride ring-resonators via atomic layer deposition", Opt. Express **20**, 27661–27669 (2012).

[102]J. Liu, V. Brasch, M. H. Pfeiffer, A. Kordts, A. N. Kamel, H. Guo, M. Geiselmann, and T. J. Kippenberg, "Frequency-comb-assisted broadband precision spectroscopy with cascaded diode lasers", Optics Letters **41**, 3134–3137 (2016) 10.1364/OL.41.003134.

[103]S.-W. Huang, H. Zhou, J. Yang, J. McMillan, A. Matsko, M. Yu, D.-L. Kwong, L. Maleki, and C. Wong, "Mode-locked ultrashort pulse generation from on-chip normal dispersion microresonators", Physical review letters **114**, 053901 (2015).

[104]S.-W. Huang, H. Liu, J. Yang, M. Yu, D.-L. Kwong, and C. Wong, "Smooth and flat phase-locked kerr frequency comb generation by higher order mode suppression", Scientific reports **6** (2016).

[105]Q.-F. Yang†, X. Yi†, **K.Y. Yang**, and K. Vahala, "Stokes solitons in optical microcavities", **Nature Physics 13**, 53–57 (2017) 10.1038/nphys3875.

[106]P. Del'Haye, K. Beha, S. B. Papp, and S. A. Diddams, "Self-injection locking and phase-locked states in microresonator-based optical frequency combs", Physical review letters **112**, 043905 (2014).

[107]K. Beha, D. C. Cole, P. DelHaye, A. Coillet, S. A. Diddams, and S. B. Papp, "Electronic synthesis of light", Optica **4**, 406–411 (2017).

[108]B. E. Deal, and A. Grove, "General relationship for the thermal oxidation of silicon", Journal of Applied Physics **36**, 3770–3778 (1965).

[109]K. White, and B. Nelson, "Zero total dispersion in step-index monomode fibres at 1.30 and 1.55 μm", Electron. Lett. **15**, 396–397 (1979).

[110]L. Maleki, A. A. Savchenkov, V. S. Ilchenko, and A. B. Matsko, "Whispering gallery mode lithium niobate microresonators for photonics applications", in Aerosense 2003 (International Society for Optics and Photonics, 2003), pp. 1–13.

[111]A. Matsko, A. Savchenkov, D. Strekalov, V. Ilchenko, and L. Maleki, "Review of applications of whispering-gallery mode resonators in photonics and nonlinear optics", IPN Progress Report **42**, 1–51 (2005).

[112]T. Carmon, H. G. Schwefel, L. Yang, M. Oxborrow, A. D. Stone, and K. J. Vahala, "Static envelope patterns in composite resonances generated by level crossing in optical toroidal microcavities", Physical Review Letters **100**, 103905 (2008).

[113]S. Ramelow, A. Farsi, S. Clemmen, J. S. Levy, A. R. Johnson, Y. Okawachi, M. R. Lamont, M. Lipson, and A. L. Gaeta, "Strong polarization mode coupling in microresonators", Optics letters **39**, 5134–5137 (2014).

[114]A. Kordts, M. Pfeiffer, H. Guo, V. Brasch, and T. J. Kippenberg, "Higher order mode suppression in high-Q anomalous dispersion sin microresonators for temporal dissipative kerr soliton formation", Optics letters **41**, 452–455 (2016).

[115]L. Razzari, D. Duchesne, M. Ferrera, R. Morandotti, S. Chu, B. Little, and D. Moss, "Cmos-compatible integrated optical hyper-parametric oscillator", Nature Photonics **4**, 41–45 (2010).

[116]H. Jung, C. Xiong, K. Y. Fong, X. Zhang, and H. X. Tang, "Optical frequency comb generation from aluminum nitride microring resonator", Optics letters **38**, 2810–2813 (2013).

[117]M. Pu, L. Ottaviano, E. Semenova, and K. Yvind, "Efficient frequency comb generation in algaas-on-insulator", Optica **3**, 823–826 (2016).

[118]X. Yi, Q.-F. Yang, K. Y. Yang, and K. Vahala, "Active capture and stabilization of temporal solitons in microresonators", Optics letters **41**, 2037–2040 (2016).

[119]Y. Yang, X. Jiang, S. Kasumie, G. Zhao, L. Xu, J. M. Ward, L. Yang, and S. N. Chormaic, "Four-wave mixing parametric oscillation and frequency comb generation at visible wavelengths in a silica microbubble resonator", Optics Letters **41**, 5266–5269 (2016).

[120]Q.-F. Yang, X. Yi, K. Y. Yang, and K. Vahala, "Spatial-mode-interaction-induced dispersive waves and their active tuning in microresonators", Optica **3**, 1132–1135 (2016).

[121]A. Cherenkov, V. Lobanov, and M. Gorodetsky, "Dissipative kerr solitons and cherenkov radiation in optical microresonators with third-order dispersion", Physical Review A **95**, 033810 (2017).

[122]S. Fujii, T. Kato, R. Suzuki, and T. Tanabe, "Third-harmonic blue light generation from kerr clustered combs and dispersive waves", Optics Letters **42**, 2010–2013 (2017).

[123]L. Cohen, W. Mammel, and S. Jang, "Low-loss quadruple-clad single-mode lightguides with dispersion below 2 ps/km-nm over the 1.28 μm–1.65 μm wavelength range", Electron. Lett. **18**, 1023–1024 (1982).

[124]B. J. Ainslie, and C. R. Day, "A review of single-mode fibers with modified dispersion characteristics", J. Lightwave Technol. **4**, 967–979 (1986).

[125]H. Tsuchiya, and N. Imoto, "Dispersion-free single-mode fibre in 1.5 μm wavelength region", Electron. Lett. **15**, 476–478 (1979).

[126]S. Kawakami, and S. Nishida, "Characteristics of a doubly clad optical fiber with a low-index inner cladding", IEEE J. Quant. Electron. **10**, 879–887 (1974).

[127]H. Etzkorn, and W. Heinlein, "Low-dispersion single-mode silica fibre with undoped core and three F-doped claddings", Electron. Lett. **20**, 423–424 (1984).

[128]I. Malitson, "Interspecimen comparison of the refractive index of fused silica*", Journal of the Optical Society of America **55**, 1205–1209 (1965).

[129]M. Soltani, A. Matsko, and L. Maleki, "Enabling arbitrary wavelength frequency combs on chip", Laser & Photonics Reviews **10**, 158–162 (2016) 10.1002/lpor.201500226.

[130]S. Kim, K. Han, C. Wang, J. A. Jaramillo-Villegas, X. Xue, C. Bao, Y. Xuan, D. E. Leaird, A. M. Weiner, and M. Qi, "Frequency comb generation in 300 nm thick sin concentric-racetrack-resonators: overcoming the material dispersion limit", arXiv preprint arXiv:1607.01850 (2016).

[131]X. Zhang, M. Harrison, A. Harker, and A. M. Armani, "Serpentine low loss trapezoidal silica waveguides on silicon", Optics express **20**, 22298–22307 (2012) 10.1364/OE.20.022298.

[132]http://www.suss.com/en/products-solutions/technologies/alignment.html.

[133]http://www.cnf.cornell.edu/cnf_process_photo_step_align.html.

[134]K. Tamura, L. Nelson, H. Haus, and E. Ippen, "Soliton versus nonsoliton operation of fiber ring lasers", Applied physics letters **64**, 149–151 (1994).

[135]K. Y. Yang, K. Beha, D. C. Cole, X. Yi, P. Del'Haye, H. Lee, J. Li, D. Y. Oh, S. A. Diddams, S. B. Papp, et al., "Dispersion engineered high-q resonators on a chip", in Cleo: science and innovations (Optical Society of America, 2016), STu4Q–5.

[136]P. Del'Haye, A. Coillet, W. Loh, K. Beha, S. B. Papp, and S. A. Diddams, "Phase steps and resonator detuning measurements in microresonator frequency combs", Nature communications **6** (2015).

[137]A. R. Johnson, Y. Okawachi, J. S. Levy, J. Cardenas, K. Saha, M. Lipson, and A. L. Gaeta, "Chip-based frequency combs with sub-100 ghz repetition rates", Optics letters **37**, 875–877 (2012).

[138]K. Saha, Y. Okawachi, B. Shim, J. S. Levy, R. Salem, A. R. Johnson, M. A. Foster, M. R. Lamont, M. Lipson, and A. L. Gaeta, "Modelocking and femtosecond pulse generation in chip-based frequency combs", Optics express **21**, 1335–1343 (2013).

[139]I. S. Grudinin, and N. Yu, "Dispersion engineering of crystalline resonators via microstructuring", Optica **2**, 221–224 (2015) 10.1364/OPTICA.2.000221.

[140]A. A. Savchenkov, A. B. Matsko, V. S. Ilchenko, I. Solomatine, D. Seidel, and L. Maleki, "Tunable optical frequency comb with a crystalline whispering gallery mode resonator", Physical review letters **101**, 093902 (2008).

[141]I. S. Grudinin, and N. Yu, "Frequency combs from crystalline resonators: influence of cavity parameters on comb dynamics", Optical Engineering **53**, 122609–122609 (2014).

[142]Y. Okawachi, M. R. Lamont, K. Luke, D. O. Carvalho, M. Yu, M. Lipson, and A. L. Gaeta, "Bandwidth shaping of microresonator-based frequency combs via dispersion engineering", Optics letters **39**, 3535–3538 (2014).

[143]S. H. Lee†, D. Y. Oh†, Q.-F. Yang†, B. Shen†, H. Wang†, **K.Y. Yang**, Y.-H. Lai, X. Yi, and K. Vahala, "Towards visible soliton microcomb generation", **Nature Communications 8**, 1295 (2017) 10.1038/s41467-017-01473-9.

[144]X. Xue, Y. Xuan, Y. Liu, P.-H. Wang, S. Chen, J. Wang, D. E. Leaird, M. Qi, and A. M. Weiner, "Mode-locked dark pulse kerr combs in normal-dispersion microresonators", Nature Photonics **9**, 594–600 (2015).

[145]C. Phillips, C. Langrock, J. Pelc, M. Fejer, J. Jiang, M. E. Fermann, and I. Hartl, "Supercontinuum generation in quasi-phase-matched linbo3 waveguide pumped by a tm-doped fiber laser system", Optics letters **36**, 3912–3914 (2011).

[146]X. Gai, D.-Y. Choi, S. Madden, Z. Yang, R. Wang, and B. Luther-Davies, "Supercontinuum generation in the mid-infrared from a dispersion-engineered As_2S_3 glass rib waveguide", Optics letters **37**, 3870–3872 (2012).

[147]M. R. Lamont, B. Luther-Davies, D.-Y. Choi, S. Madden, and B. J. Eggleton, "Supercontinuum generation in dispersion engineered highly nonlinear (γ= 10/w/m) As_2S_3 chalcogenide planar waveguide", Optics Express **16**, 14938–14944 (2008).

[148]N. Singh, D. D. Hudson, Y. Yu, C. Grillet, S. D. Jackson, A. Casas-Bedoya, A. Read, P. Atanackovic, S. G. Duvall, S. Palomba, et al., "Midinfrared supercontinuum generation from 2 to 6 μm in a silicon nanowire", Optica **2**, 797–802 (2015).

[149]B. Kuyken, T. Ideguchi, S. Holzner, M. Yan, T. W. Hänsch, J. Van Campenhout, P. Verheyen, S. Coen, F. Leo, R. Baets, et al., "An octave-spanning mid-infrared frequency comb generated in a silicon nanophotonic wire waveguide", Nature communications **6** (2015).

[150]F. Leo, S.-P. Gorza, J. Safioui, P. Kockaert, S. Coen, U. Dave, B. Kuyken, and G. Roelkens, "Dispersive wave emission and supercontinuum generation in a silicon wire waveguide pumped around the 1550 nm telecommunication wavelength", Optics letters **39**, 3623–3626 (2014).

[151]J. P. Epping, T. Hellwig, M. Hoekman, R. Mateman, A. Leinse, R. G. Heideman, A. van Rees, P. J. van der Slot, C. J. Lee, C. Fallnich, et al., "On-chip visible-to-infrared supercontinuum generation with more than 495 thz spectral bandwidth", Optics express **23**, 19596–19604 (2015).

[152]H. Zhao, B. Kuyken, S. Clemmen, F. Leo, A. Subramanian, A. Dhakal, P. Helin, S. Severi, E. Brainis, G. Roelkens, et al., "Visible-to-near-infrared octave spanning supercontinuum generation in a silicon nitride waveguide", Optics letters **40**, 2177–2180 (2015).

[153]A. R. Johnson, A. S. Mayer, A. Klenner, K. Luke, E. S. Lamb, M. R. Lamont, C. Joshi, Y. Okawachi, F. W. Wise, M. Lipson, et al., "Octave-spanning coherent supercontinuum generation in a silicon nitride waveguide", Optics letters **40**, 5117–5120 (2015).

[154]D. Y. Oh, D. Sell, H. Lee, K. Y. Yang, S. A. Diddams, and K. J. Vahala, "Supercontinuum generation in an on-chip silica waveguide", Optics letters **39**, 1046–1048 (2014).

[155]M. A. Foster, A. C. Turner, M. Lipson, and A. L. Gaeta, "Nonlinear optics in photonic nanowires", Optics Express **16**, 1300–1320 (2008).

[156]F. Leo, J. Safioui, B. Kuyken, G. Roelkens, and S.-P. Gorza, "Generation of coherent supercontinuum in a-si: h waveguides: experiment and modeling based on measured dispersion profile", Optics express **22**, 28997–29007 (2014).

[157]R. K. Lau, M. R. Lamont, A. G. Griffith, Y. Okawachi, M. Lipson, and A. L. Gaeta, "Octave-spanning mid-infrared supercontinuum generation in silicon nanowaveguides", Optics letters **39**, 4518–4521 (2014).

[158]A. Mayer, A. Klenner, A. Johnson, K. Luke, M. Lamont, Y. Okawachi, M. Lipson, A. Gaeta, and U. Keller, "Frequency comb offset detection using supercontinuum generation in silicon nitride waveguides", Optics express **23**, 15440–15451 (2015).

[159]D. Träutlein, F. Adler, K. Moutzouris, A. Jeromin, A. Leitenstorfer, and E. Ferrando-May, "Highly versatile confocal microscopy system based on a tunable femtosecond er: fiber source", Journal of biophotonics **1**, 53–61 (2008).

[160]I. Cristiani, R. Tediosi, L. Tartara, and V. Degiorgio, "Dispersive wave generation by solitons in microstructured optical fibers", Optics express **12**, 124–135 (2004).

[161]G. Chang, L.-J. Chen, and F. X. Kärtner, "Highly efficient cherenkov radiation in photonic crystal fibers for broadband visible wavelength generation", Optics letters **35**, 2361–2363 (2010).

[162]M. Hu, C.-y. Wang, Y. Li, Z. Wang, L. Chai, and A. M. Zheltikov, "Multiplex frequency conversion of unamplified 30-fs ti: sapphire laser pulses by an array of waveguiding wires in a random-hole microstructure fiber", Optics express **12**, 6129–6134 (2004).

[163]S. Stark, J. Travers, and P. S. J. Russell, "Extreme supercontinuum generation to the deep uv", Optics letters **37**, 770–772 (2012).

[164]X. Jiang, N. Y. Joly, M. A. Finger, F. Babic, G. K. Wong, J. C. Travers, and P. S. J. Russell, "Deep-ultraviolet to mid-infrared supercontinuum generated in solid-core zblan photonic crystal fibre", Nature Photonics **9**, 133–139 (2015).

[165]H. Lee, T. Chen, J. Li, O. Painter, and K. J. Vahala, "Ultra-low-loss optical delay line on a silicon chip", Nature communications **3**, 867 (2012).

[166]F. Vollmer, and S. Arnold, "Whispering-gallery-mode biosensing: label-free detection down to single molecules", Nature Methods **5**, 591–596 (2008).

[167]T. Lu, H. Lee, T. Chen, S. Herchak, J.-H. Kim, S. E. Fraser, R. C. Flagan, and K. Vahala, "High sensitivity nanoparticle detection using optical microcavities", Proceedings of the National Academy of Sciences **108**, 5976–5979 (2011).

[168]F. Vollmer, and L. Yang, "Label-free detection with high-Q microcavities: a review of biosensing mechanisms for integrated devices", Nanophotonics **1**, 267–291 (2012).

[169]H. J. Kimble, "The quantum internet", Nature **453**, 1023–1030 (2008).

[170]T. J. Kippenberg, and K. J. Vahala, "Cavity optomechanics: back-action at the mesoscale", Science **321**, 1172–1176 (2008).

[171]D. T. Spencer, et al., "Towards an integrated-photonics optical-frequency synthesizer with <1 Hz residual frequency noise", in Optical fiber communication conference (2017), M2J.2.

[172]F. DellOlio, T. Tatoli, C. Ciminelli, and M. Armenise, "Recent advances in miniaturized optical gyroscopes", Journal of the European Optical Society - Rapid publications **9** (2014).

[173]I. Frank, et al., "A low-power, chip-scale optical atomic clock with enhanced stability", in Joint navigation conference (2017).

[174]Q. Li, A. A. Eftekhar, M. Sodagar, Z. Xia, A. H. Atabaki, and A. Adibi, "Vertical integration of high-q silicon nitride microresonators into silicon-on-insulator platform", Optics express **21**, 18236–18248 (2013).

[175]A. Gondarenko, J. S. Levy, and M. Lipson, "High confinement micron-scale silicon nitride high q ring resonator", Optics express **17**, 11366–11370 (2009).

[176]K. Luke, A. Dutt, C. B. Poitras, and M. Lipson, "Overcoming Si_3N_4 film stress limitations for high quality factor ring resonators", Optics express **21**, 22829–22833 (2013).

[177]L. Zhuang, D. Marpaung, M. Burla, W. Beeker, A. Leinse, and C. Roeloffzen, "Low-loss, high-index-contrast si 3 n 4/sio 2 optical waveguides for optical delay lines in microwave photonics signal processing", Optics express **19**, 23162–23170 (2011).

[178]M. Borselli, T. J. Johnson, and O. Painter, "Beyond the rayleigh scattering limit in high-q silicon microdisks: theory and experiment", Optics express **13**, 1515–1530 (2005).

[179]A. Biberman, M. J. Shaw, E. Timurdogan, J. B. Wright, and M. R. Watts, "Ultralow-loss silicon ring resonators", Optics letters **37**, 4236–4238 (2012).

[180]R. Adar, Y. Shani, C. Henry, R. Kistler, G. Blonder, and N. Olsson, "Measurement of very low-loss silica on silicon waveguides with a ring resonator", Applied physics letters **58**, 444–445 (1991).

[181]R. Adar, M. Serbin, and V. Mizrahi, "Less than 1 db per meter propagation loss of silica waveguides measured using a ring resonator", Journal of lightwave technology **12**, 1369–1372 (1994).

[182]M. J. Heck, J. F. Bauters, M. L. Davenport, D. T. Spencer, and J. E. Bowers, "Ultra-low loss waveguide platform and its integration with silicon photonics", Laser & Photonics Reviews **8**, 667–686 (2014).

[183]F. Xia, L. Sekaric, and Y. Vlasov, "Ultracompact optical buffers on a silicon chip", Nature photonics **1**, 65–71 (2007).

[184]F. Xia, M. Rooks, L. Sekaric, and Y. Vlasov, "Ultra-compact high order ring resonator filters using submicron silicon photonic wires for on-chip optical interconnects", Optics express **15**, 11934–11941 (2007).

[185]A. Shacham, K. Bergman, and L. P. Carloni, "Photonic networks-on-chip for future generations of chip multiprocessors", IEEE Transactions on Computers **57**, 1246–1260 (2008).

[186]W. Bogaerts, P. De Heyn, T. Van Vaerenbergh, K. De Vos, S. Kumar Selvaraja, T. Claes, P. Dumon, P. Bienstman, D. Van Thourhout, and R. Baets, "Silicon microring resonators", Laser & Photonics Reviews **6**, 47–73 (2012).

[187]D. Marpaung, C. Roeloffzen, R. Heideman, A. Leinse, S. Sales, and J. Capmany, "Integrated microwave photonics", Laser & Photonics Reviews **7**, 506–538 (2013).

[188]W. Loh, A. A. Green, F. N. Baynes, D. C. Cole, F. J. Quinlan, H. Lee, K. J. Vahala, S. B. Papp, and S. A. Diddams, "Dual-microcavity narrow-linewidth brillouin laser", Optica **2**, 225–232 (2015).

[189]J. Li, X. Yi, H. Lee, S. A. Diddams, and K. J. Vahala, "Electro-optical frequency division and stable microwave synthesis", Science **345**, 309–313 (2014).

[190]J. R. Vig, *Introduction to quartz frequency standards. revision*, tech. rep. (DTIC Document, 1992).

[191]J. Li, M.-G. Suh, and K. Vahala, "Microresonator brillouin gyroscope", Optica **4**, 346–348 (2017) 10.1364/OPTICA.4.000346.

[192]W. Liang, V. S. Ilchenko, A. A. Savchenkov, E. Dale, D. Eliyahu, A. B. Matsko, and L. Maleki, "Resonant microphotonic gyroscope", Optica **4**, 114–117 (2017).

[193]M. H. Pfeiffer, C. Herkommer, J. Liu, H. Guo, M. Karpov, E. Lucas, M. Zervas, and T. J. Kippenberg, "Octave-spanning dissipative kerr soliton frequency combs in Si_3N_4 microresonators", arXiv preprint arXiv:1701.08594 (2017).

[194]Q. Li, T. C. Briles, D. A. Westly, T. E. Drake, J. R. Stone, B. R. Ilic, S. A. Diddams, S. B. Papp, and K. Srinivasan, "Stably accessing octave-spanning microresonator frequency combs in the soliton regime", Optica **4**, 193–203 (2017).

[195]N. T. Otterstrom, R. O. Behunin, E. A. Kittlaus, Z. Wang, and P. T. Rakich, "A silicon brillouin laser", arXiv preprint arXiv:1705.05813 (2017).

[196]B. Morrison, A. Casas-Bedoya, G. Ren, K. Vu, Y. Liu, A. Zarifi, T. Nguyen, D. Choi, D. Marpaung, S. Madden, et al., "Compact brillouin devices through hybrid integration on silicon", arXiv preprint arXiv:1702.05233 (2017).

[197]C. Lecaplain, C. Javerzac-Galy, M. Gorodetsky, and T. Kippenberg, "Mid-infrared ultra-high-Q resonators based on fluoride crystalline materials", Nature Communications **7** (2016).

[198]A. Yariv, and P. Yeh, *Photonics: optical electronics in modern communications*, Vol. 6 (oxford university press New York, 2007).

[199]K. Y. Yang, D. Y. Oh, S. H. Lee, and K. J. Vahala, "Ultra-high-q silica-on-silicon ridge-ring-resonator with an integrated silicon nitride waveguide", in Cleo: qels_fundamental science (Optical Society of America, 2016), JTh4B–7.

[200]M. L. Davenport, S. Skendzic, N. Volet, and J. E. Bowers, "Heterogeneous silicon/inp semiconductor optical amplifiers with high gain and high saturation power", in Lasers and electro-optics (cleo), 2016 conference on (IEEE, 2016), pp. 1–2.

[201]M. H. Pfeiffer, J. Liu, M. Geiselmann, and T. J. Kippenberg, "Coupling ideality of integrated planar high-Q microresonators", Physical Review Applied **7**, 024026 (2017).

[202]T. Chen, H. Lee, and K. J. Vahala, "Design and characterization of whispering-gallery spiral waveguides", Optics express **22**, 5196–5208 (2014).

[203]D. T. Spencer, Y. Tang, J. F. Bauters, M. J. Heck, and J. E. Bowers, "Integrated si3n4/sio 2 ultra high q ring resonators", in Photonics conference (ipc), 2012 ieee (IEEE, 2012), pp. 141–142.

[204]Y. A. Vlasov, and S. J. McNab, "Losses in single-mode silicon-on-insulator strip waveguides and bends", Optics express **12**, 1622–1631 (2004).

[205]G. Grand, J. Jadot, H. Denis, S. Valette, A. Fournier, and A. Grouillet, "Low-loss pecvd silica channel waveguides for optical communications", Electronics letters **26**, 2135–2137 (1990).

[206]V. R. Almeida, R. R. Panepucci, and M. Lipson, "Nanotaper for compact mode conversion", Optics letters **28**, 1302–1304 (2003).

[207]C. Joshi, J. K. Jang, K. Luke, X. Ji, S. A. Miller, A. Klenner, Y. Okawachi, M. Lipson, and A. L. Gaeta, "Thermally controlled comb generation and soliton modelocking in microresonators", Optics letters **41**, 2565–2568 (2016).

[208]P.-H. Wang, J. A. Jaramillo-Villegas, Y. Xuan, X. Xue, C. Bao, D. E. Leaird, M. Qi, and A. M. Weiner, "Intracavity characterization of micro-comb generation in the single-soliton regime", Optics express **24**, 10890–10897 (2016).

[209]R. C. Figueiredo, N. S. Ribeiro, A. M. O. Ribeiro, C. M. Gallep, and E. Conforti, "Hundred-picoseconds electro-optical switching with semiconductor optical amplifiers using multi-impulse step injection current", Journal of Lightwave Technology **33**, 69–77 (2015).

[210]M. L. Davenport, S. Skendzic, N. Volet, and J. E. Bowers, "Heterogeneous silicon/inp semiconductor optical amplifiers with high gain and high saturation power", in Lasers and electro-optics (cleo), 2016 conference on (IEEE, 2016), pp. 1–2.

[211]Z. Zhou, B. Yin, and J. Michel, "On-chip light sources for silicon photonics", Light: Science and Applications **4**, e358 (2015).

[212]S. Chen, W. Li, J. Wu, Q. Jiang, M. Tang, S. Shutts, S. N. Elliott, A. Sobiesierski, A. J. Seeds, I. Ross, et al., "Electrically pumped continuous-wave iii–v quantum dot lasers on silicon", Nature Photonics (2016).

[213]T. C. Briles, T. Drake, D. Spencer, J. R. Stone, C. Fredrick, Q. Li, D. Westly, B. Ilic, X. Yi, K. Y. Yang, et al., "Optical frequency synthesis using a dual-kerr-microresonator frequency comb", in Cleo: science and innovations (Optical Society of America, 2017), SW4N–3.

[214]P. Del'Haye, A. Coillet, T. Fortier, K. Beha, D. C. Cole, **K.Y. Yang**, H. Lee, K. J. Vahala, S. B. Papp, and S. A. Diddams, "Phase-coherent microwave-to-optical link with a self-referenced microcomb", **Nature Photonics 10**, 516–520 (2016) `10.1038/nphoton.2016.105`.

[215]L. Chang, Y. Li, N. Volet, L. Wang, J. Peters, and J. E. Bowers, "Thin film wavelength converters for photonic integrated circuits", Optica **3**, 531–535 (2016).

[216]X. Guo, C.-L. Zou, and H. X. Tang, "Second-harmonic generation in aluminum nitride microrings with 2500%/w conversion efficiency", Optica **3**, 1126–1131 (2016).

[217]T. Komljenovic, S. Srinivasan, E. Norberg, M. Davenport, G. Fish, and J. E. Bowers, "Widely tunable narrow-linewidth monolithically integrated external-cavity semiconductor lasers", IEEE Journal of Selected Topics in Quantum Electronics **21**, 214–222 (2015).

[218]R. Lutwak, "The chip-scale atomic clock-recent developments", in Frequency control symposium, 2009 joint with the 22nd european frequency and time forum. ieee international (IEEE, 2009), pp. 573–577.